Late-stage infall of material onto planet-forming disks

Aashish Gupta

München 2024

Late-stage infall of material onto planet-forming disks

Aashish Gupta

Dissertation
der Fakultät für Physik
der Ludwig-Maximilians-Universität
München

vorgelegt von
Aashish Gupta
aus Dhansara, Indien

München, den 19.09.2024

Erstgutachter: Prof. Dr. Til Birnstiel
Zweitgutachter: Prof. Dr. Barbara Ercolano
Tag der mündlichen Prüfung: 12.11.2024

Contents

List of Figures

List of Tables

Zusammenfassung

Die meisten Sterne werden in Gruppen in ausgedehnten ($\gtrsim$ 1 pc) molekularen Wolken geboren. Die Lehrbuchbeschreibung des Sternentstehungsprozesses legt nahe, dass sich die umgebenden Gashüllen vollständig auflösen, wenn sich die Protosterne vom Stadium der eingebetteten Klasse I zur Klasse II entwickeln. Zurück bleiben Protostern-Scheiben-Systeme, von denen man annimmt, dass sie sich isoliert zu Planetensystemen wie unserem Sonnensystem weiterentwickeln. Wir wissen jedoch, dass sich diese entwickelten Klasse-II-Quellen immer noch innerhalb großer Wolken bewegen, und Simulationen zeigen, dass sie weiterhin frisches Material aus ihrer Umgebung akkretieren. Der Zufluss von Material in diesen späteren Stadien kann die physikalischen und chemischen Eigenschaften protoplanetarer Scheiben erheblich verändern und möglicherweise viele offene Probleme bei der Stern- und Planetenbildung lösen. Wir wissen jedoch noch nicht, wie verbreitet und wirkungsvoll dieses Phänomen ist.

Anzeichen eines solchen Zuflusses von Material, insbesondere längliche Spuren einfallenden Gases, die oft als *Streamers* bezeichnet werden, sind in der Nähe mehrerer Quellen beobachtet worden. Diese Entdeckungen waren jedoch meist zufällig, sodass es uns verwehrt bleibt, die Häufigkeit dieses Phänomens zu verstehen. Um dies zu erreichen, untersuchten wir, ob die Nähe zu Reflexionsnebeln, bei denen es sich im Wesentlichen um Wolken in der Nähe von YSOs handelt, als Kriterium für die Identifizierung von Late-Infall-Kandidaten verwendet werden kann, wie in Kapitel 2 berichtet. Wir fanden heraus, dass alle Quellen der Klasse II mit bekannten ausgedehnten Gasstrukturen, die wahrscheinlich auf einfallendes Material zurückzuführen sind, Reflexionsnebel in ihrer Umgebung aufweisen. Darüber hinaus haben wir eine unabhängige Stichprobe von Quellen der Klasse II erstellt, die mit Reflexionsnebeln assoziiert sind, und alle Ziele mit adäquaten Archivbeobachtungen zeigen einige Anzeichen von Zufluss. Da Reflexionsnebel häufig in der Nähe von Klasse-II-Systemen zu sehen sind, deuten unsere Ergebnisse darauf hin, dass dieses Phänomen bei einem signifikanten Teil der Klasse-II-Systeme auftritt.

Obwohl zufließende Streamer inzwischen routinemäßig entdeckt werden, ist es nicht einfach, ihren Einfluss auf die Stern- und Planetenentstehungsprozesse zu beurteilen, insbesondere bei den weiter entwickelten YSOs. Um die zufließende Natur der beobachteten Streamer zu bestimmen und ihre Dynamik zu charakterisieren, haben wir einen neuartigen Code TIPSY (Trajectory of Infalling Particles in Streamers around Young stars) entwickelt, wie in Kapitel 3 beschrieben. TIPSY passt gleichzeitig die Morphologie und den Geschwindigkeitsgradienten von Streamer-Beobachtungen mit theoretischen Trajektorien

von einfallendem Material an. Die am besten angepassten Trajektorien werden verwendet, um Streamer-Eigenschaften wie die spezifische Energie, die spezifischen Drehimpulse, die Zeitskala des Einfalls und die 3D-Morphologie zu bestimmen. Als Testfälle haben wir TIPSY benutzt, um Beobachtungen von Streamern um S CrA und HL Tau zu modellieren, und diese Streamer führen den Scheiben Material mit Raten von ~ 10 $M_{jupiter}$ Myr^{-1} zu.

Um die Auswirkungen des späten Einfalls auf die allgemeine Population von Klasse-II-Systemen zu beurteilen, ist eine einheitliche Untersuchung solcher Strukturen erforderlich. DECO (Disk-Exoplanet C/Onnection) ist ein großes ALMA-Programm zur Untersuchung der Scheibenchemie von 80 Klasse-II-Quellen, die über vier Sternentstehungsgebiete verteilt sind. Interessanterweise haben die mäßig aufgelösten und tiefen Beobachtungen von DECO ausgedehnte ($\gtrsim 500$ au) gebundene Strukturen um $\sim 40\%$ der Quellen aufgedeckt, wie in Kapitel 4 diskutiert. Außerdem variiert die Häufigkeit dieser Strukturen in den vier Regionen erheblich. Wir finden auch einen vermuteten Einfluss der Masse der gebundenen Strukturen auf die Masse, die von den zentralen Protosternen aus den Scheiben akkretiert wird. Diese Beobachtungen stellen die traditionelle Annahme von isolierten planetenbildenden Scheiben in Frage.

Künftig werden wir durch gezielte Untersuchungen der Signaturen von Zuflüssen in der Umgebung von Klasse-II-Systemen in Verbindung mit einem besseren Verständnis der Zeitskalen solcher Ereignisse mehr über deren Häufigkeit und deren Abhängigkeit von der Sternentstehungsumgebung erfahren. Darüber hinaus wird eine verbesserte Charakterisierung der physikalischen und chemischen Eigenschaften des einfallenden Gases und der Systeme, auf die sie einwirken, es uns ermöglichen, das Ausmaß ihres Einflusses auf die Stern- und Planetenbildung zu verstehen.

Abstract

Most stars are born in groups in large-scale ($\gtrsim$ 1 pc) molecular clouds. The textbook description of the star formation process suggests that as the protostars evolve from the embedded Class I to Class II stage, the surrounding gaseous envelopes are fully dispersed. This leaves behind protostar-disk systems which are assumed to evolve in isolation to form planetary systems like our Solar System. However, we know that these evolved Class II sources are still moving within large-scale clouds and simulations show that they continue to accrete fresh material from their surroundings. Infall of material at these later stages can considerably alter the physical and chemical properties of protoplanetary disks, potentially resolving many open problems in star and planet formation. However, we do not yet know how common and impactful this phenomenon is.

Signatures of such infall, particularly elongated trails of infalling gas often referred to as *streamers*, have been observed around several sources. However, these detections have mostly been serendipitous which does not allow us to understand the frequency of this phenomenon. To systematically study this, we examined whether proximity to reflection nebulae, which are essentially clouds in the vicinity of YSOs, could be used as a criterion for identifying late-infall candidates, as reported in Chapter 2. We found that all the Class II sources with known large-scale gas structures, likely due to infalling material, have reflection nebulosity in the vicinity. Moreover, we built an independent sample of Class II sources associated with reflection nebulae and all targets with adequate archival observations show some signatures of infall. As reflection nebulae are commonly seen around Class II systems, our results suggested that a significant fraction of Class II systems undergo this phenomenon.

Although infalling streamers are now being routinely detected, it is not straight-forward to assess their impact on the star and planet formation processes, especially in the more evolved YSOs. To ascertain the infalling nature of observed streamers and to characterise their dynamics, we developed a novel code TIPSY (Trajectory of Infalling Particles in Streamers around Young stars), as described in Chapter 3. TIPSY simultaneously fits the morphology and velocity gradient of streamer observations with theoretical trajectories of infalling material. The best-fit trajectories are used to constrain streamer features like the specific energy, the specific angular momenta, the infall timescale, and the 3D morphology. As test cases, we used TIPSY to fit observations of streamers around S CrA and HL Tau and these streamers to be feeding material to the disks at rates of $\sim 10\ \mathrm{M}_{jupiter}\ \mathrm{Myr}^{-1}$.

To assess the impact of late infall over the general population of Class II systems,

a uniform survey of such structures is needed. DECO (Disk-Exoplanet C/Onnection) is an ALMA Large Program designed to study disk chemistry for 80 Class II sources distributed across four star-forming regions. Interestingly, the moderate-resolution and deep observations of DECO have revealed large-scale ($\gtrsim 500$ au) bound structures around $\sim 40\%$ of the sources, as discussed in Chapter 4. Moreover, the frequency of these structures varies significantly among the four regions. We also find a tentative influence of the mass of bound structures onto the mass being accreted by the central protostars from the disks. These observations strongly challenge the traditional assumption of isolated planet-forming disks.

In the future, dedicated surveys of infalling signatures around Class II systems, combined with a better understanding of the timescales of such events, will tell us more about their frequency and how it varies with star-forming environments. Furthermore, improved characterisation of the physical and chemical properties of the infalling gas and the systems they are impacting will allow us to comprehend the extent of their influence on star and planet formation.

Chapter 1

Introduction

Humanity has always been fascinated by celestial objects, as evidenced by the numerous stories we have crafted about the Sun, Moon, planets, comets, stars, constellations, and nebulae. This fascination naturally led us to use our logical and imaginative abilities to make sense of the cosmos. Even after $\gtrsim 100,000$ yr of humanity (Marean et al., 2007), we continue to seek a deeper understanding of the Universe and our place within it. Among the innumerable astronomical advances we have made so far, one that particularly stands out is that the nature of the Universe determined the origin of life like us. A crucial aspect of this connection lies in comprehending how stars, like our Sun, and planets, like our Earth, form.

1.1 Traditional view of star formation

The classical picture of star and planet formation suggests that Young Stellar Objects (YSOs) form due to the gravitational collapse of dense cores of molecular gas (e.g., Shu, 1977; Terebey et al., 1984). As the infalling gas has a non-zero angular momentum, it settles into a rotating disk-like structure as a consequence of angular momentum conservation. This structure further feeds mass into the forming protostar in the center. Moreover, some of the material in the circumstellar disks clump together to form planets.

This picture suggests that individual protostellar systems can be roughly divided into four evolutionary stages, as shown in Figure 1.1 (e.g., Dunham et al., 2014). Generally, the classification of young stellar sources (YSOs) among the different evolutionary stages are done based on the infrared spectral index (α) (e.g., Dunham et al., 2015). These empirically defined classes and corresponding theoretically expected evolutionary stages are:

- Class 0 ($\alpha \geq 0.3$, $L_{\text{submillimeter}}/L_{\text{bolometric}} > 0.5\%$): Deeply embedded sources, in which the central protostars are not directly observed.

- Class I ($\alpha \geq 0.3$, $L_{\text{submillimeter}}/L_{\text{bolometric}} < 0.5\%$): Sources where an infalling envelope, remanant of the natal protostellar core, is feeding circumstellar disks around central protostars. Here, the central protostars begin to be observed.

- Class II ($-1.6 \leq \alpha < -0.3$): Sources where natal dense core and infalling envelopes have been dissipated leaving behind an isolated disk and protostar system.
- Class III ($\alpha < -1.6$): Sources where almost no circumstellar material remain and the protostar is approaching main sequence.

There is another observationally defined class of flat-spectrum sources ($-0.3 \leq \alpha < 0.3$), however they do not have a clear theoretical counterpart. In general, they are assumed to be Class I sources transitioning to Class II stage.

One should note, however, that YSOs are prone to misclassification due to effects of inclination and foreground extinction on α measurements (e.g., Robitaille et al., 2006). This can cause the observationally defined classes of YSOs to not always refer to a theoretically expected evolutionary stages. In particular, Kuffmeier et al. (2023) demonstrated that a Class II type system can be misclassified as a Class I or Class 0 source if it is interacting with it's surrounding clouds.

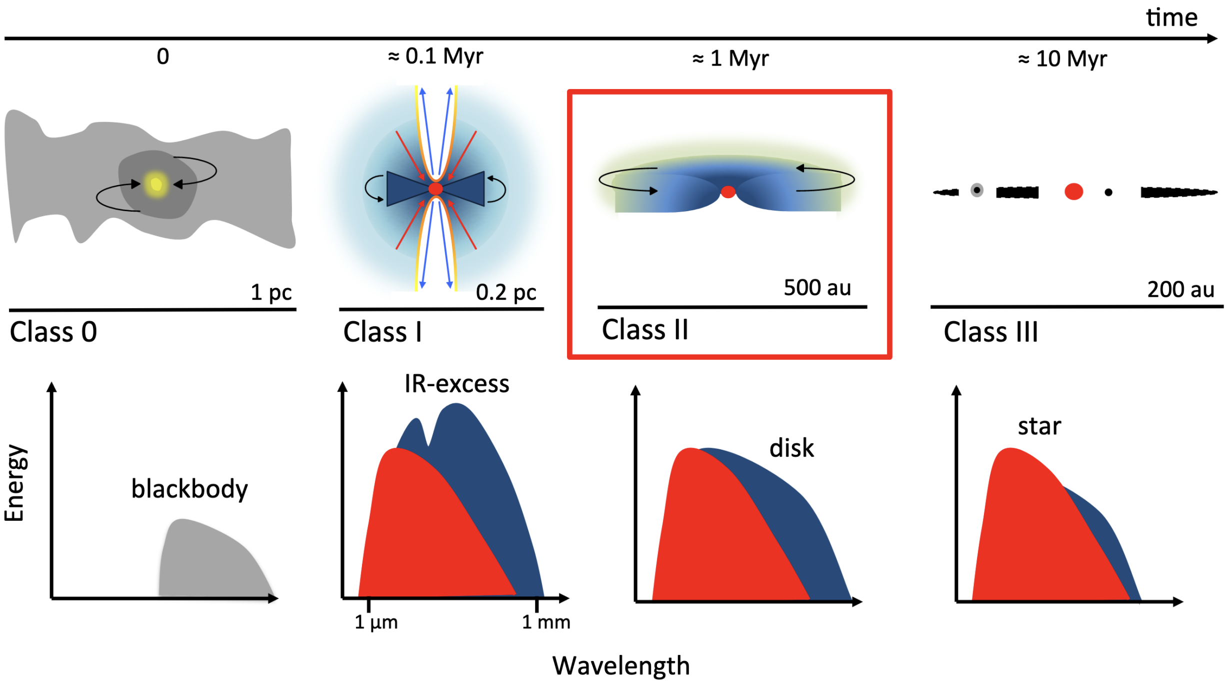

Figure 1.1: Schematic diagram of different evolutionary stages of low-mass star formation. The star formation starts due to gravitational collapse of a prestellar core, and as it proceeds more and more circumstellar material is dissipated. Bottom panels show corresponding Spectral Energy Distribution (SEDs) which are used for observational classification of these sources. Original figure from Miotello (2018).

Observationally, we know that most of YSOs form and evolve in groups, embedded in large-scale ($\gtrsim 1$ pc) molecular clouds (see Figure 1.2). As a consequence of interplay between gravity, magnetic fields, turbulence, and stellar feedback, these clouds exhibit highly structured morphologies (Pineda et al., 2023, and reference therein). In particular, most of the mass of clouds are stored in filamentary structures which can range from sub-parsec to kilo-parsec scales in length (Hacar et al., 2023). These filaments are inherently turbulent in nature and thus, prone to fragmentation into dense cores of molecular gas. Sufficiently massive cores can collapse to form protostellar systems.

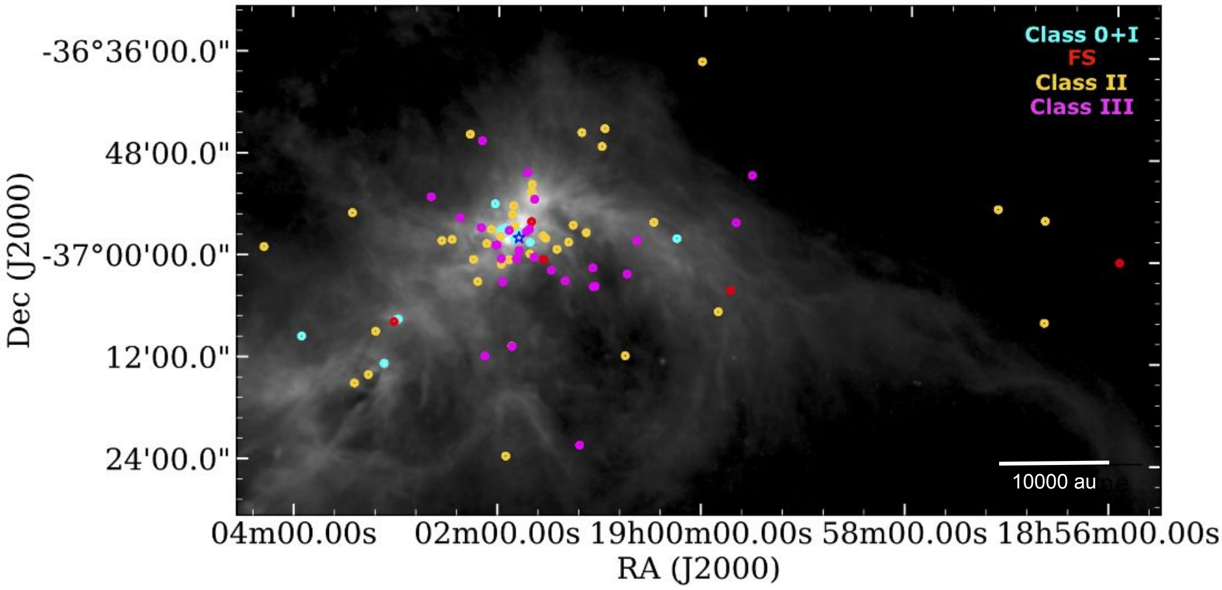

Figure 1.2: Spatial distribution of YSOs in Corona Australis star forming region overplotted on *Herschel* 250 μm map. Class 0/I, flat-spectrum (intermediate state between Class I and Class II), Class II, and Class II sources are denoted as cyan, red, yellow, and purple circles, respectively. Adapted from Cazzoletti et al. (2019).

Numerical simulations that follow collapse of prestellar cores in large-scale molecular clouds, suggest that YSOs continue to interact with their surrounding molecular clouds even in traditionally assumed to be isolated Class II stages (e.g., Pelkonen et al., 2021; Kuffmeier et al., 2023). These interactions are expected to result in late-stage infall of material onto Class II disks, contrary to the traditional picture of star formation where Class II disks are assumed to be isolated. This late infall, approximated as Bondi-Hoyle accretion (Bondi, 1952), is expected to transfer mass at the rate of $\sim 10^{-8}$ $M_\odot$ yr^{-1} (or ~ 10 $M_{jupiter}$ Myr^{-1}) to the disks around solar-type protostars (Padoan et al., 2005; Winter et al., 2024).

1.2 Protoplanetary disks

Protoplanetary disks (also referred to as planet-forming disks and circumstellar disks) around YSOs, especially in Class II stage, are expected to be sites of planet formation processes. This notion has been further supported by the observations of a large amount of disk substructures, particularly of rings and gaps, which are expected to be carved by forming protoplanets (e.g., Bae et al., 2023). Recently, there has been direct detections of two protoplanets in a Class II system PDS 70 which are actively accreting mass from the disk (Haffert et al., 2019).

Although the presence of protoplanetary disks were expected from spectral energy distributions (SEDs), O'Dell et al. (1993) reported the first direct detection of a disk using Hubble Space Telescope (HST) observations. As the bulk of the material in these disks is quite cold (<100 K), we usually rely on sub-millimetre/millimetre wavelengths to observe them. In general, most of the recent studies focus on three types of observations to resolve and study disks (see Figure 1.3 & 1.4):

- Thermal emission: Large (millimetre-sized) dust grains in disks emit most of thermal radiation in wavelengths between $\sim 1\mu$m – 1cm. This emission is particularly well suited to study the disk midplane, where such grains are settled in (e.g., Andrews et al., 2018). By combining observations of different wavelengths, thermal emission also allows us to better understand dust properties (e.g., Testi et al., 2014).

- Molecular line emission: Molecular line emissions at sub-millimetre/millimetre wavelengths are observed generally from rotational transitions of various molecules (e.g., Öberg et al., 2021). Different lines trace different vertical surfaces of the disk. Using doppler shift, these lines can also provide information on disk kinematics (e.g., Pinte et al., 2023).

- Scattered light emission: Small (micron-sized) dust grains are generally well coupled with the gas and suspended in the disk atmosphere. They scatter light from the central star and can be observed in optical/near-infrared wavelengths. They allow us to study sub-structures in disk atmospheres (e.g., Benisty et al., 2023).

Over their lifetimes, disks loose their mass and angular momentum. Exact understanding of how they evolve is crucial to understand planet formation processes happening within them (Morbidelli & Raymond, 2016). Traditionally, the disk evolution was expected to be driven by viscosity, generally associated with turbulence due to disk instabilities such as the magneto-rotational instability (Balbus & Hawley, 1991), vertical-shear instability (Nelson et al., 2013), and gravitational instability (Lodato & Rice, 2004). However, it is becoming hard to comprehensively describe the evolution of disk using this model, particularly due to low level of turbulence being observed in disks (e.g., Rosotti, 2023). A characteristic feature of this model it that a disks is expected to expand until the outer less dense part of disk dissipates due to external photoevaporation (see bottom panel, Figure 1.5).

An alternative theory for disk evolution is that is predominantly influenced by magnetohydrodynamic (MHD) winds which are expected to carry away mass and angular momentum from the disk (e.g., Lesur, 2021). Compared to the viscous evolution, MHD winds would not lead to expansion of disks (see top panel, Figure 1.5). MHD winds would also have observable imprints on disk lifetimes, which will be shorter. Observationally, the

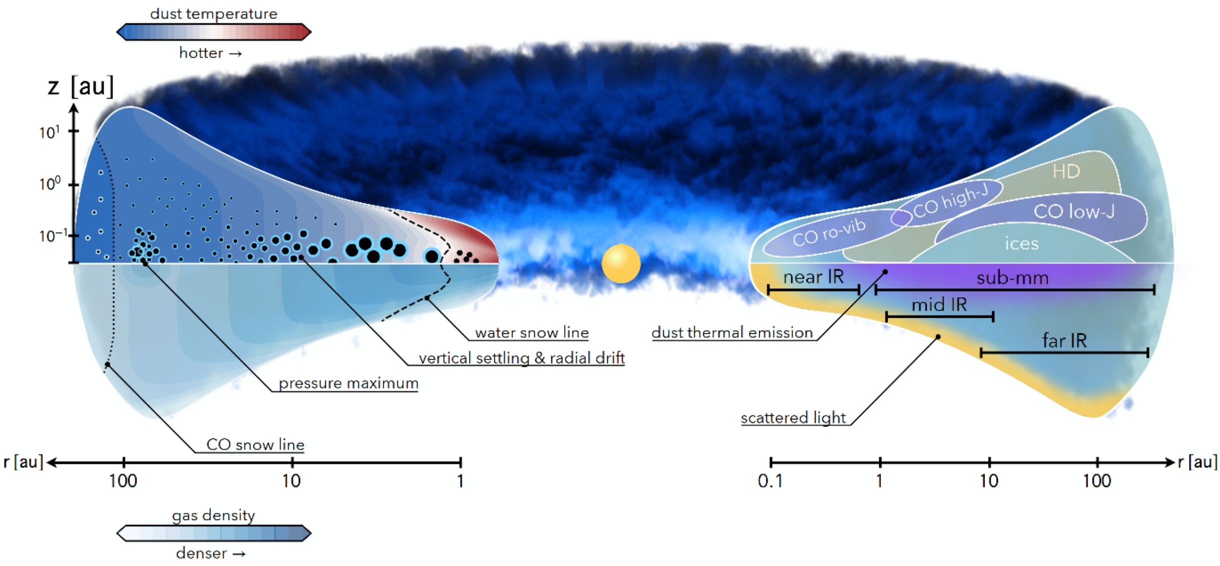

Figure 1.3: Schematic diagram of a protoplanetary disk. Left: An illustration of the dust temperature (top panel) and gas density structure (bottom panel) in protoplanetary disks. The black circles represent the distribution of dust particles, with their size variations indicated by the symbol size. Right: The top panel shows a simplified representation of the emission regions of the main simple molecules, while the bottom panel highlights the primary regions of dust thermal and scattered light emission in purple and yellow, respectively. Original figure by Miotello et al. (2023).

dominant mode of disk evolution is still unclear as both of these models can be fine-tuned to reproduce observed disk properties (Manara et al., 2023). A larger sample of observed disks, particularly with accurate measurements of gas disk sizes, will allow us to better understand disk evolution (e.g., Somigliana et al., 2023).

A common assumption within these two competing models is that disk evolution is driven by disk-internal processes. Recently, another model is emerging which suggests that disk evolution can be regulated by their environment. In particular late-stage infall of material onto protoplanetary disks is being suggested as a way to explain most of the observed disk properties (Winter et al., 2024).

1.3 Submillimeter interferometric observations

Interferometric observations allow us to achieve drastically better angular resolution than single dish observations. This is particularly crucial to study protoplanetary disks, which are generally a few tens of au in size. Let's suppose that we want to study a large disk of ~ 100 au which is located relatively nearby at ~ 100 pc. Such a disk will appear ~ 1 arcsec wide on the place of sky. If we want to resolve such a system by at least 10 independent resolution elements, we need an angular resolution of 0.1 arcsec (Ilee & Greaves, 2015).

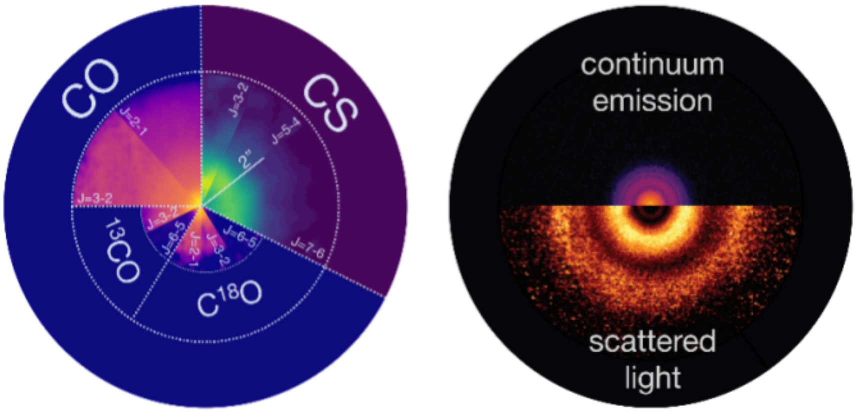

Figure 1.4: Collage of observations of TW Hya in different gas and dust tracers. Left panel: Disk observed in different CO, ^{13}CO, C^{18}O , and CS molecular lines. Right panel: Disk observed in thermal continuum emission (top panel) and scattered light emission (bottom panel). Adapted from Miotello et al. (2023).

If we want to study the disk at a wavelength of $\sim$ 1 mm, a typical wavelength to study their thermal emission as discussed in Section 1.2, we can use Rayleigh criterion to estimate the required size of single dish telescope as

$$D = 1.22\,\frac{\lambda}{\theta} \tag{1.1}$$

where λ is the wavelength of 1 mm and θ is the required resolution of 0.1 arcsec. Then we will need a single dish telescope with a diameter of $\sim 2.5 \times 10^3$ m. This is five times the size of FAST radio telescope, the largest single dish telescope in the world. Moreover, even FAST is constructed in a geological depression and thus have very limited pointing capabilities.

On the other hand, for interferometers the angular resolution is not determined by the size of individual telescopes but by the distances between telescopes. In other words, interferometers allow you to use multiple smaller telescopes spread out over an area to simulate a much larger telescope. To better understand this principle of interferometers, we can think of a simple two antenna interferometer as two slits in a classic Young's slit experiment (see Figure 1.6).

If a planar wavefront of radiation from an astrophysical source passes through a screen with two slits (representing two antennas), it will result in a non-uniform illumination pattern. This pattern will have consecutive bright and dark bands (see red curve in Figure 1.6), which is a consequence of constructive and destructive interference, respectively, between rays of light escaping through the two slits. Here, an interference is constructive (bright bands) when the path difference between the two rays is an integer multiple of their wavelength. The condition for constructive interference can then be approximated as

$$B\,\sin\theta = m\,\lambda \tag{1.2}$$

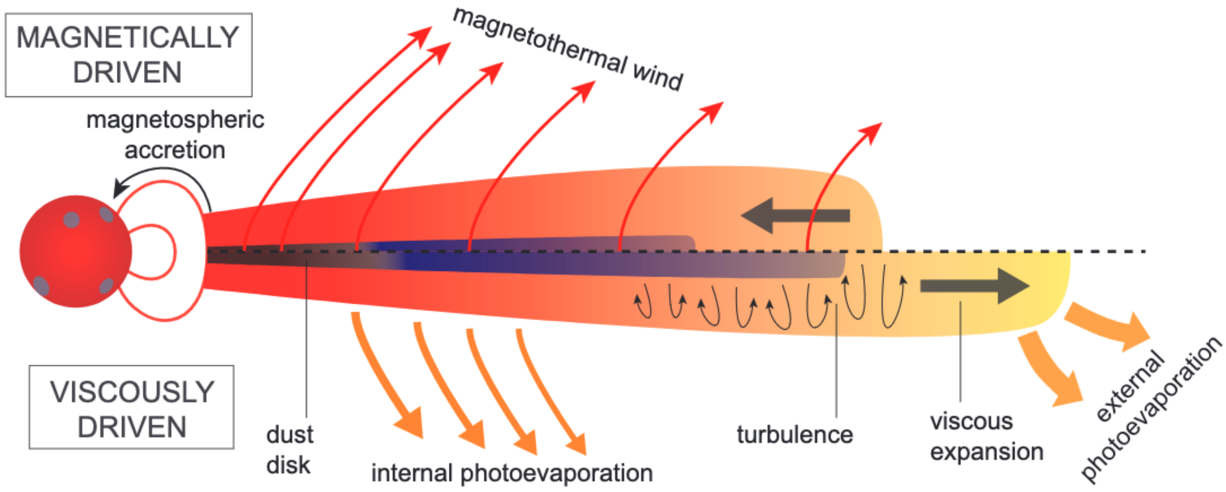

Figure 1.5: Schematic diagram of evolution of protoplanetary disks under the MHD winds driven model (top panel) and viscosity driven model (bottom panel). Adapted from Manara et al. (2023).

where B is distance between the two slits, θ is the angular distance between two constructive interference peaks, m is an integer, and λ is the wavelength of radiation. For sufficiently small B, $\theta \propto \lambda/B$. Here, θ represents the angular scale this simple interferometer can resolve. As it is inversely proportional to distance between the two antennas, interferometers allows us to resolve much better than single dish telescopes by combining data from antennas further away.

However, interferometers have a few important drawbacks. One particularly important for the following chapters is that the interferometers cannot recover scales beyond a certain threshold, determined by the smallest spacing between individual telescopes. This limitation on 'largest recoverable scale' can filter out emission of large-scale structures around protoplanetary disks (as discussed in Section 1.4) if observations are designed to resolve the disks themselves.

The research presented in this thesis primarily rely on data from the Atacama Large Millimeter/Submillimeter Array (ALMA), the largest sub-mm interferometer to date, located in the Atacama desert in Chile. ALMA main array consists of 50 antennas, each 12m in diameter. These antennas can be spread up to distances of 16 km, allowing ALMA to reach 0.01 arcsec-scale angular resolution at the typical wavelengths used to study protoplanetary disks. Moreover, as these antennas can be moved into different configurations, more compact configurations can be used to retrieve larger scale emission at the cost of worse resolution. Furthermore, ALMA also have two additional independent arrays, the ALMA Compact Array (ACA) consisting of 12 7m antennas and the Total Power (TP) array consisting of four 12 m antennas, which can be used to recover even larger scales.

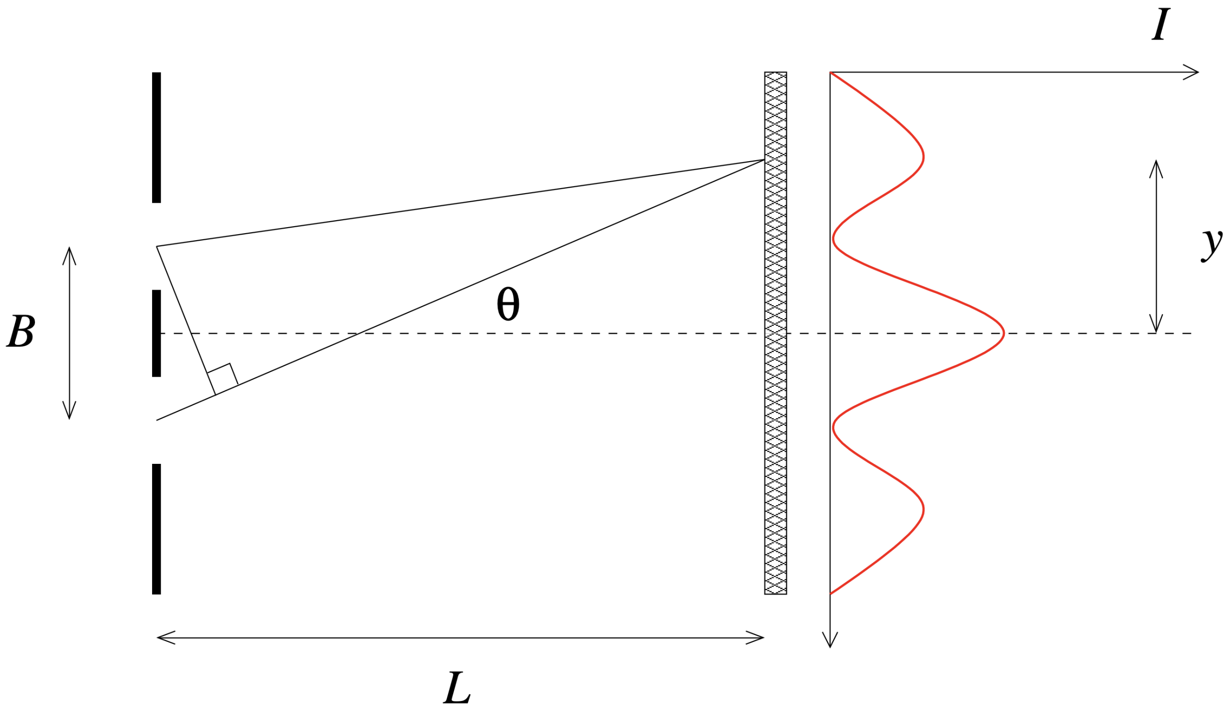

Figure 1.6: Schematic diagram illustrating the basic principle of interferometric observations. The black solid line in the left denotes a screen with two slits, representing two antennas. The shaded rectangle in the right denotes the detection screen where the interference pattern (red curve) emerges. Original figure from Ilee & Greaves (2015).

1.4 Streamers

As discussed in Section 1.1, stars form in highly structured molecular clouds, where the starting conditions for star and disk formation cannot be depicted as isolated spherical cores (e.g., Pineda et al., 2023; Hacar et al., 2023). Numerical simulations of these molecular clouds, which follow the collapse of multiple protostellar cores, reveal that star formation processes are often highly asymmetrical (e.g., Padoan et al., 2014; Haugbølle et al., 2018; Bate, 2018; Kuznetsova et al., 2019; Lebreuilly et al., 2021; Pelkonen et al., 2021; Kuffmeier et al., 2017, 2023). In particular, these simulations reveal that protostellar are generally connected to filamentary channels of infalling material, more commonly known as 'streamers'.

Recently, the enhanced sensitivity of interferometric observations (see Section 1.3) has enabled the detection of these streamers around YSOs at different stages of their evolution, as shown in Figure 1.8. To begin with, there have been a plethora of detections of these structures around young Class 0 and I sources (e.g., Tobin et al., 2012; Yen et al., 2014; Tokuda et al., 2018; Pineda et al., 2020; Thieme et al., 2022; Valdivia-Mena et al., 2022; Murillo et al., 2022; Hsieh et al., 2023; Lee et al., 2023; Mercimek et al., 2023; Cacciapuoti et al., 2023; Valdivia-Mena et al., 2023; Hales et al., 2024; Tanious et al., 2024; Valdivia-

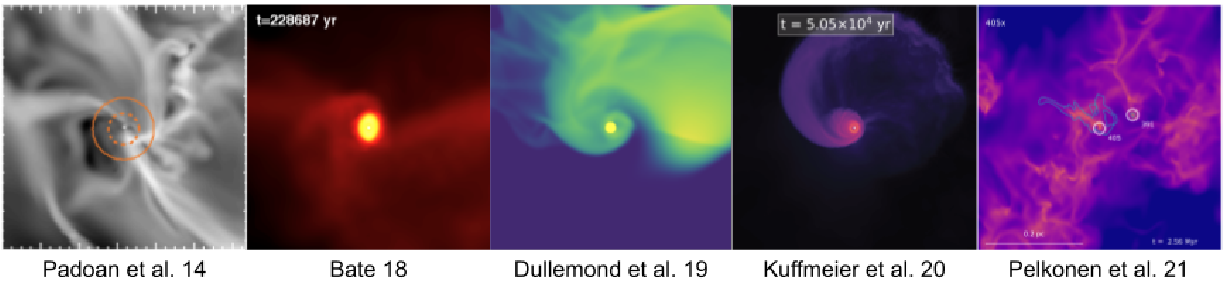

Figure 1.7: Snapshots of numerical simulations revealing filamentary infall of material or 'streamers'.

Mena et al., 2024). This suggests that the initial stages of star formation are not as axisymmetric as was traditionally assumed (see Section 1.1).

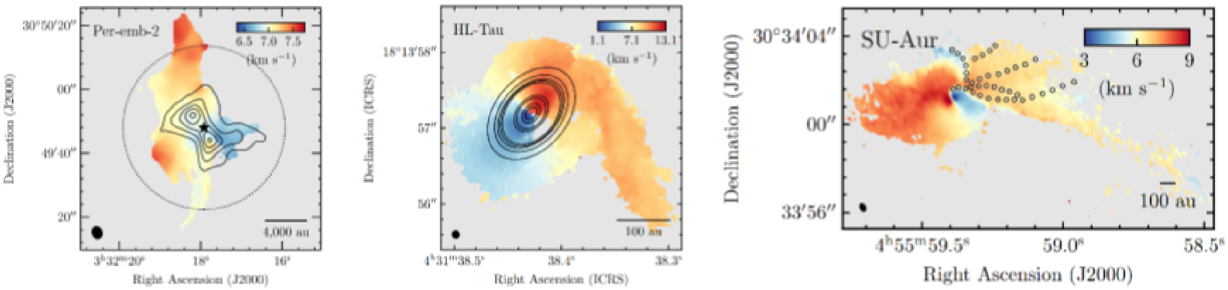

Figure 1.8: Intensity-weighted velocity (moment 1) maps of streamers observed in YSOs at different evolutionary stages. There sources, from left to right, are: Per-emb-2 (Class 0 source), HL Tau (Class I/II source), and SU Aur (Class II source). Adapted from Pineda et al. (2023).

Furthermore, various observational studies have also revealed streamer-like structures around more evolved Class I and Class II sources (e.g., Tang et al., 2012; Akiyama et al., 2019; Yen et al., 2019; Alves et al., 2020; Garufi et al., 2022; Huang et al., 2020, 2021, 2022, 2023; Gupta et al., 2023). These sources were traditionally expected to have negligible infall of material. A lot of disk evolution and planet formation studies assume that the Class II disks are isolated from the environment (see Section 1.2), which is in contradiction with observations of streamer-like structures, expected to be trails of infalling gas. Although the frequency of these structures around evolved sources is still unclear, the results presented in Chapter 2 (indirect search of streamers using reflection nebulae) and Chapter 4 (survey of 80 Class II systems) suggest that a significant fraction of evolved sources continue to interact with the surrounding clouds.

This late-stage infall of material can considerably alter the physical and chemical properties of protoplanetary disks. Late infall, approximated as Bondi-Hoyle accretion, is expected to transfer mass at the rate of $\sim 10^{-8}$ M$_\odot$ yr^{-1} (or ~ 10 M$_{jupiter}$ Myr^{-1}) to the disks around solar-type protostars (Padoan et al., 2005). Such high-mass infall rates can resolve the 'mass-budget problem' of planet-forming disks, where snapshot observations suggest that protoplanetary disks are typically not massive enough to form observed planetary systems (e.g., Manara et al., 2018). If instead material from the environment constantly feeds disks over their lifetime, the accreted mass integrated over time could be enough for forming the observed exoplanet population. Thies et al. (2011) and Kuffmeier et al. (2021) demonstrated that late-infall can also tilt protoplanetary disks, which can produce the observed misalignments in planetary systems. Late-infall can bring chemically fresh material to the system, which can explain observed chemical diversity from scales of meteorites (e.g., Nanne et al., 2019) to globular clusters (Winter & Clarke, 2023). Infalling material can also create shocks in disks which can further influence disk chemistry (Garufi et al., 2022). Finally, this phenomenon can also explain some of the observed mass accretion relations (e.g., Padoan et al., 2005), accretion outbursts (e.g., Jensen & Haugbølle, 2018), old (> 10 Myr) disks (e.g. Scicluna et al., 2014), and disk substructures (e.g., Kuznetsova et al., 2022).

1.4.1 Streamer dynamics

To observationally understand the impact of streamers on disk evolution, we need to model their dynamics to ascertain their infalling nature and then to constrain their dynamical properties like infalling timescale, angular momentum, impact velocity, etc. The earliest efforts of modelling streamers was to fit their velocity gradients (e.g., Yen et al., 2019; Alves et al., 2020). Although this allowed us to confirm the infalling nature of streamers, the dynamical properties were still not well-constrained. This is partly because information stored in the morphology of streamers, in addition to the velocity gradients, is also crucial to get a comprehensive view of streamer dynamics (e.g., Gupta et al., 2024, see Chapter 3).

More recent efforts in modelling of streamers rely on comparing both streamer morphologies and velocity gradients to theoretically expected trajectories of infalling gas. Pineda et al. (2020) pioneered this by comparing infalling trajectories by Mendoza et al. (2009) to the observed streamer around Per-emb-2, a Class 0 source (left panel, Figure 1.8). Since then, this method has been used in a few other observational studies (Valdivia-Mena et al., 2022, 2023; Garufi et al., 2022). However, one important drawback of this method is that the 'best-fit' infalling trajectory is identified based on visual inspection, which may be prone to human biases. Furthermore, it is often not straightforward to estimate uncertainties in the fitting parameters using a qualitative fitting approach.

Quantitative fitting of streamers is being explored in three-dimensional (3D) position-position-velocity (PPV) space. In this approach, a cube of molecular-line observations of a streamer - with three axes being R.A., Decl. and line-of-sight velocity - is fitted to simultaneously reproduce the morphology and the velocity profile. This was first demonstrated by Thieme et al. (2022), who fitted Ulrich-Cassen-Moosman (UCM) trajectories (e.g., Ulrich, 1976; Cassen & Moosman, 1981) to streamers around a Class 0 protostar Lupus 3-MMS. However, in this approach Thieme et al. (2022) had to make a number of assumption on streamer properties, which may not always be possible. Gupta et al. (2024) expanded this idea to develop a streamer fitting code Trajectory of Infalling Particles in Streamers around Young Stars (TIPSY)[1] which fits more generalised infalling trajectories, following a generalised version of Mendoza et al. (2009) equations, to streamer observations in same PPV space (see Chapter 3 for a more detailed explanation). As the fitting is done using a grid of free parameters, best fit solutions can also be used to quantify uncertainties on dynamical properties of fitted streamers.

As most of the recent studies (e.g., Pineda et al., 2020; Valdivia-Mena et al., 2022, 2023; Garufi et al., 2022; Gupta et al., 2024; Hales et al., 2024; Tanious et al., 2024) on characterisation of streamer dynamics rely on the analytical trajectories of infalling gas provided by Mendoza et al. (2009), it is worth reviewing the derivation of these solutions. The equations are expressed in spherical coordinates r, θ, and ϕ, which represent the radial coordinate, the polar angle, and the azimuthal angle, respectively, as illustrated in Fig. 1.9. The initial position of the infalling particle is then given as r_0, θ_0, and ϕ_0. The source of gravity (protostar) is set to be at the origin.

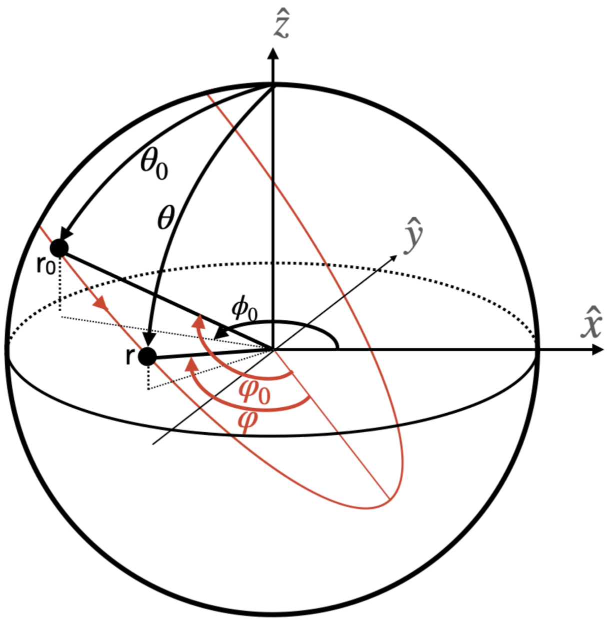

Figure 1.9: Schematic diagram of spherical coordinate system used to derive Mendoza et al. (2009) solutions. The red curve represents an infalling trajectory around a central protostar. r_0, ϕ_0, and θ_0 denote the initial position, polar angle, and azimuthal angle, respectively. Similarly, r, ϕ, and θ denote the position, polar angle, and azimuthal angle, respectively, at an arbitrary point along the trajectory. φ is a parametric azimuthal angle along the trajectory. Original figure from Mena (2024)

To begin with, two dimensionless parameters, μ and ν, can be defined as

$$\mu^2 \equiv \frac{h_0^2}{r_0^2 E_0} = \frac{r_\mathrm{u}^2}{r_0^2}, \qquad \nu^2 \equiv \frac{v_{r0}^2}{E_0}, \tag{1.3}$$

[1]https://github.com/AashishGpta/TIPSY

where, h_0 is the initial specific angular momentum w.r.t. azimuthal axis (z-axis in Fig. 3.1). Here, $r_u \equiv h_0^2/GM$ is analogous to the disk's radius in the UCM model (Ulrich, 1976). $E_0 \equiv GM/r_u$ is the specific gravitational potential energy of infalling gas at r_u. In the following equations, distances are measured in the units of r_u and velocities are measured in the units of $\sqrt{E_0}$ (Keplerian velocity at r_u).

Over the course of particle's motion, the trajectory is defined as a function of a parametric angle, φ, which is the azimuthal angle within the plane of trajectory. The trajectory of an infalling particle, given by standard equations of conic sections, is then represented as

$$r = \frac{\sin^2\theta_0}{1 - e\cos\varphi}, \tag{1.4}$$

with the eccentricity of the orbit, e, is given by

$$e = \sqrt{1 + \varepsilon \sin^2\theta_0}. \tag{1.5}$$

Here, ε represents a dimensionless energy parameter, calculated as $\varepsilon = \nu^2 + \mu^2 \sin^2\theta_0 - 2\mu$. At the border of the cloud, $r = r_0 = 1/\mu$. After substituting this in Eq. (1.4) and performing spatial rotations, the following formulae are obtained:

$$\cos(\varphi - \varphi_0) = \frac{\cos\theta}{\cos\theta_0}, \qquad \cos(\phi - \phi_0) = \frac{\tan\theta_0}{\tan\theta}. \tag{1.6}$$

Using the previous equations and standard definitions of azimuthal (v_ϕ), polar (v_θ), and radial (v_r) components of a velocity vector, the equations for velocities are derived as

$$v_\phi = \frac{\sin^2\theta_0}{r\sin\theta}, \tag{1.7}$$

$$v_\theta = \frac{\sin\theta_0}{r\sin\theta}\left(\cos^2\theta_0 - \cos^2\theta\right)^{1/2}, \tag{1.8}$$

$$v_r = -\frac{e\sin\xi\sin\theta_0}{r(1 - e\cos\xi)}, \tag{1.9}$$

where

$$\xi = \cos^{-1}\left(\frac{\cos\theta}{\cos\theta_0}\right) + \varphi_0. \tag{1.10}$$

Equations 1.4 to 1.6 can be used to compute position of infalling particle along the trajectory. The corresponding velocities are given by equations 1.7 to 1.9.

1.4.2 Mass estimation

Besides characterising the dynamics of streamers, it is also important to constrain the amount of material they can carry. This allows us to assess how much mass streamers can add to the protostellar systems over their evolutionary time. Moreover, if the chemical composition of material in streamers is different, e.g. more pristine that what found in the disks (e.g., Pineda et al., 2020), understanding the gas column density becomes important for evaluating the impact of streamers on disk chemistry.

Typically, streamers are detected using interferometric observations which filter out emission larger than a certain scale, as described in Section 1.3. Therefore, it is usually not possible to observe the entire mass reservoir feeding into a streamer without complementary observations from shorter-baseline interferometers and single-dish telescopes. Even in this case, mass of observed streamer, which is the lower limit on total mass that can fall, can be used to derive mass infall rates $\dot{M}_{\rm inf} = M_{\rm streamer}/T_{\rm inf}$, where $M_{\rm streamer}$ and $T_{\rm inf}$ refers to the mass and infall time for the observed streamer, respectively (e.g., Pineda et al., 2020; Gupta et al., 2024).

The mass of streamers or similar gaseous structures can be estimated using line flux of optically thin emission in the following way (e.g., Bergin et al., 2013; Gupta et al., 2024):

1. Estimating the total number of molecules of emitting molecule ($\mathcal{N}_{\rm mol.}$) from line flux (F_l) using:

$$F_l = \frac{\mathcal{N}_{\rm mol.} A_{\rm trans.} h\nu f_u}{4\pi D^2}. \tag{1.11}$$

   where, $A_{\rm trans.}$ is the Einstein A coefficient of the observed line transition, h is the Planck constant, ν is the line frequency, and D is the distance to the source. f_u is the fraction of molecules in the upper energy state of the transition and can be estimated as $f_u = 3.0 * exp(-128.5\ {\rm K}/T)/Q(T)$, where T represents the temperature of gas and $Q(T)$ is the value of partition function of the molecule at that temperature.

2. Estimating total gas mass ($M_{\rm streamer}$) from number of molecules ($\mathcal{N}_{\rm mol.}$) using:

$$M_{\rm streamer} = 2.37 m_{\rm H} \mathcal{N}_{\rm mol.}/x_{\rm mol.} \tag{1.12}$$

   where, 2.37 denotes mean molecular weight per particle, $m_{\rm H}$ is the mass of a hydrogen atom, and $x_{\rm mol.}$ is abundance of molecule relative to H_2.

A key assumption made in the above method is that the emission is optically thin. While this is generally valid for streamers due to their low-density, for streamers with a higher column density an appropriately less abundant molecular tracer should be used. For the above method, a temperature (T) needs to be assumed as well. If multiple transitions of molecules are observed, temperature and optical depth can be directly inferred from the observations.

Generally, studies with multiple transitions rely on solutions from RADEX, a one-dimensional non-LTE radiative transfer code (van der Tak et al., 2007) for estimating column density of observed gas structures directly from brightness temperature of observed lines (e.g., Pineda et al., 2020; Hales et al., 2024). The total mass of the molecular gas is then estimated by integrating the column density over the projected area of emission. This value can be multiplied by the molecular abundance factor ($x_{\rm mol.}$) to obtain the total gas mass.

1.5 Outlook

This thesis focuses on two key questions around the role of star-formation environment on the evolution of planet-forming disks. These questions are:

- How common is late-stage infall of material onto protoplanetary disks?
- What is the impact of this infall of material on protoplanetary disks?

The results presented in this thesis demonstrate that late-infall is significantly more frequent and impactful than traditionally assumed. This thesis presents the first of their kind studies to understand complex interactions between disks and their environments.

In Chapter 2, we present a novel systematic search for late-stage infall of material using reflection nebulae (RNe). The basic idea is that Class II sources undergoing infall of material from the environment should be surrounded by clouds. The small dust grains in such clouds should reflect the light from the protostar and appear as RNe. We demonstrate that the association with RNe can indeed be useful in identifying late-infall candidates. This would further suggest that this phenomenon is quite frequent because reflection nebulae are commonly observed around Class II sources (e.g., Cohen, 1980) and this was one of the original defining characteristics of such sources (Joy, 1945).

Subsequently, Chapter 3 addresses the second question: how impactful is late-stage infall of material? As discussed in Section 1.4, a signpost of this phenomena is the observation of streamers. However, it is important to confirm the infalling nature of these structures, as they can also form due to tidal interaction among stellar companions (e.g. Zapata et al., 2020), stellar fly-bys (e.g. Cuello et al., 2019), gravitational instabilities in disks (e.g. Dong et al., 2015), and ejection of gas (e.g., Vorobyov et al., 2020). In order to ascertain the infalling nature of observed streamer-like structures and then to quantify their impact on disks, we developed a novel streamer analysis code TIPSY. Using TIPSY, we demonstrate that infalling streamers can drastically enhance mass budget in disks to form planetary systems.

However, the analysis presented in Chapter 3 is limited to only two sources. In order to assess the impact of infalling material on a larger sample of sources, we need a uniform molecular-line survey of large-scale structures around such disks. In Chapter 4, we presented preliminary results from an ALMA Large Program DECO (Disk-Exoplanet C/Onnection, PI: L. Ilsedore Cleeves). DECO is the first such survey of protoplanetary disks in molecular-line emission, covering a well-sampled range of stellar masses (~ 0.2–$1.5\ M_\odot$) in four nearby (< 200 pc) star-forming regions. Although this program was primarily designed to study disk chemistry, the requested moderate resolution and deep observations reveal large-scale structures around $\sim 40\%$ of the targeted sources. The data suggests that significant infall is quite common, but it can vary considerably for different star-forming regions.

A detailed multi-scale analysis of a large-sample of Class II systems in different star-forming environments, including complementary observations like scattered-light emission (e.g., Garufi et al., 2024), is required to really answer the questions mentioned above.

Furthermore, these observational efforts need to be supported by numerical simulations of this phenomena, which will allow us to draw accurate inferences from the observations. Chemical surveys and modelling are needed to further understand the impact of streamers on disk chemistry, which will be inherited by the planetary systems they form. To conclude, there is still much to be done to obtain a comprehensive view of this phenomenon, however, the subsequent chapters demonstrate that the star formation environments influence planet formation processes, and thus, also the possibility of life emerging on them.

Chapter 2

Reflections on nebulae around young stars

This chapter reproduces the paper Gupta et al. (2023), titled *"Reflections on nebulae around young stars. A systematic search for late-stage infall of material onto Class II disks."*, and published in the journal Astronomy & Astrophysics.

2.1 Motivation

Most stars are born in groups in giant molecular clouds through the gravitational collapse of dense molecular cores (McKee & Ostriker, 2007). As these protostellar systems evolve from the Class 0/I to the Class II stage, the surrounding gaseous envelope is thought to be completely dispersed and, traditionally, Class II systems are believed to evolve in general isolation to form planetary systems.

However, in reality, these systems are still in the vicinity of molecular clouds on large scales ($\gtrsim 1$ pc) and may continue to dynamically interact with them. Such interactions were observed in younger Class 0/I and flat-spectrum objects, where 1000 au scale streamers of molecular gas infalling onto the protostar were detected (e.g. Pineda et al., 2020; Alves et al., 2020; Garufi et al., 2022). There have been some recent serendipitous detections of ~ 1000 au, generally stream-like, gaseous structures around Class II disks too, which are likely due to such interactions (Tang et al., 2012; Ginski et al., 2021; Huang et al., 2020, 2021, 2022).

Late infall of material can greatly influence the physical and chemical properties of Class II disks, and thus, of the planets they form. For example, the supply of fresh material can help solve the 'mass-budget problem' of planet-forming disks (e.g. Manara et al., 2018; Mulders et al., 2021), and explain the observed chemical diversity among meteorites (Nanne et al., 2019). Thies et al. (2011) and Kuffmeier et al. (2021) demonstrated that late infall can torque disks and explain the observed misalignment of some planetary systems. Approximated as Bondi-Hoyle accretion (Bondi & Hoyle, 1944), late infall can explain the steep dependence of mass accretion on stellar mass (Padoan et al., 2005, 2014). Finally, this phenomenon may also produce disk sub-structures and instabilities as seen in vortices (Bae et al., 2015; Kuznetsova et al., 2022), spiral waves (Hennebelle et al., 2017; Kuffmeier et al., 2018), and FU Orionis outbursts (Dullemond et al., 2019).

A characterisation of the frequency and efficiency of late infall is therefore crucial for establishing a holistic view of the star and planet formation process. Simulations suggest that a signpost of such accretion events could be $\sim 10^3$ au-scale arc-shaped structures, generally referred to as 'streamers' (e.g. Kuffmeier et al., 2020). However, only a few have been detected, mainly because these spatial scales lie at the limits of single-dish resolution and they are largely filtered out in interferometric observations designed to resolve protoplanetary disks. To comprehensively study late-stage infall, a survey of large-scale structures around Class II sources is needed and a first step in this direction would be to systematically identify suitable targets.

In order to find disks that are potentially undergoing late infall, one should first identify Class II sources that are close enough to clouds to gravitationally interact with them. Such clouds will scatter the protostellar light in optical and near-infrared (NIR) wavelengths and appear as reflection nebulae (RNe) (e.g. Hubble, 1922). Historically, RNe were used to identify young stellar objects (YSOs) (e.g. Cohen, 1980) and they were indeed one of the original defining characteristics of T Tauri stars (Joy, 1945). Recently, hydrodynamical simulations have demonstrated that kilo-au scale RNe can appear due to cloud-protostar interactions, some of which lead to late infall of material (Dullemond et al., 2019). In this Letter we pioneer the use of RN detections close to Class II stars to identify late-infall candidates.

2.2 Class II sources with large-scale CO structures

Large-scale non-Keplerian gaseous structures have been detected around a few Class II sources. In order to test the hypothesis that RNe might indicate late infall, we looked for signs of nebulosity around these sources, as discussed below:

AB Aur: Tang et al. (2012) found four ~ 500 au spirals around AB Aur in CO observations using the Instituto de Radioastronomía Milimétrica (IRAM) 30-m telescope, Plateau de Bure interferometer (PbDI), and Submillimeter Array (SMA). Analysis of the gas kinematics in these spirals, which seems to be counter-rotating with respect to the Keplerian disk, suggests that they are likely formed due to late-stage infall of gas. This source is also known to be associated with a bright arc-shaped RN (e.g. Dullemond et al., 2019), as shown in Figure 2.1 (panel a).

SU Aur: Akiyama et al. (2019) reported an ~ 1000 au long tail-like streamer using the Atacama Large Millimeter/submillimeter Array (ALMA) in CO emission. Later, Ginski et al. (2021) studied the morphology of its dust tails in scattered light using the Very Large Telescope (VLT), along with a kinematic study of CO gas, and found that the material is likely moving towards the disk. A bright RN is visible in the immediate vicinity of SU Aur (Figure 2.1, panel b).

RU Lup: Huang et al. (2020) reported at least five CO spiral arms stretching up to ~ 1000 au around RU Lup using ALMA observations and suggested late infall as a possible explanation. Archival Digital Sky Survey (DSS) images show faint nebulosity just north of RU Lup, as shown in Figure 2.1 (panel c).

GM Aur: Huang et al. (2021) found extended elongated structures around GM Aur, ~ 1000–2000 au in length, using ALMA CO observations with a morphology and kinematics indicative of late infall. No RNe have been found in archival DSS or Panoramic Survey Telescope and Rapid Response System (Pan-STARRS) images, but there are elongated features in more sensitive Hubble Space Telescope (HST) NIR images, as reported in Schneider et al. (2003) and shown in Figure 2.1 (panel d).

DO Tau: Huang et al. (2022) studied the kilo-au environment of DO Tau using VLT/SPHERE, HST, and ALMA observations, and found the disk to be connected to multiple ~ 1000 au scale stream-like structures. Larger-scale Herschel observations show that these structures are probably due to an interaction with the neighbouring YSO HV Tau, but late accretion of material onto DO Tau is not ruled out. The source is associated with a prominent RN (Figure 2.1, panel e).

To summarise, the five known Class II sources that have large-scale CO structures suggestive of an interaction with surrounding gas have either a prominent RN or some hints of reflection nebulosity. Following this lead, we exploit the association of YSOs with RNe to search for candidate Class II sources undergoing late-stage infall of material.

2.3 Class II sources near reflection nebulae

As a first step, we compiled a catalogue of RNe using the published lists in Magakian (2003) and Connelley et al. (2007). Magakian (2003) merged previously published RNe catalogues and presented a final list of 913 objects. Most of the sources in their list have been manually identified by visual inspection of DSS optical images. Connelley et al. (2007) surveyed 197 nearby, mostly Class I, protostars at $2.2\,\mu$m using the University of Hawaii 2.2 m telescope. They detected 106 RNe, out of which 41 were reported as new discoveries. The fact that $\gtrsim 40\%$ of RNe were not detected before suggests that the previous RNe catalogues were rather incomplete. For example, the prominent RNe around SU Aur (see Figure 2.1, panel b) and HD 100546 (Ardila et al., 2007) were not in these RNe catalogues.

Connelley et al. (2007) estimated sizes of RNe as the square root of their area with a mean (μ) and standard deviation (σ) of ~ 18 arcsec and ~ 15 arcsec, respectively. Using a cross-matching radius of 30 arcsec ($\sim \mu + 1\sigma$), we found ten RNe present in both of the catalogues. After removing duplicates, we merged the two catalogues to have a final sample of 1009 RNe.

To avoid spurious detections and have a well-characterised sample of YSOs with RNe that can be further followed up on using molecular-line observations (as discussed in Appendix A.4), we focus on nearby well-studied star-forming regions (SFRs). The regions considered in this study are listed in Table 2.1 and shown in Figure A.1. The radii reported in the fifth column in Table 2.1 were used to define circular boundaries around the

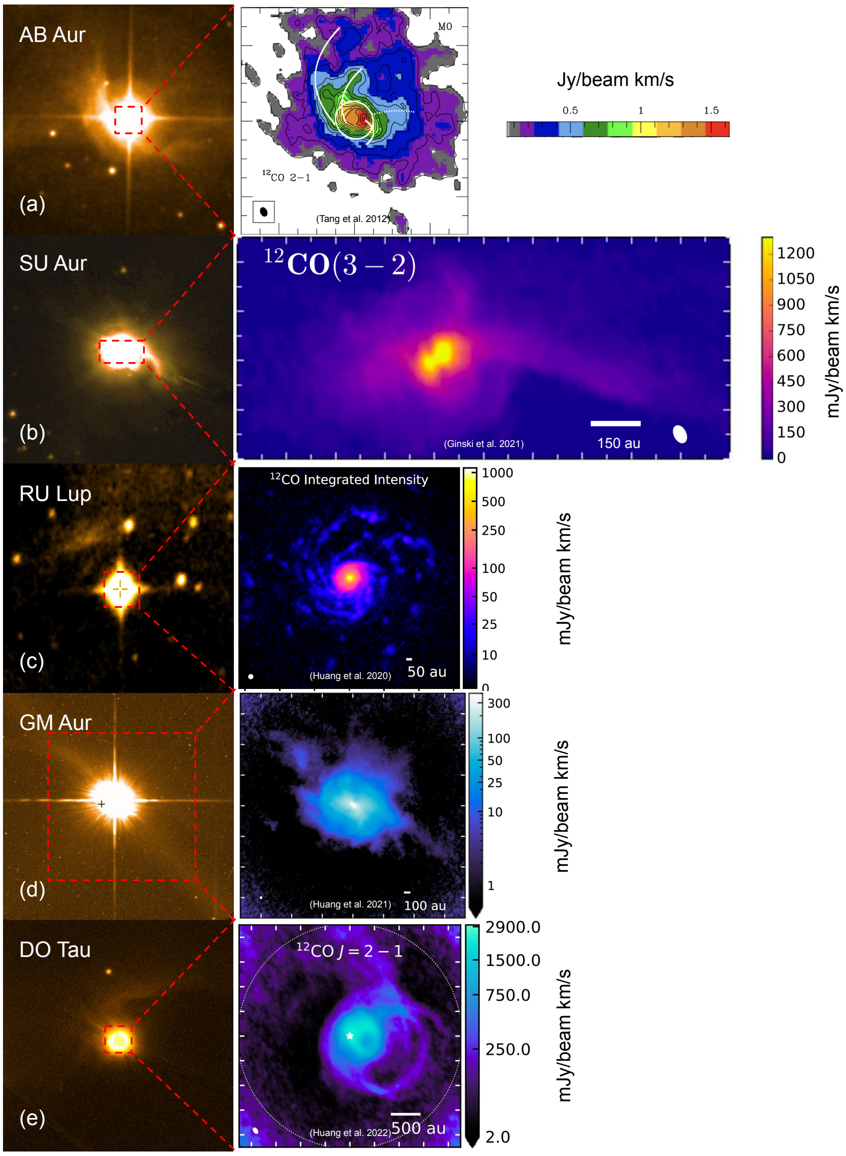

Figure 2.1: Optical and NIR images (left) and ^{12}CO integrated intensity moment 0 maps (right) of Class II sources with known large-scale structures, as discussed in Section 2.2. *Panel a*: AB Aur's DSS2 optical image and the PdBI ^{12}CO (2–1) moment 0 map from Tang et al. (2012). *Panel b*: SU Aur's Pan-STARRS optical image and the ALMA ^{12}CO (3–2) moment 0 map from Ginski et al. (2021). *Panel c*: RU Lup's DSS2 (red) optical image and the ALMA ^{12}CO (2–1) moment 0 map from Huang et al. (2020). *Panel d*: GM Aur's HST (NICMOS) NIR image and the ALMA ^{12}CO (2–1) moment 0 map from Huang et al. (2021). *Panel e*: DO Tau's Pan-STARRS optical image and ALMA ^{12}CO (2–1) moment 0 map from Huang et al. (2022). Angular resolutions for the moment 0 maps are roughly 0.5 arcsec, 0.3 arcsec, 0.3 arcsec, 0.2 arcsec, and 0.7 arcsec for panels a to e, respectively.

SFR	R.A. [deg]	Decl. [deg]	Distance [pc]	Radius [deg]	YSOs	RNe
Ophiuchus	249.07	-23.64	128.0	6.0	450	13
Taurus	67.11	26.62	148.0	8.0	190	28
Corona Australis	287.96	-38.11	155.0	4.0	80	6
Lupus	240.08	-36.56	158.0	8.0	480	10
Chamaeleon	169.5	-78.17	190.0	8.0	148	7
Perseus	54.21	31.57	284.0	4.0	435	19
Orion	85.2	-3.5	420.0	6.0	978	44
Serpens	277.66	-1.91	495.0	3.0	2169	14

Table 2.1: List of SFRs considered in this study. The median coordinates and distances are from Zucker et al. (2020). The last three columns refer to the radii used to define the SFR boundaries (see Figure A.1) and the number of RNe and YSOs found.

central coordinates listed in the second and third columns, and they are marked with black circles in Figure A.1. We found 141 sources from our catalogue of 1009 RNe within these region boundaries.

The next step was to compile a catalogue of YSOs in these regions. For this we started with the all-sky catalogue of 133980 Class I/II sources reported in Marton et al. (2016). Marton et al. (2016) analysed *WISE* and *2MASS* photometry of these sources, using the support vector machine algorithm to identify them as YSOs. For a more complete sample of nearby YSOs, we also used the list of 2966 YSOs identified using *Spitzer*'s 'cores to disks' and 'Gould Belt' surveys, as reported in Dunham et al. (2015). Among the SFRs considered in this study, Taurus and Orion were not part of the Dunham et al. (2015) catalogue. Using a cross-matching radius of 5 arcsec, we found 781 common sources in both datasets. Our final catalogue consists of 136165 YSOs of which 4930 lie within the SFR boundaries.

The spectral indices, α, or slope of the spectral energy distributions in the infrared regime ($\sim$ 2–25 μm) were given in the Dunham et al. (2015) catalogue. We used their values, α', corrected for foreground extinction to classify the source evolutionary state.

Similarly, we determined α for sources exclusively in the Marton et al. (2016) catalogue using the provided *WISE* and *2MASS* (K band) photometry, and discarding those with fitting uncertainties > 0.6, that is roughly half of the range of values for Class II sources. In order to estimate extinction-corrected spectral indices (α'), we computed a correction factor of -0.31 as the median of differences between all the α' and α values reported in Dunham et al. (2015). We note that this method only provides a rough estimate of α' as it does not account for extinction values for individual sources. A comparison of our α and α' values is shown in Figure A.3. Following the same classification criteria as Dunham et al. (2015), that is $-1.6 \leq \alpha' < -0.3$, 2562 out of 4930 YSOs in our SFRs were classified as Class II sources.

The next step was to cross match our list of Class II sources with the merged catalogue of RNe. For the specific goal of this work, the cross-matching distance between a YSO and RN can be empirically estimated as the length scale from where ambient gas can be accreted onto an isolated star (Bondi-Hoyle accretion, Bondi & Hoyle, 1944; Throop & Bally, 2008; Padoan et al., 2014). The typical length scale for this interaction is given as $L_{BH} = 2GM_*/v^2$, where G is the gravitational constant, M_* is the stellar mass, and v is the stellar speed relative to the gas. For a stellar mass of 1 $M_\odot$ and typical stellar velocity of 1 km s^{-1}, $L_{BH} \sim 2000$ au. The 21 late-infall Class II candidates that we found using this threshold are listed in Appendix A.3.

We note that this distance threshold is a lower limit for an interaction between clouds and YSOs because we do not account for the sizes of RNe. These show a range of physical sizes ($\sim 10^3$–10^5 au) and have highly asymmetrical shapes (e.g. Connelley et al., 2007). When mining the ALMA archive, we ignored this diversity as we aimed to identify a reliable sample of YSOs potentially interacting with RNe clouds. The implications of a more realistic distance threshold is discussed in Section 2.4.

ALMA archive search: To target higher-quality observations, we focussed on nearby SFRs ($d \lesssim 200$ pc), where 16 out of the 21 Class II disks near RNe are located. For these nearby sources, we searched for existing observations in the ALMA Science Archive. We are primarily interested in ^{12}CO emission ($J = 2-1$ in Band 6 and $J = 3-2$ in Band 7) since this molecule is expected to be a good tracer of large-scale diffuse gas structures (see e.g. Figure 2.1). We found a total of 66 Band 6 and 7 observations for 16 sources in our sample, as shown in Figure 2.2.

Among these datasets, we found 13 observations with the largest angular scale (LAS) corresponding to at least 1000 au to recover the expected large-scale structures (see Kuffmeier et al., 2020). As such large-scale structures are expected to have low column densities, and therefore faint emission, the observational sensitivity is important. We selected a subset of five observations with rms noise (over a channel width of 10 km s^{-1}) smaller than a 2.3 mJy $beam^{-1}$, equal to the line sensitivity reported in the ALMA archive for SU Aur observations (Ginski et al., 2021). For the typical angular resolution of 0.7 arcsec for these observations, the sensitivity threshold of the 2.3 mJy $beam^{-1}$ corresponds to ~ 100 mK. The sensitivity and recoverable scale thresholds are marked as dashed-grey lines in Figure 2.2.

Among these five observations, two targeted HD 142527 (Figure 2.2, red circles), a well-studied binary Class II system. These data have been published and show non-Keplerian spiral structures extending to ~ 700 au, beyond the disk radius of ~ 200–300 au (Christiaens et al., 2014; Garg et al., 2021), as shown in Figure 2.3 (panel a). Similar structures have also been observed in optical and NIR images (Casassus et al., 2012; Hunziker et al., 2021). Christiaens et al. (2014) suggested that the innermost spiral can be explained by acoustic waves due to an embedded companion; however, the origin of the outer spirals is less clear, and stellar encounters and gravitational instabilities have been suggested as possible causes. We note that spiral structures have been predicted to form due to late infall (Hennebelle et al., 2017; Kuffmeier et al., 2017, 2018) and a detailed kinematic analysis can be done to distinguish among these scenarios, as discussed in Appendix A.4. HD 142527 also exhibits inner and outer disk misalignment (Bohn et al., 2022), which can be explained by late infall (Thies et al., 2011; Kuffmeier et al., 2021).

The other three datasets are of S CrA, HD 97048, and Sz 68. The selected large-scale observation for Sz 68 (Project 2019.1.01135.S) does not cover any CO lines and is therefore not discussed further. For S CrA (Project 2019.1.01792.S) and HD 97048 (Project 2015.1.00192.S), we used the standard pipeline calibration and imaged the ^{12}CO (2–1) data using CASA 6.4. For both datasets, imaging was carried out using 'briggs' weighting with robust=0.5, a cell size of 0.05", and 'auto-multithresh' masking with default parameters. The resulting integrated intensity (moment 0) maps and intensity-weighted velocity (moment 1) maps are shown in Figure 2.3 (panel b and c). Appendix A.6 shows corresponding channel maps for both of the datasets.

For S CrA, at least one ~ 1000 au streamer is clearly visible (solid cyan line), north-west of the binary disks (green contours), as seen in the moment 0 map (Figure 2.3, panel b, middle panel). This streamer seems to be redshifted with respect to the disk emission, as seen in the corresponding moment 1 map (see Figure 2.3, panel b, right panel and channels from 12.93 to 8.57 km s^{-1} in Figure A.4). Furthermore, there are hints of two more streamers, denoted as dashed-cyan lines in the moment 0 map (Figure 2.3, panel b, middle panel). This is the first discovery of large-scale streamers around S CrA. As discussed in Section 2.2, such elongated structures can form due to the late infall of material, but they could also be a consequence of a binary interaction. Further analysis is required to ascertain the dynamical nature of these features and will follow in a future publication.

For HD 97048, no clear streamers are visible in the moment 0 map (Figure 2.3, panel c, middle panel). However, significant negative emission was observed in the central channels (Figure A.5, channels 5.32 to 3.57 km s^{-1}), suggesting that the source may be surrounded by large-scale gas that may absorb or otherwise obscure, through spatial filtering, kilo-au features around the star.

These initial results suggest that at least two (HD 142527 and S CrA) out of the three Class II sources associated with RNe, and with good-enough ALMA data, exhibit large-scale spirals or streamer-like structures, as are expected to form due to cloud-disk interactions, particularly late-stage infall of material (Hennebelle et al., 2017; Dullemond et al., 2019; Kuffmeier et al., 2017, 2020; Kuznetsova et al., 2020). These two sources are in addition to the already known similar sources discussed in Section 2.2. Other possible explanations for these large-scale structures are discussed in Appendix A.5. Irrespective of the actual origin of such features, it is promising to see that large-scale gas emission is found around YSOs close to RNe. This may indicate that an association with RNe can be used to look for similar structures around a wider population of Class II disks, as discussed further in Section 2.4.

2.4 Discussion

We have found 21 Class II sources associated with RNe in the SFRs listed in Table 2.1, using a distance threshold of $\sim$ 2000 au, equivalent to the typical Bondi-Hoyle accretion length scale. However, this distance threshold does not account for the observed range of physical extents and asymmetric shapes of RNe. Connelley et al. (2007) provided angular sizes and distances for RNe in their catalogue, which correspond to a mean radius $\sim 10^4$ au. The exact distances between the centres of YSOs and RNe that result in late infall can vary greatly for different sources depending on their stellar (mass and velocity) and RNe properties (size and shape) and it is likely that more Class II sources in our sample may be interacting with neighbouring material than discussed here.

Figure A.2 plots the fraction of Class II sources and all YSOs associated with RNe as a function of the offset distance for different SFRs. Considerable differences can be seen in the association probability of YSOs with RNe for different SFRs, mostly due to different catalogue completeness levels. The incompleteness of the available RNe catalogues is a major obstacle in providing reliable statistics at the moment (see discussion in Sec. 2.3). However, even with this limitation, it is clear that there are potentially many Class II disks interacting with their parent cloud. For at least four SFRs (Taurus, Lupus, Corona Australis, and Chamaeleon), $\sim$ 5–10% of Class II sources are close-enough ($\lesssim 10^4$ au) to RNe. If the threshold is slightly increased to $\lesssim 4 \times 10^4$ au, $\sim$ 50% of Class II sources in Corona Australis would be associated with a RN, and therefore potentially accreting material from the ambient cloud.

Accounting for stellar kinematics, the number of Class II systems that pass by RNe at some point in their lifetime could be even greater. If an association with RNe is indeed related to late infall, this may be an important phenomenon especially since it can have important implications for disk evolution and planet formation, as described in Section 2.1. To further test the tentative link between RNe and an interaction between disks and surrounding clouds, a survey of structures and kinematics around Class II sources with known RNe is needed, as discussed in Appendix A.4. Coupled with a better RNe catalogue, such a survey will allow us to understand how frequent late infall is for Class II sources.

2.5 Conclusions

In this Letter we pioneer the use of the detections of RNe close to Class II stars to identify late-infall candidates. We find that all of the sources with known large-scale CO structures, where late infall is invoked as a possible explanation, also exhibit some reflection nebulosity at OIR wavelengths. Furthermore, at least five out of the six sources which are associated with a prominent RNe and for which adequate ALMA observations are available – that is, known sources AB Aur, SU Aur, and DO Tau along with independently identified sources S CrA and HD 142527 – exhibit some large scale structure that may be indicative of late infall. This per se suggests that association with RNe may be used to identify candidate

Class II sources undergoing late-stage infall of material. Finally, in nearby SFRs, the fraction of Class II sources associated with RNe can be as large as 50%, depending on the distance threshold, but a proper statistical analysis is still pending improved RNe catalogues. If RNe are indeed related to late infall, this suggests that a significant fraction of Class II sources could be undergoing this phenomenon, with a non-negligible impact on disk evolution and planet formation. The catalogue of potential late accretors obtained serves as a starting point for more systematic studies of late infall onto disks.

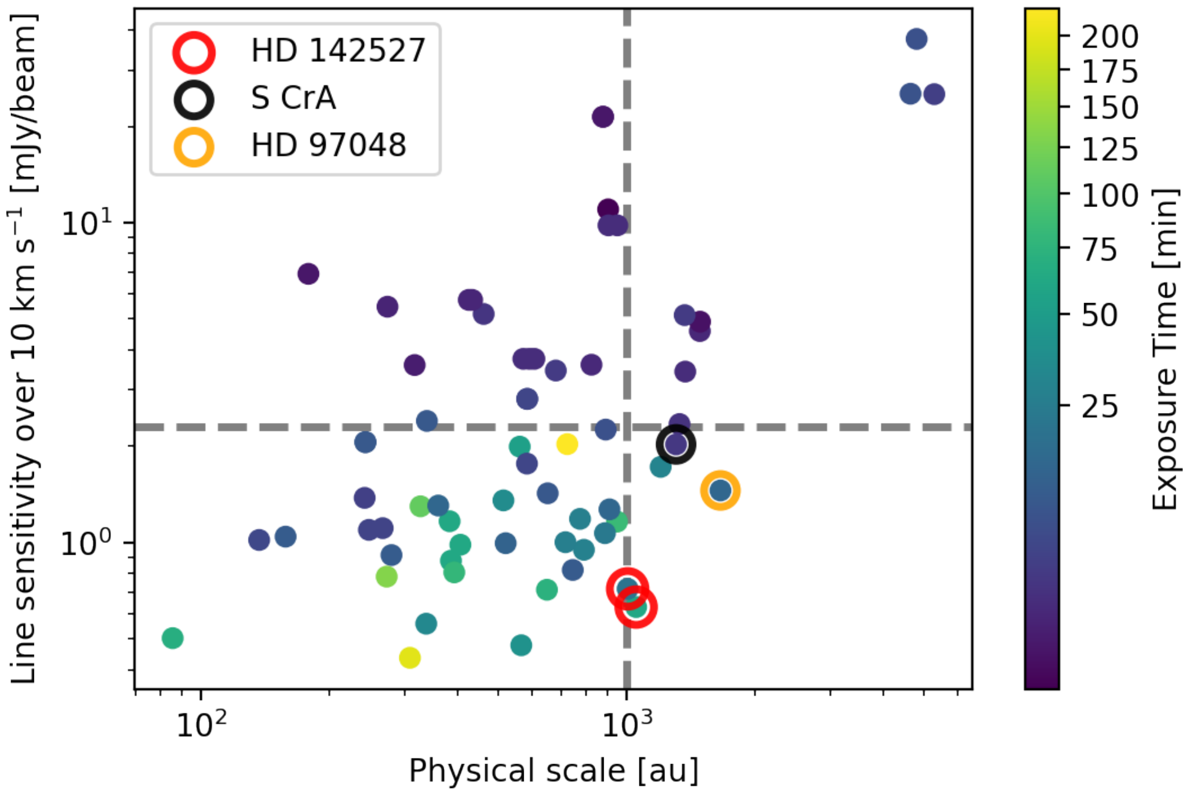

Figure 2.2: Largest recoverable physical scale vs line sensitivity (over 10 km s^{-1}) for archival ALMA observations, in Band 6 and 7, of the 16 nearby Class II YSOs associated with RNe, as discussed in Section 2.3. Marker colours denote the exposure time for each observation in minutes. The vertical dashed line denotes a recoverable scale of 1000 au. The horizontal dashed line denotes a line sensitivity of 2.3 mJy beam^{-1} (the line sensitivity reported in the ALMA archive for SU Aur observations by Ginski et al. (2021)). Markers with open circles denote the observations discussed in Section 2.3, with red circles for HD 142527, black circle for S CrA, and an orange circle for HD 97048.

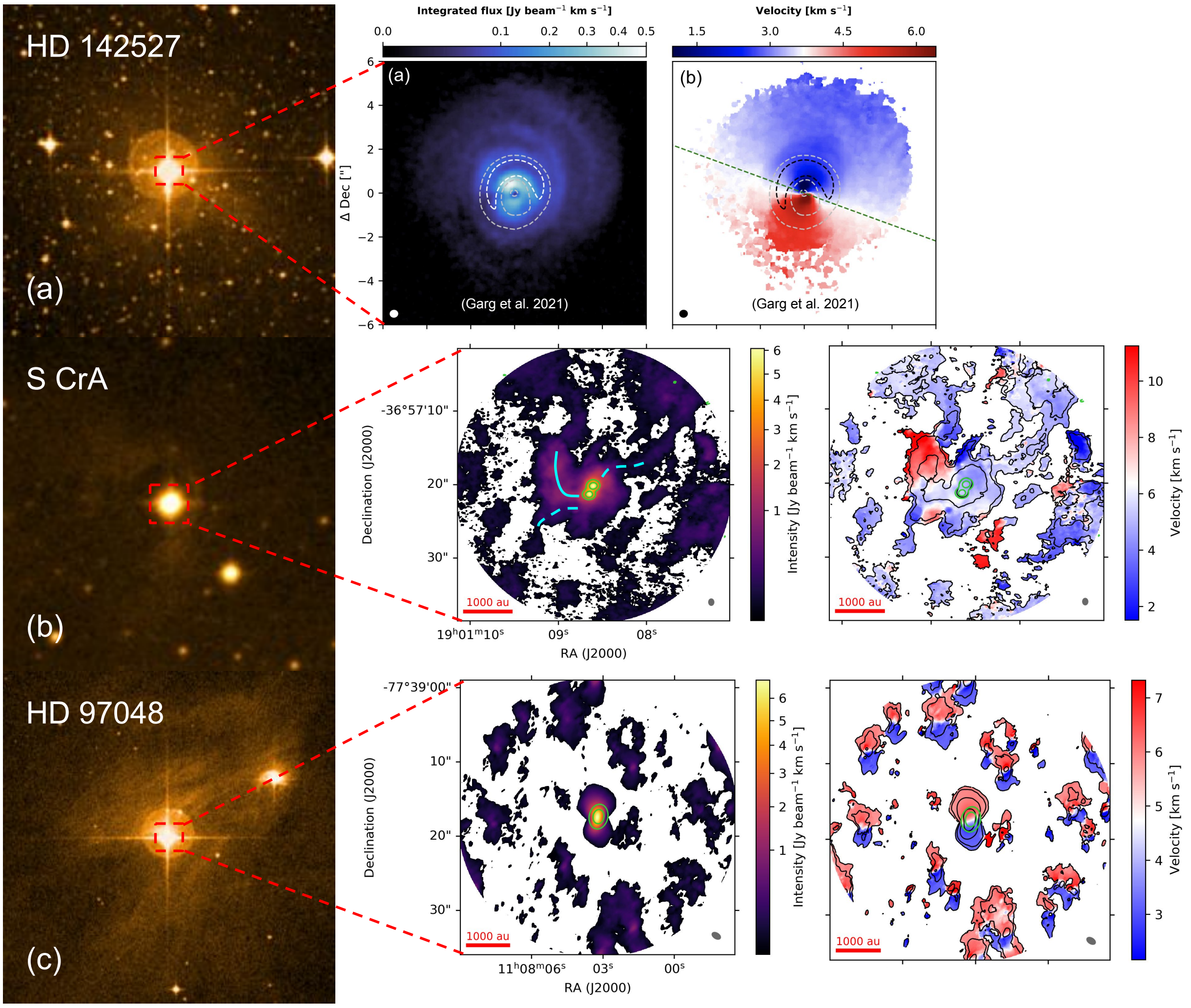

Figure 2.3: Optical images (left), ^{12}CO integrated intensity (moment 0) maps (middle), and ^{12}CO intensity-weighted velocity (moment 1) maps (right) of nearby Class II sources associated with RNe, as discussed in Section 2.3. *Panel a*: HD 142527's DSS optical image and the ALMA ^{12}CO (2–1) moment maps from Garg et al. (2021). *Panel b*: S CrA's DSS2 (red) optical image and the ALMA ^{12}CO (2–1) moment maps. Solid and dashed curved-cyan lines denote prominent and potential streamer-like features, respectively. *Panel c*: HD 97048's DSS optical image and the ALMA ^{12}CO (2–1) moment maps. For the moment maps (middle and right) in panel b and c, only pixels with an intensity $> 3\sigma$ are considered. In these panels, green contours represent continuum emission (~ 1.3 mm, 3σ and 15σ levels) from protoplanetary disks, horizontal red lines in the bottom-left corner represent a 1000 au length scale, the grey ellipse in the bottom-right corner represent the beam size, and black contours in moment 1 maps (right) represent moment 0 emission (starting from the error in moment 0, increased by a factor of five). Errors in moment 0 emission are 22.1 and 20.6 mJy beam^{-1} km s^{-1} for S CrA and HD 97048, respectively.

Chapter 3

TIPSY: Trajectory of Infalling Particles in Streamers around Young stars

This chapter reproduces the paper Gupta et al. (2024), titled *“TIPSY: Trajectory of Infalling Particles in Streamers around Young stars. Dynamical analysis of the streamers around S CrA and HL Tau.”*, and published in the journal Astronomy & Astrophysics.

3.1 Introduction

The traditional picture of low-mass star formation assumes that protostars, together with their circumstellar disks, form due to the axisymmetric collapse of dense protostellar cores (e.g., Shu, 1977; Terebey et al., 1984). Then, as the surrounding gas envelope disperses, protostars evolve from the embedded Class 0 and I stage to the Class II stage. These Class II systems are then traditionally assumed to evolve in isolation to form planetary systems, such as our Solar System.

However, stars form in turbulent giant molecular clouds, where the initial conditions for star and disk formation cannot be represented as isolated non-turbulent spheres (e.g., Pineda et al., 2023; Hacar et al., 2023). Numerical simulations of molecular clouds that follow the collapse of many protostellar cores show that the star-formation processes can be highly asymmetrical, with material usually falling onto protostellar systems via elongated channels, or "streamers" (e.g., Padoan et al., 2014; Haugbølle et al., 2018; Kuznetsova et al., 2019; Lebreuilly et al., 2021; Pelkonen et al., 2021; Kuffmeier et al., 2017, 2023). Recently, with the increased sensitivity of interferometric observations, such streamers have started to be observed around young stellar objects (YSOs) at various evolutionary stages, from the embedded Class 0 and I sources (e.g., Tobin et al., 2012; Yen et al., 2014; Tokuda et al., 2018; Pineda et al., 2020; Thieme et al., 2022; Valdivia-Mena et al., 2022; Murillo et al., 2022; Hsieh et al., 2023; Lee et al., 2023; Mercimek et al., 2023; Cacciapuoti et al., 2023) to the more evolved Class I/II and II sources (e.g., Tang et al., 2012; Akiyama et al., 2019;

Yen et al., 2019; Alves et al., 2020; Garufi et al., 2022; Huang et al., 2020, 2021, 2022, 2023; Gupta et al., 2023). The infalling streamers observed around more evolved YSOs further challenge our assumption that these systems evolve in isolation to form planetary systems; in reality, they are still embedded in large-scale molecular clouds ($\gtrsim$ 1 pc) and may continue to accrete material from them.

The infall of material in evolved sources can greatly influence the physical and chemical properties of protoplanetary disks and, thus, of the planets they form. For example, the supply of fresh material can help solve the "mass-budget problem" of protoplanetary disks, in which observations suggest that they are typically not massive enough to form the observed planetary systems (e.g., Manara et al., 2018; Mulders et al., 2021). Moreover, observations (Ginski et al., 2021) and simulations (Thies et al., 2011; Dullemond et al., 2019; Kuffmeier et al., 2021) have shown that material falling at these late stages can be dynamically different from the original parental core and can induce misalignments in disks. This can further explain the misalignments observed in evolved planetary systems (e.g., Albrecht et al., 2022). Late infall can also bring chemically different material to the system, which can explain the observed chemical diversity among meteorites (Nanne et al., 2019). Simulations (Vorobyov & Basu, 2005; Dunham & Vorobyov, 2012; Padoan et al., 2014; Jensen & Haugbølle, 2018) have shown that infall-induced accretion bursts can naturally resolve the accretion luminosity problem in protostars (see Kenyon et al., 1990). Kuffmeier et al. (2023) demonstrated that infall of material onto Class II systems can also make them seem less evolved, which may affect studies on populations of YSOs. Finally, this phenomenon may also produce some of the observed protoplanetary disk substructures, such as rings (Kuznetsova et al., 2022), spirals (Hennebelle et al., 2017; Kuffmeier et al., 2018), and vortices (Bae et al., 2015).

However, the dynamics of observed streamers need to be characterized to assess their impact on the star and planet formation processes. This has only been done for a few streamers, using methods such as analyzing velocity gradients along the streamers in position–velocity space (e.g., Yen et al., 2014, 2019; Alves et al., 2020), qualitatively comparing infalling trajectories from Mendoza et al. (2009) to the streamer velocity gradients and morphologies (e.g., Pineda et al., 2020; Valdivia-Mena et al., 2022; Garufi et al., 2022), and fitting infalling trajectories determined using the Ulrich-Cassen-Moosman (UCM) model (e.g., Ulrich, 1976; Cassen & Moosman, 1981) to the streamer structures in position–position–velocity (PPV) space (Thieme et al., 2022). These studies suggest that infalling streamers can transfer significant mass to the protostellar systems. However, these parameters are usually estimated only for embedded sources, and the range of their possible values is generally not well constrained. For more evolved Class I/II and II sources, the infalling material can be dynamically unrelated to the protostellar system, and thus we need to explore a wider range of initial configurations to identify the infalling trajectories that best represent observed structures.

To address these issues, we have developed the code Trajectory of Infalling Particles in Streamers around Young Stars (TIPSY)[1], which was designed to fit theoretical trajectories

[1] https://github.com/AashishGpta/TIPSY

of infalling gas to molecular-line observations of streamers, without assuming any initial configuration (relative position and velocity) for the gas. We further used this code to analyze streamers around two evolved sources: the Class II binary system S CrA, for which a ∼1000 au streamer-like structure was reported by Gupta et al. (2023), and the Class I/II system HL Tau, for which a kinematic analysis of a ∼ 500 au streamer (Yen et al., 2019) and the corresponding shock observations (Garufi et al., 2022) suggest an infalling motion of gas. Evolved sources are also more suitable for this kind of analysis because the protostellar masses can be estimated independently of streamer modeling, as done by using spectroscopy for S CrA (Gahm et al., 2018) and via the modeling of a Keplerian disk for HL Tau (Yen et al., 2019).

The fitting methodology employed by TIPSY is detailed in Section 3.2. Subsequently, we demonstrate TIPSY by using it to analyze the streamers around S CrA (Sect. 3.3.1) and HL Tau (Sect. 3.3.2). The results are discussed in Sect. 4.5, and we conclude in Sect. 4.6.

3.2 Fitting methodology

TIPSY fits theoretical trajectories expected for infalling gas, following the model given in Mendoza et al. (2009), to the molecular-line observations of streamers. The fitting is done in three-dimensional (3D) PPV space: right ascension (RA), declination (Decl.), and line-of-sight (LOS) velocity or radial velocity (RV); in other words, the morphology and velocity gradient of streamers are fitted simultaneously. To define a general initial configuration of infalling gas, we needed to define the 3D position ($\overrightarrow{r_0}$) and velocity ($\overrightarrow{v_0}$) vectors relative to the protostar (see Fig. 3.1). Relative position in RA and Decl. direction as well as the relative speed in the LOS direction can be inferred directly from the observations. The remaining three parameters, required to define an initial configuration, are the separation in the LOS direction and the relative speeds in the RA and Decl. directions. For a range of possible initial configurations, we computed theoretical trajectories (see Sect. 3.2.1) and compared them to the observations (see Sect. 3.2.2 and Figs. 3.2 and 3.3). The distribution of free parameters with reasonable fits was used to estimate uncertainties (see Sect. 3.2.3 and Fig. 3.4). Some of the known caveats associated with this kind of analysis are mentioned in Sect. 3.2.4.

The idea of comparing streamer observations to the infalling trajectories in the PPV space is similar to the fitting of UCM trajectories to elongated structures around the Class 0 protostar Lupus 3-MMS by Thieme et al. (2022). However, the UCM model assumes the particle to be in a parabolic orbit with no initial RV (e.g., Ulrich, 1976). Moreover, Thieme et al. (2022) had to make further assumptions about the configuration of infalling gas, for example an initial radius of 10000 au and a final centrifugal radius of 105 au. Such assumptions are less likely to be valid for more evolved (Class I/II and II) sources because the infalling material can be dynamically unrelated to the original parental core of the protostellar system.

3.2.1 Physical model

One of the first models for gas infalling onto a protostellar system was given by Bondi (1952); however, it did not consider the rotation of the infalling gas. Later, the UCM model developed, which provides analytical solutions for the trajectory of a particle infalling around a protostar, assuming that the initial rotation of the particle is about the rotational-axis of the central protostellar system or the "z-axis" (Ulrich, 1976; Cassen & Moosman, 1981; Chevalier, 1983; Terebey et al., 1984; Visser et al., 2009; Shariff et al., 2022). This model has been used to analyze infalling motion of material in streamers around young protostellar systems (e.g., Thieme et al., 2022).

The boundary conditions used in the UCM model also assume that the infalling gas starts with a zero RV and it is just bound to the protostar, that is to say, it is on a zero energy parabolic orbit. However, for any general initial configuration of infalling gas, especially in the context of late infall of material onto a Class II system, these assumptions may not hold true. Mendoza et al. (2009) extended the UCM model to account for possible nonzero initial RVs and energies. This model has also been used to study kinematics of material in streamers around protostars at different evolutionary stages (e.g., Pineda et al., 2020; Valdivia-Mena et al., 2022; Garufi et al., 2022). The equations derived by Mendoza et al. (2009) to compute positions and velocities of an infalling particle along its trajectory are listed in Section 1.4.1

However, the original Mendoza et al. (2009) model still assumes the initial rotation is only about the z-axis. This assumption can be mitigated by solving the equations in a rotated coordinate frame, where the z-axis is defined not as the rotational axis of central protostellar system but as a vector normal to the plane of the particle trajectory. This is defined as the plane containing the initial position ($\overrightarrow{r_0}$) and velocity vector ($\overrightarrow{v_0}$) of the particle with respect to the protostar, as illustrated in Fig. 3.1. We used this generalized implementation of the Mendoza et al. (2009) model to generate trajectories of infalling particles without making any assumptions about their initial position or velocity. The results obtained from our implementation of Mendoza et al. (2009) models were also validated through two-body simulations using the REBOUND framework (Rein & Liu, 2012), as shown in Appendix B.1.

3.2.2 Fitting procedure

TIPSY is designed to analyze molecular-line observations of streamers with a large enough recoverable scale to capture the streamer morphology, a sufficient spectral resolution to resolve the velocity profile, and a significant detection ($\gtrsim 3\sigma$) of streamer emission in each of the channels (see Sect. 3.4.1 for a further discussion). The first step in characterizing streamer observations involves separating the streamer emission from other sources of emission, such as disks. Given the wide range of morphologies exhibited by disks and streamers in different sources, which depend on the observational parameters and molecular lines used, it is hard to automate this step. Therefore, we visually examine the emission maps and define a boundary for a sub-cube that encompasses the streamer emission using RA,

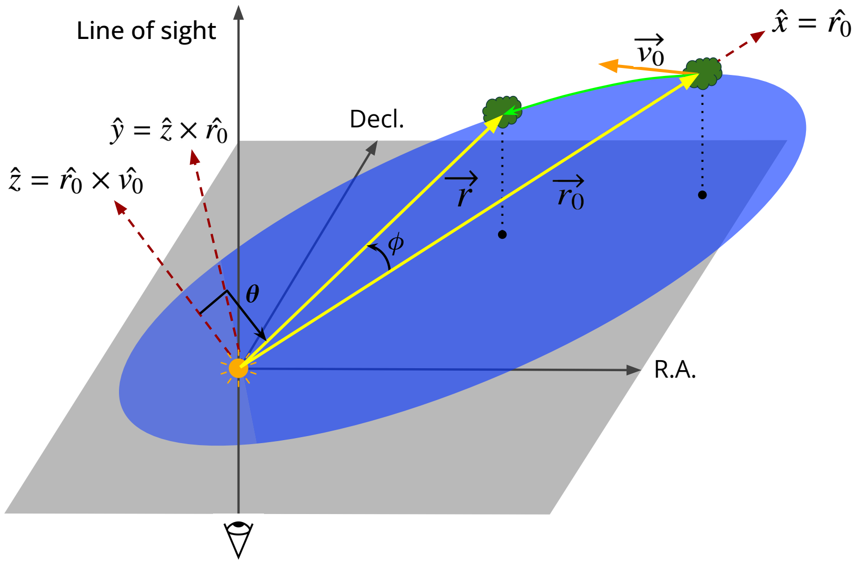

Figure 3.1: Schematic diagram of coordinate axes used to compute the theoretical trajectories of infalling gas (green cloud) around a protostellar system (orange star), as discussed in Sect. 3.2.1. $\vec{r_0}$ and $\vec{v_0}$ denote the initial position and velocity vector of infalling gas, respectively. $\vec{r}$ represents the position vector of gas at a future point in its trajectory (circumference of blue ellipse), with θ and ϕ denoting the polar and azimuthal angles, respectively. The dashed red arrows show the unit vectors $\hat{x}$, $\hat{y}$, and $\hat{z}$, defined using the directions of $\vec{r_0}$ and $\vec{v_0}$. Together they set the coordinate frame in which TIPSY solves the Mendoza et al. (2009) equations. The gray plane represents the POS, with the overlaid dark gray arrows denoting the coordinate frame of our observations.

Decl., and RV limits. Next, we eliminate pixels with flux values below a specified noise (σ) level. Table 3.1 lists the values used for selecting streamers around S CrA and HL Tau. As long as the selected boundaries fully capture the observed streamer emission, the final results are not very sensitive to the exact values of these limits. This is because we primarily rely on the central brighter emission throughout the structure for the fitting, as described in more detail later.

The resulting sub-cube, comprising mainly of streamer emission, may still contain some unrelated emission features from residual noise or other gas structures. To get a more cleanly isolated streamer emission, we use a clustering algorithm to identify and remove seemingly unrelated emission. By default, we use the sklearn (Pedregosa et al., 2011) implementation of the Ordering Points To Identify the Clustering Structure (OPTICS; Ankerst et al., 1999) clustering algorithm, which computes density-based reachability distances to reveal clusters within a dataset. The biggest coherent cluster of emission in the selected sub-cube is identified as the streamer and the smaller clusters generally correspond to noise peaks. This step is designed to allow users to set liberal boundaries and noise thresholds while selecting the streamer sub-cube, as noise peaks can then be removed without reducing streamer emission.

Parameter	S CrA	HL Tau
Stellar mass [$M_\odot$]	2	2.1
Distance [pc]	160	147
Systemic velocity [km / s]	5.86	7.14
Min. RV offset [km / s]	4.5	7
Max. RV offset [km / s]	7	10
Min. RA offset [arcsec]	2	-3
Max. RA offset [arcsec]	15	-1
Min. Decl. offset [arcsec]	-7	-3
Max. Decl. offset [arcsec]	7	0.5
Significance (σ) level	3	4

Table 3.1: Parameters used to isolate and fit the HL Tau and S CrA streamers. See Appendix B.3 for more details on the stellar parameters used.

This isolated and cleaned streamer emission can be imagined as a point cloud in 3D PPV space, as shown in Figs. 3.2 and 3.3 (panel c). The theoretical trajectories of infalling material (as discussed in Sect. 3.2.1) that we aim to fit to the data can be represented as curves in the same 3D space. In order to directly compare the observation to the theoretical curves, we define a curve that would be representative of the observed streamer structure in the PPV space. To do this, we first divide the streamer points into several bins, set to ten by default, based on a distance metric. Then within each of these bins, we compute intensity-weighted means and intensity-weighted standard deviations of the RA, Decl., and RV values of all the points (red squares and their error bars in panel c of Figs. 3.2 and 3.3). This gives us a string of a few points, ten by default, in the same 3D space, which can be directly compared to the theoretical curves (panels c and d in Figs. 3.2 and 3.3). This method also reduces the dependence of fitting results on the fainter parts of the streamers, selected streamer boundaries, and the spatial and spectral resolution of the data. As long as an adequate number of bins are used (i.e., enough to capture the overall streamer curvature), the final fitting results will not be sensitive to the number of bins.

The distance metric (d) we use to bin the data is defined as $d = \sqrt{r^2 + (wr\theta)^2}$, where r and θ are the polar coordinates of a point on the plane of the sky (POS), with respect to the protostar and the orientation of the streamer very close to the protostar (see Appendix B.2 for more details). The w represents a weighting factor to adjust the importance of $r\theta$ distance (azimuthal direction) relative to the r distance (radial direction) in the distance metric calculation and is by default equal to one. Overall, larger values of d should denote points in the streamers that are expected to be farther away from the protostar. Figure B.2 shows the computation of the distance metric values for all the points in the streamers around S CrA and HL Tau. In addition to the binning of the data, the distance metric is also used as an independent variable for comparing theoretical curves to the observations, as discussed later.

To compare theoretical trajectories with observed streamers, we need to establish a parameter space that covers all the possible initial conditions. For a particle falling onto a protostar, there are seven initial configuration parameters: three for the particle's initial relative position in 3D, three for its initial relative velocity in 3D, and the protostar's mass. To determine the relative position in the RA and Decl. directions in physical units, we use the physical distance to the protostellar system and the projected separation of the farthest point of the streamer. The separation in the LOS direction is unknown and treated as a free parameter. For the relative velocity, we use the systemic velocity of the central protostar and the LOS velocity of the farthest point of the streamer to obtain the relative speed in the LOS direction. The relative speed in the RA (v_{RA}) and Decl. ($v_{Decl.}$) directions are free parameters. To reduce computations, instead of treating v_{RA} and $v_{Decl.}$ separately, we use the total speed on the POS ($\sqrt{v_{RA}^2 + v_{Decl.}^2}$) and the initial direction of the particle on the POS ($\arctan(v_{Decl.}/v_{RA})$). Here, the initial direction on the POS can be constrained more easily by the projected shape of the streamer. For evolved sources (Class I/II and II), the protostellar mass is typically assumed to be known from other measurements such as disk rotation (e.g., Yen et al., 2018) or protostellar luminosity (e.g., Manara et al., 2023, and references therein). We note that mass estimates using luminosity can be quite uncertain for young Class I/II sources (e.g., Baraffe et al., 2012). In conclusion, we have three free parameters: relative separation in the LOS direction, relative speed on the POS, and the direction of the relative velocity on the POS. TIPSY allows users to set a range of possible values for each of these parameters, which creates a 3D parameter space that is used for the fitting.

Using this parameter space and the Mendoza et al. (2009) model (Sect. 3.2.1), we calculate infalling trajectories for every parameter combinations. These trajectories are compared to the observed streamer curve (intensity-weighted means and standard deviations) to find the best fit. We independently compare the representative RA, Decl., and RV values using the distance metric, defined earlier as $d = \sqrt{r^2 + (wr\theta)^2}$, as the independent variable for fitting. We use the first-order spline interpolation, as implemented in scipy (Virtanen et al., 2020), to get the theoretical values at the same distance metric values as the points of the observed streamer curve (panel d in Fig. 3.2 and 3.3). Then, we examine what fraction of the RA, Decl., and RV values of the observed streamer curve match within the error bars (standard deviations) to the theoretical values. This fraction is referred to as the "fitting fraction" in Fig. 3.4. We consider the best-fit trajectory as the one that can accommodate the highest fraction of mean values representing the observed streamer, within their error bars. In cases where multiple trajectories fit the same fraction of values, we choose the trajectory with the lowest chi-squared deviation as the best fit.

3.2.3 Error estimation

As discussed in Sect. 3.2.2, we compute theoretical infalling trajectories for each of the parameter combinations and check the fraction of values (RA/Decl./RV) of observed streamer's curve-like representation (intensity-weighted means) that agree with the theoretical values within the error bars (intensity-weighted standard deviations). To estimate

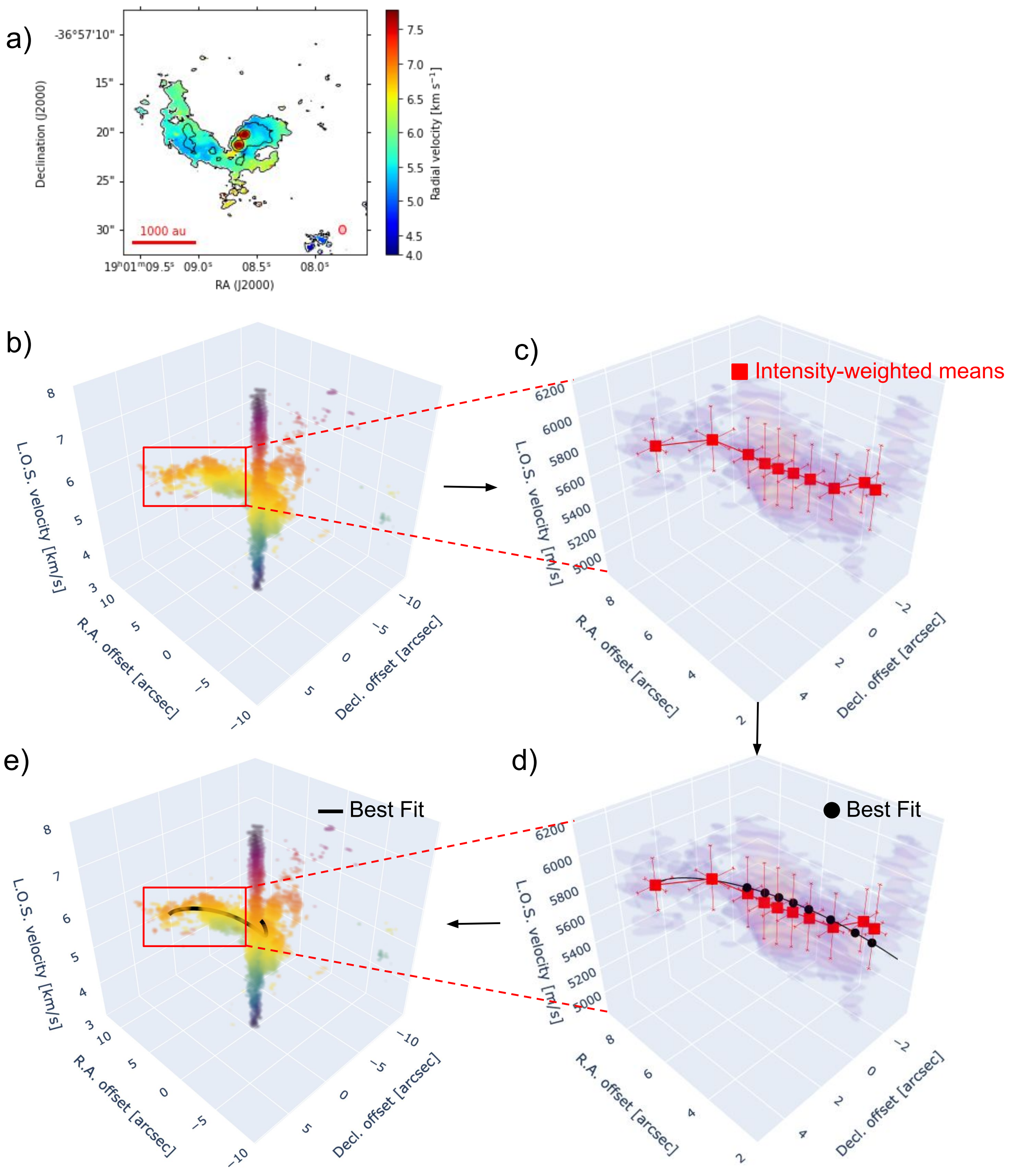

Figure 3.2: Flow of S CrA ^{13}CO (2–1) data in the TIPSY pipeline. *Panel a*: Intensity-weighted velocity (moment 1) map in colors, overlaid with contours representing the integrated intensity (moment 0; see Fig. B.3). The red segments in the bottom-left corners depict a length scale of 1,000 au. The pink ellipses in the bottom-right corners depicts the beam size of the data. *Panel b*: Isometric projection of the 3D PPV diagram of pixels with intensity $> 5\sigma$ in the whole field of view. *Panel c*: Isometric projection of the PPV diagram of an isolated and cleaned streamer. The red square and its error bars represent intensity-weighted means and standard deviations, respectively. *Panel d*: Same as Panel c, but with the best-fit trajectory, as represented by the black line. Black circles denote the interpolated values of the theoretical trajectory, which are directly compared to the intensity-weighted means. *Panel e*: Same as Panel b, but with the best-fit trajectory, as represented by the black line. *Note*: 3D interactive versions of panels d and e are available online.

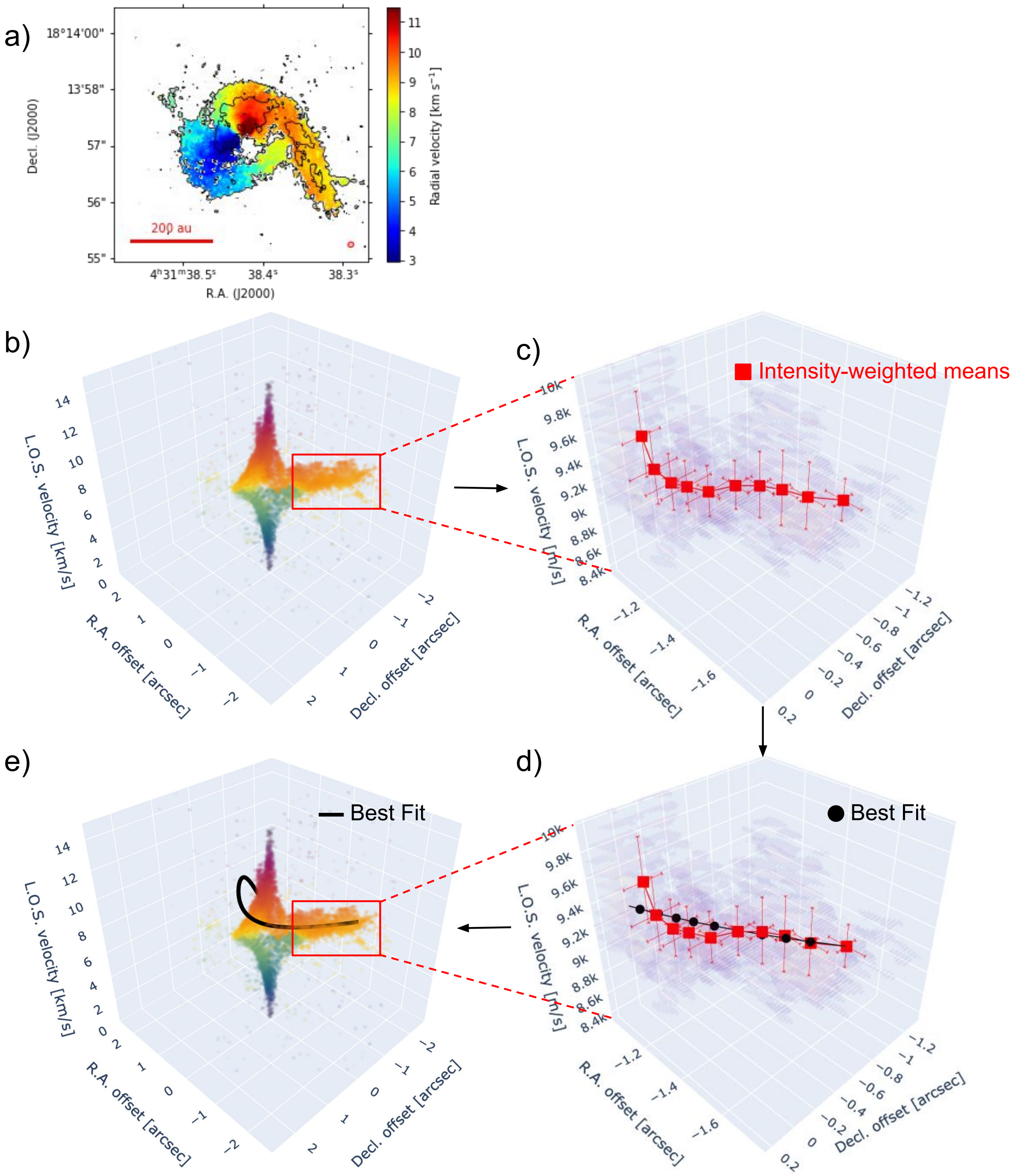

Figure 3.3: Same procedure as described in Figure 3.2, but for HL Tau instead of S CrA. *Note*: 3D interactive versions of panels d and e are available online.

errors in the fitted free parameters (LOS distance, projected speed on the POS, direction on the POS), we select trajectories that can fit at least a certain fraction, 0.9 by default, of the values of observed streamer curve. For each of these trajectories, we store the parameter combinations used to produce them. Subsequently, the errors are estimated as the standard deviations of each parameter for these parameter combinations with sufficiently good fits (fitting fraction greater ≥ 0.9). Figure 3.4 display these errors in LOS distances and speed on the POS for the best fits of S CrA and HL Tau.

These error estimates are, by default, also compared to the spatial and velocity resolution of free parameters, used for generating the parameter space. If the error (standard deviation) computed for a parameter is less than the resolution used, the error estimate is increased to this parameter resolution. This generally suggests that the resolution used to create the initial parameter space was too coarse to capture the true fitting uncertainty.

For the parameters estimated directly from the observation (i.e., the offset in RA, Decl. and RV), intensity-weighted standard deviations corresponding to the outermost point of the observed streamer curve is used. All these uncertainties are further propagated to the derived physical parameters, as listed in Table 3.2. TIPSY also provides a table of goodness-of-fit measurements (fitting fraction and chi-squared deviation) for all parameter combinations, enabling users to independently estimate errors using their preferred methodology.

We note that TIPSY does not currently propagate errors in the fixed parameters to the errors of fitted parameters. These fixed parameters include stellar parameters (stellar mass, systematic velocity, and distance) as well as the parameters corresponding to the observed initial offset of the streamer with respect to to the protostar (offset in RA, Decl., and RV).

3.2.4 Caveats

An important assumption in the Mendoza et al. (2009) models (see Sect. 3.2.1) used to compute infalling trajectories is that we consider only one force acting on the infalling material: the gravitational force of a point mass (protostar). To begin with, this means that we neglect the contribution of gravitational and tidal effects of circumstellar material. This assumption is valid as long as most of the mass is concentrated within the central region, which is usually the case, especially in the evolved sources. More importantly, we also do not account for the tidal forces from a multiple system, as briefly discussed in Sect. 3.3.1. We also neglect the effects of gas pressure gradients and shocks (e.g., Shariff et al., 2022), magnetic fields (e.g., Unno et al., 2022), and turbulence (e.g., Seifried et al., 2013). However, these assumptions are generally valid at the length scales of streamers, which are farther away from the protostar, and thus, protostellar systems can be approximated as a point source and the gas density is low. Moreover, the fitting methodology of TIPSY can also be adapted to fit more complicated models to the streamer emission.

While fitting the observed streamer structures, we also assume that the observed intensity of molecular-line emission represents the actual density distribution of gas. This assumption should mostly be valid for low-density streamers; for streamers with a higher density of gas, an appropriately less abundant molecular tracer should be used.

Finally, it is important to note that the current implementation of TIPSY does not necessarily rule out the other possible causes of large-scale elongated structures, such as stellar flybys (e.g., Dong et al., 2022; Cuello et al., 2023), the ejection of gas (e.g., Vorobyov et al., 2020), or gravitational instability in disks (e.g., Dong et al., 2015). However, a good fit of observed structures by TIPSY would mean that the observed structures can be explained as infalling streamers. Ideally, a comparative analysis with other competing models would be required to identify the most likely cause. The analytical model used to compute infalling trajectories, as described in Sect. 3.2.1, also allows us to generate unbound hyperbolic trajectories, which may be useful in identifying ejections of unbound gas (e.g., Vorobyov et al., 2020). Complimentary observations, such as polarization in the near-infrared (e.g., Ginski et al., 2021) and molecules tracing shocks (e.g., Garufi et al., 2022), can be used to further ascertain the dynamical nature of the streamers.

3.3 Applications

In order to test the TIPSY methodology, we used two protostellar systems with known streamers: the Class II binary source S CrA (Gupta et al., 2023) and the Class I/II source HL Tau (Yen et al., 2019; Garufi et al., 2022). As TIPSY requires a prior estimation of protostellar mass, it is better suited to analyzing streamers around more evolved Class I/II and II sources. For these sources, most of the streamers have been serendipitously observed in bright ^{12}CO emission and generally suffer from significant cloud absorption and contamination. This may result in an inaccurate judgement of the extent of the streamers and, thus, an unreliable modeling of them. We present the fitting results for ^{13}CO (2–1) data of S CrA and HCO^{+} (3–2) data of HL Tau in Sects. 3.3.1 and 3.3.2, respectively.

3.3.1 S CrA

S CrA is a binary system, comprising of two Class II sources with a separation of $\sim$ 200 au, in the Corona Australis star-forming region. Using spectral and photometric monitoring of both of the protostars, Gahm et al. (2018) found them to be very similar to each other, with stellar masses of 1M$_{\odot}$. These masses agree with the modeling of orbital motions by Zhang et al. (2023).

Zhang et al. (2023) also reported disk-scale spirals and a $\sim$ 200 au streamer-like structure connected to the southern protostar, as observed in SPHERE (Spectro-Polarimetric High-contrast Exoplanet REsearch) polarization observations. Furthermore, Gupta et al. (2023) found this system to be surrounded by 0.1 parsec-scale clouds, appearing as reflection nebulae, and $\sim$ 1000 au elongated structures revealed by ^{12}CO (2–1) Atacama Large Millimeter/submillimeter Array (ALMA) observations, suggesting infall of material onto the system. However, these ^{12}CO observations suffered from contamination from surrounding diffuse gas (see Fig. F.1 in Gupta et al., 2023) and also a prominent absorption feature close to systemic velocity of the source, where a lot of bound material is expected to be.

For our analysis we used the ^{13}CO (2–1) observations, taken as a part of the same ALMA project (Project Id.: 2019.1.01792.S), which show a much cleaner $\sim$ 1300 au streamer (Fig. 3.2 and B.3a). We used the standard pipeline calibrated data and the imaging was done using "Briggs" weighting with robust=0.5, a cell size of 0.05 arcsec, and "auto-multithresh" masking with default parameters. We detected the streamer at $\gtrsim 5\sigma$ level, in all the relevant channels.

TIPSY results suggest that the overall streamer is consistent with being a trail of infalling gas. For the best fits, infalling trajectories could fit all the ten points in the simplified streamer (intensity-weighted means, red squares in Fig. 3.2) within the error bars (intensity-weighted standard deviations). The best-fit parameters, as given in Table 3.2, suggest that the material is strongly bound to the protostars, with the specific (per unit mass) total energy (kinetic energy plus gravitational potential energy; see Sect. 3.4.2) of -1.1 ± 0.1 km^2 s^{-2}. This suggests that the observed structure is not an ejection of unbound material, which should be on hyperbolic trajectories. The size of observed streamer, which is at least an order of magnitude larger than the protoplanetary disks, further indicate that this is not a spiral arm induced by gravitationally unstable disk.

Moreover, we also find that the velocity profile of observed streamer changes close to the protostars, that is to say, the LOS velocities stop decreasing and start increasing, which was not reproduced in our best-fit models (panel d, Fig. 3.2). This suggests that the gas falling from behind the protostar (see Fig. B.1a) is being slowed. The change in gas dynamics closer to the protostars could be due to the tidal forces from the binary system that are expected to dominate in inner regions (e.g., Zhang et al., 2023). To test this, a detailed modeling of infalling material interacting with binaries and circumbinary material is required, which is beyond the scope of this study.

3.3.2 HL Tau

HL Tau is a Class I/II source with a ~ 2 M$_\odot$ mass protostar (Yen et al., 2019) surrounded by a protoplanetary disk with concentric rings and gaps (ALMA Partnership et al., 2015). Yen et al. (2019) found the source to be associated with a few-hundred-au-long streamer using HCO$^+$ (3–2) ALMA observations. They analyzed the velocity gradient along the structure and found it to be dominated by the infalling motion in the outer region. HL Tau is also known to be surrounded by a gas envelope with $\sim$ 1000 au scale asymmetric structures (Yen et al., 2017), which may be feeding this streamer. Furthermore, Garufi et al. (2022) also reported emission from shock tracer (SO_2 and SO) at the expected interface of the streamer and the disk, suggesting that the infalling material is impacting the disk.

For our analysis, we used the same self-calibrated HCO$^+$ (3–2) ALMA observations (Project Id.: 2016.1.00366.S) of HL Tau as described in Yen et al. (2019). These observations show significant emission ($\gtrsim 4\sigma$) from the streamer, along with a Keplerian disk, in all the relevant channels (see Figs. 3.3 and B.3b).

TIPSY results, as shown in Fig. 3.3, demonstrate that all the points of the simplified streamer curve (intensity-weighted means) can be fit within the error bars (intensity-

Quantity	S CrA	HL Tau
RA offset [AU]	1149±76	-227±12
Decl. offset [AU]	618±123	-159±15
LOS offset [AU]	300±150	-1400±573
RA speed [km / s]	0.37±0.18	0.3±0.6
Decl. speed [km / s]	-0.47±0.15	0.6±1.2
LOS speed [km / s]	0.02±0.17	1.79±0.20
Specific kinetic energy [km^2 / s^2]	0.18±0.10	1.8±0.9
Specific potential energy [km^2 / s^2]	-1.33±0.09	-1.3±0.5
Specific angular momentum [AU km / s]	791±218	606±1803
Infall time [yr]	8301±1358	2724±1237

Table 3.2: Fitting results for S CrA and HL Tau.

weighted standard deviations) by an infalling trajectory. The fitting results are listed in Table 3.2. For HL Tau, the specific kinetic energy is consistent with the specific gravitational potential energy within the error bars, suggesting that the gas is roughly in a zero-energy parabolic orbit. However, TIPSY could not constrain the trajectory of infalling particles for HL Tau well (see bottom panels, Fig. 3.4), as further discussed in Sect. 3.4.1.

3.4 Discussion

3.4.1 Data requirements

Comparing TIPSY fitting results for S CrA (Sect. 3.3.1) and HL Tau (Sect. 3.3.2), we can see that the uncertainties are much higher for HL Tau (see Table 3.2). Moreover, Fig. 3.4b shows that the distribution of best-fit parameters (higher fitting fractions, lower χ^2 deviations) are not well represented by simple symmetrical errors for HL Tau. This is likely because the HL Tau observations, limited by the largest recoverable scale, reveal only a $\sim$ 300 au part of streamer, much shorter than the $\sim$ 1300 au streamer around S CrA. This section of streamer is not long enough to capture any curvature in streamer morphology, which helps in constraining the speed of infalling particle on the POS. This is useful in breaking the degeneracy between the initial POS speed and the LOS separation and, thus, placing a stringent constraint on the streamer trajectories. This suggests that observations with higher recoverable scales ($\gtrsim$1000 au) are better for constraining streamer dynamics.

The channel width (velocity resolution) for both the S CrA and HL Tau observations is $\sim$ 0.1 km s^{-1}, which allows TIPSY to resolve the velocity profile (for further discussion, see Appendix D of Gupta et al., 2023). Besides this, TIPSY requires a significant streamer ($> 3\sigma$) emission to be observed in all the relevant channels – as is the case in the analyzed observations – in order to distinguish the streamer from the surrounding diffuse gas and the background noise.

3.4.2 Physical parameters

As discussed in Sect. 3.2.2, TIPSY fitting results provide estimates for the initial LOS distance (d_{LOS}), the initial projected speed on the POS, and the initial direction on the POS for the infalling gas. The initial speed and direction on the POS can be converted to the initial speed in the RA (v_{RA}) and Decl. ($v_{Decl.}$) directions using simple trigonometric relations. These parameters, combined with the initial LOS velocity offset (v_{LOS}) and the spatial offset in the RA (d_{RA}) and Decl. ($d_{Decl.}$) directions, inferred directly from observations, can provide complete information about the initial configuration of infalling gas relative to the protostar.

These parameters can be used to derive other physically relevant quantities. For example, specific (per unit mass) kinetic energy can be estimated as $0.5 \times (v_{RA}^2 + v_{Decl.}^2 + v_{LOS}^2)$. Similarly, assuming that the local gravitational potential is dominated by the mass of protostellar system, specific gravitational potential energy can be estimated as $-G \times M_* / \sqrt{d_{RA}^2 + d_{Decl.}^2 + d_{LOS}^2}$, where G and M_* represent universal gravitational constant and mass of protostellar system, respectively. We can sum them to get the specific total energy ($T.E.$), which can tell us if the gas is in a bound elliptical orbit ($T.E. < 0$, similar to the streamer around S CrA), a bound parabolic orbit ($T.E. \approx 0$, similar to the streamer around HL Tau), or an unbound hyperbolic orbit ($T.E. > 0$).

Using the initial position ($\overrightarrow{r_0}$) and velocity ($\overrightarrow{v_0}$) vector of infalling gas, we can also estimate the specific angular momentum as $\overrightarrow{r_0} \times \overrightarrow{v_0}$. This can be compared to the angular momentum of the disks to quantify the role of infalling material in misaligning the protoplanetary disks, as has been suggested by some hydrodynamic simulations (e.g., Thies et al., 2011; Kuffmeier et al., 2021). For the S CrA and HL Tau streamers, we find the specific angular momentum magnitudes to be 791 ± 218 AU km s^{-1} and 606 ± 1803 AU km s^{-1}, respectively. For reference, the specific angular momentum (l) in the outer part of a 100 au Keplerian disk around a 2 $M_\odot$ star protostar, similar to HL Tau, should be $\sim$ 421 AU km s^{-1} ($l = \sqrt{GM_* R_d}$, where G, M_*, and R_d are the gravitational constant, the protostellar mass, and the disk radii, respectively).

As TIPSY provides the complete trajectory of the infalling gas, until the motion is dominated by the gravitational force, we can also infer the 3D (RA, Decl., and LOS distance) morphology of the infalling streamer, as shown in Fig. B.1. These morphologies can further be validated using near-infrared polarization observations, as the degree of polarization in such observations can be correlated to the 3D orientation of dust structures (e.g., Ginski et al., 2021). A better understanding of the 3D morphology of the streamer can be useful in constraining the location and velocity of impact for material falling onto the disk, which allows us to understand the role of infalling material in creating shocks (e.g., Garufi et al., 2022) and disk substructures (e.g., Bae et al., 2015; Kuznetsova et al., 2022).

TIPSY also provides an estimate of the infall timescale for the material, defined as the time taken for the best-fit solutions to reach the point closest to the protostars, starting from the farthest point in the observed streamer. We found infall timescales of 8301 ± 1358 yr and 2724 ± 1237 yr for the S CrA and the HL Tau streamer, respectively. This implies that these structures are either short-lived ($\lesssim 10,000$ yr, $< 1\%$ of typical disk lifetime) or continuously replenished by larger-scale gas reservoirs. Both S CrA (Gupta et al., 2023) and HL Tau (Welch et al., 2000) are surrounded by large-scale clouds, which can be feeding these streamers. Serendipitously detecting short-lived structures should also be less likely, which could further suggest that these structures survive for longer by accumulating material from surrounding clouds. Large-scale clouds have been observed around other serendipitously detected streamers (e.g., Gupta et al., 2023). We also note that the derived infalling timescales are comparable to the lifetimes of tidal arms induced by stellar flybys (e.g., Cuello et al., 2023).

Moreover, the infall timescale can be combined with the mass of the streamer to estimate the mass infall rate. A rough lower limit of mass of molecular gas can be estimated from integrated flux ($F_{streamer}$), assuming optically thin emission, as

$$M_{streamer} \gtrsim \frac{2.37 m_H 4\pi D^2 F_{streamer}}{A_{trans.} h\nu x_{mol.} f_u}, \tag{3.1}$$

where m_H is the mass of a hydrogen atom, D is the distance to the source, $A_{trans.}$ is the Einstein A coefficient of observed line transition, ν is the line frequency, $x_{mol.}$ is the abundance of the molecule relative to H_2, and f_u is the fraction of molecules in the upper energy state of the transition (e.g., Bergin et al., 2013). Here, f_u can be further computed as $f_u = 3e^{E_u/T}/Q_{mol.}(T)$, where E_u is the upper state energy for the transition, T is the gas temperature, and $Q_{mol.}(T)$ is the partition function for the molecule. We took $A_{trans.}$ and E_u values for ^{13}CO (2–1) (S CrA) to be 6.038×10^{-7} s^{-1} and 15.87 K, and HCO^+ (3–2) (HL Tau) to be 1.453×10^{-3} s^{-1} and 25.68 K, respectively, from the Leiden Atomic and Molecular Database (Schöier et al., 2005). The $x_{mol.}$ values were taken to be 1.45×10^{-6} for ^{13}CO (e.g., Huang et al., 2020) and 10^{-9} for HCO^+ (e.g., Jørgensen et al., 2004). For both sources, we assumed a representative temperature of 25 K, which is typical for gas at these ∼100-1000 au scales (e.g., Jørgensen et al., 2005). At this temperature, $Q_{mol.}(T = 25\ K)$ values, interpolated from values provided in Cologne Database for Molecular Spectroscopy (Endres et al., 2016), were 19.6 and 12.0 for ^{13}CO and HCO^+, respectively. We computed $F_{streamer}$ to be 1.3×10^{-20} W m^{-2} for S CrA and 4.2×10^{-21} W m^{-2} for HL Tau by integrating the flux of the isolated streamer emission (panel c in Figs. 3.2 and 3.3) over both the position and the velocity.

Using these values, we estimated the streamer masses to be $\gtrsim 2.1\times10^{-4}$ M$_\odot$ and $\gtrsim 1.2\times10^{-5}$ M$_\odot$ for S CrA and HL Tau, respectively. Although these estimates do not include parts of the streamers beyond the primary beams of the interferometric observations, they can still be used to estimate mass infall rates as $\dot{M}_{inf} = M_{streamer}/T_{inf}$, where T_{inf} refers to the infall time for the observed streamer. Mass infall rates are found to be $\gtrsim 2.5\times10^{-8}$ M$_\odot$ yr^{-1} (or $\gtrsim 27$ M$_{jupiter}$ Myr^{-1}) for S CrA and $\gtrsim 4.5\times10^{-9}$ M$_\odot$ yr^{-1} (or $\gtrsim 4.7$ M$_{jupiter}$ Myr^{-1}) for HL Tau. Interestingly, these values are comparable to mass accretion rates of pre-main-sequence objects (e.g., Manara et al., 2023), which have been proposed to be influenced by late-accretion of material from large-scale clouds (Padoan et al., 2005). We note that typical mass accretion rates are generally an order of magnitude higher for Class I sources (e.g., Enoch et al., 2009), which may be a better comparison for HL Tau.

Moreover, over typical disk lifetimes of a few megayears, these mass infall rates can increase mass available for forming planets by an order of magnitude, which can resolve the apparent mass-budget problem in Class II disks (Manara et al., 2018; Mulders et al., 2021). The estimated mass flow rates, along with the chemical characterization of streamers, can also be used to understand their impact in shaping disk chemistry (e.g., Pineda et al., 2020). We note that these values should be treated as an order of magnitude estimates. A reliable mass estimation will require modeling multiple molecular-line tracers, which is beyond the scope of this paper.

3.5 Conclusions

We have developed a code, TIPSY, to study the gas dynamics in infalling elongated structures, often referred to as streamers. TIPSY is designed to simultaneously fit the morphology and velocity profile of the molecular-line observations of streamers with the expected trajectories of infalling gas.

To begin with, TIPSY results can be used to judge whether the observations of streamer-like structures are consistent with infalling motion, depending on how well the infalling trajectories fit the streamers. The dynamical nature of the TIPSY solutions and complementary observations (e.g., Ginski et al., 2021; Garufi et al., 2022) can be used to rule out other potential causes, such as stellar flybys (e.g., Cuello et al., 2023), the ejection of gas (e.g., Vorobyov et al., 2020), or gravitational instability in disks (e.g., Dong et al., 2015). Then, using the best-fit trajectories, TIPSY provides information about the 3D morphology and kinematics of the infalling gas. This can in turn allow us to estimate parameters such as the infall timescale, the specific angular momentum, the specific total energy, and potentially the expected impact zone of the streamer on the protoplanetary disk. These quantities, combined with a better understanding of overall gas reservoirs, can allow us to study the role of infalling material in replenishing disk masses, impacting disk chemistry, tilting disks, and creating disk substructures.

We tested TIPSY on two objects: a ~ 1300 au ^{13}CO streamer around S CrA (a Class II binary system) and a ~ 300 au HCO^{+} streamer around HL Tau (a Class I/II protostar). For S CrA, we could characterize the dynamics of the streamer well, which seems to be consistent with infalling motion. The negative total energy estimated for the observed streamer, along with the large size compared to the protoplanetary disks, suggests that the observed structure does not represent an ejection of unbound gas or spiral arms induced in the disks.

The streamer around HL Tau is also consistent with infalling motion, which is in agreement with the kinematical analysis by Yen et al. (2019) and the shocks observed by Garufi et al. (2022). However, the uncertainties estimated on the best-fit parameters are relatively large, indicating that the observations likely cover a too small spatial scale to provide stringent constraints on the overall trajectory. This result is very informative on the type of observations that are needed to study and characterize infalling streamers.

Moreover, S CrA and HL Tau appear to be accreting mass at a rate of $\gtrsim 27$ M$_{jupiter}$ Myr^{-1}

and $\gtrsim 5$ $M_{jupiter}$ Myr^{-1}, respectively. If sustained for long enough ($\gtrsim 0.1$ Myr), such mass infall rates can significantly increase the mass budget available to form planets in evolved sources.

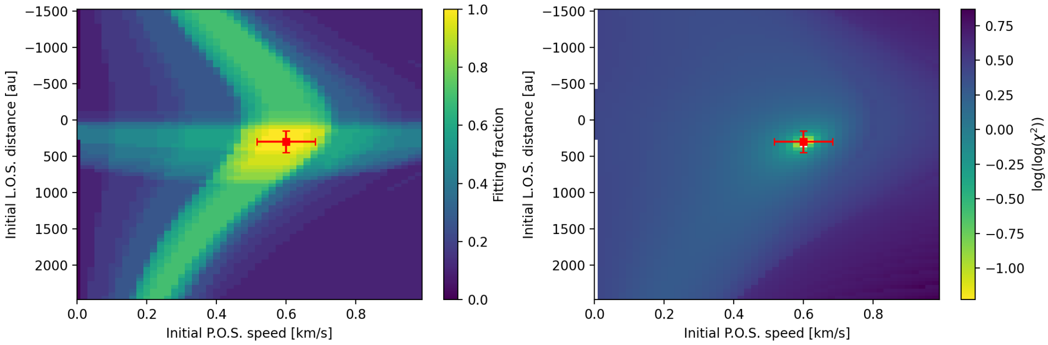

(a)

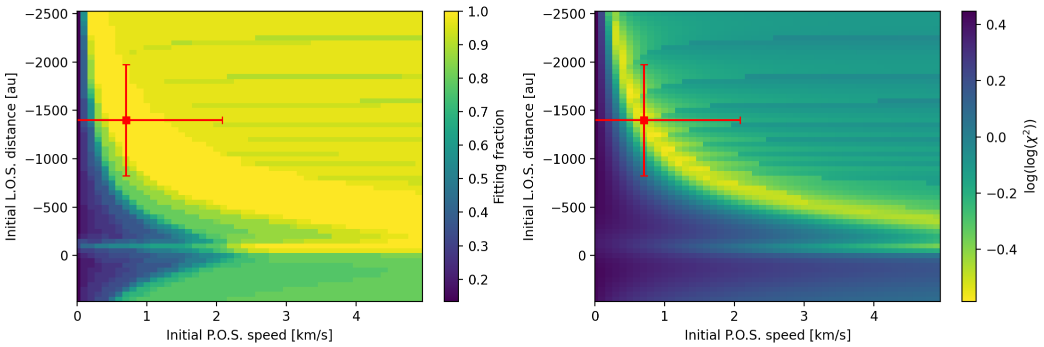

(b)

Figure 3.4: Distribution of goodness-of-fit estimates as functions of free parameters: initial speed on the POS (x-axis) and initial spatial offset in the LOS direction, for TIPSY fitting for S CrA (top panels) and HL Tau (bottom panels). Here, the initial direction of gas in the POS (third free parameter) is fixed to the value for the best fit. *Left panels*: Distribution of fractions of coordinate values of points in the observed streamer curve (intensity-weighted means and standard deviations), which is consistent with the theoretical trajectories. *Right panels*: Distribution of $\log(\log(\chi^2))$ deviations between the observed streamer curve and theoretical trajectories. In all the plots, yellow regions represent good fits. Red squares represent the best fit, as discussed in Sect. 3.2.2. The red lines passing through them represent errors, as discussed in Sect. 3.2.3.

Chapter 4

Large-scale structures around protoplanetary disks observed in DECO

4.1 Introduction

The classical model of star formation, developed more than 50 years ago, assumes that stars form out of gravitational collapse of isolated spherical prestellar cores (Larson, 1969; Shu, 1977). This picture further suggests that as star formation proceeds, due to the conservation of the angular momentum, the infalling material within these cores settles into disk-like structures around the protostars. As these Young Stellar Objects (YSOs) further evolve, they are expected to disperse most of the natal envelope, leaving behind an isolated protostar and disk system. These systems, commonly referred to as Class II sources (e.g., Dunham et al., 2014), are then assumed to evolve in isolation to form planetary systems (e.g., Morbidelli & Raymond, 2016).

Results from initial surveys of molecular-line emission from Class II disks, primarily done with Atacama Large Millimeter/submillimeter Array (ALMA), somewhat agreed with this assumption of isolated systems (e.g., Ansdell et al., 2016, 2017; Barenfeld et al., 2016). The primary goal of these surveys was to exploit ALMA's unprecedented sensitivity to homogeneously observe all known Class II objects in newrby SFRs both in continuum and CO (main isotopologues) emission(see Manara et al., 2023; Miotello et al., 2023, for a review). Such pioneering studies, also referred in the literature as "snapshot surveys", were characterised by a moderate sensitivity, that was not enough to reveal any fainter extended structures beyond the disks. Higher sensitivity ALMA observations of individual sources - generally designed to study disk chemistry and kinematics - had often also high angular resolution to resolve the disks (e.g., Öberg et al., 2021). This limited the largest recoverable scale of such observations, and much of the emission beyond disk scales was filtered out. Furthermore, as the targets of these studies were identified as Class II source through spectral energy distributions (SEDs) characterisation, such samples were inherently biased against Class II sources interacting with their environment (Kuffmeier et al., 2023).

However, despite the fact that most molecular-line observations were designed only to study disks, there have been several serendipitous detections of larger scale structures connected to them (e.g., Tang et al., 2012; Akiyama et al., 2019; Alves et al., 2020; Garufi et al., 2022; Huang et al., 2020, 2021, 2022, 2023; Gupta et al., 2023). In particular, filamentary structures connected to the disks, also referred to as streamers, and spirals have been observed. Numerical simulation suggest these structures to be a signpost of infalling material (e.g., Padoan et al., 2014; Hennebelle et al., 2017; Haugbølle et al., 2018; Bate, 2018; Kuznetsova et al., 2019; Lebreuilly et al., 2021; Pelkonen et al., 2021; Kuffmeier et al., 2017, 2023). Recent surveys of near-infrared polarimetric observations suggest that at least $\sim 15\%$ of Class II sources are likely interacting with their environment (e.g., Garufi et al., 2024). However, these observations do not provide information on gas kinematics, which makes it hard to ascertain their dynamical nature. Overall, we are increasingly identifying signs of interactions between Class II systems and their surrounding clouds, challenging the traditional view of these sources.

These interactions, resulting in late-stage infall of material onto Class II disks, can significantly impact the physical and chemical properties of protoplanetary disks, potentially solving several issues in star and planet formation. This process, modelled as Bondi-Hoyle accretion, can transfer mass to disks around solar-type stars at a rate of $\sim 10^{-8}\ M_\odot\ \mathrm{yr}^{-1}$(Padoan et al., 2005), in agreement with recent observational estimates (Gupta et al., 2024). If this is sustained for ~ 0.1 Myr, less than one-tenth of the typical disk lifetimes ($\gtrsim 1$ Myr), it can sufficiently increase the mass budget of Class II disks to form planets to resolve their 'mass-budget problem' (Manara et al., 2018; Murillo et al., 2022). As the angular momentum of infalling gas can be randomly oriented with respect to the disk, it can easily induce misalignments in disks (Thies et al., 2011; Kuffmeier et al., 2021) which can be inherited by planetary systems formed out of them (e.g., Albrecht et al., 2022). Additionally, it can explain some of the observed shocks in disks (e.g., Garufi et al., 2022), accretion outbursts (e.g., Jensen & Haugbølle, 2018), old disks (e.g., Scicluna et al., 2014) and disk substructures (e.g., Kuznetsova et al., 2022). Winter et al. (2024) even demonstrated that late-infall can be a primary driver of the overall disk evolution.

To better quantify the frequency of such interactions, we need a deep molecular-line survey of Class II disks with appreciable largest recoverable scale. DECO (Disk-Exoplanet C/Onnection, PI: L. Ilsedore Cleeves) is a novel ALMA Large Program designed to study the chemical composition of 80 Class II disks. As the observations were primarily designed to study the weak line emission emitted from disks, a relatively coarse resolution of a few tens of au was proposed. This corresponds to ALMA C-4 or C-5 configurations (~ 5" LAS in Band 6), which recovers scales of few hundred au at the typical source distances, which can reveal structures larger than the disks. Moreover, this program covers a well-sampled range of stellar masses (~ 0.2–$1.5\ M_\odot$) in four nearby (< 200 pc) star-forming regions (see Section 4.2.1 for more details), which can allow us to understand how frequency of large-scale structures vary with environmental and stellar properties.

Following a description of DECO sample in Section 4.2.1, we describe calibration and imaging procedures employed for the data presented in this paper in Section 4.2.2. Then in Section 4.3 we describe our analysis of large-scale structures observed in DECO data. We discuss our finding in Section 4.5. Finally, our key conclusions are stated in Section 4.6.

4.2 Observations

4.2.1 DECO sample

The primary science goal of DECO is to study the chemical composition of 80 Class II disks - specifically their C/O and C/H ratios - which is expected to be inherited by the planets forming in them. In order to isolate the influence of disk properties with their environments, targeted sources are evenly divided into four nearby (< 200 pc) star-forming regions, with existing disk surveys: Lupus (Ansdell et al., 2016), Taurus (Akeson et al., 2019), Chameleon I (hereafter ChaI) (Pascucci et al., 2016), and Rho Ophiuchus (hereafter ROph) Williams et al. (2019). Although all these regions are relatively young, Ophiuchus is thought to be especially younger with the YSOs typical age ranging from $\sim$ 0.3 Myr in the dense cores (Wilking et al., 2008) to $\sim$ 1 Myr in the rest of L1688 (most active sub-region) (Testi et al., 2022). In comparison, the other three regions are expected to be $\sim$ 1–3 Myr old (Testi et al., 2022; Ribas et al., 2015; Pfalzner & Dincer, 2024). We note that the exact ages of individual regions are quite uncertain and vary within a factor of two among different studies.

To investigate the dependence of disk chemistry on stellar properties, every sample within each star forming region is further evenly divided between M-dwarfs ($T_{\rm eff}$ < 3900 K) and GK-dwarfs. Moreover, within each of these sub-classes the sample is further equally divided between small and large disks, with a dust radius of 40 au as a threshold between the two populations. It is particularly important for this study that the sample selection is optimised to target clean isolated disks by minimising inclusion of binaries and sources with large ($\gtrsim$5 mag) extinction. Based on the stellar parameters provided in Manara et al. (2023) and tabulated in Table 4.2, our final sample encompasses stellar masses ranging from $\sim$ 0.2 to 1.4 $M_\odot$, with mass accretion rates around $\sim 10^{-10}$–10^{-6} $M_\odot$ yr^{-1}. This broad range allows us to explore potential correlations between the properties of large-scale structures and stellar characteristics across a significant number of sources, as discussed in Section 4.4.

However, some DECO observations are still missing in this chapter, as they are either yet to be delivered or imaged. The results presented in this chapter are based on CO (2–1), ^{13}CO (2–1), and C^{18}O (2–1) observations of 62 targets in total, specifically 18 sources in ChaI, 20 sources in Lupus, 20 sources in ROph and 4 sources in Taurus.

4.2.2 Calibration and imaging

The data for DECO was reduced using the respective pipeline for each dataset, included in each version of the CASA software (McMullin et al., 2007; CASA Team et al., 2022).

For the complementary archival observations, making up part of the DECO sample, the data reduction processing was run with the corresponding CASA version, depending on the observational cycle of each dataset. Once the calibrated visibilities were obtained, then a standalone automated self-calibration routine[1] was applied for all DECO and archival datasets, using the CASA 6.6.4.34 version. Default parameter values, as set in the routine, were used for self-calibration.

All lines were imaged using the `tclean` task with Briggs weighting of `robust`=0.5 and used automasking with the following parameters: sidelobethreshold = 2.0, noisethreshold = 3.25, minbeamfrac = 0.3, lownoisethreshold = 1.5, and negativethreshold = 7.0. All images were made using the 'multi-scale' deconvolver with pixel scales of [0,5,15,25,50,100] and were CLEANed down to a 4σ level, where σ was the RMS noise measured across five line-free channels of the dirty image.

4.3 Analysis

As discussed in Section 4.2.1, we use available DECO observations of a subset of 62 sources in this study. Figure 4.1 presents the CO (2–1) maximum intensity (moment 8) maps of these sources. These maps reveal a wide variety of large-scale ($\gtrsim$ 500 au) structures beyond the traditionally assumed isolated, central, often unresolved or marginally resolved disks. Even just from a visual inspection, these structures seem more common around sources in ROph, which is thought to be the youngest region observed by DECO, as discussed in Section 4.2.1. This observation may suggest that Class II sources in younger regions are more likely to interact with their environment, due to less dispersed clouds. Furthermore, the intensity-weighted velocity (moment 1) maps shown in Figure 4.2 display a range of complex and diverse velocity patterns in these large-scale structures. This complexity indicates that more dynamic processes may be occurring, rather than just a simple streamer-like infall of material.

For more details on gas structures around individual sources, we refer to the channel maps and integrated spectra presented in Appendix C.1. In addition, to further showing that large-scale structures are both common and diverse, these maps also reveal the relative complex morphologies of the three main CO isotopologue lines: CO (2–1), ^{13}CO (2–1), and C^{18}O (2–1). CO, being the most abundant isotopologue, is generally the brightest. However, it is also the most affected by foreground cloud absorption and contamination. In contrast, C^{18}O, the rarest isotopologue, is the least affected by these issues, but it is also much fainter. Together these three complementary isotopologues allow us to build a more comprehensive picture of gas structures. For example, in Figure C.58 we can see that CO is the brightest in most of the channels. However, in the gas line-of-sight (LOS) velocities ranging from $\sim$ 2 km s^{-1} to $\sim$ 5 km s^{-1}, the emission is dominated by ^{13}CO and not by ^{12}CO. This is likely due to ^{12}CO being absorbed by the foreground cloud or contaminated by diffuse clouds, which are filtered out in these interferometric observations. Furthermore,

[1]https://github.com/jjtobin/auto_selfcal/

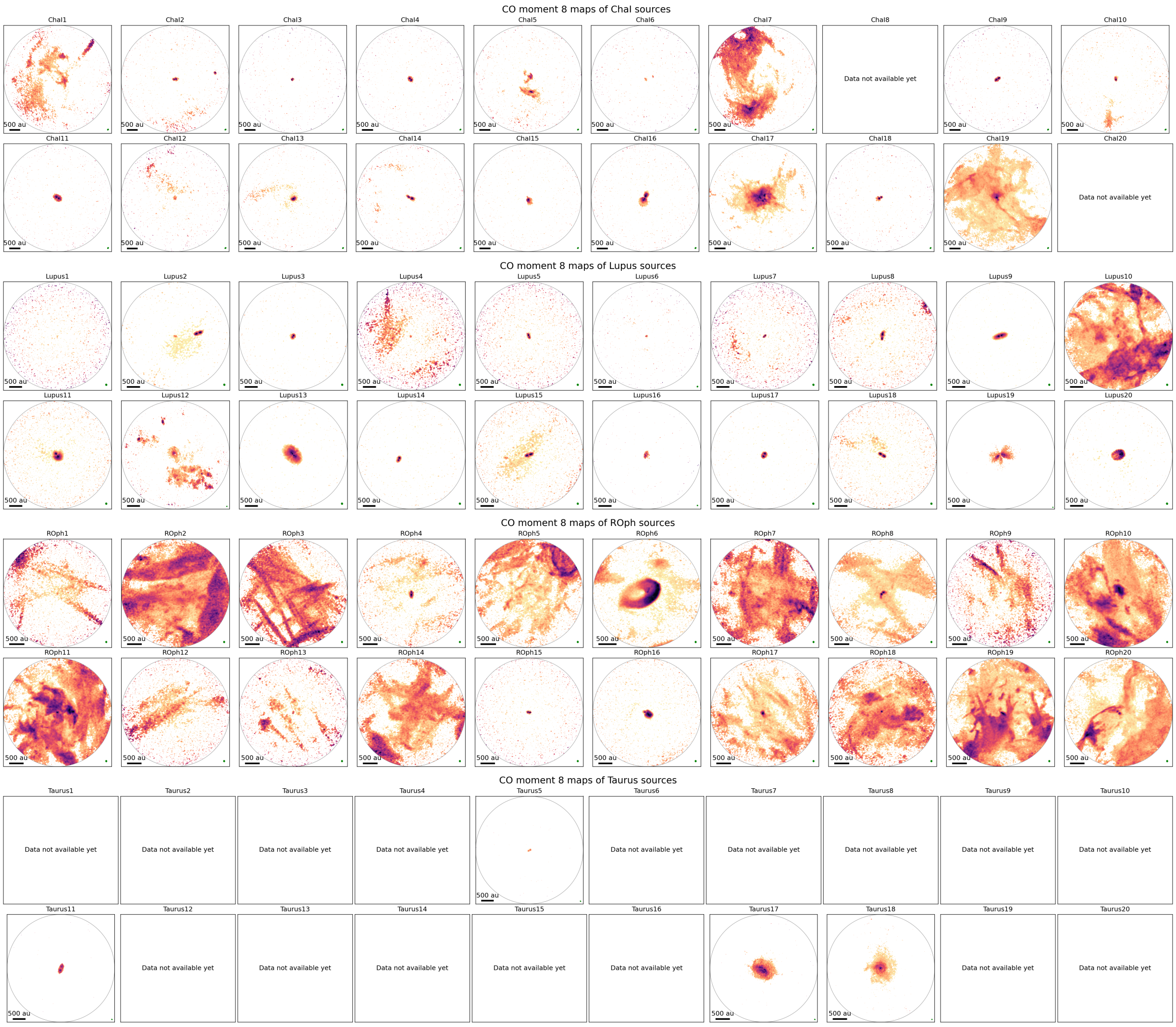

Figure 4.1: CO (2–1) maximum intensity (moment 8) maps for DECO sources. All 80 panels represent the 80 sources in DECO sample, as described in Section 4.2.1. These sources are divided into four blocks representing, from top to bottom, sources in ChaI, Lupus, ROph, and Taurus. Panels with "Data is not available yet" denote sources for which DECO observations are not yet taken or delivered. Horizontal lines in the bottom-left and ellipses in the bottom-right of each panel represent length scales of 500 au and beam sizes, respectively.

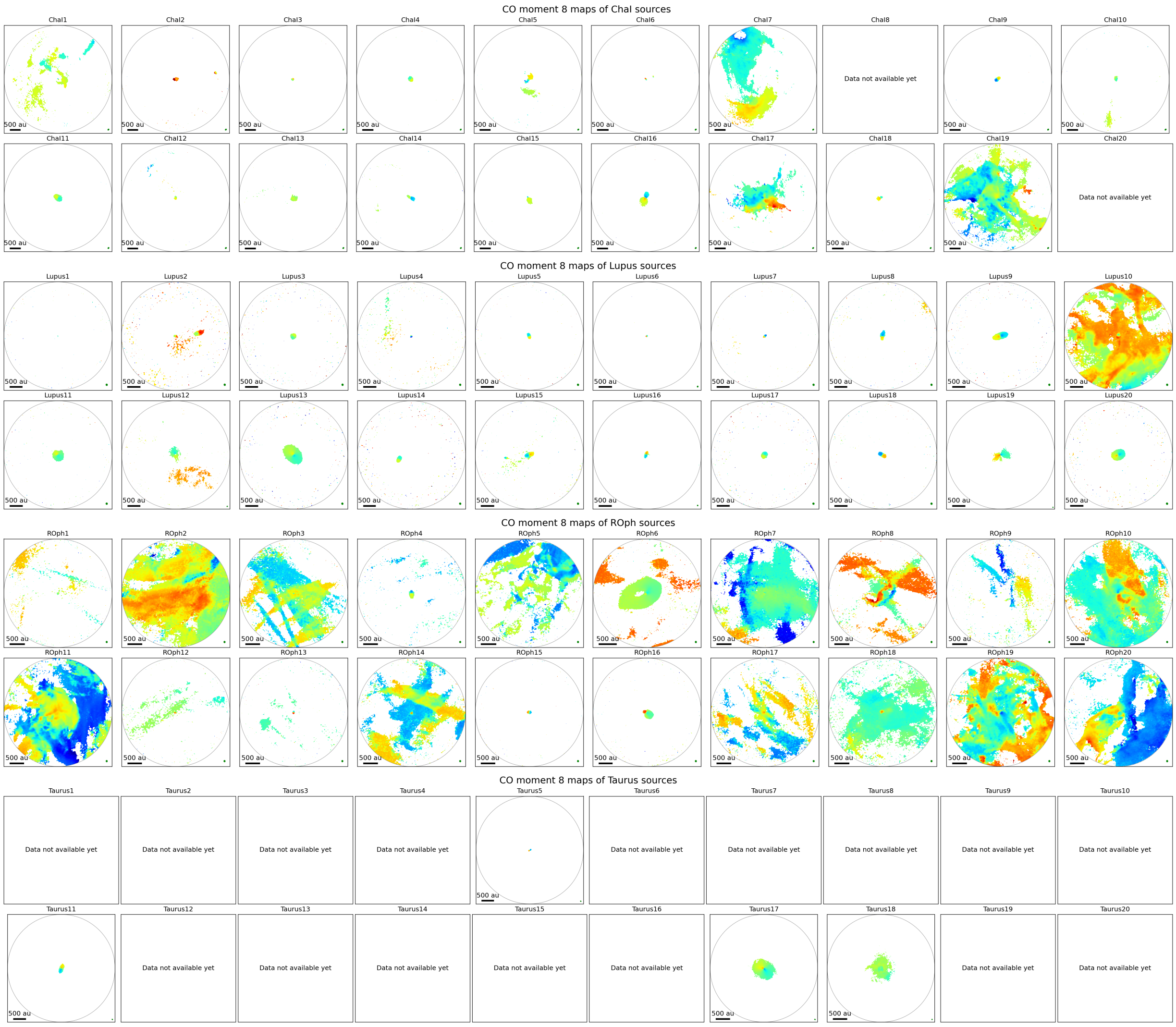

Figure 4.2: CO (2–1) intensity-weighted velocity (moment 1) maps for DECO sources. All 80 panels represent the 80 sources in DECO sample, as described in Section 4.2.1. These sources are divided into four blocks representing, from top to bottom, sources in ChaI, Lupus, ROph, and Taurus. Panels with "Data is not available yet" denote sources for which DECO observations are not yet taken or delivered. Horizontal lines in the bottom-left and ellipses in the bottom-right of each panel represent length scales of 500 au and beam sizes, respectively.

in velocities between 3 km s^{-1} and 3.4 km s^{-1}, even ^{13}CO is mostly absorbed and C^{18}O is relatively bright.

One way to do a consistent analysis of these diverse structures, particularly in the context of studying infall of material, is to characterise the amount of potentially bound material. With the current observations, we have the information of relative LOS velocities ($v_{\rm LOS}$), which can be treated as a lower limit on overall relative velocity between protostellar source and surrounding gas. Similarly, we can infer the plane-of-sky (POS) distances ($r_{\rm POS}$) between the source and the gas, providing a lower limit on the overall 3D distance. Using these we can constrain specific (per unit mass) kinetic (KE) and gravitational potential (PE) energy of the gas, relative to the protostar, as:

$$KE_{\rm min} = 0.5 v_{\rm LOS}^2 \tag{4.1}$$

$$PE_{\rm max} = GM_*/r_{\rm POS} \tag{4.2}$$

where, G is the gravitational constant and M_* is the stellar mass. Equating Equations 4.1 and 4.2, we get

$$r_{\rm POS,\ max.\ bound} = 2GM_*/v_{\rm LOS}^2 \tag{4.3}$$

where $r_{\rm POS,\ max.\ bound}$ represents the distance beyond which $KE_{\rm min} > PE_{\rm max}$. In other words, material beyond $r_{\rm POS,\ max.\ bound}$ should definitely be unbound. However, material within it may or may not be bound and thus, represents the maximum possible bound material. These circles are shown as dashed circles in the figures in Appendix C.1.

Since the available observations do not directly provide information on velocities along R.A. ($v_{\rm RA}$) and Dec. ($v_{\rm Dec}$), nor on distances along LOS ($r_{\rm LOS}$), we need to make assumptions about the 3D orientation of these structures to define a more realistic boundary between bound and unbound material. Assuming that we are looking at these systems from a fairly representative perspective, we should have $v_{\rm LOS} \sim v_{\rm RA} \sim v_{\rm Dec}$ and $r_{\rm RA} \sim r_{\rm Dec} \sim r_{\rm LOS}$. Then the 3D relative velocity and distance can be estimated as:

$$v_{\rm est} = 3^{0.5} v_{\rm LOS} \tag{4.4}$$

$$r_{\rm est} = 1.5^{0.5} r_{\rm POS} \tag{4.5}$$

Estimating kinetic and potential energy from equations 4.4 and 4.5 and equating them, we get

$$r_{\rm POS,\ est.\ bound} = (2/3)^{1.5} GM_*/v_{\rm LOS}^2 \tag{4.6}$$

where $r_{\rm POS,\ est.\ bound}$ represents a more realistic boundary between bound and unbound material and is denoted as dotted circles in the figures in Appendix C.1.

We use the flux of molecular-line emission within these boundaries to estimate both the maximum mass ($M_{\rm max.}$) and the projection-corrected mass ($M_{\rm proj.\ corr.}$) of material bound to protostellar systems. As previously noted, different CO isotopologues dominate emission in different channels. Thus, we estimate the mass of each CO isotopologue corresponding to their emission in each channel. For determining the actual mass in each channel, we select the mass estimate from the most dominant CO isotopologue emission. This approach minimizes the effects of optical depth and cloud absorption, particularly in channels where the mass estimate from more abundant isotopologues might be lower than that from less abundant isotopologues. It also ensures that we can use the mass estimate from the more abundant isotopologue emissions in cases where the less abundant isotopologues are too faint.

For the actual mass estimation, we only consider pixels with emission greater than 3σ. We also mask out the circumstellar disks using their expected Keplerian rotational profiles, so that we only consider the mass of the large-scale structures beyond the disks. The mass of molecular gas can be estimated from the integrated flux ($F_{\rm gas}$), assuming optically thin emission, as:

$$M_{\rm gas} \approx \frac{2.37 m_H 4\pi D^2 F_{\rm gas}}{A_{\rm trans.} h\nu x_{\rm mol.} f_u}, \tag{4.7}$$

where m_H is the mass of a hydrogen atom, D is the distance to the source, $A_{\rm trans.}$ is the Einstein A coefficient of observed line transition, ν is the line frequency, $x_{\rm mol.}$ is the abundance of the molecule relative to H_2, and f_u is the fraction of molecules in the upper energy state of the transition (e.g., Bergin et al., 2013). Here, f_u can be further computed as $f_u = 3e^{E_u/T}/Q_{\rm mol.}(T)$, where E_u is the upper state energy for the transition, T is the gas temperature, and $Q_{\rm mol.}(T)$ is the partition function for the molecule. For both sources, we assumed a representative temperature of 25 K, which is typical for gas at these ∼100-1000 au scales (e.g., Jørgensen et al., 2005). All the values used for each molecular line are tabulated in Table 4.1.

Molecular Line	ν [GHz]	$A_{\rm trans}$ [s^{-1}]	E_u [K]	$Q_{\rm mol.}$(25 K)	$x_{\rm mol.}$
CO (2–1)	230.54	6.910×10^{-7}	16.60	8.8995	1×10^{-4}
^{13}CO (2–1)	220.40	6.038×10^{-7}	15.87	18.5837	1.30×10^{-6}
C^{18}O (2–1)	219.56	6.011×10^{-7}	15.81	9.3268	1.79×10^{-7}

Table 4.1: Frequencies (ν), Einstein coefficients ($A_{\rm trans}$), upper state energies (E_u), partition functions ($Q_{\rm mol.}$), and abundances ($x_{\rm mol.}$) for estimating the mass of the three molecular lines. $A_{\rm trans}$ and E_u values were taken from the Leiden Atomic and Molecular Database (Schöier et al., 2005). $Q_{\rm mol.}$ values were interpolated from the values provided in Cologne Database for Molecular Spectroscopy (Endres et al., 2016). $x_{\rm mol.}$ values are from Wilson & Rood (1994).

However, there are inherent uncertainties on stellar masses and systemic velocities used for defining boundary of bound material and thus, estimating the mass of bound gas. To account for these uncertainties, we assume a typical uncertainty on stellar mass of $\sim 10\%$ and a typical uncertainty on systemic velocity of ~ 0.5 km s^{-1}. These uncertainties are then propagated to determine the uncertainties in $r_{\rm POS,\, max.\, bound}$ and $r_{\rm POS,\, est.\, bound}$. We compute the flux using slightly larger and smaller radii ($r_{\rm POS} \pm \Delta r_{\rm POS}$) to estimate the uncertainty in the flux of bound gas, which is subsequently propagated to calculate the errors in the bound mass.

Besides propagating the uncertainties from stellar properties, we also need to account for the noise of the flux observations. Even though we only consider pixels with flux greater than 3σ, there will still be a few pixels ($\sim 0.5\%$) with some relic noisy emission. In general, the number of such pixels should be very small and therefore should not significantly affect bright structures. However, the emission from many structures is faint enough that we need to account for this observational noise to only pick structures with significant emission. We do this in two steps. First, for each channel and CO isotopologue we check if the total bound emission is significantly larger than that expected from the few noisy pixels with flux $> 3\sigma$, assuming Gaussian noise. This is important to do for different isotopologues, because mass estimations from noisy $C^{18}O$ data can dominate over the mass estimated from CO, as $C^{18}O$ is roughly two orders of magnitude less abundant. Second, and more important, we also check the noisy emission expected from all the bound pixels for the CO isotopologue that dominates the overall mass estimation. This overall noisy emission determines the observational lower limit on observable mass.

4.3.1 Caveats

A major caveat in such an analysis is that we do not confirm the infalling nature of these structures individually, for example by fitting their morphology and velocity gradients as done in Gupta et al. (2024). This is because our structures exhibit complicated spatial and kinematic patterns, which cannot be easily represented as a simple infalling trajectory. Furthermore, these patterns are visible in different isotopologue emission at different velocity ranges. Therefore, here we present a relatively simpler approach to consistently quantify the presence of large-scale structures across these diverse sources.

We would like to stress that our effort is in determining the reservoir of gas that can potentially fall onto the protostellar systems we study. It is possible that other environmental parameters such as turbulence, magnetic fields, gas pressure gradients and even stellar feedback may significantly alter gas dynamics. However, in these low-mass star-forming environments and scales of $\lesssim 1000$ au, we expect the dynamics to be dominated by the gravity from protostellar system, in most cases.

Furthermore, we had to make a few assumption on the physical properties of the surrounding gas to derive its mass. To begin with, we assumed a constant temperature of 25 K across all gas structures. In reality, the temperature can not only vary for material around different sources but also spatially around each source. To characterise these temperature profiles, we will need to model multiple transitions of the same molecule which is beyond the scope of this study. Such an analysis can also allow us to have a more realistic prescription for the optical depth of our tracers.

Quite certainly, we miss flux due to filtering out of large-scale structures by interferometric observations. To recover this flux, we will need additional data with shorter baselines and single-dish observations. However, our next step is to experiment with imaging procedures. The parameters used for the imaging presented in this chapter is currently optimised to study disks, to assess how much flux we miss due to filtering out. We also miss some flux due to absorption by foreground cloud but we minimise this effect by also using emission from rarer CO isotopologues for mass estimation.

Overall, our mass estimates should be considered as order-of-magnitude estimates rather than precise measurements of the gas that will fall onto these systems. Despite this, they provide valuable insights into global trends between properties of protostellar sources and their environments, as discussed in Section 4.4. Complementary observations (multiple transitions, shorter baselines, etc.) and more detailed analysis of individual sources will follow and will allow us to further refine these results.

Source	$M_{\text{disk, dust}}$ $M_\oplus$	M_* $M_\odot$	$\log(\dot{M}_{\text{acc}})$ $M_\odot\,\text{yr}^{-1}$	$M_{\text{max.}}$ $M_\odot$	$\Delta M_{\text{max.}}$ $M_\odot$	$M_{\text{proj. corr.}}$ $M_\odot$	$\Delta M_{\text{proj. corr.}}$ $M_\odot$
ROph1	1.79	0.37	-8.17	3.62×10^{-5}	1.85×10^{-5}	1.05×10^{-5}	9.93×10^{-6}
ROph2	1.95	0.54	-8.08	5.73×10^{-4}	1.09×10^{-4}	2.06×10^{-4}	9.77×10^{-5}
ROph3	3.50	0.57	-8.70	5.58×10^{-5}	1.33×10^{-5}	2.50×10^{-5}	1.21×10^{-5}
ROph4	7.58	0.40	-	2.82×10^{-6}	3.17×10^{-6}	5.07×10^{-8}	3.67×10^{-7}
ROph5	11.48	0.29	-7.22	3.47×10^{-4}	1.18×10^{-4}	4.77×10^{-5}	5.21×10^{-5}
ROph6	113.81	0.56	-7.38	1.14×10^{-4}	2.92×10^{-5}	5.72×10^{-5}	3.01×10^{-5}
ROph7	8.55	0.63	-9.57	2.01×10^{-5}	2.53×10^{-6}	1.25×10^{-5}	1.69×10^{-6}
ROph8	36.61	0.55	-7.89	2.45×10^{-5}	3.95×10^{-6}	1.24×10^{-5}	4.83×10^{-6}
ROph9	53.83	0.21	-7.93	4.79×10^{-5}	1.34×10^{-5}	1.68×10^{-5}	1.04×10^{-5}
ROph10	54.86	0.59	-6.71	5.35×10^{-4}	1.05×10^{-4}	2.35×10^{-4}	1.05×10^{-4}
ROph11	3.48	0.60	-7.89	9.75×10^{-3}	9.37×10^{-4}	6.66×10^{-3}	1.72×10^{-3}
ROph12	4.62	0.84	-8.64	7.60×10^{-6}	3.14×10^{-6}	5.88×10^{-6}	5.41×10^{-6}
ROph13	8.63	0.62	-	2.74×10^{-4}	5.80×10^{-5}	1.41×10^{-4}	6.58×10^{-5}
ROph14	15.30	0.88	-7.17	6.54×10^{-5}	1.44×10^{-5}	8.88×10^{-6}	3.34×10^{-6}
ROph15	20.26	0.69	-	3.50×10^{-6}	6.89×10^{-7}	3.22×10^{-6}	5.50×10^{-6}
ROph16	10.99	0.69	-	3.77×10^{-6}	1.74×10^{-6}	1.24×10^{-6}	6.43×10^{-7}
ROph17	14.83	0.65	-7.96	4.21×10^{-5}	8.37×10^{-6}	1.60×10^{-5}	8.78×10^{-6}
ROph18	38.45	0.61	-6.88	7.08×10^{-4}	7.49×10^{-5}	4.08×10^{-4}	1.06×10^{-4}
ROph19	80.97	0.69	-8.50	7.77×10^{-3}	1.18×10^{-3}	3.30×10^{-3}	1.22×10^{-3}
ROph20	210.52	0.94	-6.22	1.47×10^{-3}	2.25×10^{-4}	7.69×10^{-4}	1.23×10^{-4}
Lupus1	1.10	0.29	-9.38	5.86×10^{-7}	2.00×10^{-6}	4.22×10^{-7}	4.00×10^{-6}
Lupus2	3.75	0.29	-8.51	1.81×10^{-6}	2.29×10^{-6}	1.41×10^{-6}	2.12×10^{-6}
Lupus3	1.64	0.39	-9.10	1.37×10^{-5}	7.72×10^{-6}	1.33×10^{-6}	9.12×10^{-6}
Lupus4	1.04	0.46	-9.39	5.96×10^{-6}	3.62×10^{-6}	4.78×10^{-7}	5.52×10^{-6}
Lupus5	7.98	0.47	-9.08	1.64×10^{-7}	1.71×10^{-7}	2.65×10^{-7}	2.12×10^{-6}
Lupus6	1.23	0.67	-8.69	4.24×10^{-7}	1.67×10^{-7}	8.79×10^{-8}	2.76×10^{-7}
Lupus7	5.87	0.73	-8.93	5.58×10^{-7}	3.38×10^{-7}	2.15×10^{-7}	2.74×10^{-7}
Lupus8	17.25	0.83	-9.11	6.05×10^{-6}	6.52×10^{-7}	4.53×10^{-6}	1.90×10^{-6}
Lupus9	35.29	1.27	-9.20	2.71×10^{-6}	1.33×10^{-6}	1.38×10^{-6}	1.19×10^{-6}
Lupus10	39.22	1.32	-8.12	3.29×10^{-4}	2.36×10^{-4}	3.79×10^{-5}	1.54×10^{-5}
Lupus11	41.79	0.41	-9.03	2.09×10^{-6}	2.15×10^{-6}	1.54×10^{-6}	4.86×10^{-6}
Lupus12	10.89	0.52	-9.08	3.52×10^{-5}	5.82×10^{-6}	1.86×10^{-5}	3.27×10^{-6}
Lupus13	47.01	0.52	-9.47	1.07×10^{-5}	8.09×10^{-6}	3.22×10^{-7}	1.95×10^{-7}
Lupus14	11.17	0.56	-9.18	6.30×10^{-6}	4.24×10^{-6}	1.98×10^{-6}	5.76×10^{-6}

Lupus15	15.87	0.61	-9.48	6.93×10^{-6}	3.09×10^{-6}	5.94×10^{-7}	1.60×10^{-6}
Lupus16	20.35	0.61	-7.44	1.86×10^{-6}	6.15×10^{-7}	3.63×10^{-7}	5.17×10^{-7}
Lupus17	48.53	0.73	-8.27	1.46×10^{-6}	3.56×10^{-7}	3.04×10^{-7}	3.51×10^{-7}
Lupus18	46.12	1.19	-8.00	1.39×10^{-5}	6.14×10^{-6}	7.99×10^{-6}	2.82×10^{-6}
Lupus19	144.29	0.92	-	4.45×10^{-5}	8.74×10^{-6}	3.22×10^{-5}	1.54×10^{-5}
Lupus20	60.55	0.55	-7.44	6.41×10^{-7}	2.74×10^{-7}	1.27×10^{-8}	3.44×10^{-8}
Taurus5	19.61	0.47	-9.14	1.27×10^{-6}	6.57×10^{-7}	1.27×10^{-10}	9.88×10^{-8}
Taurus11	10.61	0.50	-7.30	2.22×10^{-6}	3.38×10^{-7}	2.07×10^{-7}	9.29×10^{-8}
Taurus17	113.54	0.69	-7.97	4.86×10^{-6}	2.17×10^{-6}	2.83×10^{-6}	6.60×10^{-7}
Taurus18	65.41	0.60	-6.71	1.55×10^{-4}	1.13×10^{-5}	1.12×10^{-4}	1.92×10^{-5}
ChaI1	3.90	0.65	-9.37	1.74×10^{-4}	2.61×10^{-5}	1.23×10^{-4}	4.30×10^{-5}
ChaI2	4.76	0.58	-7.77	1.67×10^{-6}	8.02×10^{-7}	8.52×10^{-7}	3.19×10^{-6}
ChaI3	8.12	0.25	-7.17	1.59×10^{-7}	9.84×10^{-8}	1.37×10^{-7}	1.11×10^{-6}
ChaI4	10.44	0.52	-7.89	7.39×10^{-7}	4.06×10^{-7}	1.09×10^{-6}	8.22×10^{-6}
ChaI5	11.52	0.54	-9.12	6.94×10^{-5}	1.69×10^{-5}	2.35×10^{-5}	1.91×10^{-5}
ChaI6	11.89	0.79	-8.42	3.95×10^{-6}	1.59×10^{-6}	3.83×10^{-7}	2.85×10^{-6}
ChaI7	2.71	0.63	-8.39	8.73×10^{-5}	2.36×10^{-5}	1.89×10^{-5}	1.98×10^{-5}
ChaI9	13.39	1.27	-7.83	2.65×10^{-6}	1.57×10^{-6}	4.55×10^{-7}	6.63×10^{-7}
ChaI10	16.77	0.70	-7.38	2.12×10^{-6}	5.28×10^{-7}	2.44×10^{-6}	1.45×10^{-5}
ChaI11	9.25	0.50	-7.91	2.97×10^{-6}	1.18×10^{-6}	1.53×10^{-7}	3.29×10^{-6}
ChaI12	12.00	0.29	-7.70	1.16×10^{-5}	4.50×10^{-6}	1.24×10^{-5}	7.16×10^{-6}
ChaI13	46.58	0.50	-7.11	1.57×10^{-6}	3.50×10^{-7}	1.34×10^{-6}	3.81×10^{-6}
ChaI14	21.07	0.38	-7.58	8.67×10^{-7}	1.19×10^{-6}	0.00×10^{0}	9.64×10^{-8}
ChaI15	56.12	0.56	-8.96	3.51×10^{-6}	4.48×10^{-6}	1.03×10^{-6}	3.95×10^{-6}
ChaI16	117.22	1.27	-7.55	1.13×10^{-6}	4.45×10^{-7}	8.48×10^{-7}	7.16×10^{-7}
ChaI17	7.50	0.82	-7.99	2.03×10^{-3}	2.79×10^{-5}	1.77×10^{-3}	2.84×10^{-4}
ChaI18	22.70	0.70	-8.62	2.38×10^{-6}	5.20×10^{-6}	6.64×10^{-7}	5.24×10^{-6}
ChaI19	28.76	0.65	-6.77	1.74×10^{-3}	2.82×10^{-4}	9.72×10^{-4}	3.66×10^{-4}

Table 4.2: Disk dust masses ($M_{\text{disk, dust}}$), stellar mass (M_*), and mass accretion rates ($\dot{M}_{\text{acc}}$) from Manara et al. (2023) along with maximum bound mass ($M_{\text{max.}}$) and projection corrected bound mass ($M_{\text{proj. corr.}}$) estimated in this study, for the current sample of DECO sources.

4.4 Results

Table 4.2 presents the masses of material bound to the observed sample of DECO sources. If we only identify sources with significant bound mass, i.e., mass greater than the corresponding lower limit due to noise in observed flux as defined in Section 4.3, $39 \pm 6\%$ of sources in our sample are associated with large-scale gaseous structures. Furthermore, the fraction of sources with bound structures vary greatly among the four regions, as show in Table 4.3. We note that currently results for Taurus are quite uncertain as the observations of only four sources have been delivered so far.

For DECO sources, we also have information on the disk dust masses ($M_{\text{disk, dust}}$), the

Region	% with bound material	$\mu(M_{\rm max.})$ $M_\odot$	$\sigma(M_{\rm max.})$ $M_\odot$	$\mu(M_{\rm proj.\ corr.})$ $M_\odot$	$\sigma(M_{\rm proj.\ corr.})$ $M_\odot$
ROph	75 ± 10	1.09×10^{-3}	2.67×10^{-3}	5.97×10^{-4}	1.61×10^{-3}
Lupus	5 ± 5	2.42×10^{-5}	7.28×10^{-5}	5.60×10^{-6}	1.10×10^{-5}
Taurus	50 ± 25	4.09×10^{-5}	7.62×10^{-5}	2.88×10^{-5}	5.56×10^{-5}
ChaI	33 ± 11	2.30×10^{-4}	6.07×10^{-4}	1.63×10^{-4}	4.62×10^{-4}

Table 4.3: Percentage of source with significant bound structures (% with bound material) for all the targeted DECO region. $\mu(M_{\rm max.})$ and $\mu(M_{\rm proj.\ corr.})$ represent mean masses corresponding to bound emission around all sources, including those with non-significant structures. $\sigma(M_{\rm max.})$ and $\sigma(M_{\rm proj.\ corr.})$ represent corresponding standard deviations. We note that the percentages are calculated using $M_{\rm max.}$ and percentages computed using $M_{\rm proj.\ corr.}$ agree within the uncertainties.

stellar masses (M_*), and the mass accretion rates ($\dot{M}_{\rm acc}$), from Manara et al. (2023). This allows us to investigate trends between these properties of protostellar systems with the mass of large-scale bound material around them, as shown in Figure 4.3, 4.4, and 4.5. We do not see any strong correlation between large-scale bound material with disk masses, stellar mass, or mass accretion rates. This is also in agreement with the Spearman correlation coefficients and corresponding p-values computed using `scipy` package (Virtanen et al., 2020) in Python, where all the p-values are greater than 0.1.

We know that mass accretion rates are strongly correlated to stellar masses, in particular $\dot{M}_{\rm acc} \propto M_*^2$ (Manara et al., 2023). In order to minimise the effect of stellar mass on mass accretion, we define the normalised mass accretion rate as $\dot{M}_{\rm acc}/M_*^2$, similar to the analysis by Winter et al. (submitted), and study its variation with bound mass. Interestingly, we see a tentative correlation among these quantities, as shown in Figure 4.6. This correlation is particularly prominent with projection corrected bound mass, when we consider all the data points in Figure 4.5, including smaller markers with relatively low masses. For this, the correlation coefficient is 0.3 with the corresponding p-value of 0.09. A least squares power-law fit, represented by the dashed line in Figure 4.5, suggests a tentative relation of $M_{\rm proj.\ corr.} \propto (\dot{M}_{\rm acc}/M_*^2)^{0.3\pm0.2}$.

4.5 Discussion

As mentioned in Section 4.4, significant large-scale bound material has been observed around $\sim 40\%$ of sources in the DECO sample. This is contradiction to the traditionally assumed picture of isolate Class II disks, as discussed in Section 4.1. Moreover, this fraction is for sources which are currently surrounded with large-scale structures. As these sources tend to have substantial spatial motions, with relative velocities around ~ 1 km s^{-1} or ~ 1 pc Myr^{-1} (e.g., Gupta & Chen, 2022), the fraction of Class II systems that interact with such gas structures at some point of their lifetime will be even greater. This suggests that the interaction between these sources and their surroundings must be better characterised

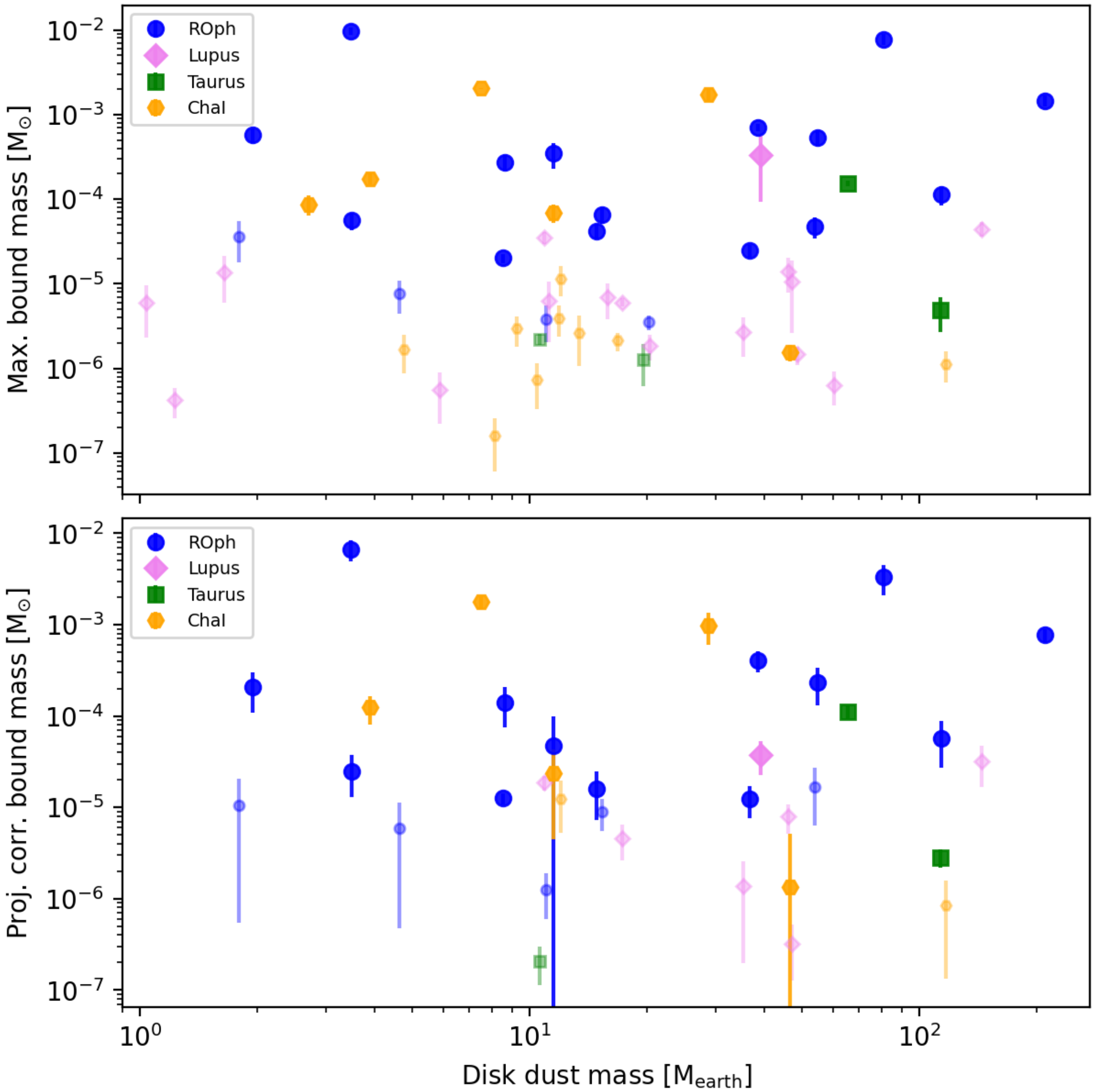

Figure 4.3: Dust mass of disks ($M_{\mathrm{disk,\,dust}}$) vs. max. bound mass ($M_{\mathrm{max.}}$, top panel) and projection corrected bound mass ($M_{\mathrm{proj.\,corr.}}$, bottom panel). Blue circles, pink diamonds, green squares, and orange hexagons represent sources from ROph, Lupus, Taurus, and ChaI, respectively. Smaller and fainter markers represent sources for which the estimated mass of bound gas is smaller than their estimated observational lower limit but still greater than their uncertainty due to stellar parameters.

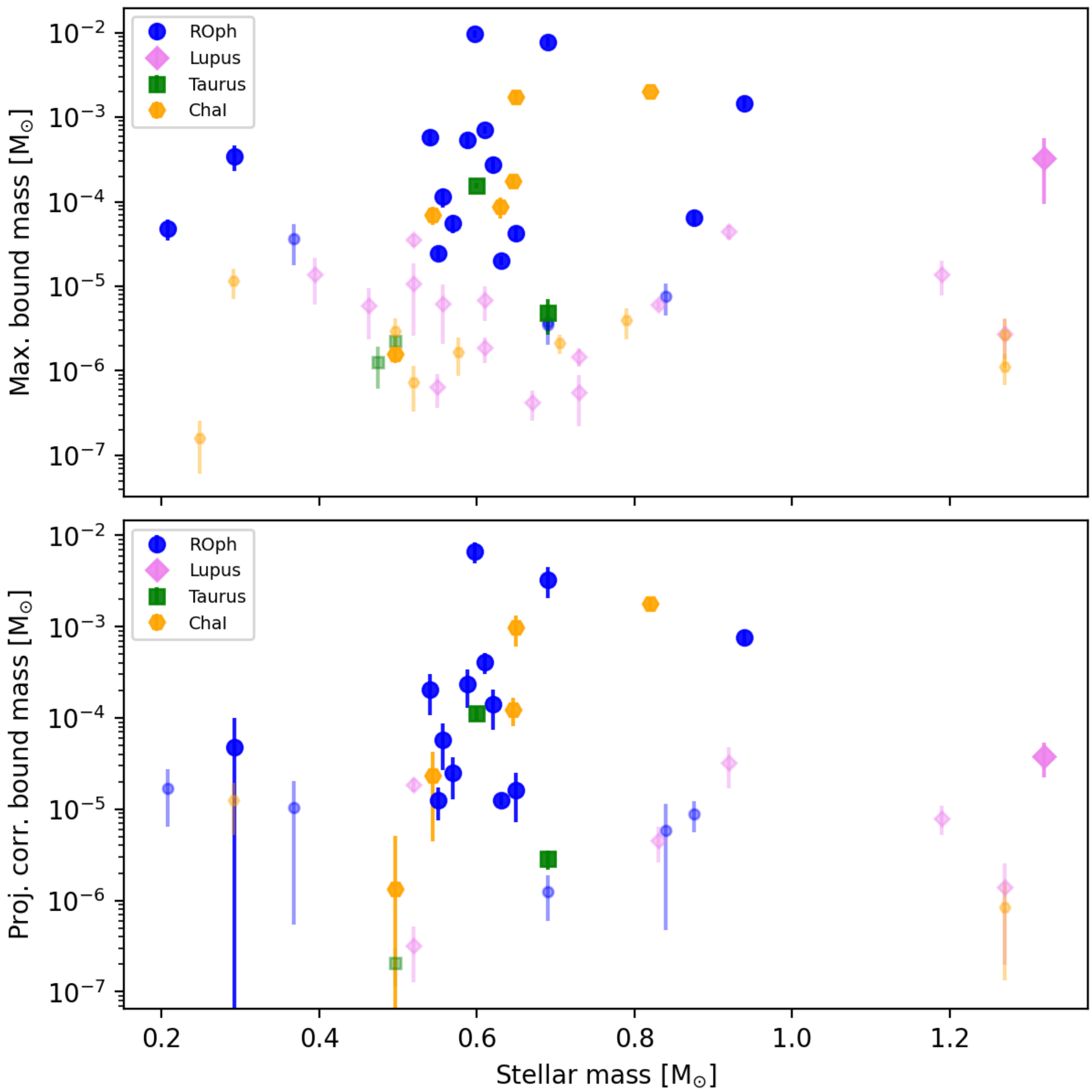

Figure 4.4: Stellar mass (M_*) vs. max. bound mass ($M_{\mathrm{max.}}$, top panel) and projection corrected bound mass ($M_{\mathrm{proj.\ corr.}}$, bottom panel). Markers are as described in Figure 4.3.

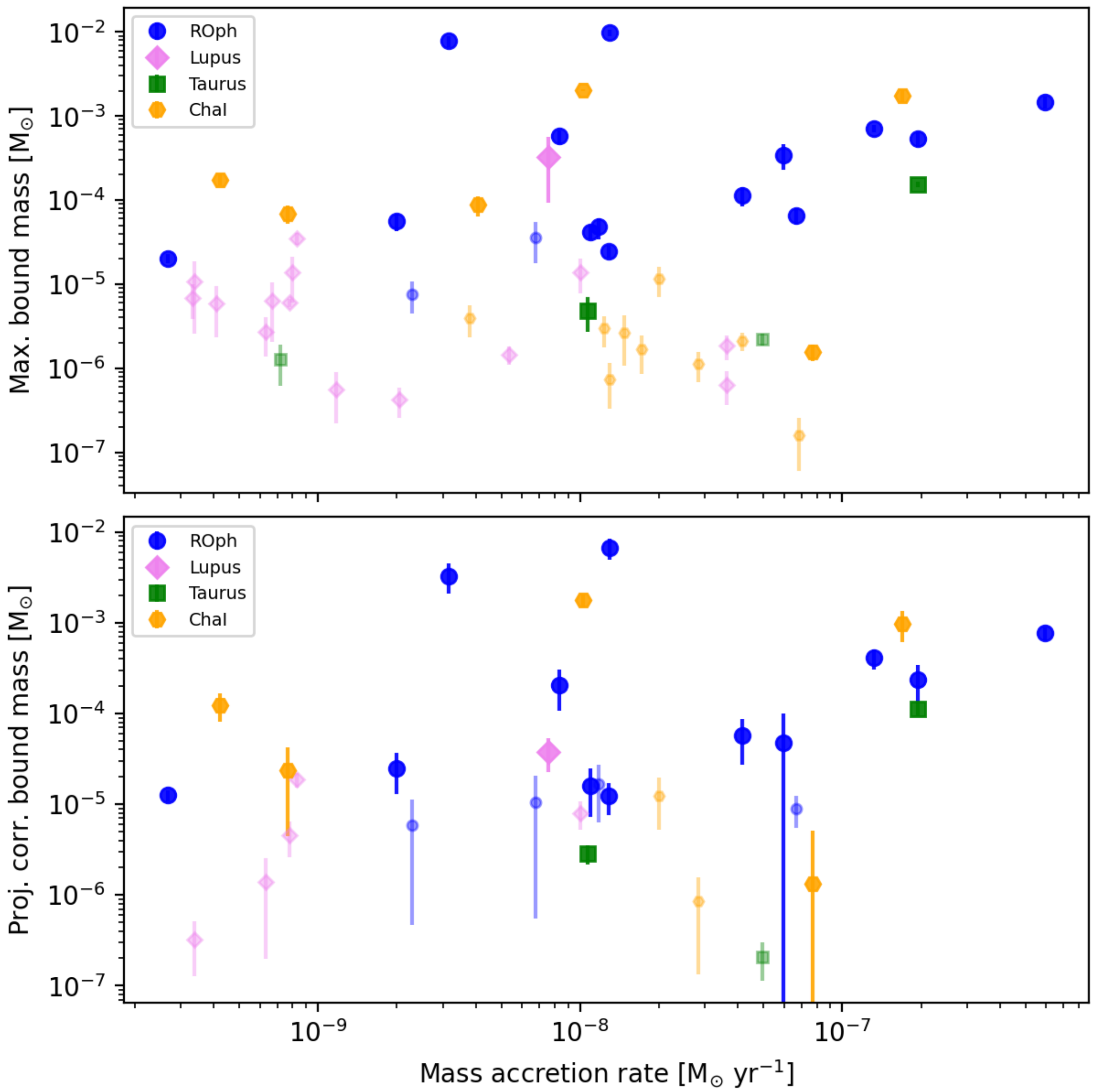

Figure 4.5: Mass accretion rates ($\dot{M}_{\rm acc}$) vs. max. bound mass ($M_{\rm max.}$, top panel) and projection corrected bound mass ($M_{\rm proj.\ corr.}$, bottom panel). Markers are as described in Figure 4.3.

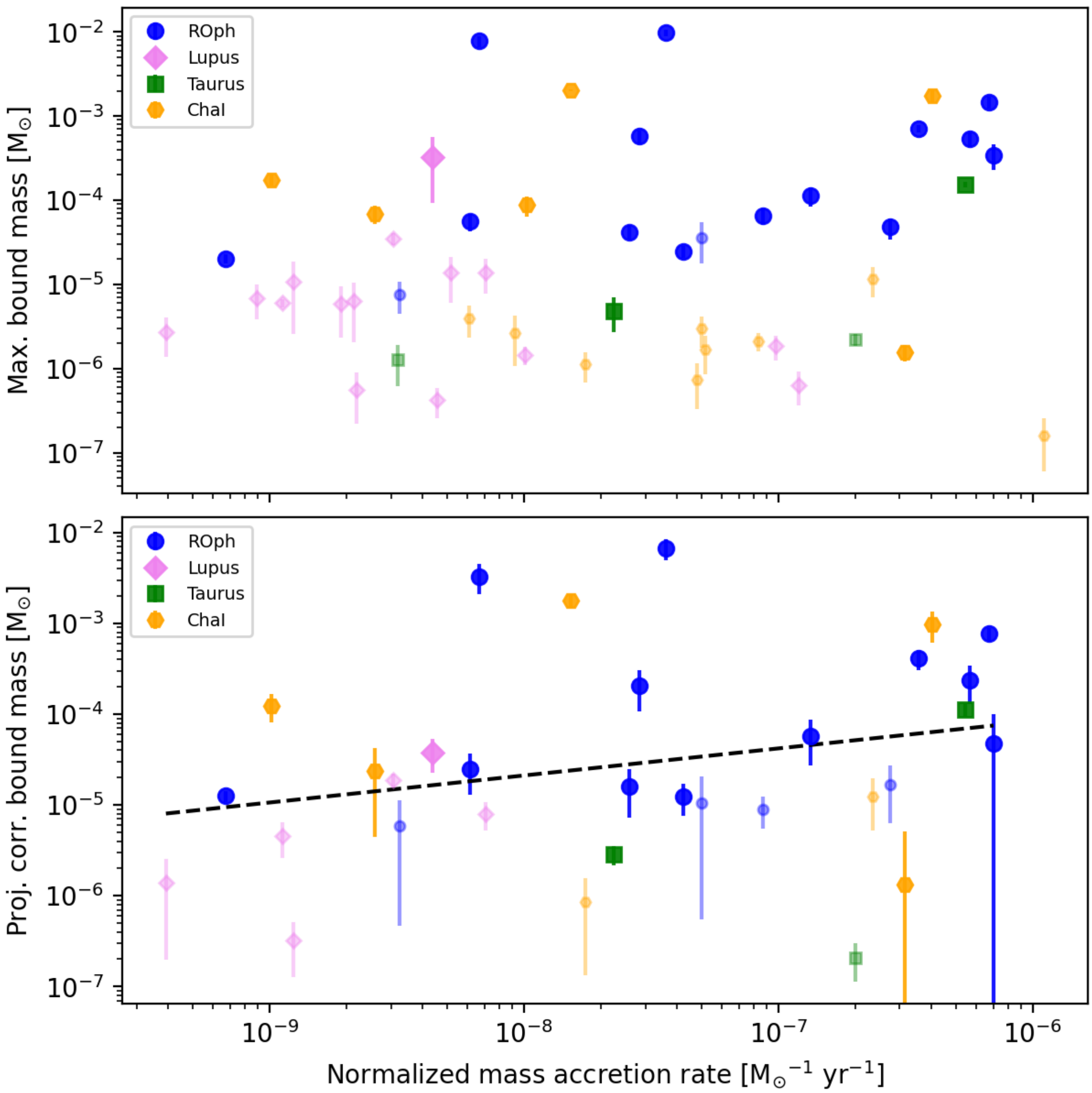

Figure 4.6: Normalized mass accretion rates ($\dot{M}_{\rm acc}/M_*^2$) vs. max. bound mass ($M_{\rm max.}$, top panel) and projection corrected bound mass ($M_{\rm proj.\ corr.}$, bottom panel). Markers are as described in Figure 4.3. Dashed black line represents the best power-law fit.

to get a more comprehensive picture of their evolution.

For ROph in particular, the majority ($\sim 75\%$) of sources have a significant amount of bound material, with an average mass of $\sim 10^{-3}$ $M_{\odot}$ or ~ 1 $M_{\rm Jupiter}$. The accretion of such an amount of gas mass - similar to the whole gas disk mass for some known sources (Miotello et al., 2017) - can resolve the 'mass-budget' problem of Class II disks, where these disks appear to lack material to form the observed population of planetary systems (Manara et al., 2018; Mulders et al., 2021).

Interestingly, ROph is also the youngest region targeted in DECO. This may suggest that the likelihood of such interactions is higher when the region is younger, possibly due to a larger amount of gas yet to be dispersed. As discussed in Section 4.2.1, the ages of the other three regions are estimated to be around $\sim$ 1–3 Myr, though the exact relative ages remain uncertain. A more precise determination of the ages of all regions, particularly for the sub-regions observed by DECO, will allow us to better this hypothesis. Besides age, other environmental parameters like gas density and density distribution within a star-forming region may also play a role in determining influence of surrounding gas on Class II systems.

Another key result of this study is that the masses of bound structures are not significantly correlated with the disk or stellar masses. This may be because these disk and stellar masses are time-integrated quantities and thus, heavily influenced by initial conditions and the entire evolutionary history of these systems.

In contrast, mass accretion rates are instantaneous and primarily governed by the current angular momentum transport within disks. Although we do not find a clear correlation with mass accretion rates, we do observe a tentative positive correlation (p-value of 0.09) with accretion rates normalized by stellar masses. Interestingly, this aligns with the expected behavior for a Bondi-Hoyle-Lyttleton-type accretion mechanism, where the mass infall rate ($\dot{M}_{\rm BHL}$) scales with stellar and environmental properties as $\dot{M}_{\rm BHL} \propto M_*^2 \rho_{\rm gas}/\Delta v_{\rm gas}^3$, where $\rho_{\rm gas}$ and $\Delta v_{\rm gas}$ represent the local gas density and relative velocity, respectively (e.g., Bondi & Hoyle, 1944; Padoan et al., 2005; Winter et al., 2024). In this scenario, normalized mass accretion rates are expected to depend more strongly on the environment (Winter et al., submitted). This can further suggest that the environment can influence the angular momentum transport within disks, potentially by enhancing turbulence as discussed by Winter et al. (2024). However, more data points are needed to say something more conclusive. Data for about 25% DECO sources is yet to be delivered. Including these additional data points will allow us to better understand impact of large-scale gas structures onto properties of protostellar systems.

One of the key caveats regarding the results presented in this study, particularly in the context of the actual fraction of sources with large-scale structures, is that the sample selection focuses on Class II sources, which are traditionally determined using spectral energy distributions in near-infrared wavelengths (e.g., Dunham et al., 2014). As Kuffmeier et al. (2023) demonstrated, some Class II sources can be misclassified as less evolved sources if they are interacting with their environments. Moreover, the observations were primarily designed to study disk chemistry and may not be optimal to detect and analyse large-scale structures. Therefore, the fraction of sources we observed with large-scale structures is more of a lower limit. Furthermore, as pointed out in Section 3.2.4, we are likely missing flux from these structures due to filtering out of large-scale emission and cloud absorption. This may further suggest that we are underestimating the mass of bound structures.

4.6 Conclusions

DECO is a moderate-resolution survey of 80 Class II systems spread over four star-forming regions. Although the survey was primarily designed to study disk chemistry, we detect large-scale ($\gtrsim$ 500 au) bound structures around $\sim$ 40% of DECO sources observed so far. Accounting for selection biases and stellar kinematics, the fraction of Class II sources that interact with surrounding gas at some point in their lifetime will be even greater. This contradicts the traditional assumption of isolated Class II disks. Furthermore, we see significant differences in the fraction of sources with large-scale structures among the four star-forming region. Most of such structures are observed in ROph, the youngest region targeted in this study. This may suggest that age and/or environment is an important factor in determining the likelihood of interactions between disks and surrounding gas.

We do not see any clear dependence of disk and stellar masses on masses of bound structures, likely because these quantities are time-integrated over the whole lifetime of these sources and thus, not significantly altered by the immediate surroundings. Although we do not see a clear correlation with mass accretion rates, we do see a tentative correlation for mass accretion rates normalised by stellar masses. This indicates that the environment may influence angular momentum transport within disks. However, more data points are needed to make a firm conclusion.

Data for about one-fourth of the DECO sources, which includes most of the Taurus disks, are yet to be delivered. Including these additional data points will allow us to better test the interplay between large-scale structures and properties of YSOs. Moreover, we can include more realistic temperature and optical depth prescriptions to get more accurate mass estimates. Morphology and velocity gradient of the structures with high enough signal-to-noise ratio data can be modelled to further ascertain their dynamical nature.

Overall, our results suggest that disks do not evolve in isolation from their environments. Their interactions need to be better characterised to understand the evolution of these systems and thus, to develop a more comprehensive view of planet formation.

Appendix A

Appendices for Chapter 2

A.1 Star-forming regions

Figure A.1 shows DSS optical images of all the SFRs listed in Table 2.1, as discussed in Section 2.3. Figure A.2 shows fraction of all YSOs (solid lines) and just Class II sources (dashed lines) which are associated with RNe as a function of offset thresholds used to define association, as discussed in Section 2.4.

A.2 Distribution of spectral indices

Figure A.3 shows the distribution of extinction-corrected spectral indices (α', solid bars) and originally measured spectral indices (α, dashed-grey line), as discussed in Section 2.3. The distribution of α values are shifted to the right because foreground extinction can artificially increase the observed infrared excess for a source.

A.3 Class II sources near RNe

Table A.1 gives coordinates (first two columns), SIMBAD identifiers (third column), the SFR (fourth column), spectral indices (fifth and sixth columns), and RNe catalogue identifiers (last two columns) for all the Class II sources in the vicinity of RNe, as discussed in Section 2.3.

A.4 Required observations and analysis

In order to further test a possible link between RNe and late infall, a deep uniform survey of large-scale structures is needed for Class II sources associated with RNe, as suggested in Section 2.4. Ideal observational parameters for such a survey are discussed below.

For what concerns the angular scales, both observations (Figure 2.1) and simulations (e.g. Kuffmeier et al., 2020) suggest that the infalling streamers should be roughly kilo-au

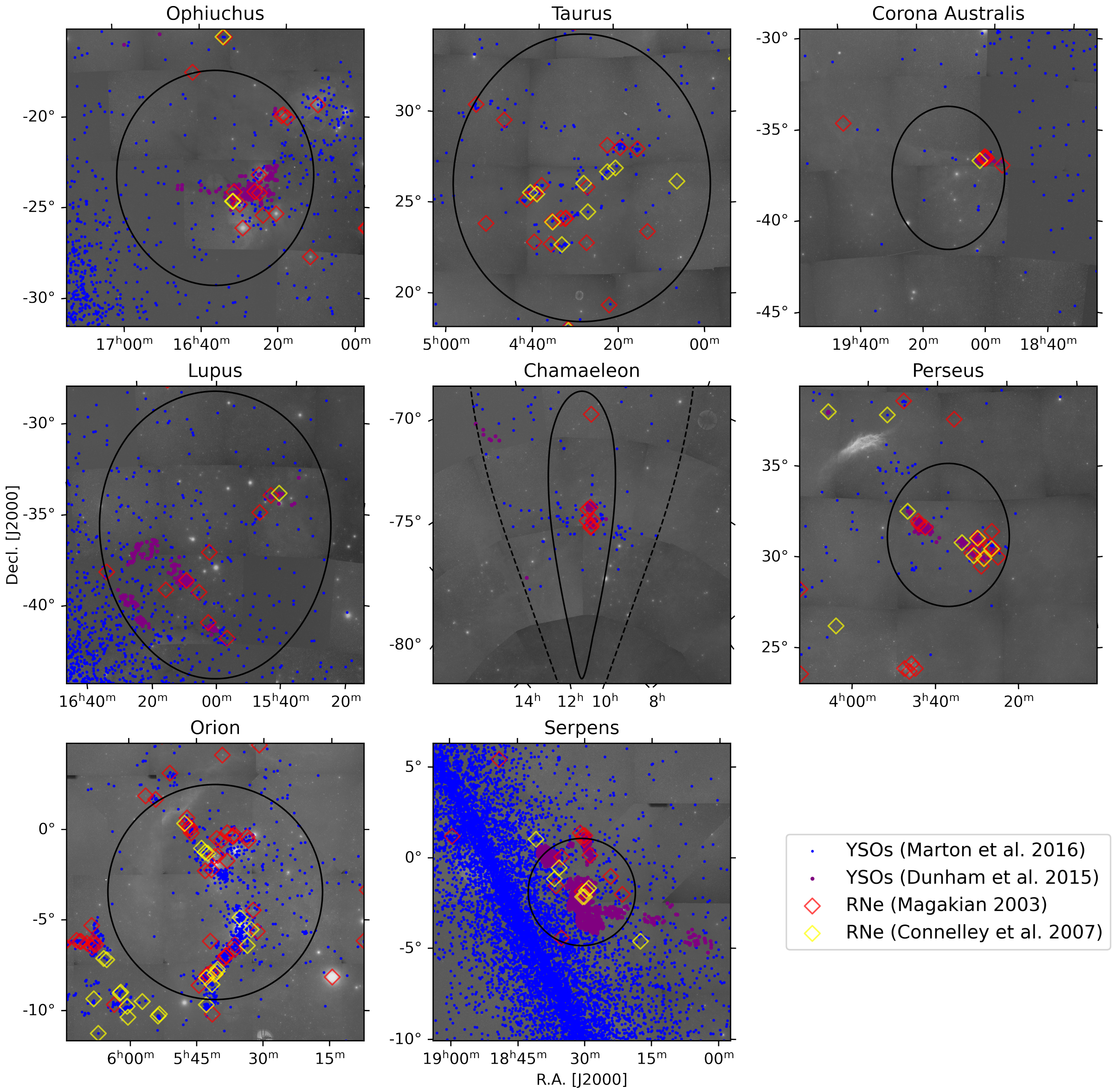

Figure A.1: DSS optical images of all the SFRs listed in Table 2.1. Solid-black curves denotes circular boundaries of these SFRs, as parameterized by the "Radius" column of Table 2.1. Blue and purple circles represent YSOs from Marton et al. (2016) and Dunham et al. (2015) catalogues, respectively. Red and yellow open diamonds represent RNe from Magakian (2003) and Connelley et al. (2007) catalogues, respectively. Dashed-black curve in Chamaeleon's map denote a circle with radius of 20°.

scales in length. Therefore, observations needed to study these structures should have a large enough maximum recoverable angular scale ($\gtrsim$ 1000 au), so as to not filter out large-scale emission. For the typical distance of 150 pc to nearby SFRs, this physical scale

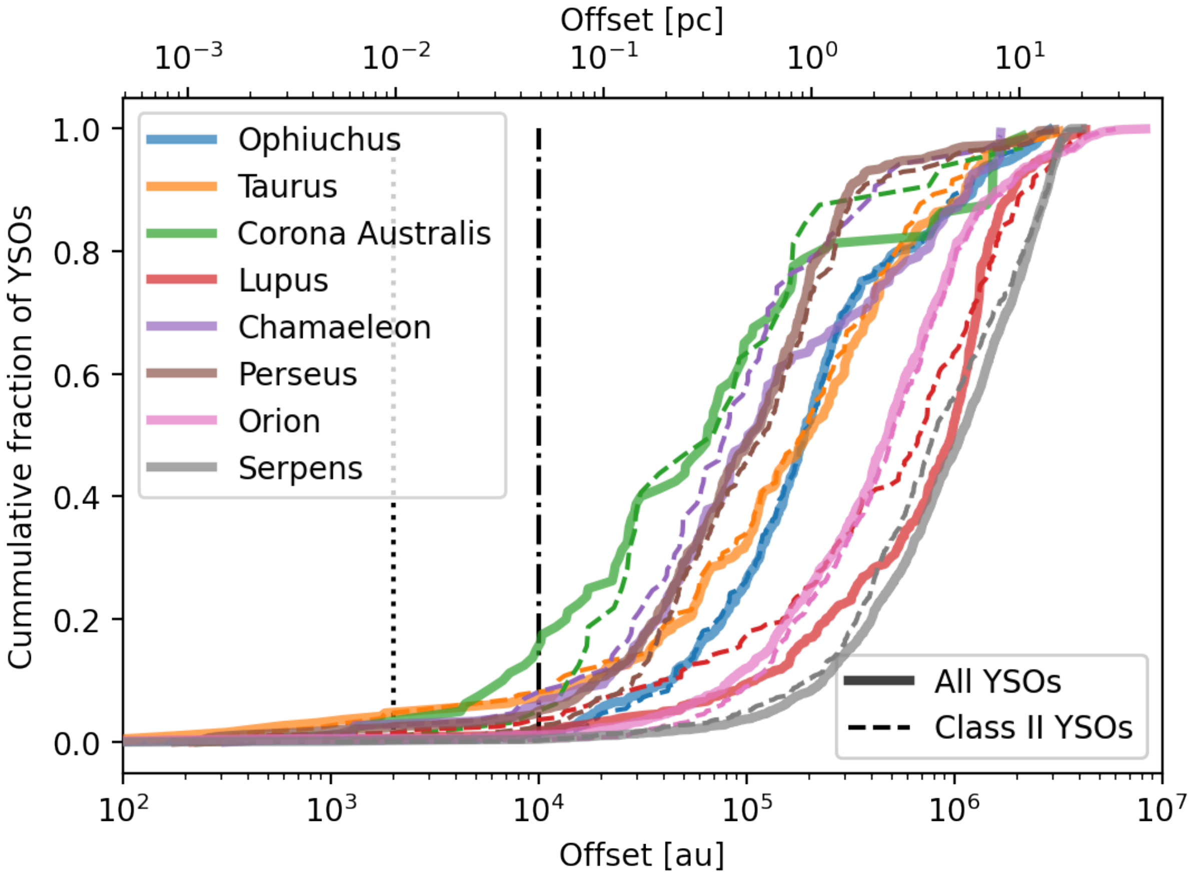

Figure A.2: Cumulative distribution of the fraction of YSOs with distance to the nearest RNe less than the given offset, as discussed in Section 2.4, for different SFRs. Solid lines represent all the YSOs and dashed lines represent only Class II sources. Vertical dotted and dash-dotted lines denote offset values of 2000 and 10000 au, respectively.

corresponds to the largest angular scale of $\gtrsim 7$ arcsec. On the other hand, spatial resolution of such observations should be roughly $\lesssim$ 100 au ($\lesssim$ 0.7 arcsec at a distance of 150 pc), in order to resolve the connection between large-scale structures and protoplanetary disks. Such a resolution should also be adequate to resolve the width of infalling streamers (Figure 2.1).

In terms of spectral resolution, free-fall velocity for the infall of material can be estimated as $v = \sqrt{2GM_*/R}$, where G is the gravitational constant, M_* is the stellar mass, and R is the free-fall length scale. For the typical stellar mass of $\sim 0.5M_\odot$ and expected infall length scale of $\sim 1,000$ au, the free-fall velocity should be ~ 0.95 km s^{-1}. Assuming we see such an infalling streamer at an intermediate inclination of 45°, observed velocity difference would be ~ 0.65 km s^{-1}. In order to resolve the velocity profile, we would need at least three independent data points, and thus a spectral resolution of $\lesssim 0.2$ km s^{-1}.

The sensitivity requirements of the ideal observations can be based on the past obser-

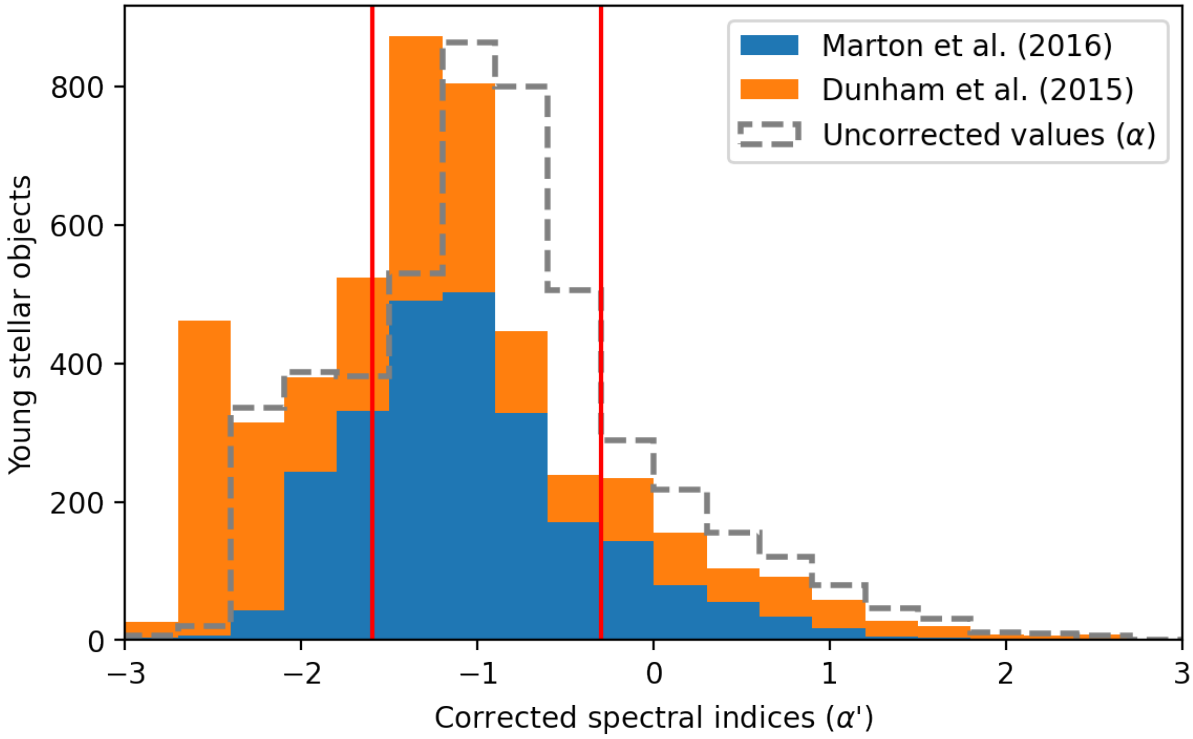

Figure A.3: Distribution of extinction-corrected infrared spectral indices (α', solid bars) and measured spectral indices (α, grey-dashed steps) for all the 4930 YSOs in SFRs, as discussed in Section 2.4. Blue bars denote α' values estimated for sources exclusively from Marton et al. (2016). Orange bars denote α' values for sources from Dunham et al. (2015). Red vertical lines mark the range of values for a YSO to be classified as a Class II source ($-1.6 \leq \alpha' < -0.3$).

vations of such large-scale structures. Among the five sources discussed in Section 2.2, AB Aur and SU Aur are exceptionally bright and may not be representatives for the overall sample. For RU Lup, the signal-to-noise ratio for the spiral structures was sub-optimal ($\lesssim 3$) in the individual channel (see Figure 5, Huang et al., 2020), which can make it hard to study the background dynamical processes. Thus, sensitivity requirements of the observations can be based on observations of GM Aur and DO Tau, and for both of which the brightness-temperature sensitivity was ~ 250 mK (normalised to a channel width of 0.2 km s^{-1}).

If large-scale structures are observed around other Class II sources, gas kinematics can be analysed to understand the dominant dynamical processes. A first step could be to check if the material is gravitationally bound to the protostellar system. For this the kinetic energy can be computed along the streamer, using the relative line-of-sight velocities, and compared to gravitational energy, similar to the analysis done for DO Tau by Huang et al. (2022) (see Figure 12). Furthermore, position-velocity diagrams, along

R.A. [°]	Decl. [°]	Simbad Id.	Region	α	α'	Magakian RNe Id.	Connelley RNe Id.
247.96698	-24.93782	ISO-Oph 204	Ophiuchus	-0.17	-0.51	-	66
239.17449	-42.32318	HD 142527	Lupus	-0.6	-0.91	641	-
236.30347	-34.29186	CD-33 10685	Lupus	-0.64	-0.95	634	-
237.02178	-35.26469	V* HN Lup	Lupus	-0.84	-1.15	636	-
277.19941	0.14439	V* VV Ser	Serpens	-0.78	-1.05	766	-
85.20028	-8.09964	CoKu DL Ori G1	Orion	-0.93	-1.24	132	-
167.01364	-77.65476	HD 97048b	Chamaeleon	-0.07	-0.38	533	-
168.11282	-76.73947	BRAN 341D	Chamaeleon	-0.76	-1.11	545	-
168.12797	-76.73998	V* CW Cha	Chamaeleon	-0.61	-1.09	545	-
285.28588	-36.95575	V* S CrA B	Corona Australis	-0.8	-1.22	781	-
68.13232	24.33411	V* FZ Tau	Taurus	-0.86	-1.17	74	-
68.39192	24.35472	V* GI Tau	Taurus	-0.62	-0.93	75	-
68.12742	24.33257	V* FY Tau	Taurus	-1.12	-1.43	74	-
68.39412	24.35176	V* GK Tau	Taurus	-0.67	-0.98	75	-
69.61912	26.1804	V* DO Tau	Taurus	-0.51	-0.82	78	-
68.92066	24.18566	NAME CoKu Tau 3	Taurus	-0.9	-1.21	76	-
68.97004	22.90634	V* HP Tau	Taurus	-0.57	-0.88	77	-
55.73321	31.97828	2MASS J03425596+3158419	Perseus	-0.98	-0.84	48	-
52.68335	30.54634	EM* LkHA 326	Perseus	-0.64	-0.89	45	-
52.21743	30.75151	EM* LkHA 325	Perseus	-0.69	-0.78	41	-
235.755	-34.15417	HH 185	Lupus	-0.21	-0.31	-	64

Table A.1: List of 21 Class II YSOs ($-1.6 \leq \alpha' < -0.3$) associated with RNe (distance to nearest RNe $\lesssim$ 2000 au), as discussed in Section 2.3. α and α' values are measured and extinction-corrected spectral indices, respectively. Last two columns show index numbers for matched RNe in Magakian (2003) and Connelley et al. (2007) catalogues.

any detected streamer, can be modelled and compared to the velocity profiles expected for different kinematic features such as rotation ($v \propto R^{-1}$, for conserved angular momentum) and infall ($v \propto R^{-0.5}$, for free fall), similar to the analysis done for less evolved protostars HL Tau (Yen et al., 2019) and Lupus 3-MMS (Thieme et al., 2022).

Another way to infer late infall could be to study gas kinematics together with NIR polarisation observations, as was done for SU Aur by Ginski et al. (2021). The degree of polarisation in such observations can be correlated to the dust scattering angles, which are expected to depend on the three-dimensional morphology of dust structures (e.g. Stolker et al., 2016). Studying the morphology and gas kinematics in larger-scale ($\sim 10,000$ au) clouds can also allow us to judge the possibility of late infall (Tang et al., 2012; Dullemond et al., 2019).

Finally, late infall can also be inferred by observing these systems using different chemical species. Though CO has a high surface brightness, making it ideal to detect faint structures, it is also likely to be polluted by the emission from diffuse gas in these clouds. For less evolved sources, infalling streamers have also been observed in tracers such as HCO^+, HC_3N, HC_5N, CCS, ^{13}CS, HNC, and H_2CO (Yen et al., 2019; Pineda et al., 2020; Murillo et al., 2022; Valdivia-Mena et al., 2022). Moreover, material falling onto protoplanetary disks also creates shocks, which can be observed using shock tracers such as SiO, SO, and SO_2 (e.g. Garufi et al., 2022). A dedicated chemical study of streamers could also allow us to identify better chemical tracers for these structures for a large-scale survey.

A.5 Alternative explanations for large-scale structures

The large-scale CO structures discussed in Section 2.2 and 2.3 could also be due to other dynamical processes besides late infall (e.g. Huang et al., 2020). One of the other prominent causes, particularly for spiral-like structures, could be a tidal interaction of stellar companions, as it has been observed in some other multiple systems (e.g. Rodriguez et al., 2018; Kurtovic et al., 2018; Zapata et al., 2020). The two sources we found with large-scale structures, HD 142527 and S CrA (Section 2.3), are binaries, and thus some of the structures we observe around them (Figure 2.3, panel a and c) could be due to tidal interactions between protostars and surrounding gas.

Furthermore, such structures can also be created due to close encounters by neighbouring YSOs, as predicted by several hydrodynamic simulations (e.g. Cuello et al., 2019; Vorobyov et al., 2020) and likely observed for a few sources (e.g. Dong et al., 2022). The role of these stellar flybys can be checked by looking at relative distances and velocities of nearby YSOs, as was done for SU Aur (Ginski et al., 2021, Appendix D).

Gravitational instabilities can be another possible way to form spiral-like structures, if the disks are massive enough (e.g. Dong et al., 2015), as generally inferred by Toomre's Q parameter (Toomre, 1964). Such instabilities are expected to leave characteristic 'wiggle' signatures in the gas kinematics, which can be used to identify them (Hall et al., 2020). Moreover, Harsono et al. (2011) showed that such instabilities can also be triggered by the infall of material. Irrespective of the cause of such non-Keplerian structures, both approaches followed in Sec. 2.2 and in Sec. 2.3 suggest that the vicinity of a RN can be an effective criterion to identify Class II disks that present large-scale structures.

A.6 Channel maps

Figure A.4 and A.5 show channels maps of S CrA and HD 97048, respectively, as discussed in Section 2.3.

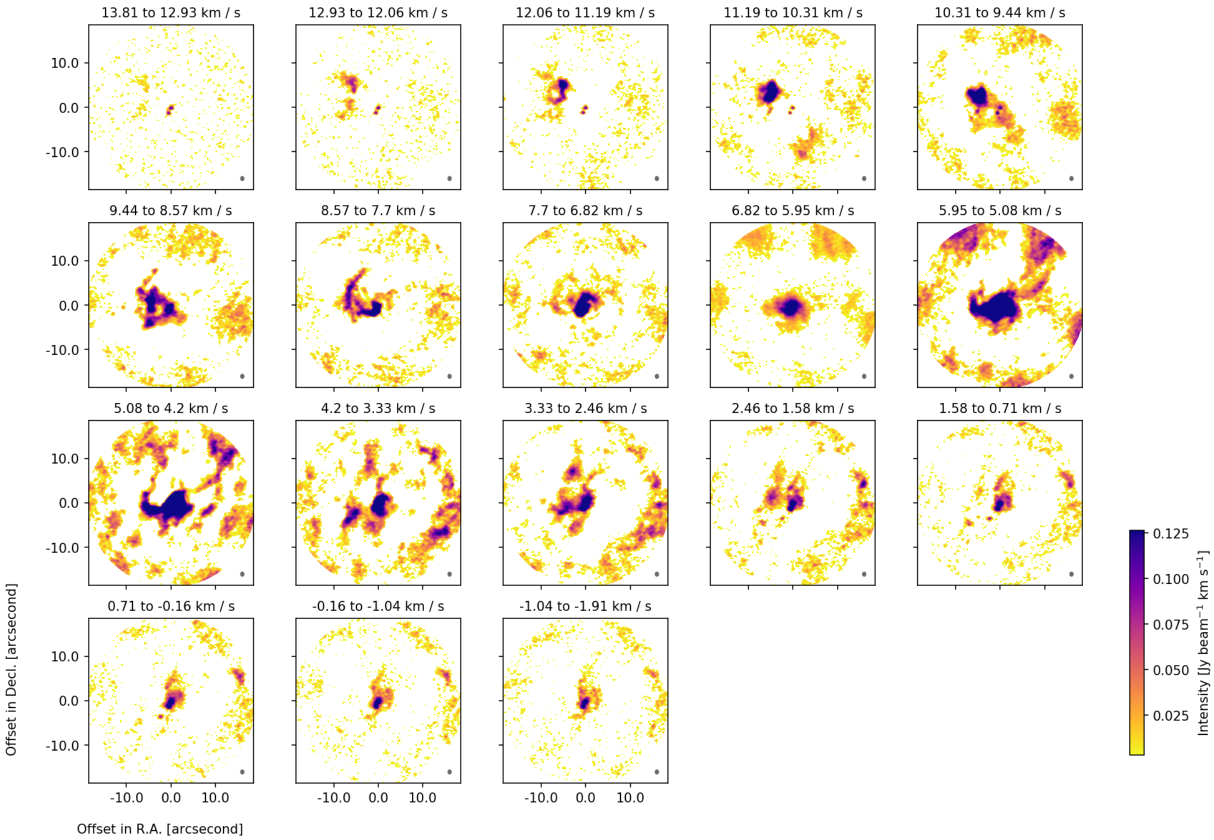

Figure A.4: ALMA ^{12}CO (2–1) channel maps for S CrA archival observations (Project code: 2019.1.01792.S). Emission only from pixels with an intensity $> 2\sigma$ was considered. Grey ellipses in the bottom right corners of the maps represent the beam size.

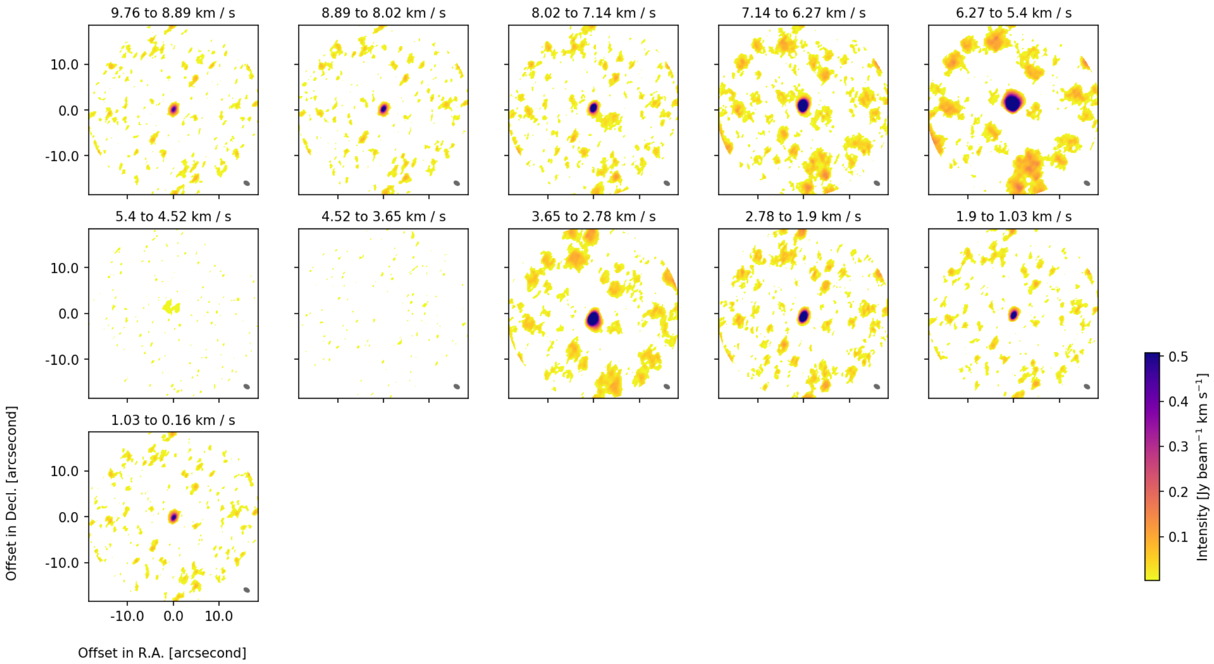

Figure A.5: ALMA ^{12}CO (2–1) channel maps for HD 97048 archival observations (Project code: 2015.1.00192.S). Emission only from pixels with an intensity $> 2\sigma$ was considered. Grey ellipses in bottom right corners of the maps represent the beam size.

Appendix B

Appendices for Chapter 3

B.1 3D morphology

The best-fit trajectories from TIPSY can also be used to infer the trajectory of infalling gas in 3D position–position–position space (RA, Decl., and LOS distance), as shown in Fig. B.1. As we expect all of the observed gas in these streamers to have similar initial conditions, these 3D trajectories represent the 3D morphologies of infalling streamers.

Figure B.1 also compares the 3D trajectory as inferred from our implementation of Mendoza et al. (2009) models (see Sect. 3.2.1) to the solutions for the same initial configuration from simple two-body REBOUND simulations (Rein & Liu, 2012). Both the solutions are always in good agreement, suggesting that our implementation of Mendoza et al. (2009) models gives an accurate description of infalling particle motion. We note that the REBOUND simulations generally take $\gtrsim 100$ times more time to compute solutions, making its use much less feasible for fitting streamers.

B.2 Distance metric

Figure B.2 illustrates computation of distance metric ($d = \sqrt{r^2 + (wr\theta)^2}$), where r and θ denote the projected radial distance (from the protostar) and polar angle (with respect to the median orientation of streamer points closer than the 10^{th} percentile of r distribution), respectively. The weighting factor (w, $= 1$ by default) sets the importance of $r\theta$ (distance in azimuthal direction) in the computation of distance metric. Setting $w = 0$, will set distance metric to be equal to the projected radial distance (r), similar to the approach by Yen et al. (2019).

Overall, a higher-value distance metric should correspond to the part of the streamer that is expected to be physically farthest away from the protostar(s). As discussed in Sect. 3.2.2, this distance metric is used to bin the data (for computing intensity-weighted means and standard deviations) and as an independent parameter for the final fitting.

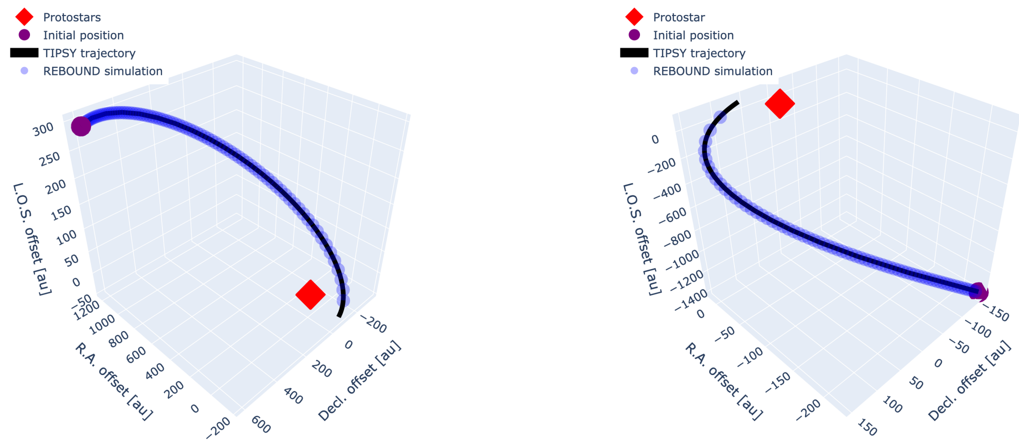

(a) (b)

Figure B.1: Isometric projection of the best-fit infalling trajectory for streamers around S CrA (left panel) and HL Tau (right panel), in 3D position–position–position space (RA, Decl., and LOS or radial distance). The black line represents the analytical trajectory from our implementation of the Mendoza et al. (2009) models, as described in Sect. 3.2.1. Blue spheres represent solutions from two-body REBOUND simulations (Rein & Liu, 2012). The red diamonds denote the position of the center of mass of the protostellar systems. The purple circles denote the initial position of the infalling gas. These trajectories are computed up to the closest approach of infalling material to the protostellar system.

B.3 Stellar parameters for S CrA and HL Tau

Stellar parameters used for fitting the streamers are fixed before running TIPSY, as listed for S CrA and HL Tau in Table 3.1. Stellar mass estimates for S CrA and HL Tau were taken from Gahm et al. (2018) and Yen et al. (2019), respectively. Distance estimate for S CrA is based on *Gaia* DR3 parallax value (Gaia Collaboration et al., 2023). *Gaia* measurements were unavailable for HL Tau, so we used the estimate of the distance to its surrounding cloud, Lynds 155 (Galli et al., 2018).

Systemic LOS velocities for S CrA A (the northern protostar) and S CrA B (the southern protostar) were inferred to be 6.07 ± 0.09 km s $^{-1}$ and 5.66 ± 0.14 km s $^{-1}$, respectively, using the peak of Gaussian fits to $C^{18}O$ (2–1) disk spectra. These $C^{18}O$ (2–1) observations were part of the same ALMA project (Project Id.: 2019.1.01792.S) as the ^{13}CO (2–1) observations discussed in Sect. 3.3.1. We used the mean systemic velocity of 5.86 km s $^{-1}$ for the TIPSY fitting of S CrA streamer. For HL Tau, the systemic velocity derived by Yen et al. (2019) was used.

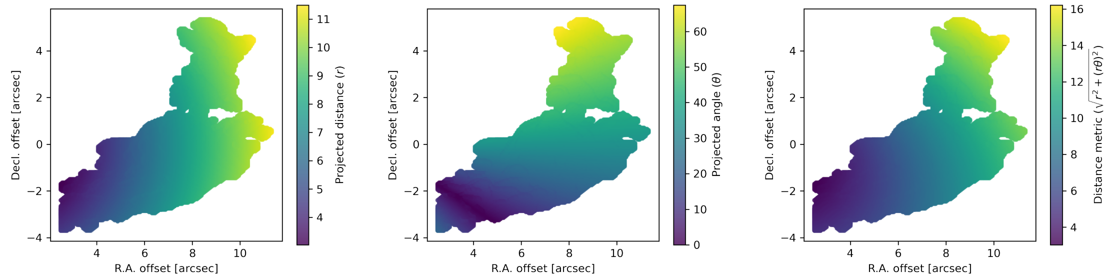

(a)

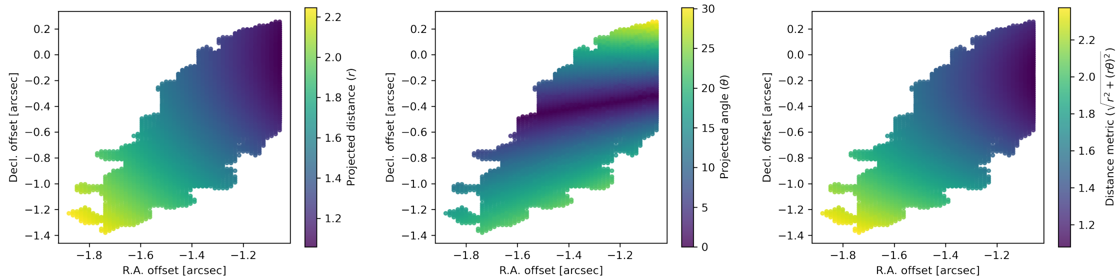

(b)

Figure B.2: Computation of the distance metric (d) using polar coordinates r and θ, as discussed in Appendix B.2, for S CrA (top panels) and HL Tau (bottom panels). *Left panels*: Radial distance ($r = \sqrt{(\Delta RA)^2 + (\Delta Decl.)^2}$) for each point on a streamer from the origin point (0,0). The origin point is also assumed to be the position of the center of mass for the protostellar system. *Middle panels*: Polar angle ($\theta = \arctan(\Delta Decl./\Delta RA)$) for each point on a streamer with respect to the mean direction of the streamer points in the bin closest to the origin. *Right panels*: Distance metric ($d = \sqrt{r^2 + (wr\theta)^2}$) for each point on a streamer computed using the polar coordinates (r and θ) and the weighting factor (w, $= 1$ by default).

B.4 Integrated intensity maps

Figure B.3 shows integrated intensity (moment 0) maps for 13CO (2–1) observations of S CrA and HCO^+ (3–2) observations of HL Tau. The streamers are visible as the elongated gas structures.

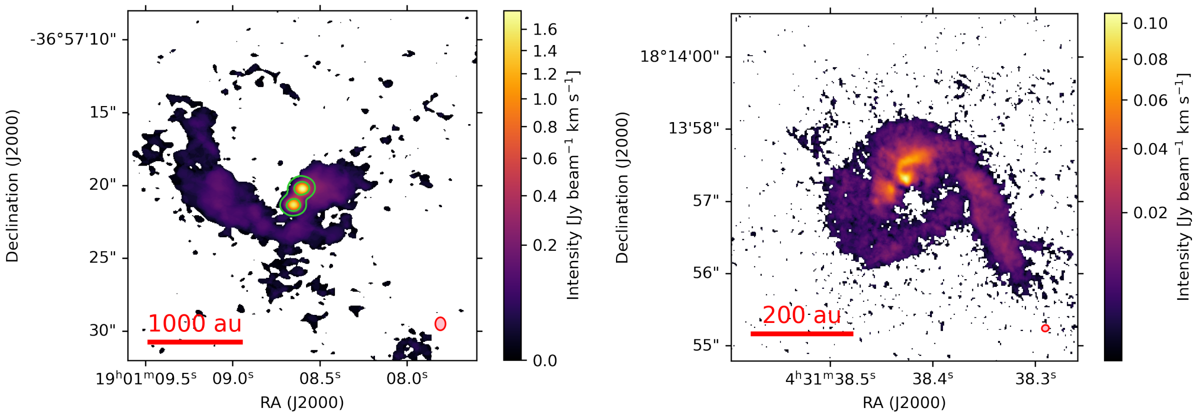

(a) (b)

Figure B.3: Integrated intensity (moment 0) maps for S CrA (left panel) and HL Tau (right panel), considering only pixels with an intensity $> 3.5\sigma$. The horizontal red lines in the bottom-left corners represent the physical length scales, and the pink ellipses in the bottom-right corners represent the beam size. Green contours in the left panel denote the continuum emission from the protoplanetary disks.

Appendix C

Appendices for Chapter 4

C.1 Channel maps and integrated spectra

Figures C.1 to C.62 display the CO (2–1), ^{13}CO (2–1), and C^{18}O (2–1) channel maps, along with the integrated spectra, for all DECO sources observed so far, as discussed in Section 4.2.1. The pink circles in the channel maps indicate the extent of bound material, as discussed in Section 4.3. The combined red-green-blue colormaps of these channel maps enable simultaneous visualization of emission from all three isotopologues.

For a significant number ($\sim 40\%$) of sources, prominent large-scale structures are visible (e.g., Fig. C.49). In many cases, the CO (2–1) emission from these structures is weaker near the systemic velocity (dashed black line in the integrated spectra), likely due to absorption by foreground clouds. For these velocity channels, the estimation of the bound gas mass primarily relies on emission from the less abundant ^{13}CO and C^{18}O isotopologues.

Some sources lack large-scale structures but still exhibit emission from Keplerian protoplanetary disks (e.g., Fig. C.15). Conversely, sources with relatively blank maps suggest that the sensitivity of the observations was insufficient to detect emission from either large-scale structures or disks (e.g., Fig. C.19). For such cases, the integrated spectra reflect the noise levels of the observations.

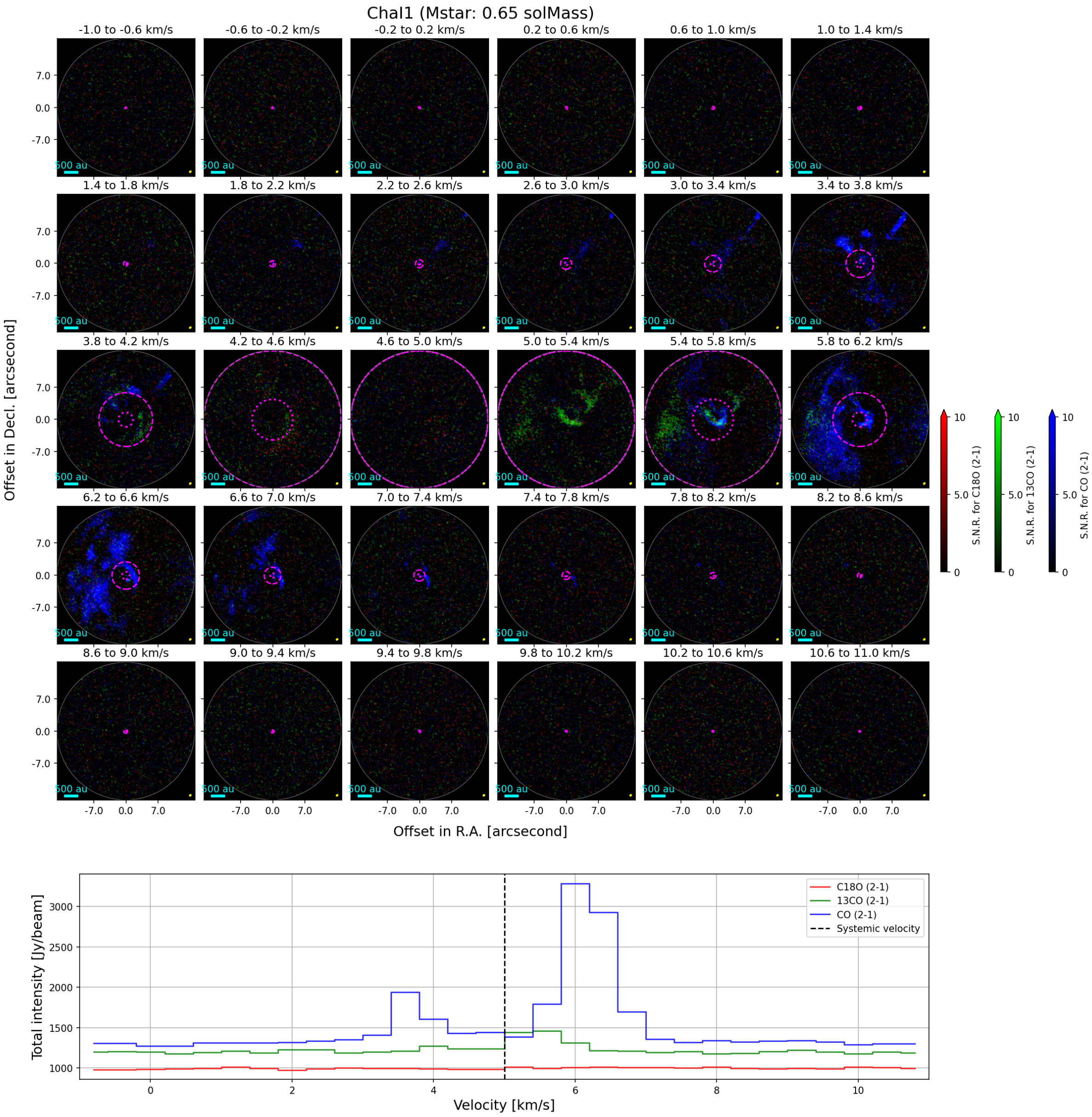

Figure C.1: CO (2–1), ^{13}CO (2–1), and C^{18}O (2–1) channel maps (top panel) and integrated spectra (bottom panel) for ChaI1. In both panels, CO (2–1), ^{13}CO (2–1), and C^{18}O (2–1) emission is represented by blue, green, and red colour, respectively. The colorbars indicate signal to noise ratio of observed emission. Dashed and dotted pink circles in channel maps denote the maximum bound radius ($r_{\mathrm{POS,\ max.\ bound}}$) and a more realistic bound radius ($r_{\mathrm{POS,\ est.\ bound}}$), respectively (see Section 4.3 for more details). Vertical dotted line overlaid on spectra represents the systemic velocity of protostellar system.

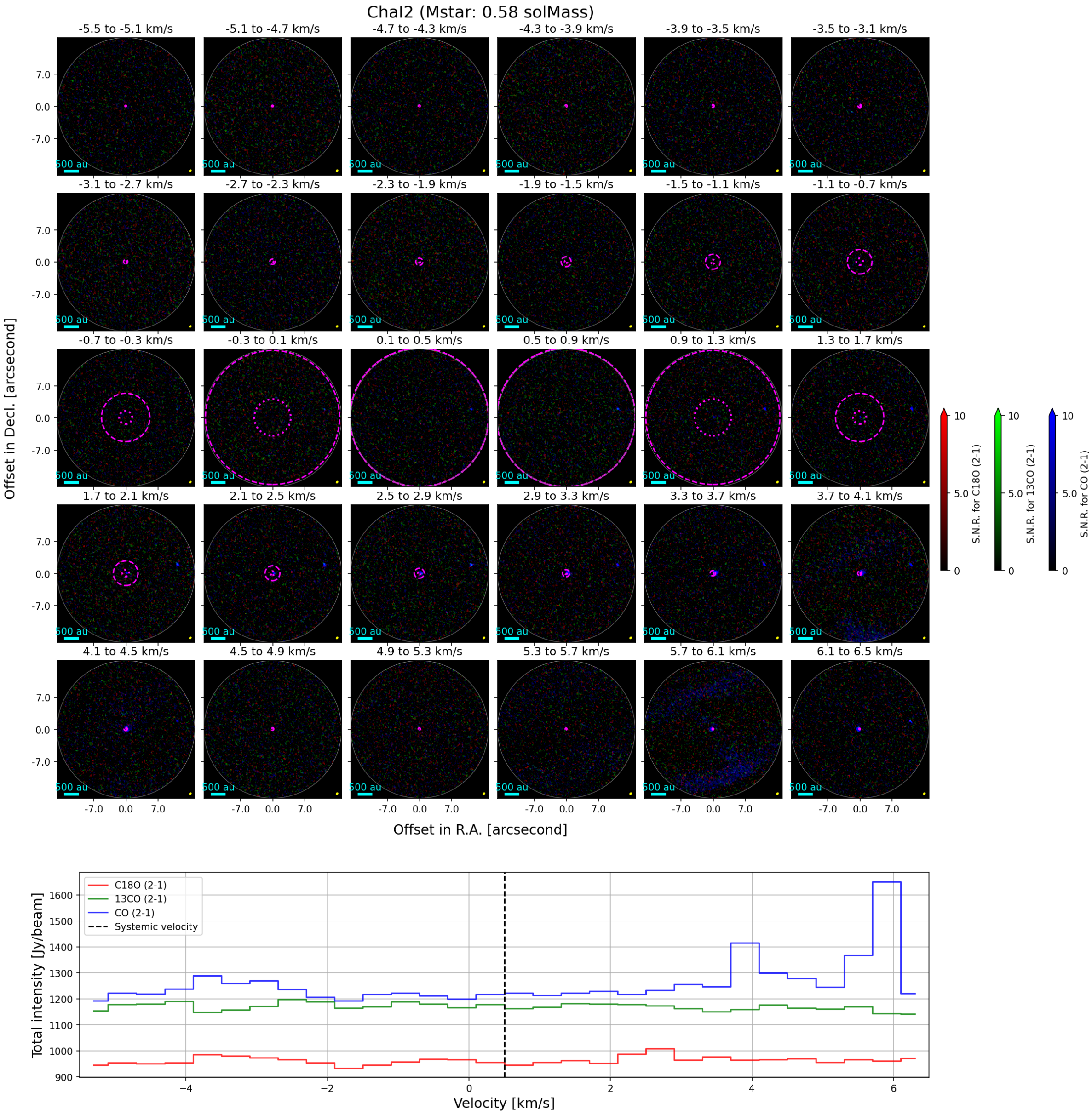

Figure C.2: CO (2–1), ^{13}CO (2–1), and C^{18}O (2–1) channel maps (top panel) and integrated spectra (bottom panel) for ChaI2. See Figure C.1 for more details.

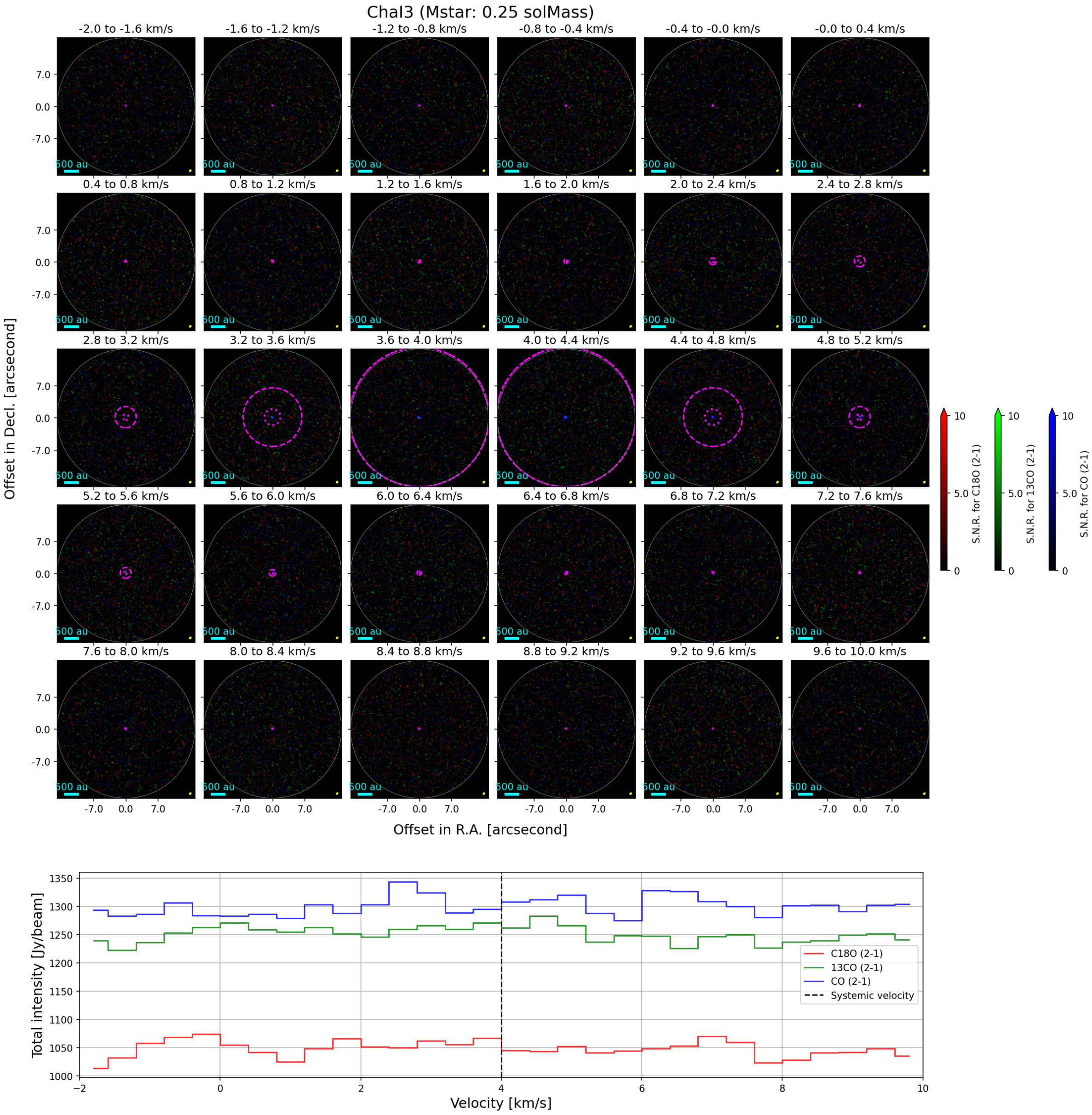

Figure C.3: CO (2–1), ^{13}CO (2–1), and C^{18}O (2–1) channel maps (top panel) and integrated spectra (bottom panel) for ChaI3. See Figure C.1 for more details.

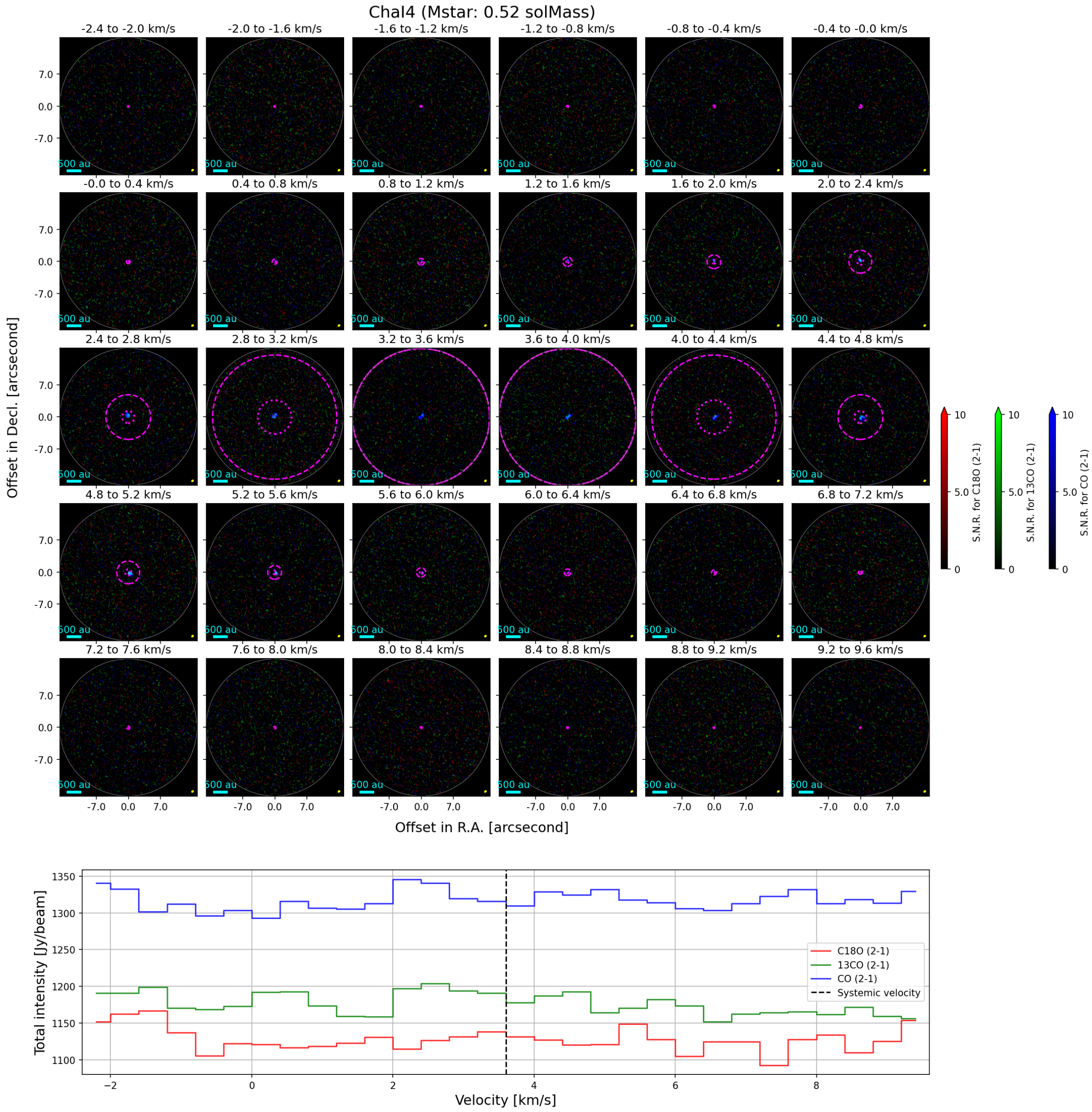

Figure C.4: CO (2–1), ^{13}CO (2–1), and C^{18}O (2–1) channel maps (top panel) and integrated spectra (bottom panel) for ChaI4. See Figure C.1 for more details.

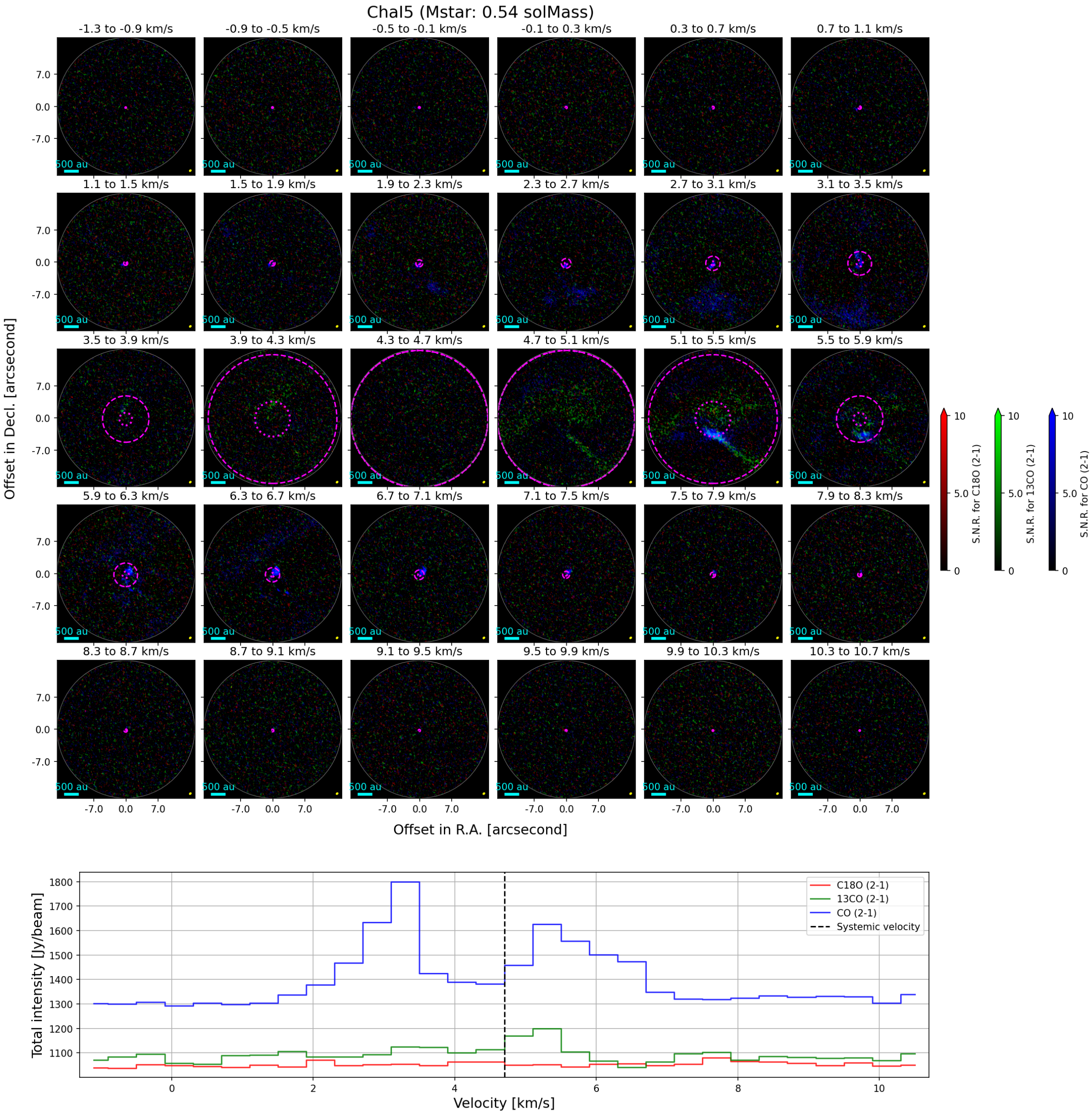

Figure C.5: CO (2–1), ^{13}CO (2–1), and C^{18}O (2–1) channel maps (top panel) and integrated spectra (bottom panel) for ChaI5. See Figure C.1 for more details.

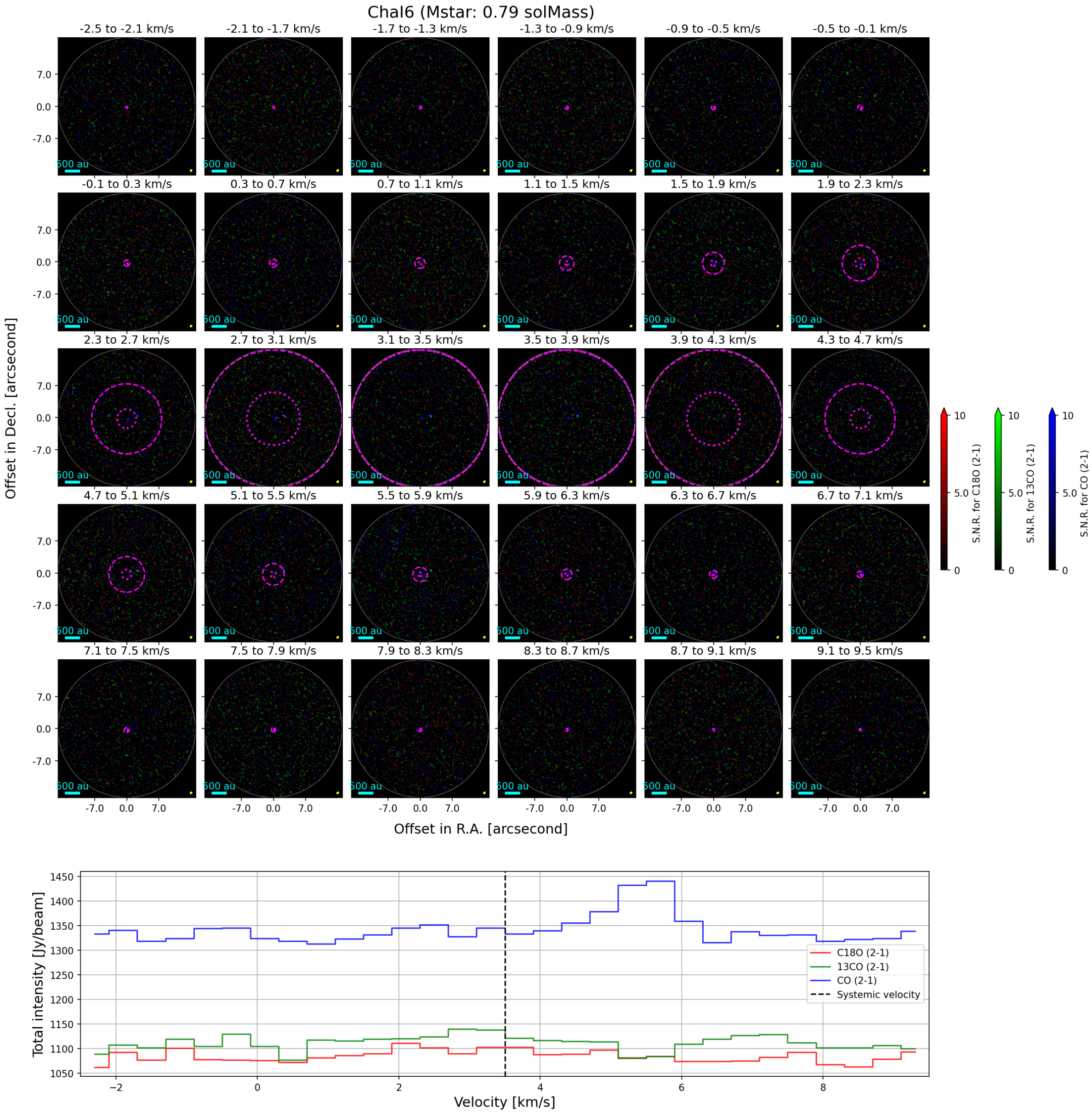

Figure C.6: CO (2–1), ^{13}CO (2–1), and C^{18}O (2–1) channel maps (top panel) and integrated spectra (bottom panel) for ChaI6. See Figure C.1 for more details.

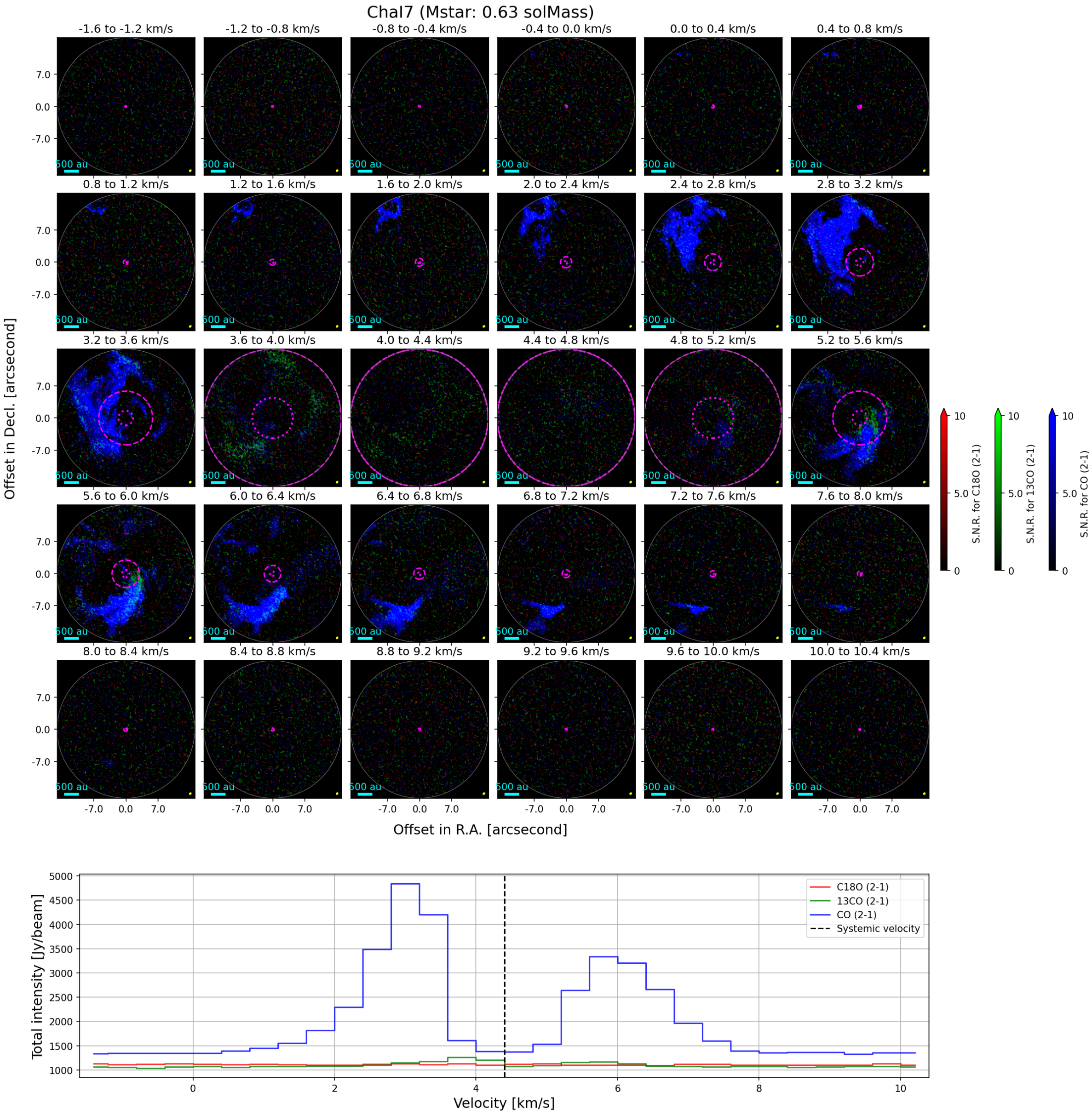

Figure C.7: CO (2–1), ^{13}CO (2–1), and C^{18}O (2–1) channel maps (top panel) and integrated spectra (bottom panel) for ChaI7. See Figure C.1 for more details.

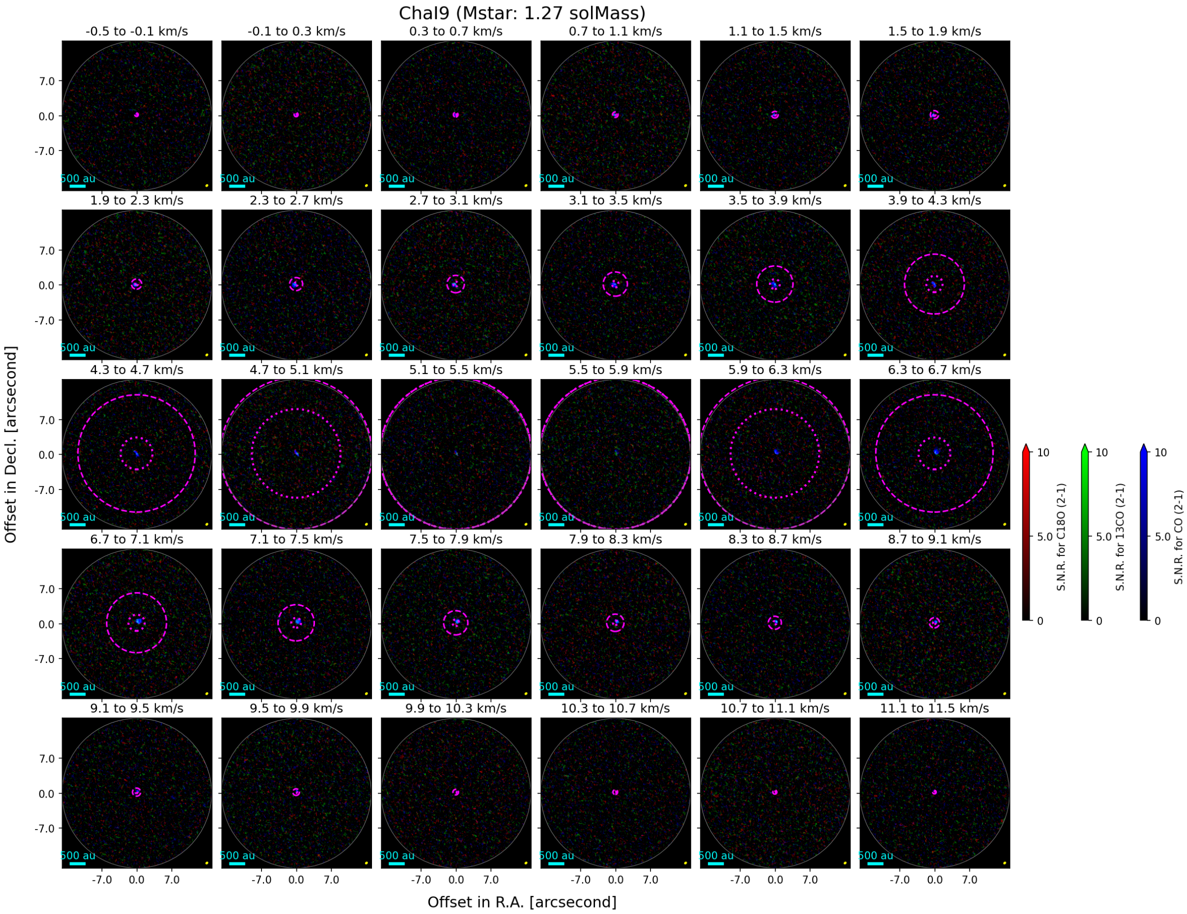

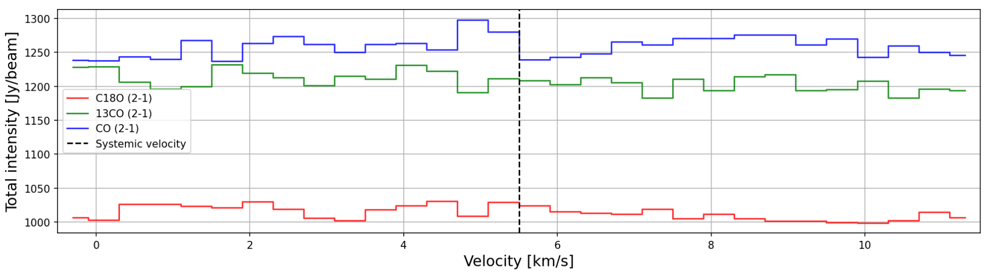

Figure C.8: CO (2–1), ^{13}CO (2–1), and C^{18}O (2–1) channel maps (top panel) and integrated spectra (bottom panel) for ChaI9. See Figure C.1 for more details.

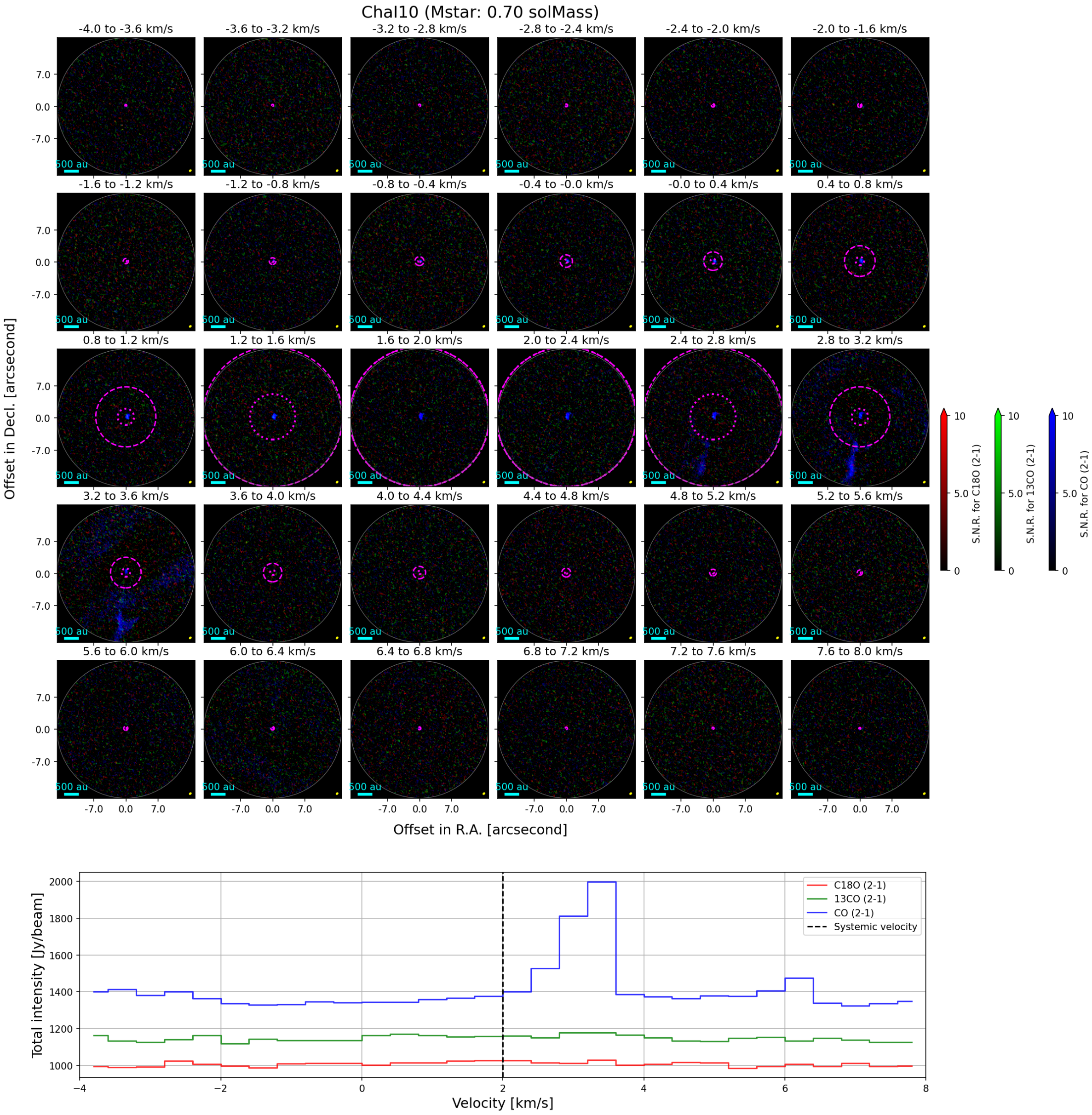

Figure C.9: CO (2–1), ^{13}CO (2–1), and C^{18}O (2–1) channel maps (top panel) and integrated spectra (bottom panel) for ChaI10. See Figure C.1 for more details.

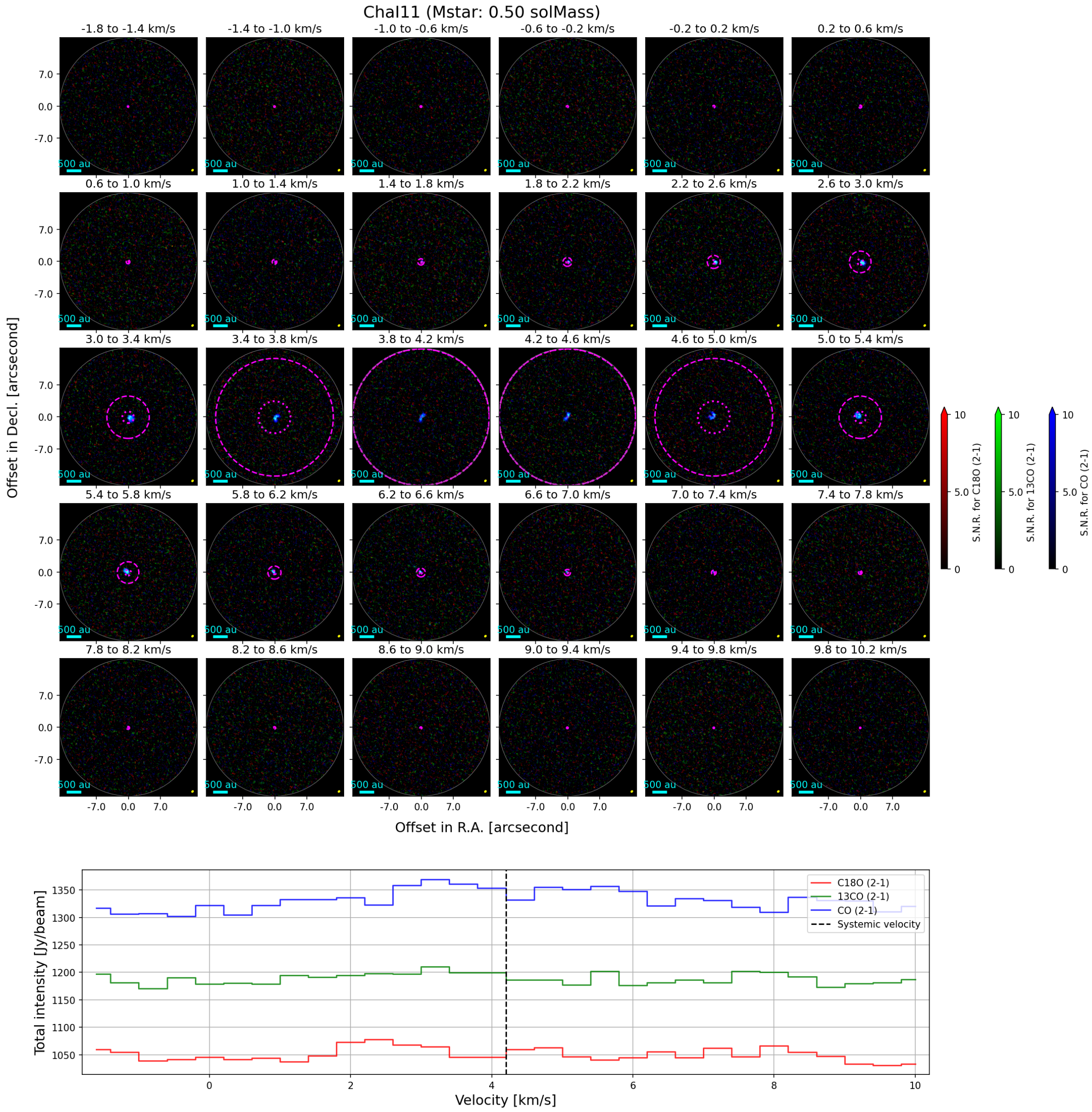

Figure C.10: CO (2–1), ^{13}CO (2–1), and C^{18}O (2–1) channel maps (top panel) and integrated spectra (bottom panel) for ChaI11. See Figure C.1 for more details.

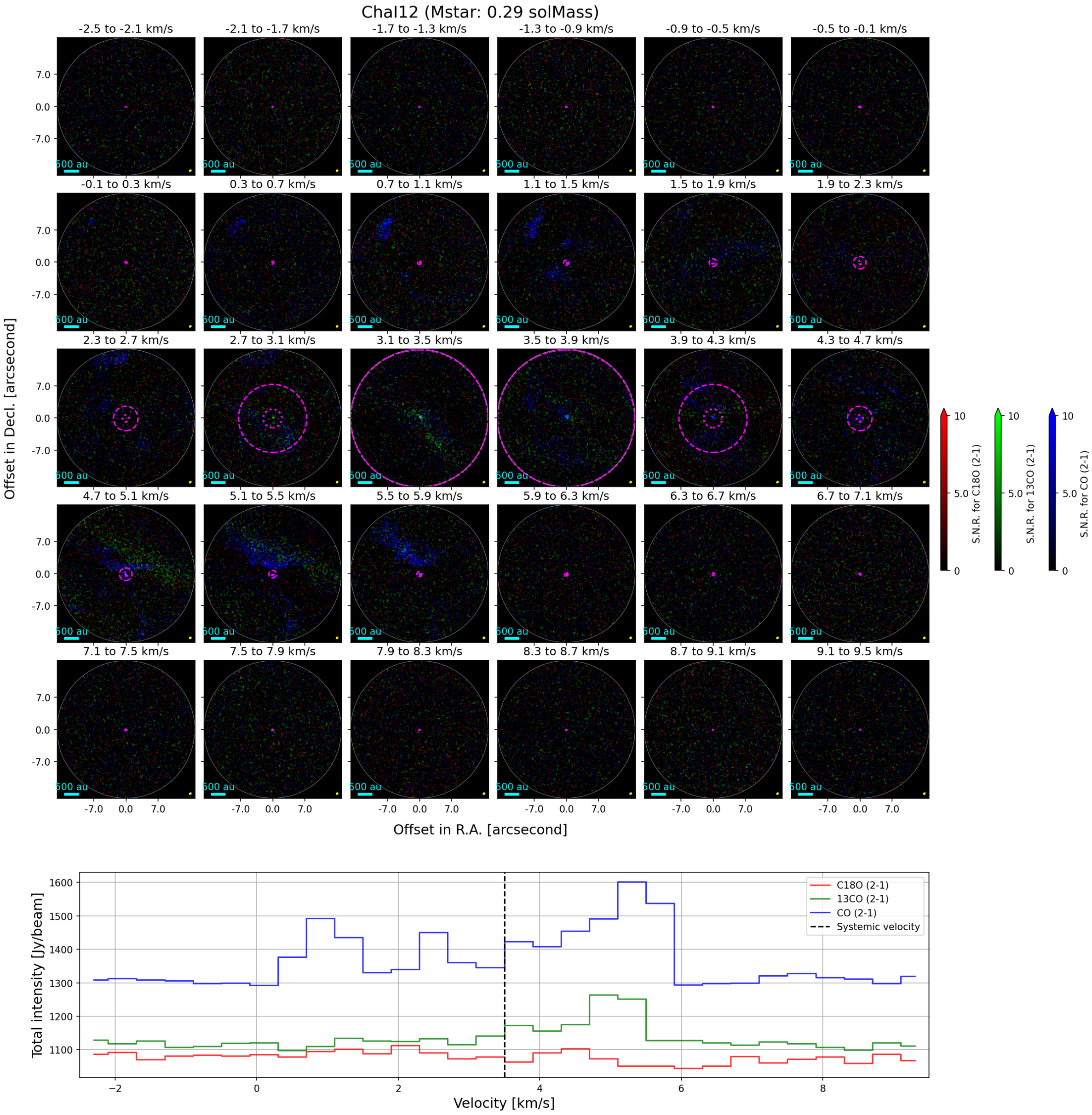

Figure C.11: CO (2–1), ^{13}CO (2–1), and C^{18}O (2–1) channel maps (top panel) and integrated spectra (bottom panel) for ChaI12. See Figure C.1 for more details.

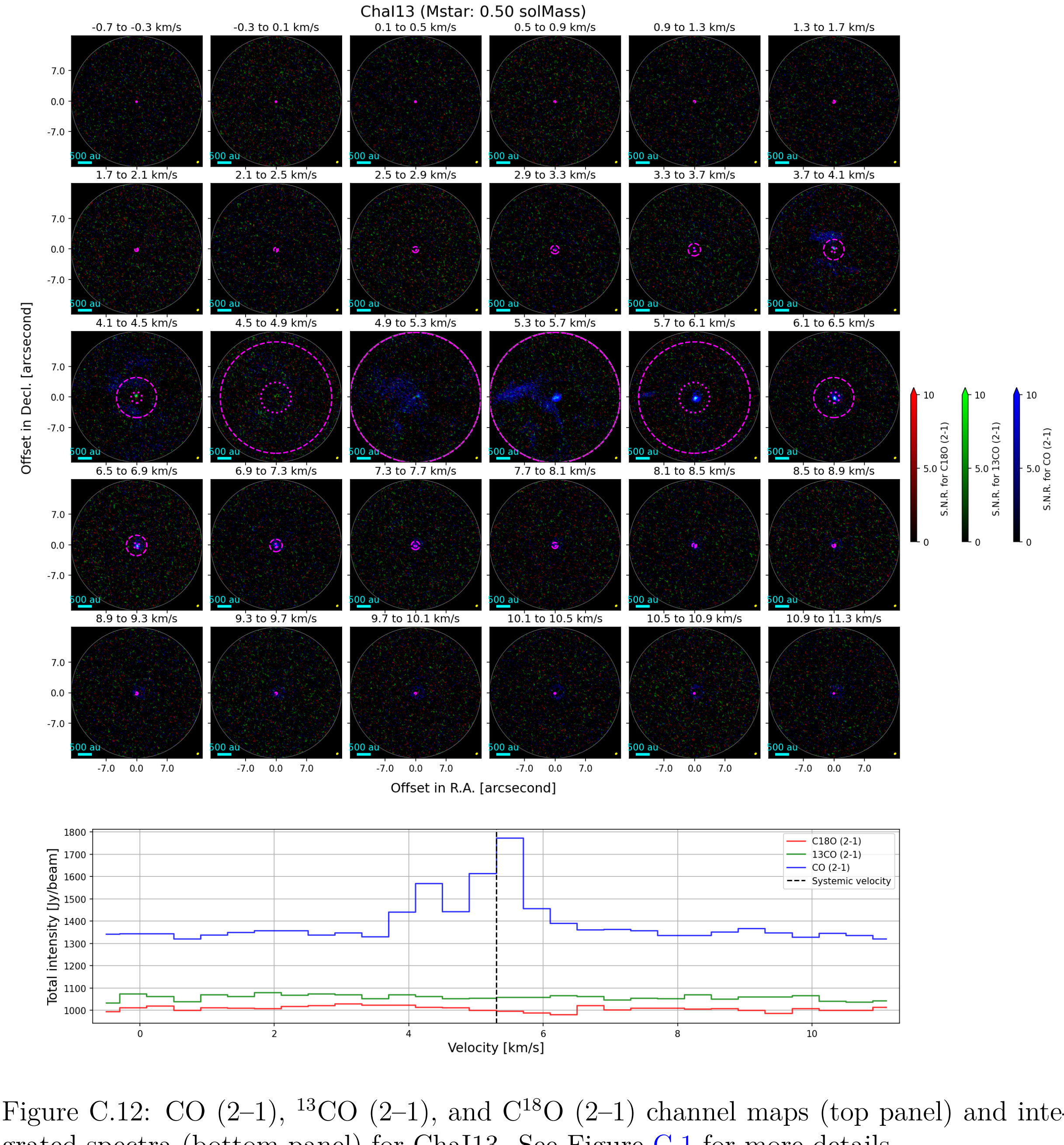

Figure C.12: CO (2–1), ^{13}CO (2–1), and C^{18}O (2–1) channel maps (top panel) and integrated spectra (bottom panel) for ChaI13. See Figure C.1 for more details.

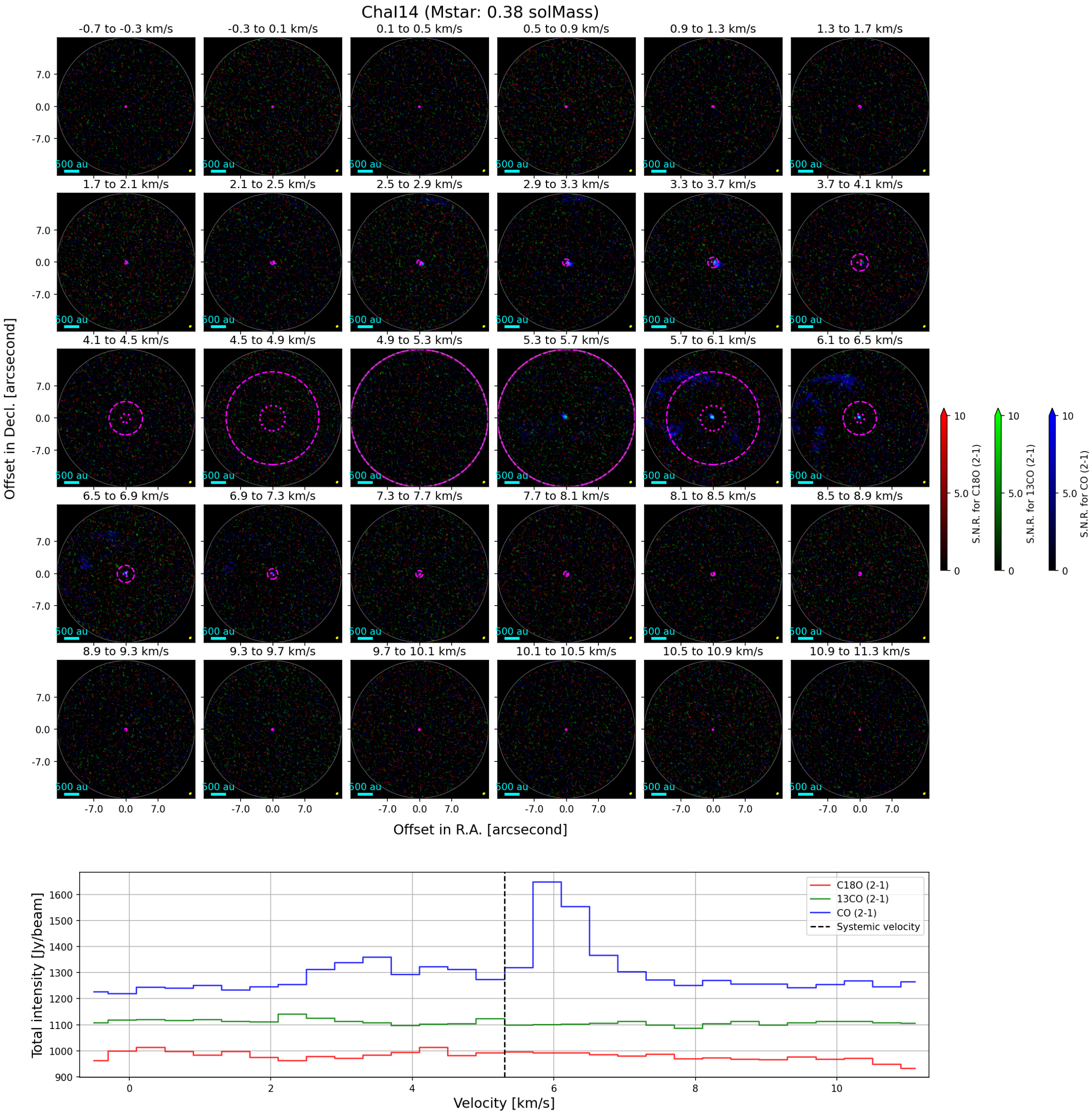

Figure C.13: CO (2–1), ^{13}CO (2–1), and C^{18}O (2–1) channel maps (top panel) and integrated spectra (bottom panel) for ChaI14. See Figure C.1 for more details.

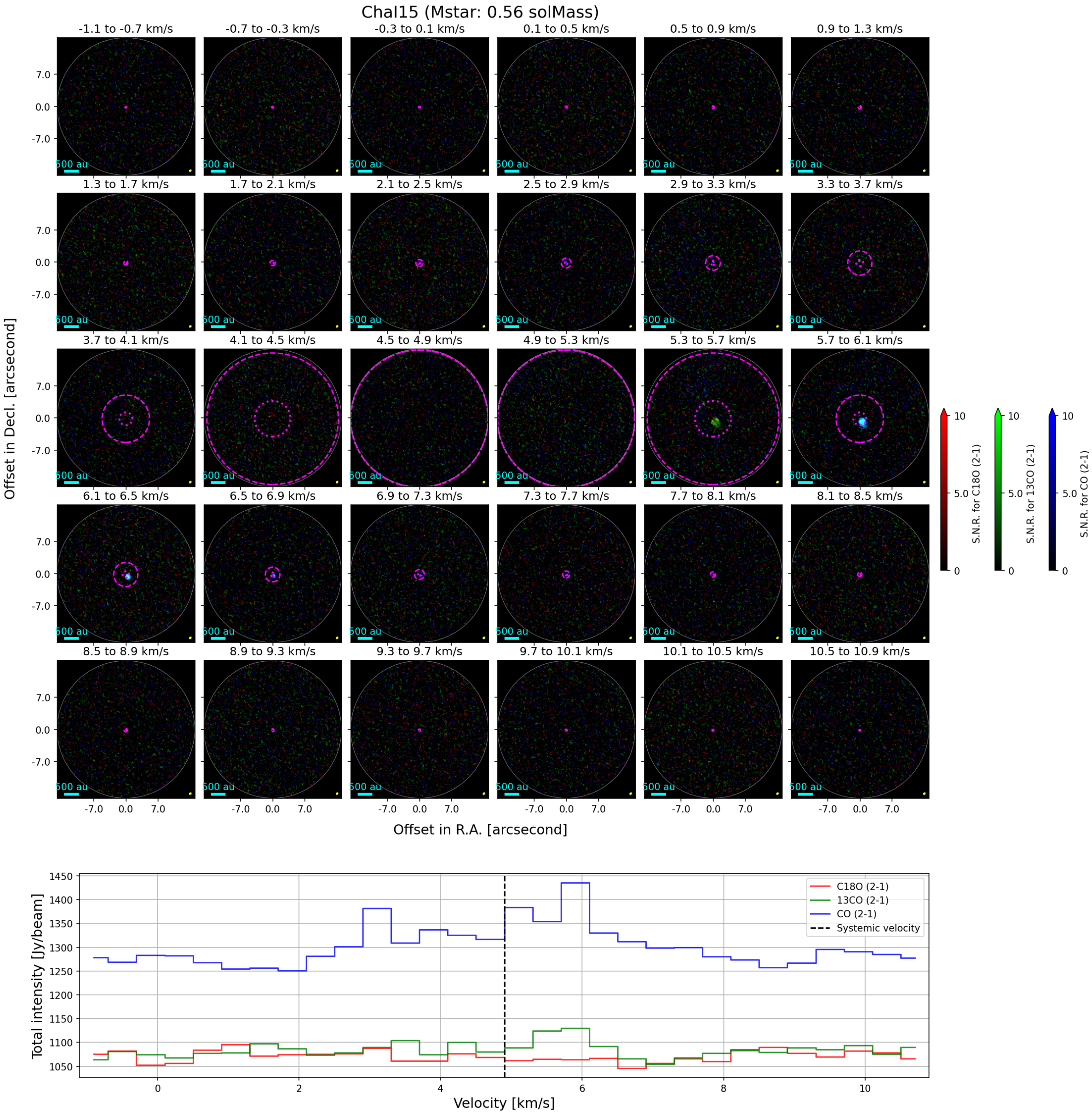

Figure C.14: CO (2–1), ^{13}CO (2–1), and C^{18}O (2–1) channel maps (top panel) and integrated spectra (bottom panel) for ChaI15. See Figure C.1 for more details.

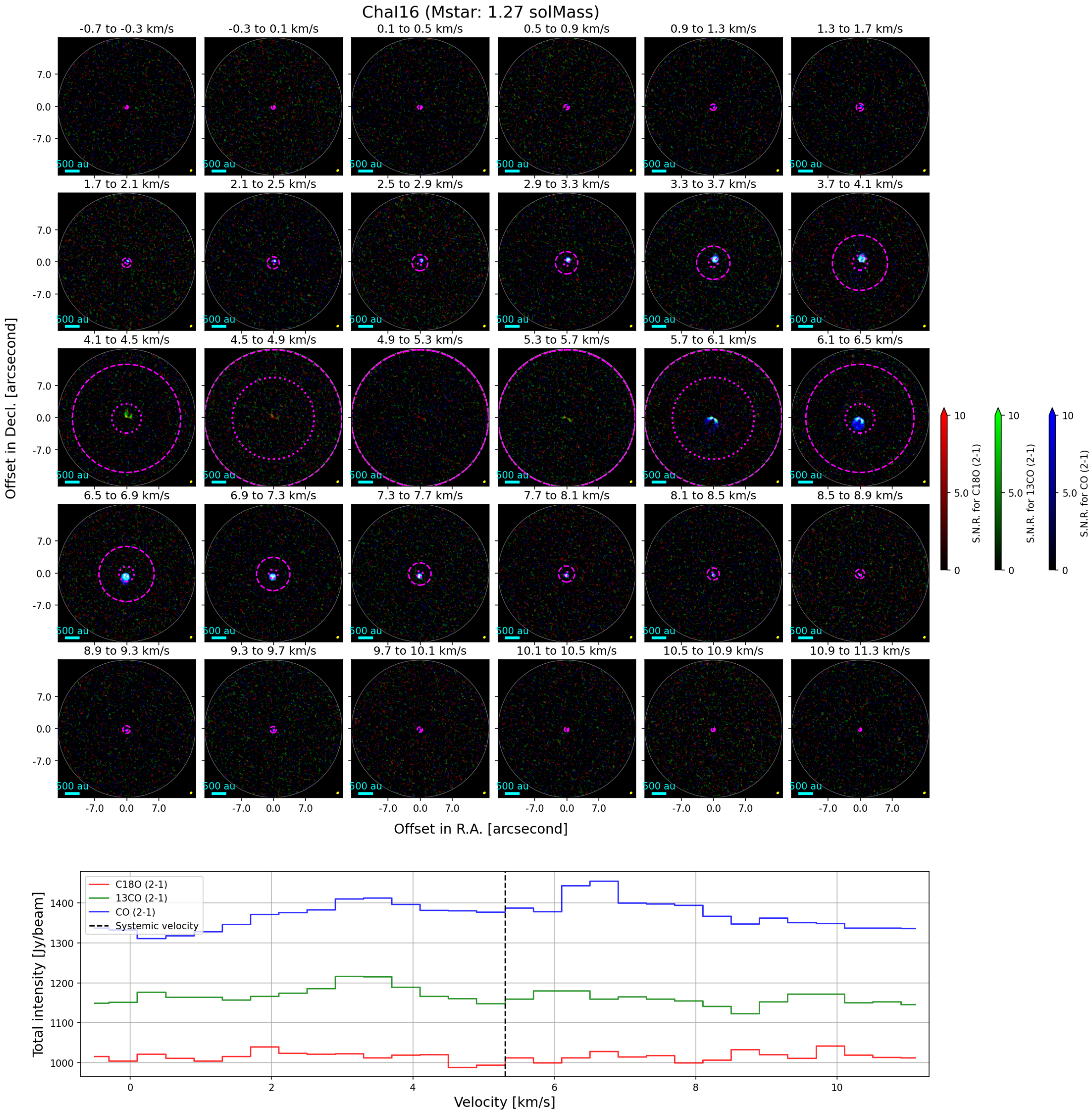

Figure C.15: CO (2–1), ^{13}CO (2–1), and C^{18}O (2–1) channel maps (top panel) and integrated spectra (bottom panel) for ChaI16. See Figure C.1 for more details.

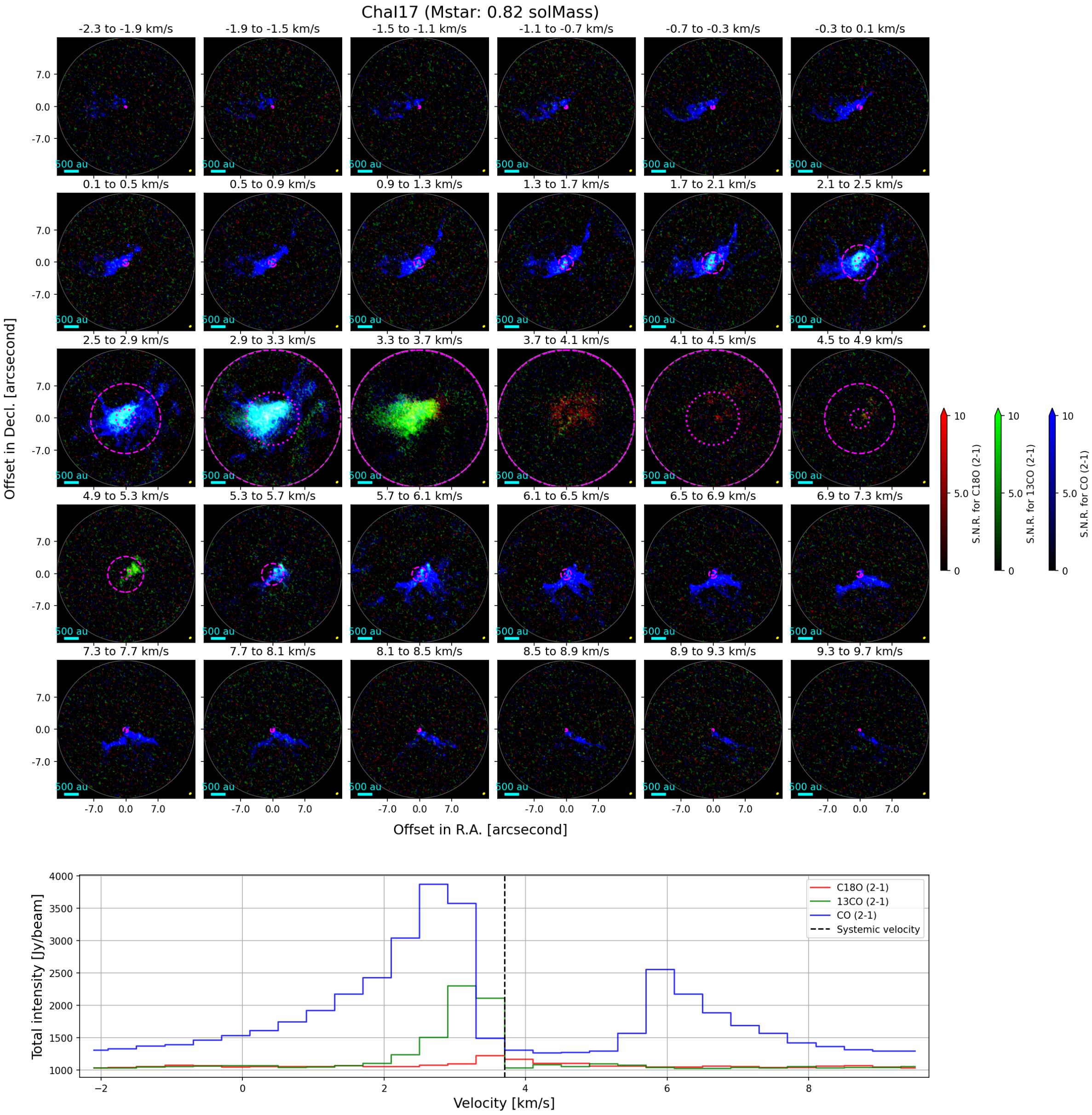

Figure C.16: CO (2–1), ^{13}CO (2–1), and C^{18}O (2–1) channel maps (top panel) and integrated spectra (bottom panel) for ChaI17. See Figure C.1 for more details.

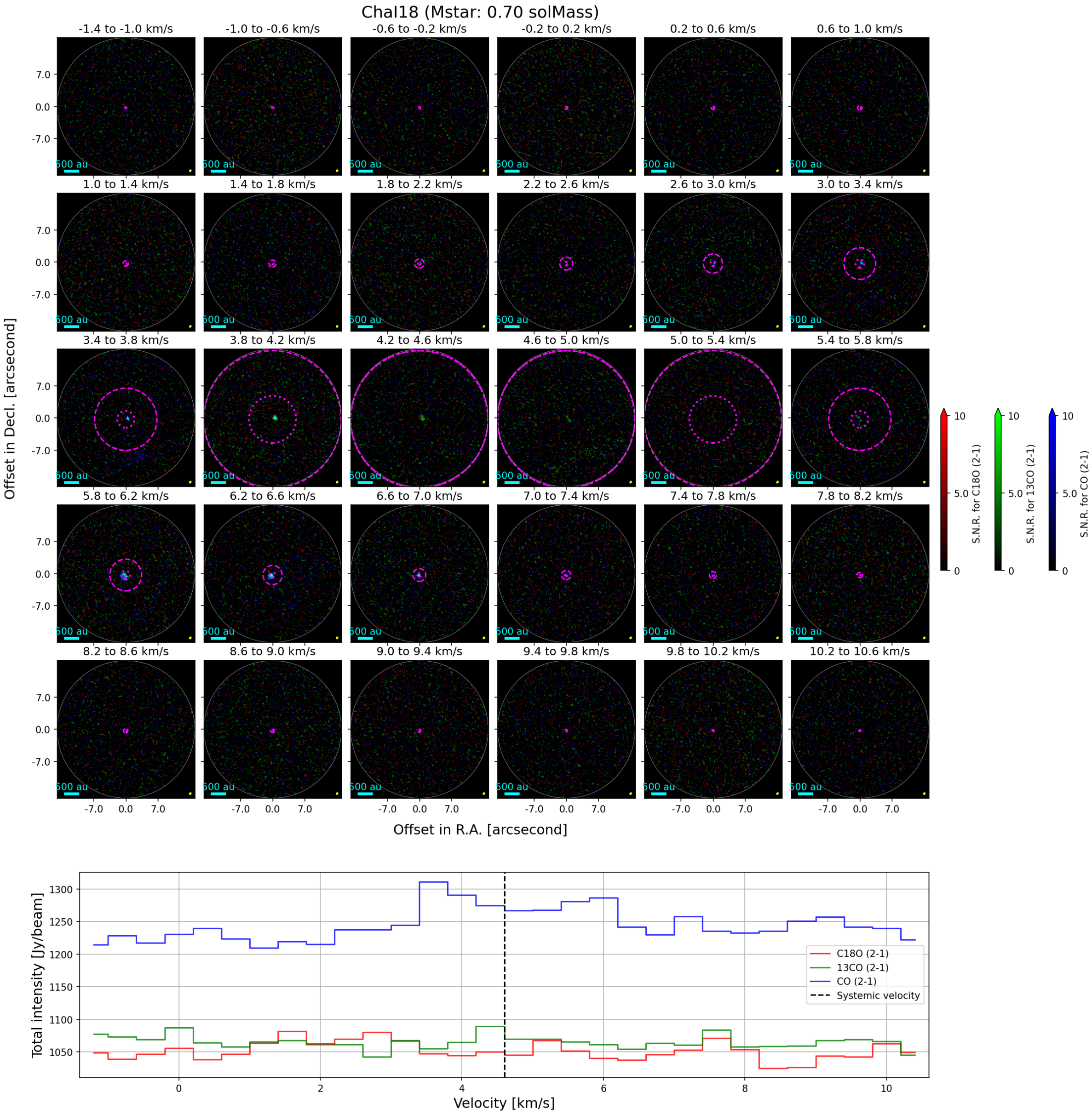

Figure C.17: CO (2–1), ^{13}CO (2–1), and C^{18}O (2–1) channel maps (top panel) and integrated spectra (bottom panel) for ChaI18. See Figure C.1 for more details.

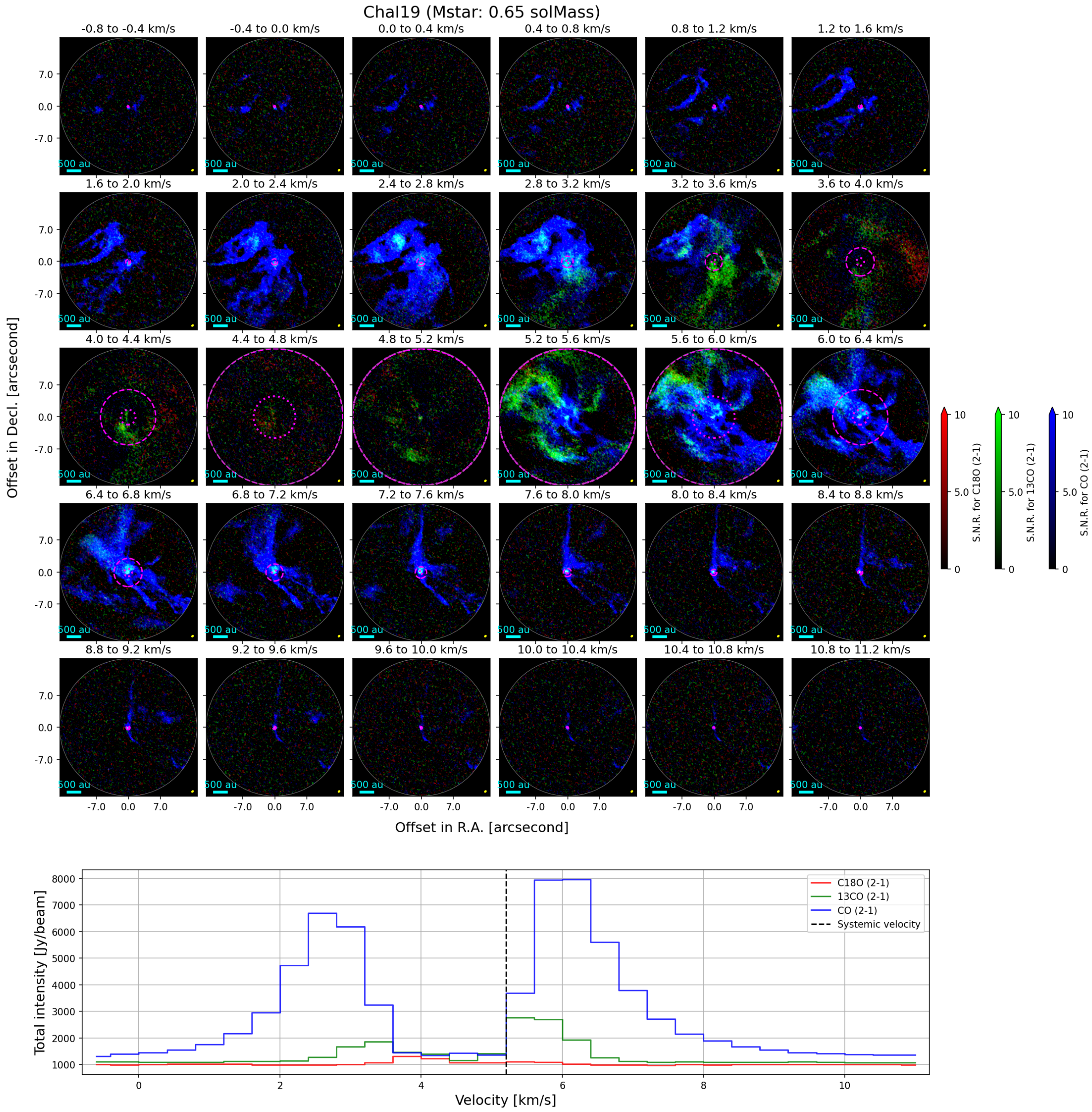

Figure C.18: CO (2–1), ^{13}CO (2–1), and C^{18}O (2–1) channel maps (top panel) and integrated spectra (bottom panel) for ChaI19. See Figure C.1 for more details.

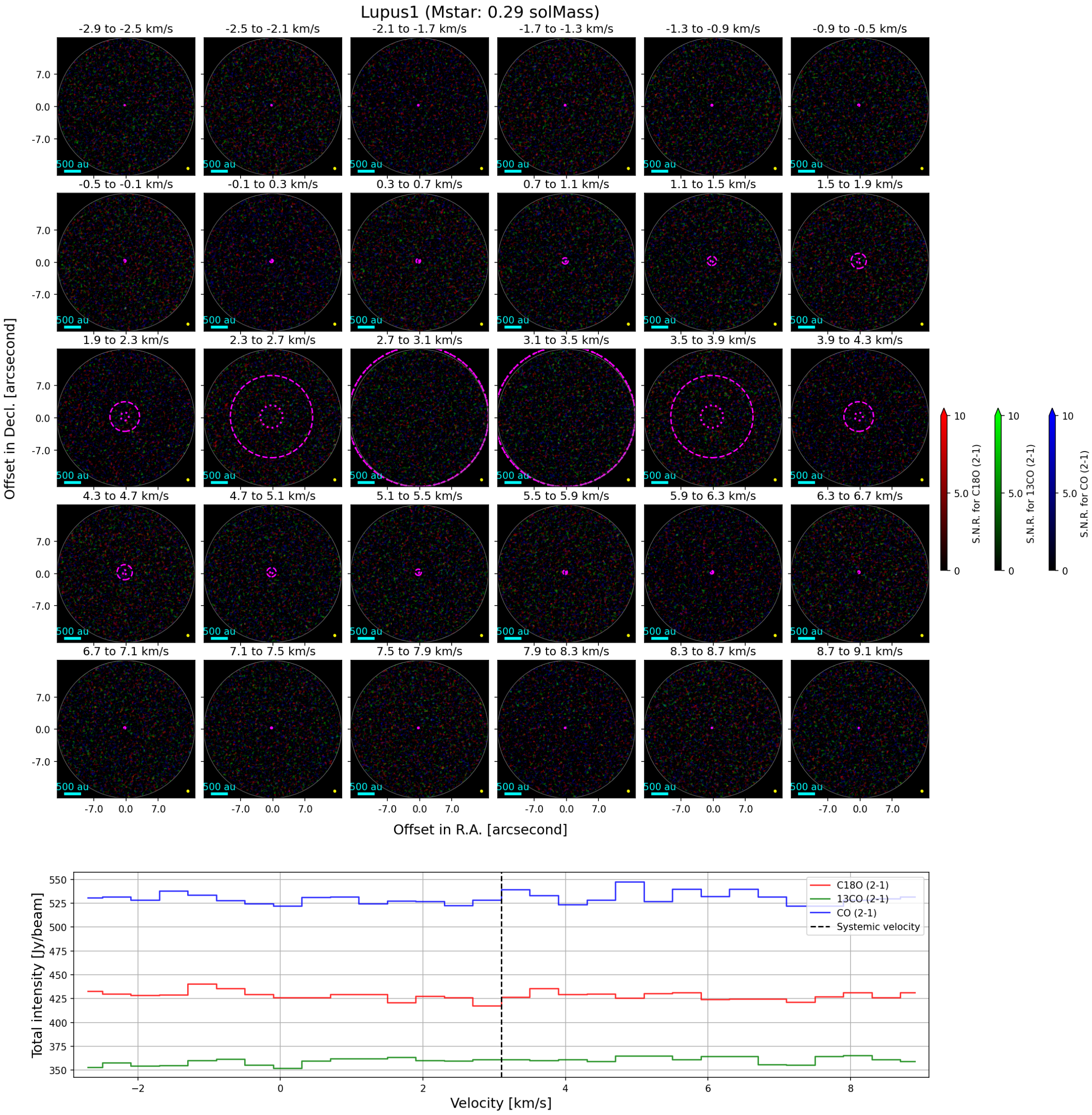

Figure C.19: CO (2–1), ^{13}CO (2–1), and C^{18}O (2–1) channel maps (top panel) and integrated spectra (bottom panel) for Lupus1. See Figure C.1 for more details.

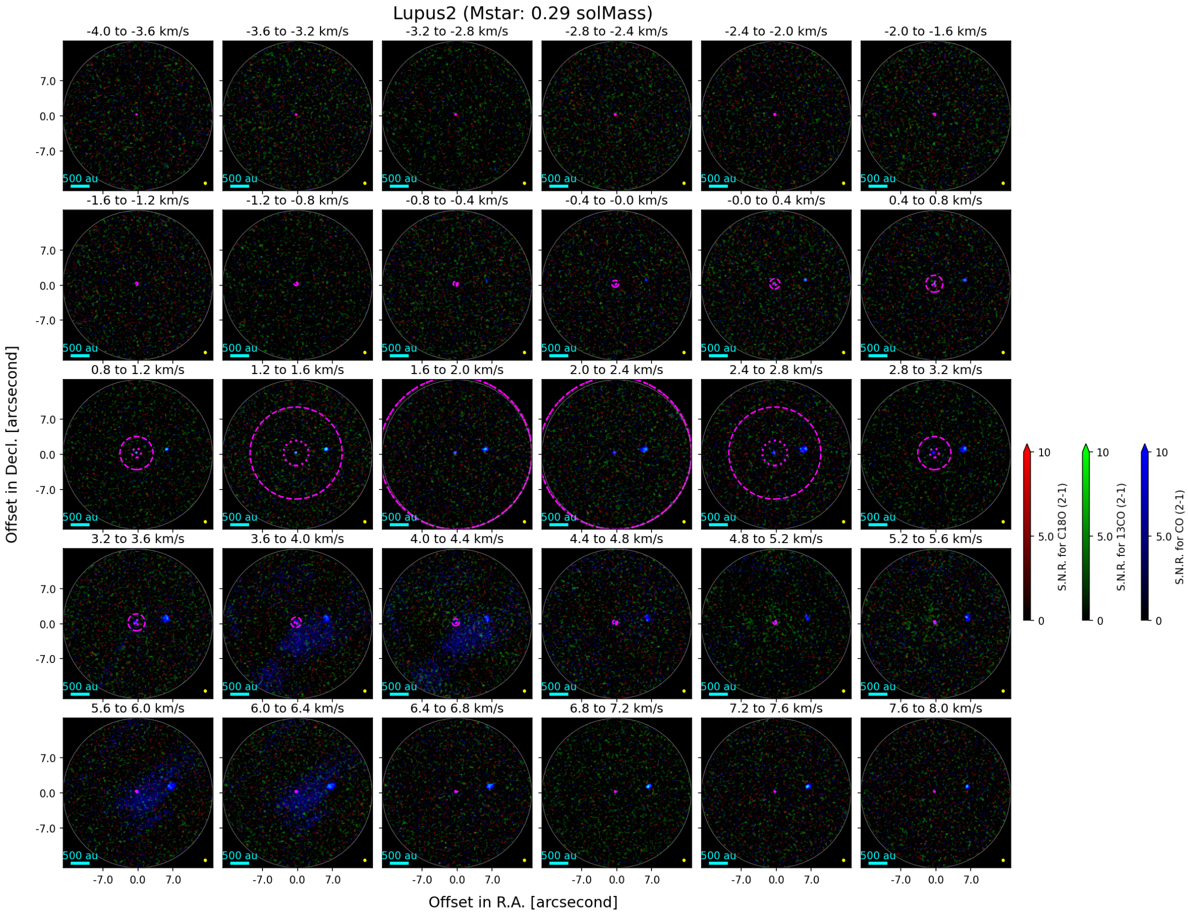

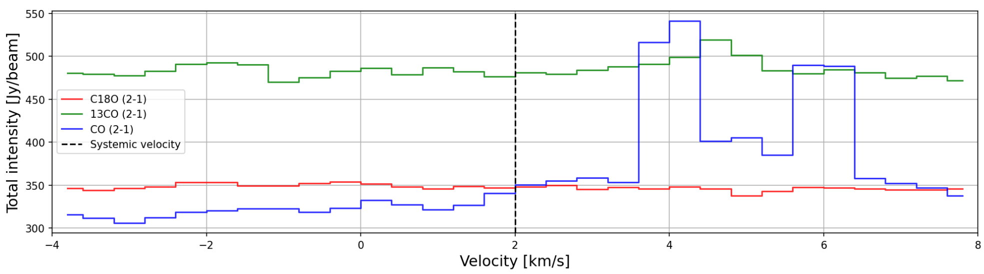

Figure C.20: CO (2–1), ^{13}CO (2–1), and C^{18}O (2–1) channel maps (top panel) and integrated spectra (bottom panel) for Lupus2. See Figure C.1 for more details.

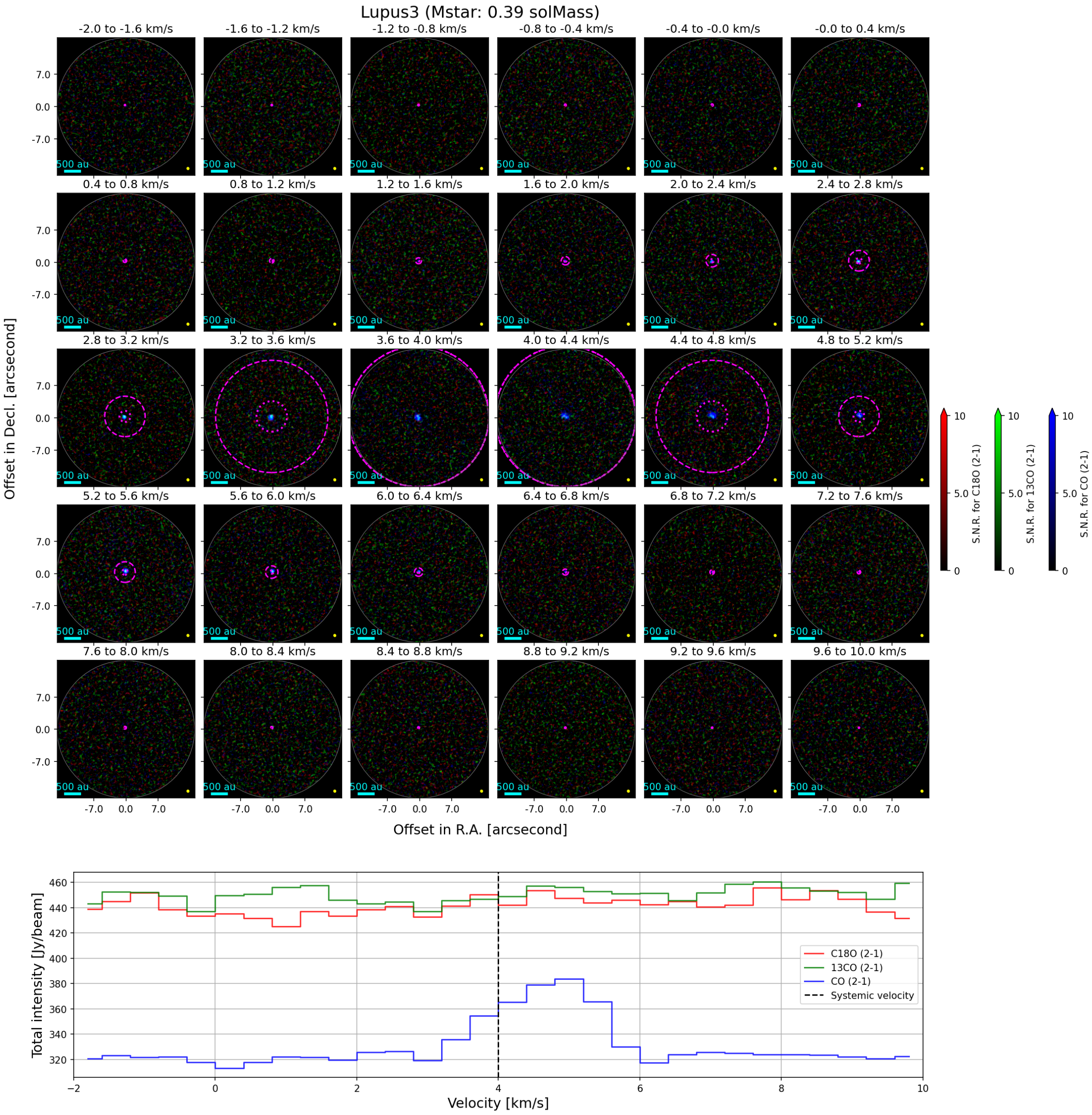

Figure C.21: CO (2–1), ^{13}CO (2–1), and C^{18}O (2–1) channel maps (top panel) and integrated spectra (bottom panel) for Lupus3. See Figure C.1 for more details.

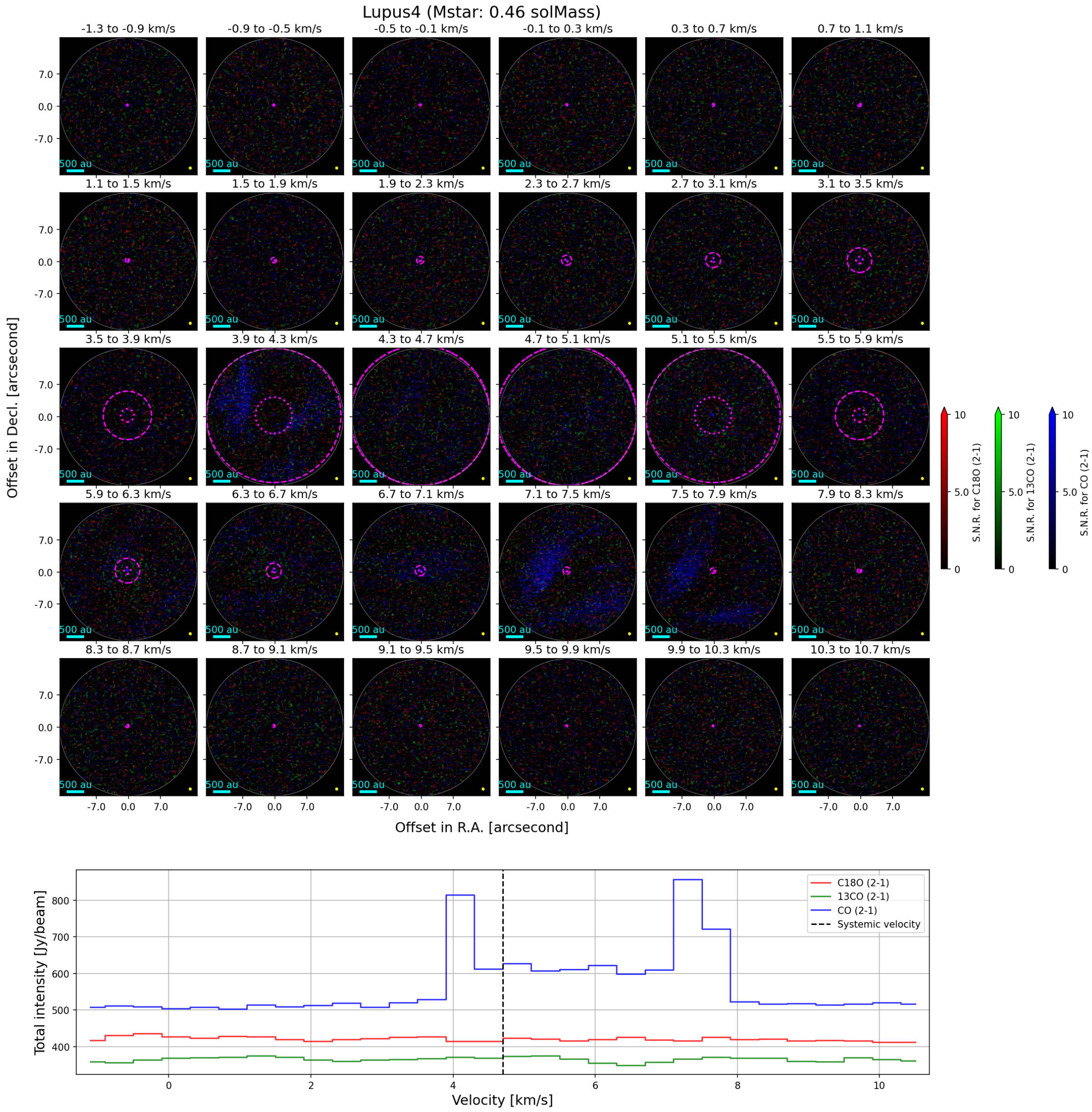

Figure C.22: CO (2–1), ^{13}CO (2–1), and C^{18}O (2–1) channel maps (top panel) and integrated spectra (bottom panel) for Lupus4. See Figure C.1 for more details.

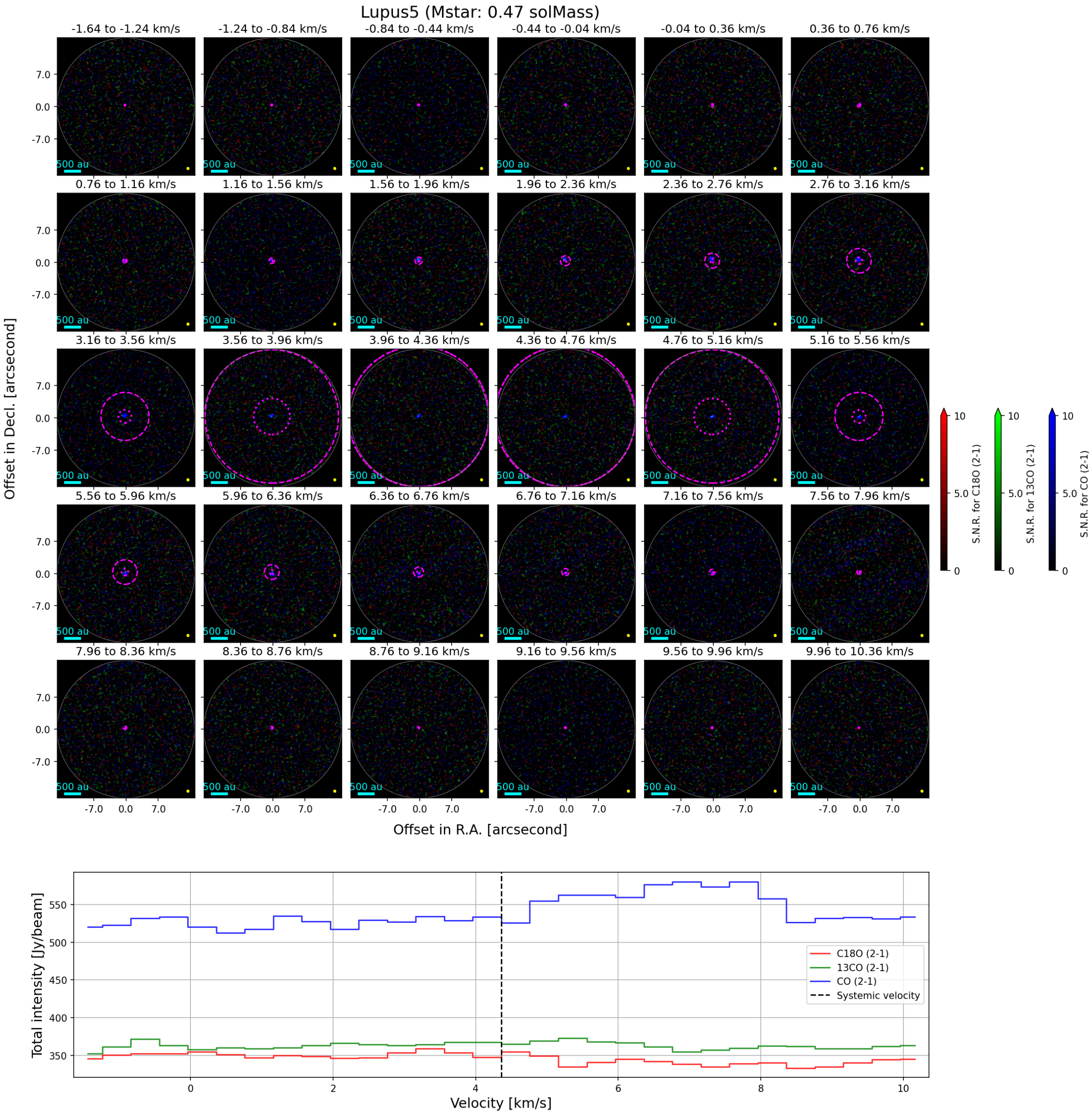

Figure C.23: CO (2–1), ^{13}CO (2–1), and C^{18}O (2–1) channel maps (top panel) and integrated spectra (bottom panel) for Lupus5. See Figure C.1 for more details.

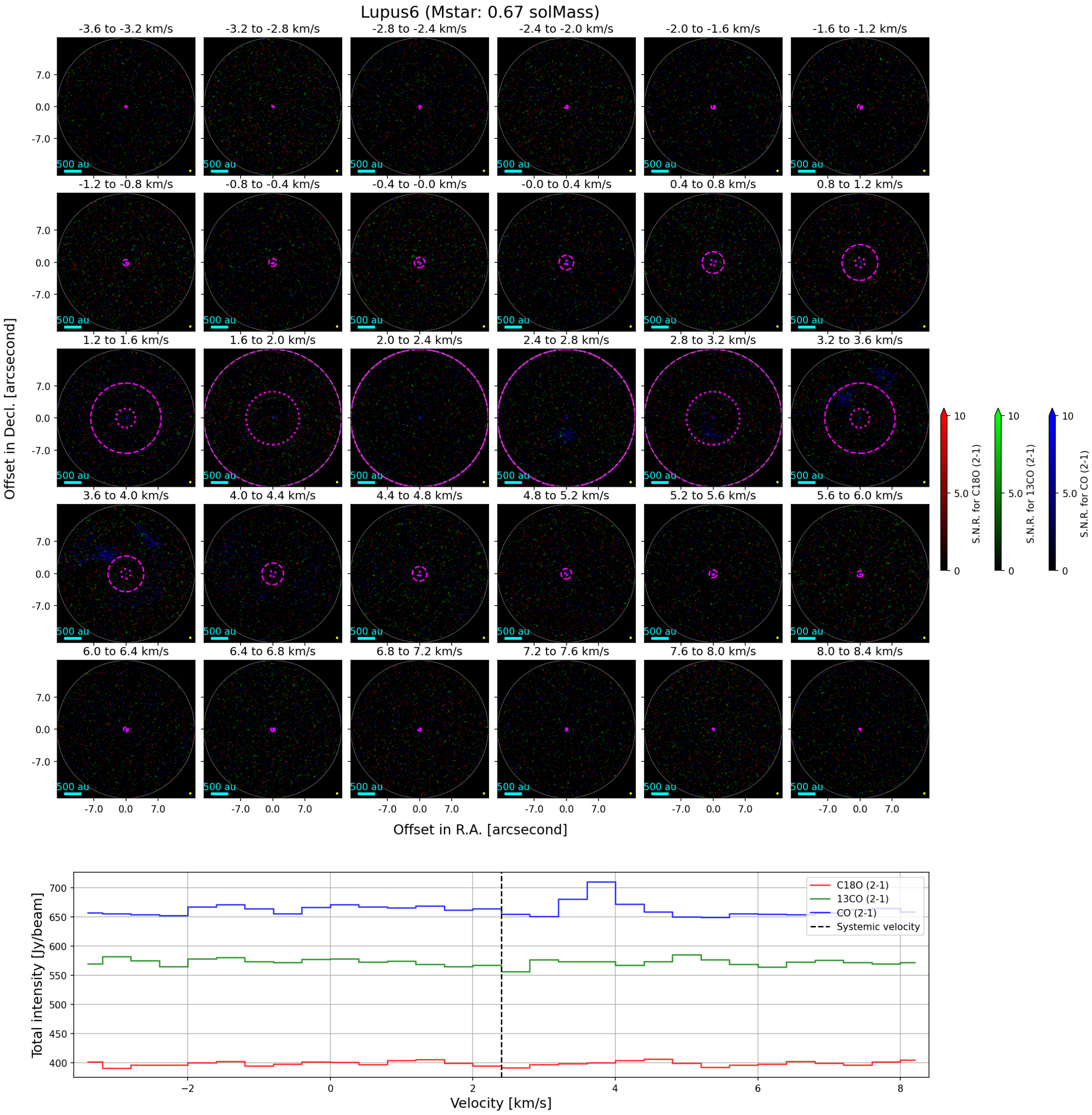

Figure C.24: CO (2–1), ^{13}CO (2–1), and C^{18}O (2–1) channel maps (top panel) and integrated spectra (bottom panel) for Lupus6. See Figure C.1 for more details.

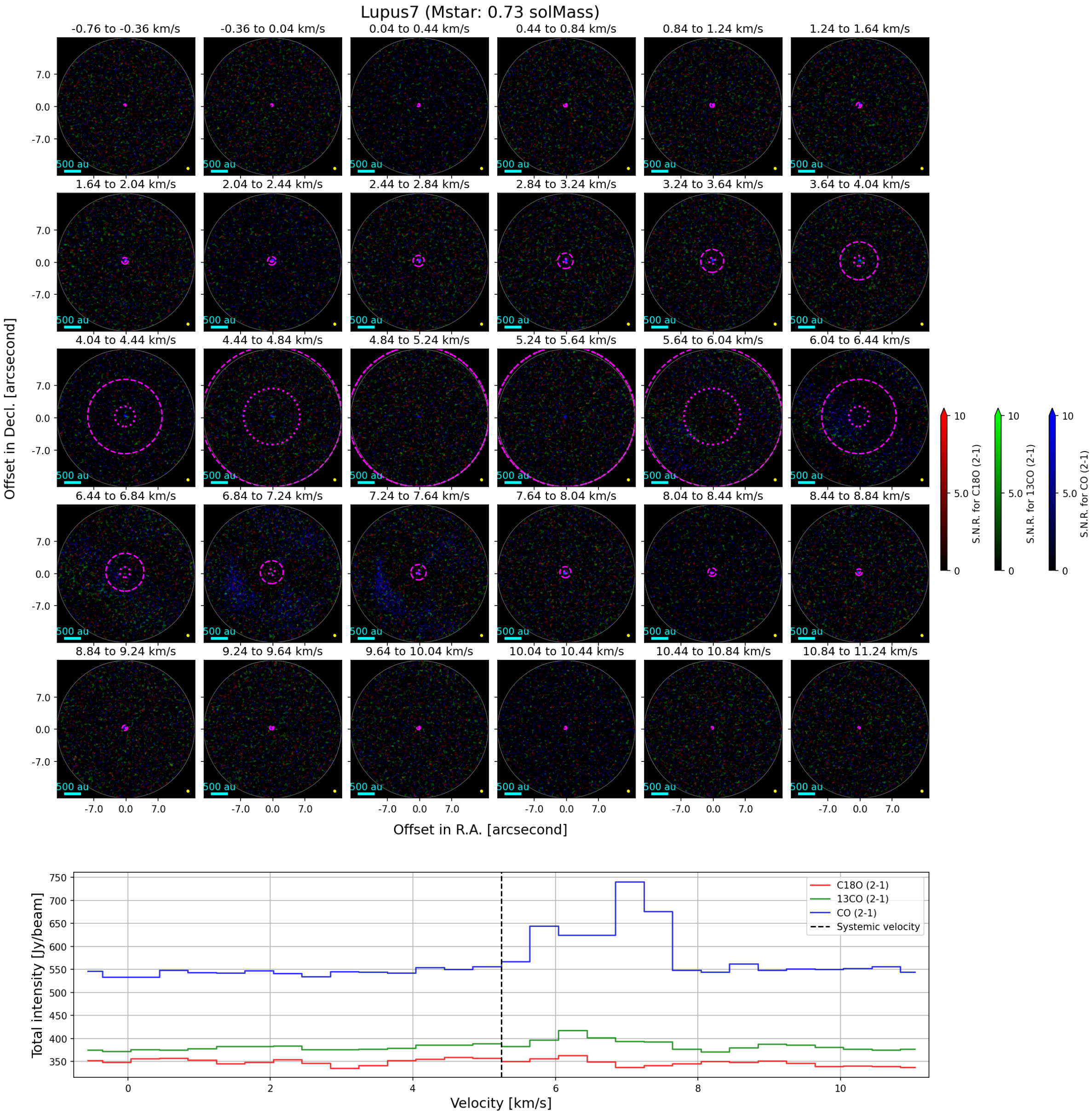

Figure C.25: CO (2–1), ^{13}CO (2–1), and C^{18}O (2–1) channel maps (top panel) and integrated spectra (bottom panel) for Lupus7. See Figure C.1 for more details.

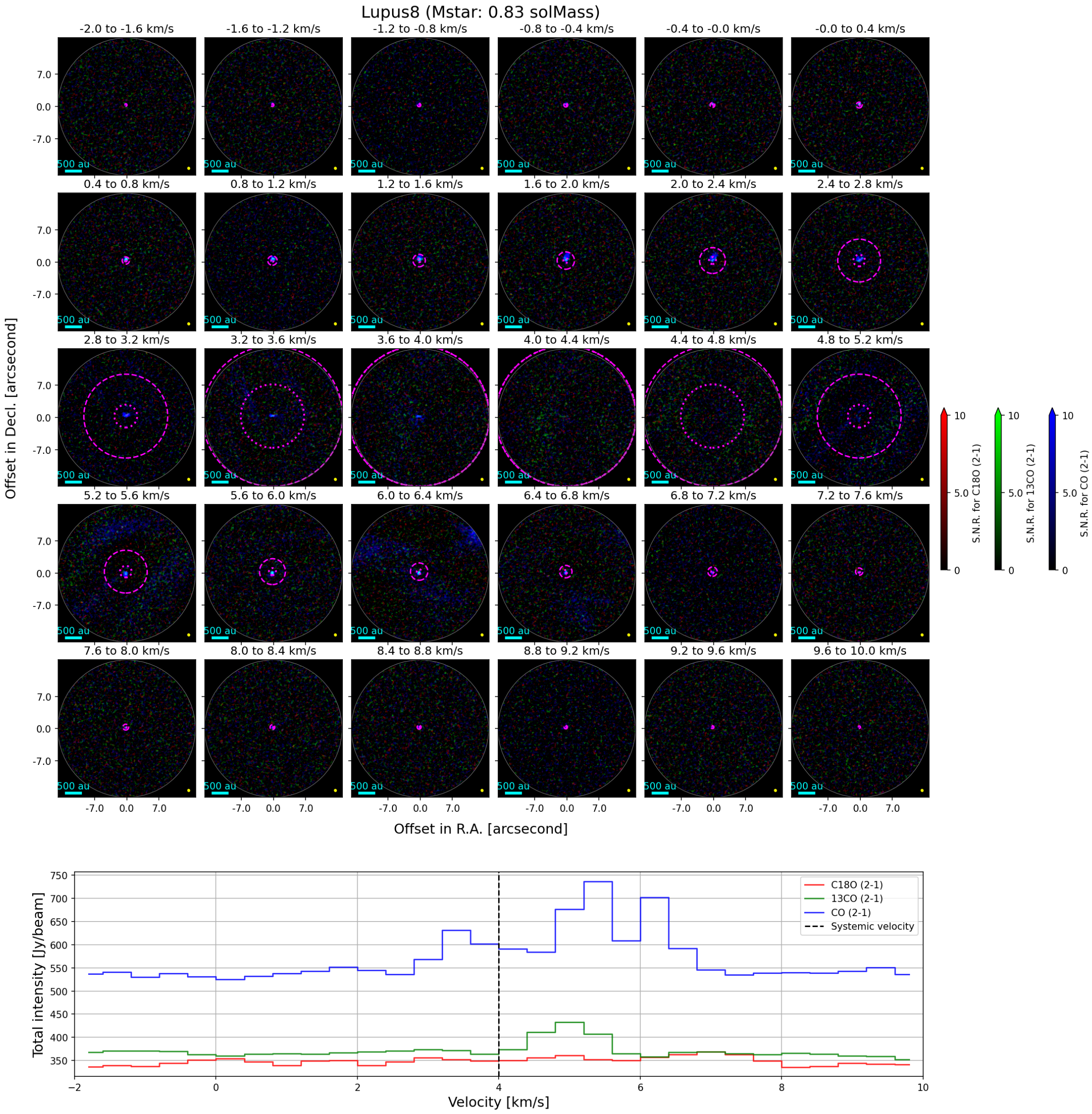

Figure C.26: CO (2–1), ^{13}CO (2–1), and C^{18}O (2–1) channel maps (top panel) and integrated spectra (bottom panel) for Lupus8. See Figure C.1 for more details.

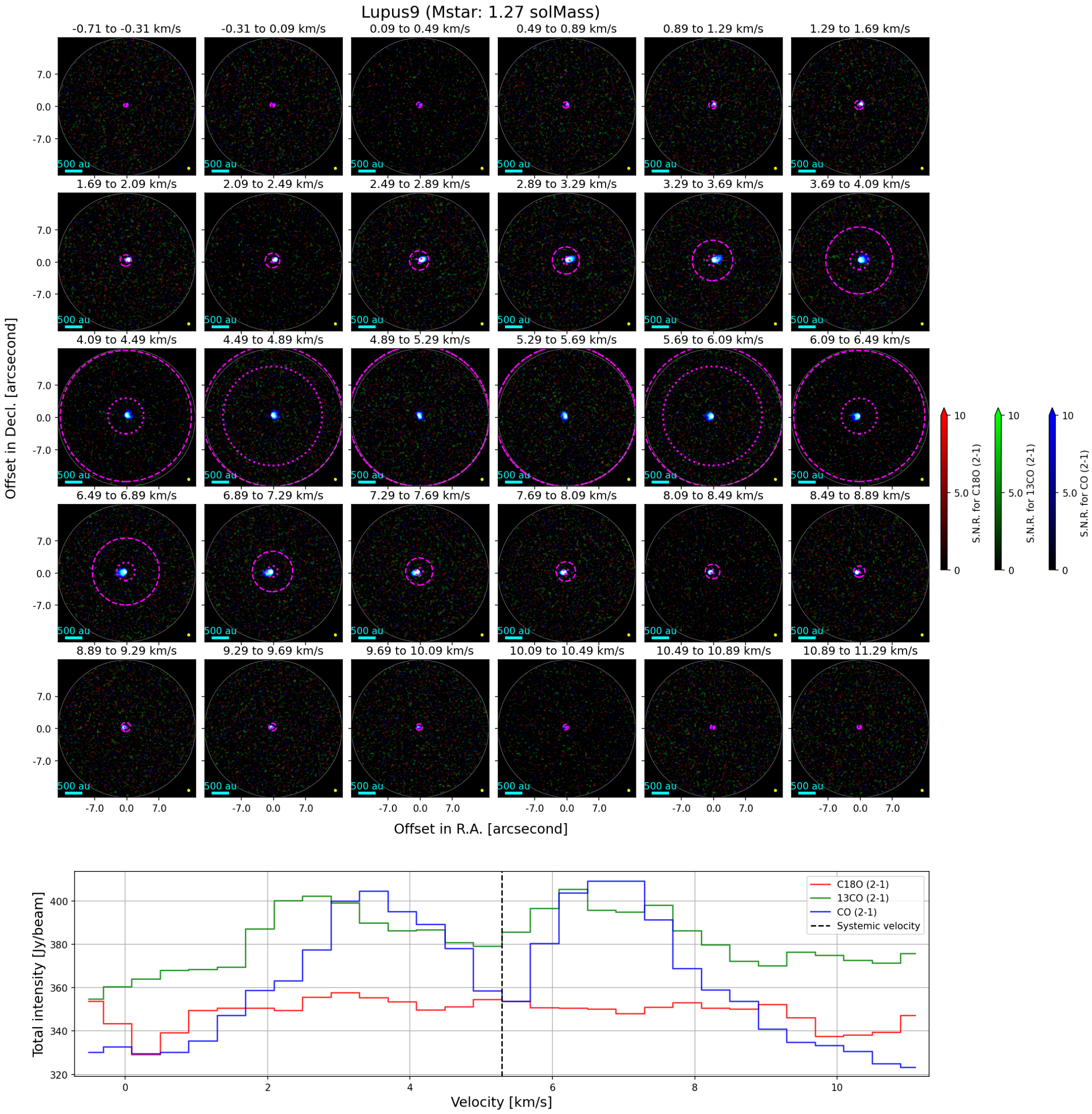

Figure C.27: CO (2–1), ^{13}CO (2–1), and C^{18}O (2–1) channel maps (top panel) and integrated spectra (bottom panel) for Lupus9. See Figure C.1 for more details.

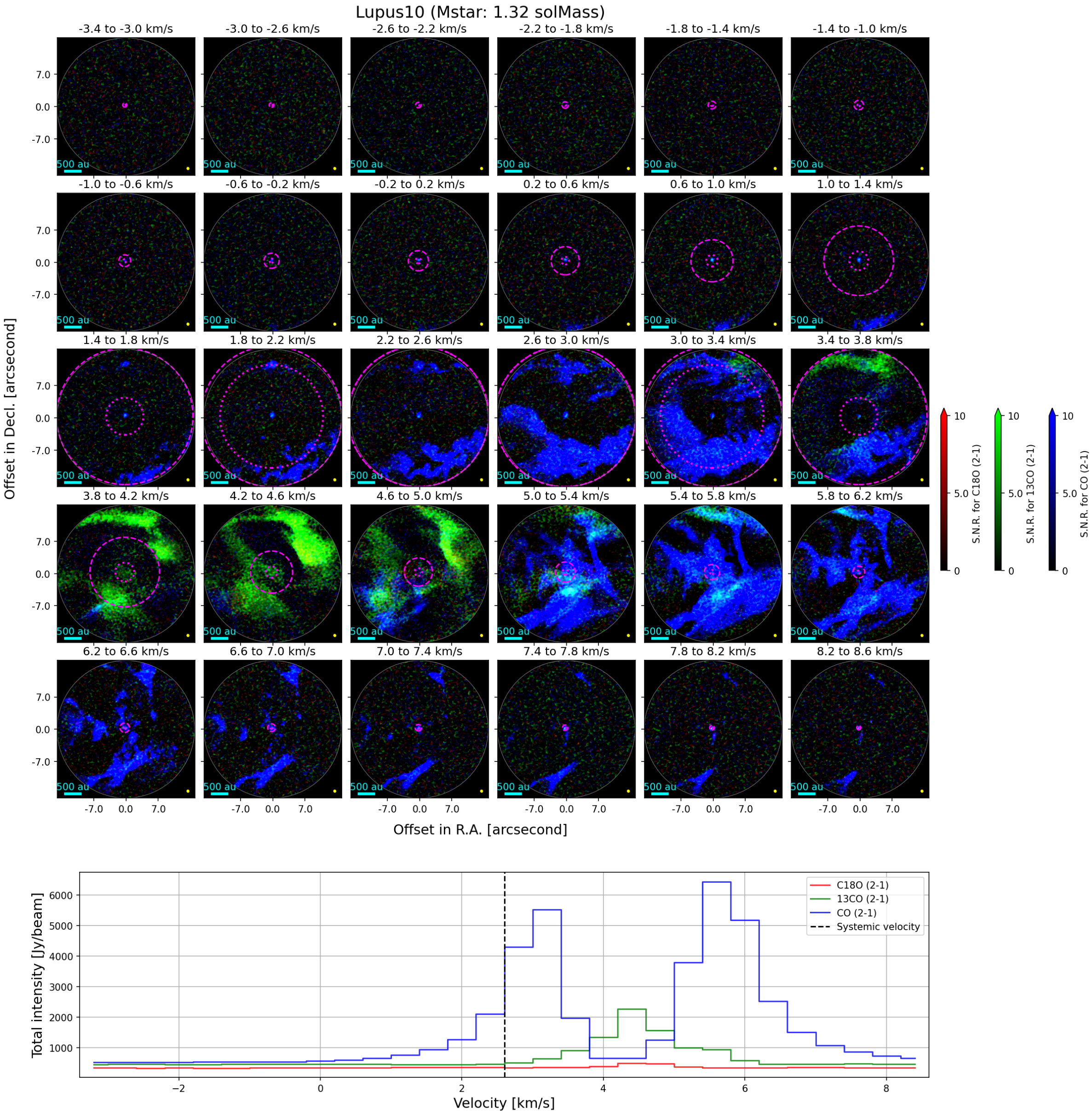

Figure C.28: CO (2–1), ^{13}CO (2–1), and C^{18}O (2–1) channel maps (top panel) and integrated spectra (bottom panel) for Lupus10. See Figure C.1 for more details.

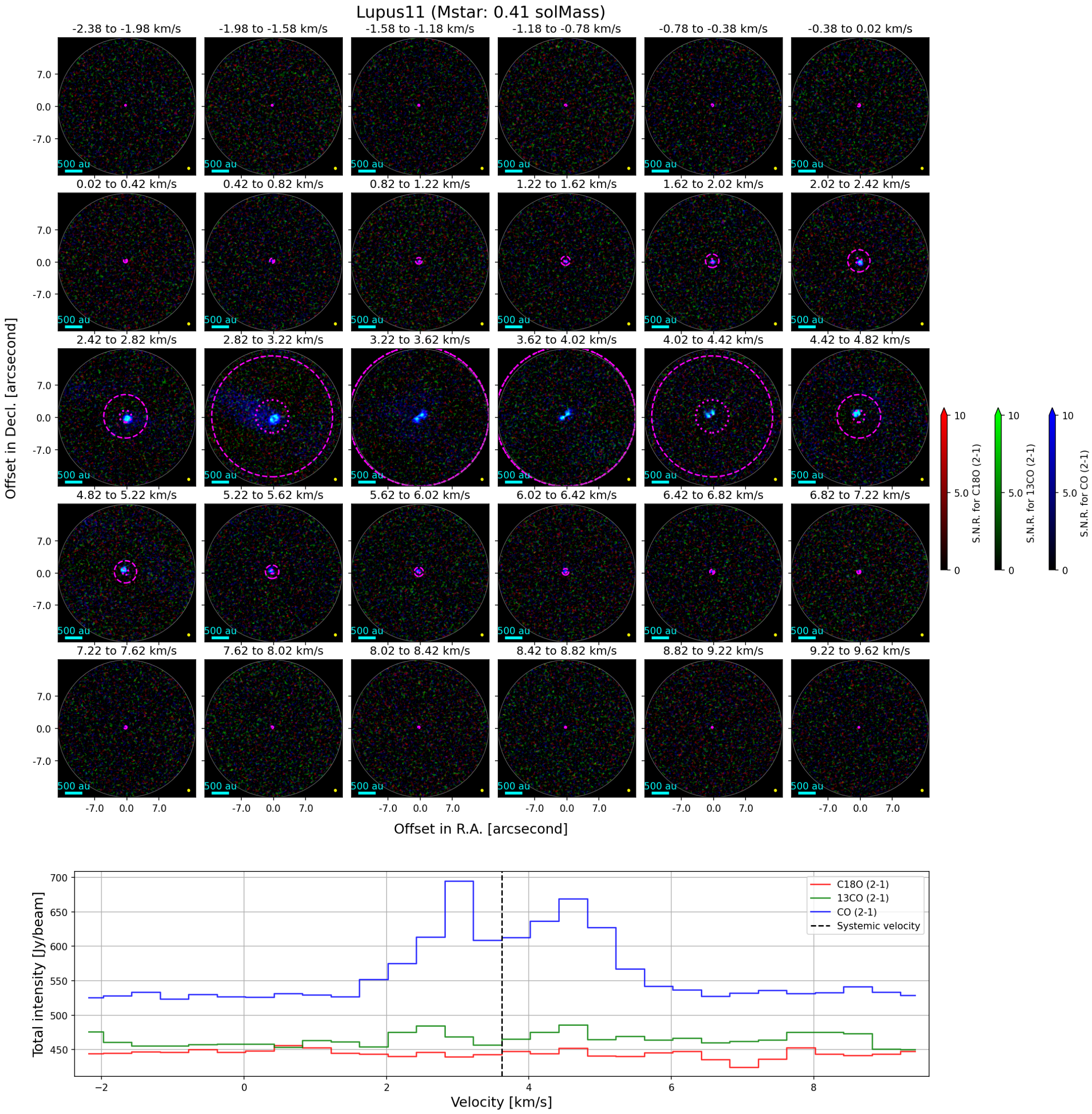

Figure C.29: CO (2–1), ^{13}CO (2–1), and C^{18}O (2–1) channel maps (top panel) and integrated spectra (bottom panel) for Lupus11. See Figure C.1 for more details.

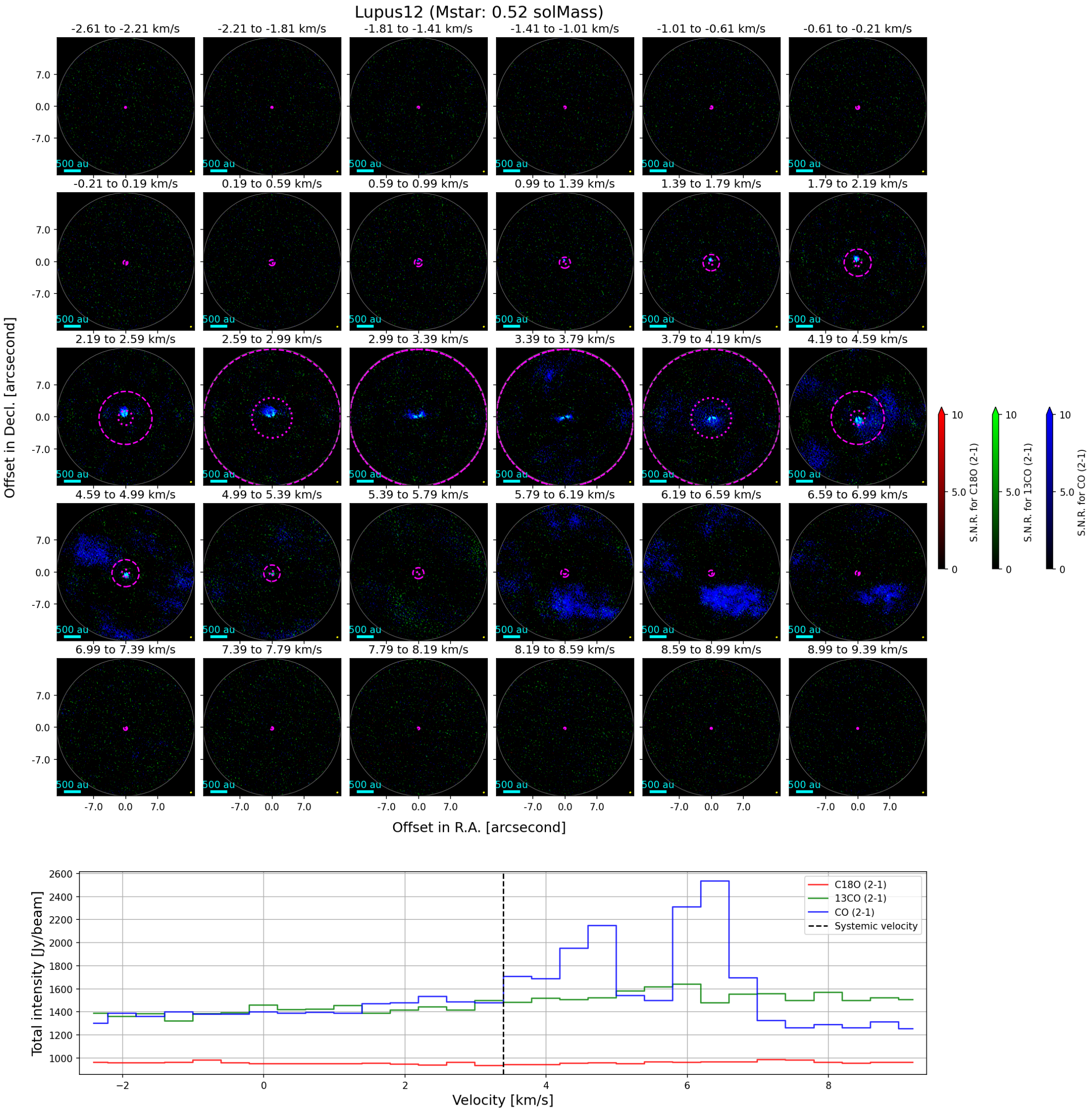

Figure C.30: CO (2–1), ^{13}CO (2–1), and C^{18}O (2–1) channel maps (top panel) and integrated spectra (bottom panel) for Lupus12. See Figure C.1 for more details.

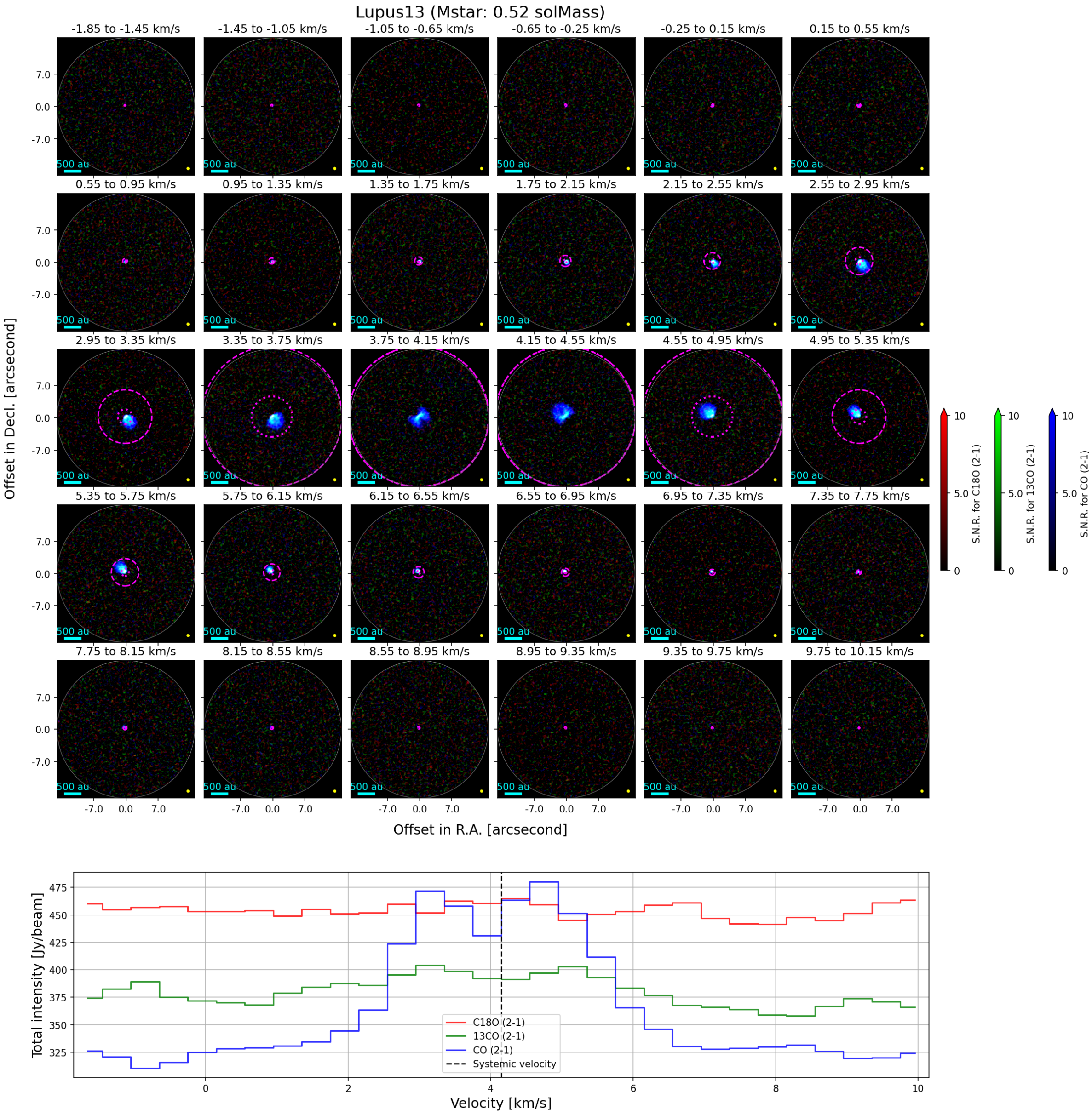

Figure C.31: CO (2–1), ^{13}CO (2–1), and C^{18}O (2–1) channel maps (top panel) and integrated spectra (bottom panel) for Lupus13. See Figure C.1 for more details.

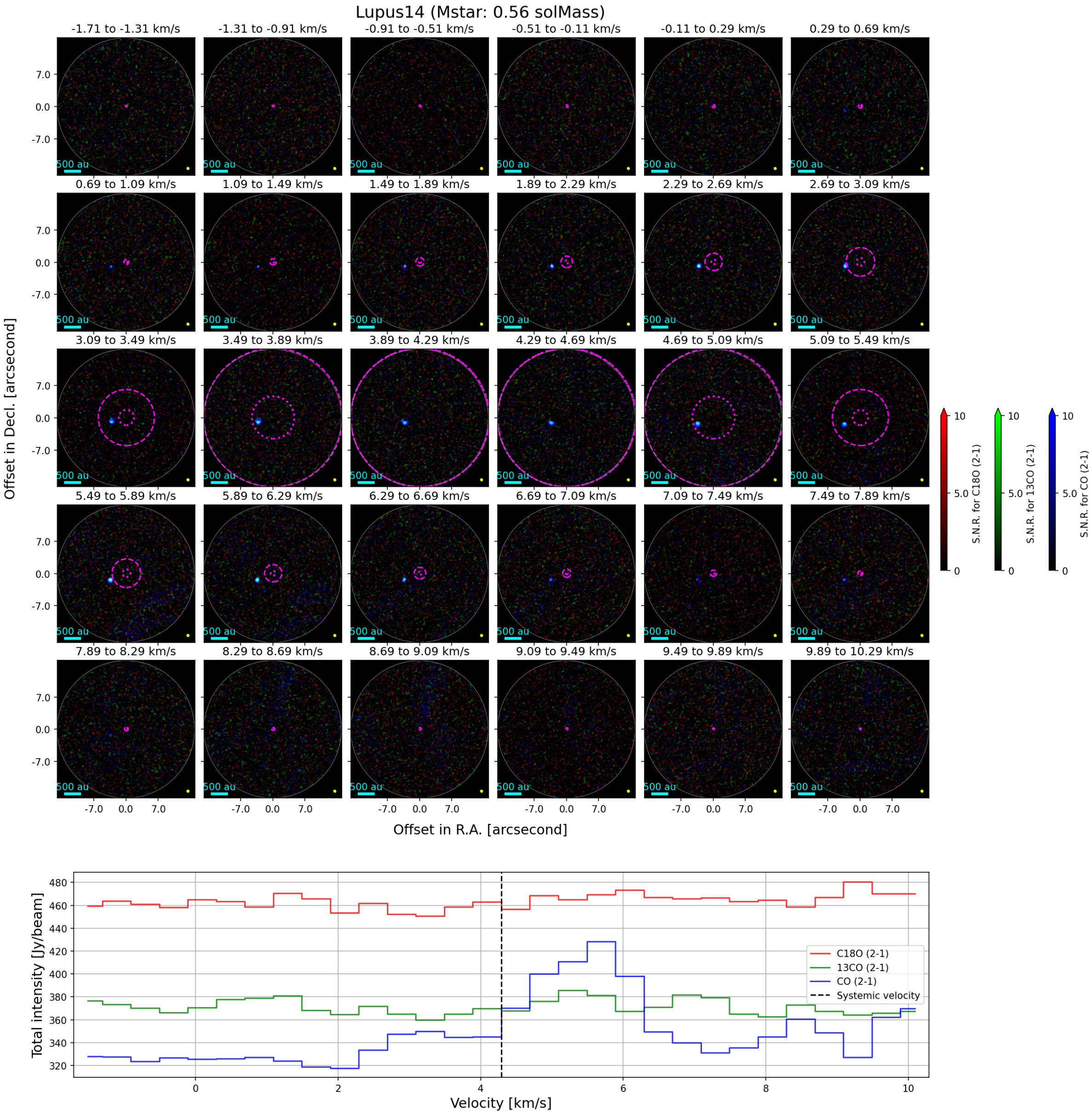

Figure C.32: CO (2–1), ^{13}CO (2–1), and C^{18}O (2–1) channel maps (top panel) and integrated spectra (bottom panel) for Lupus14. See Figure C.1 for more details.

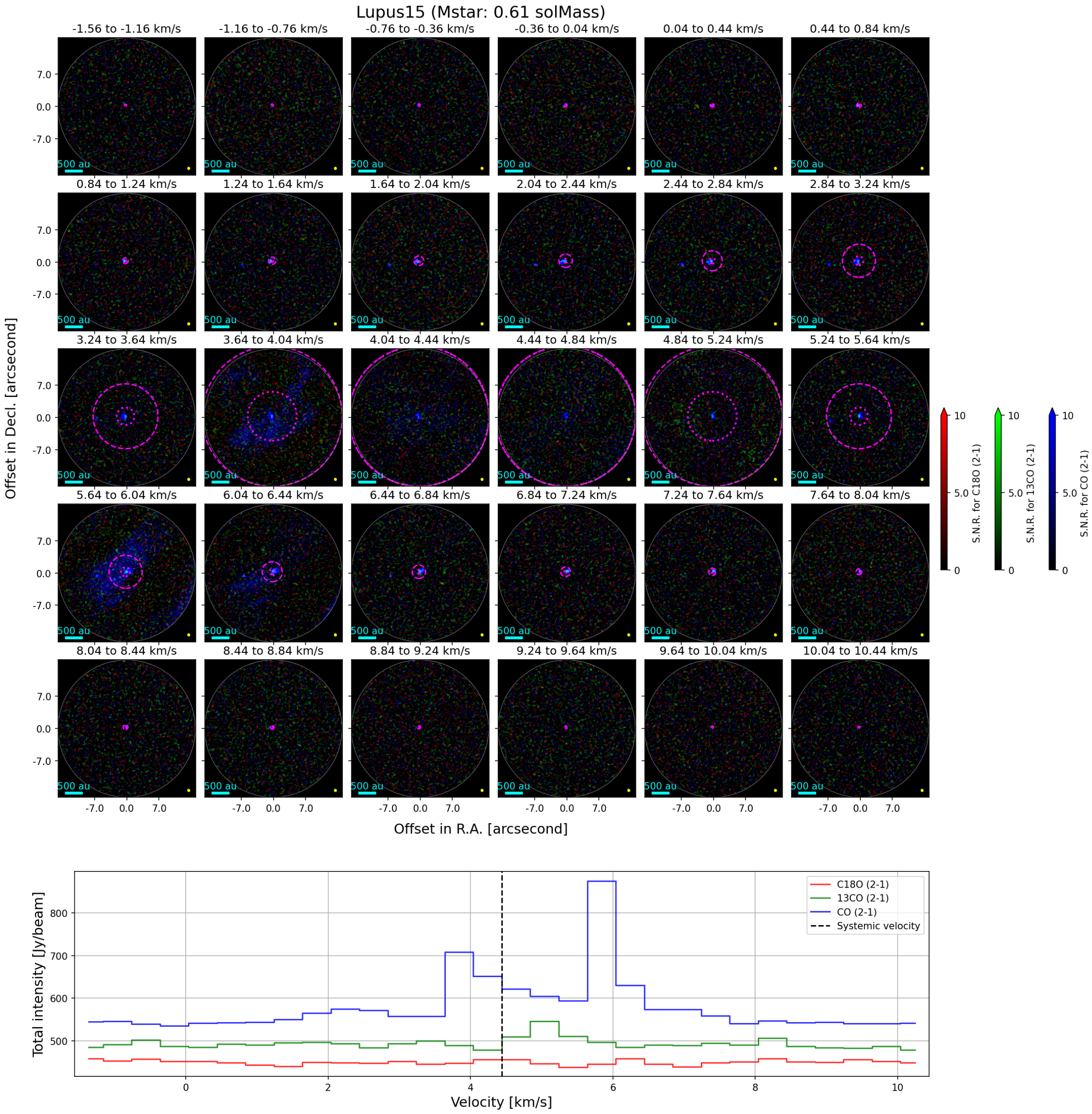

Figure C.33: CO (2–1), ^{13}CO (2–1), and C^{18}O (2–1) channel maps (top panel) and integrated spectra (bottom panel) for Lupus15. See Figure C.1 for more details.

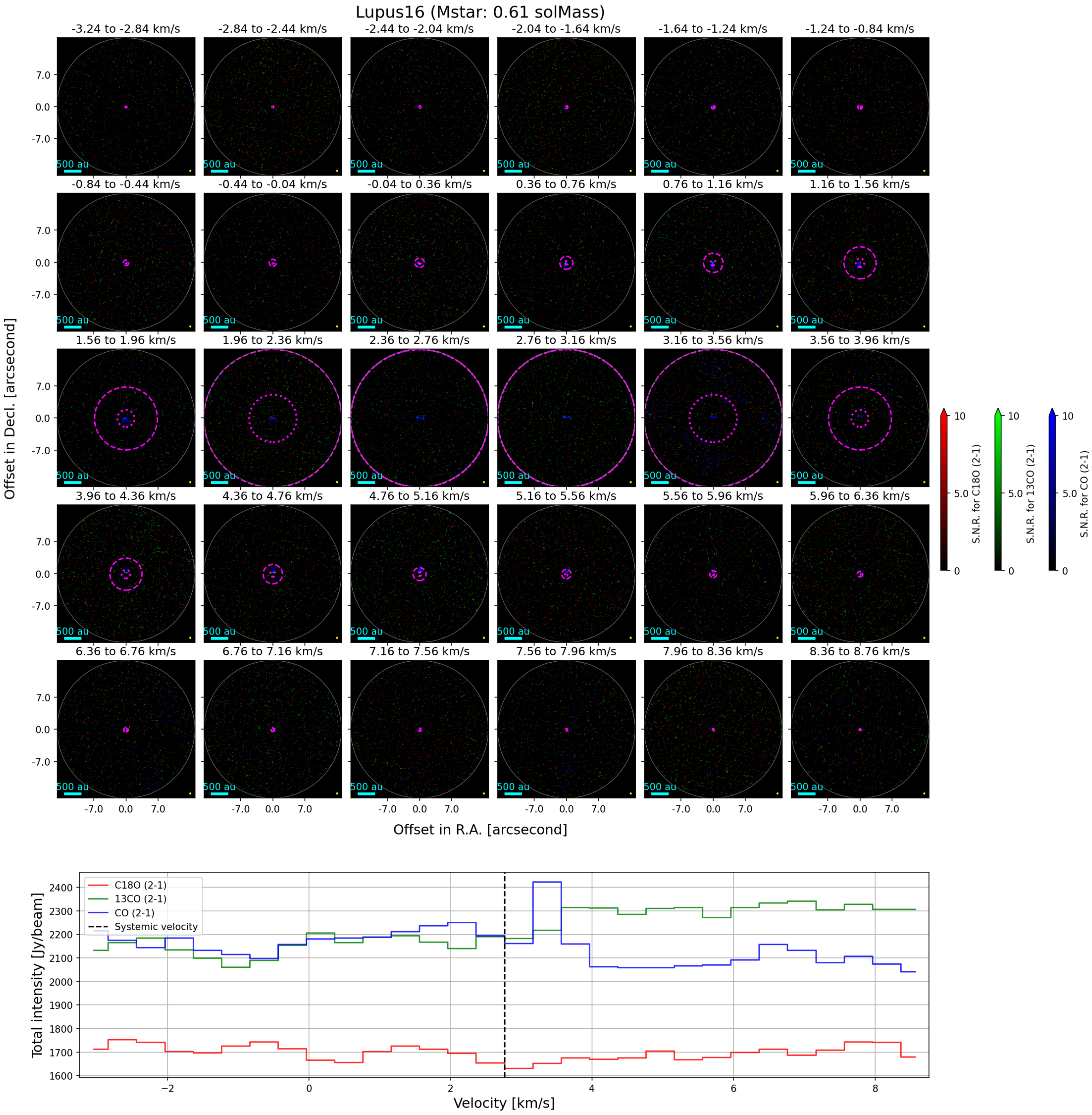

Figure C.34: CO (2–1), ^{13}CO (2–1), and C^{18}O (2–1) channel maps (top panel) and integrated spectra (bottom panel) for Lupus16. See Figure C.1 for more details.

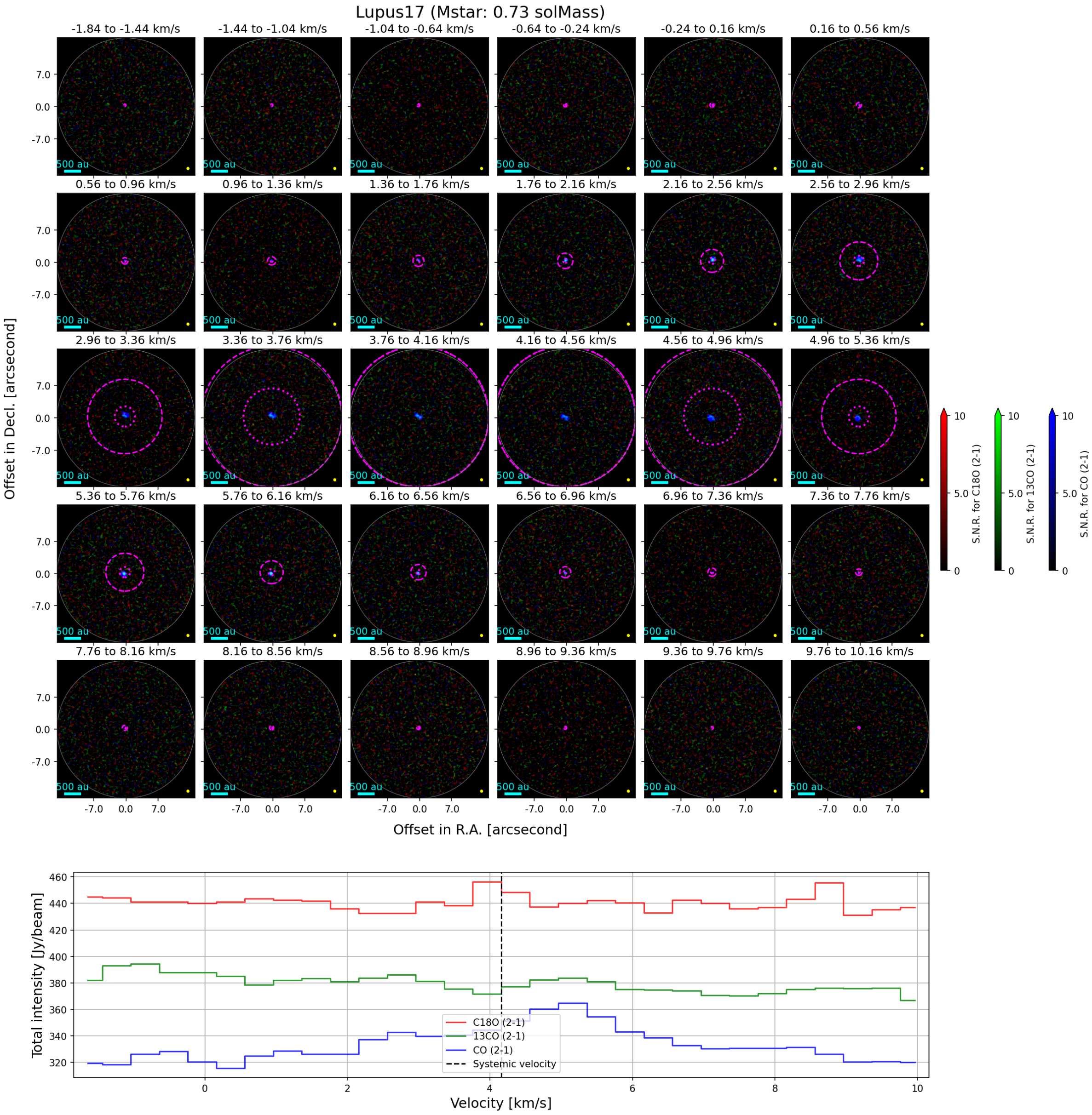

Figure C.35: CO (2–1), ^{13}CO (2–1), and C^{18}O (2–1) channel maps (top panel) and integrated spectra (bottom panel) for Lupus17. See Figure C.1 for more details.

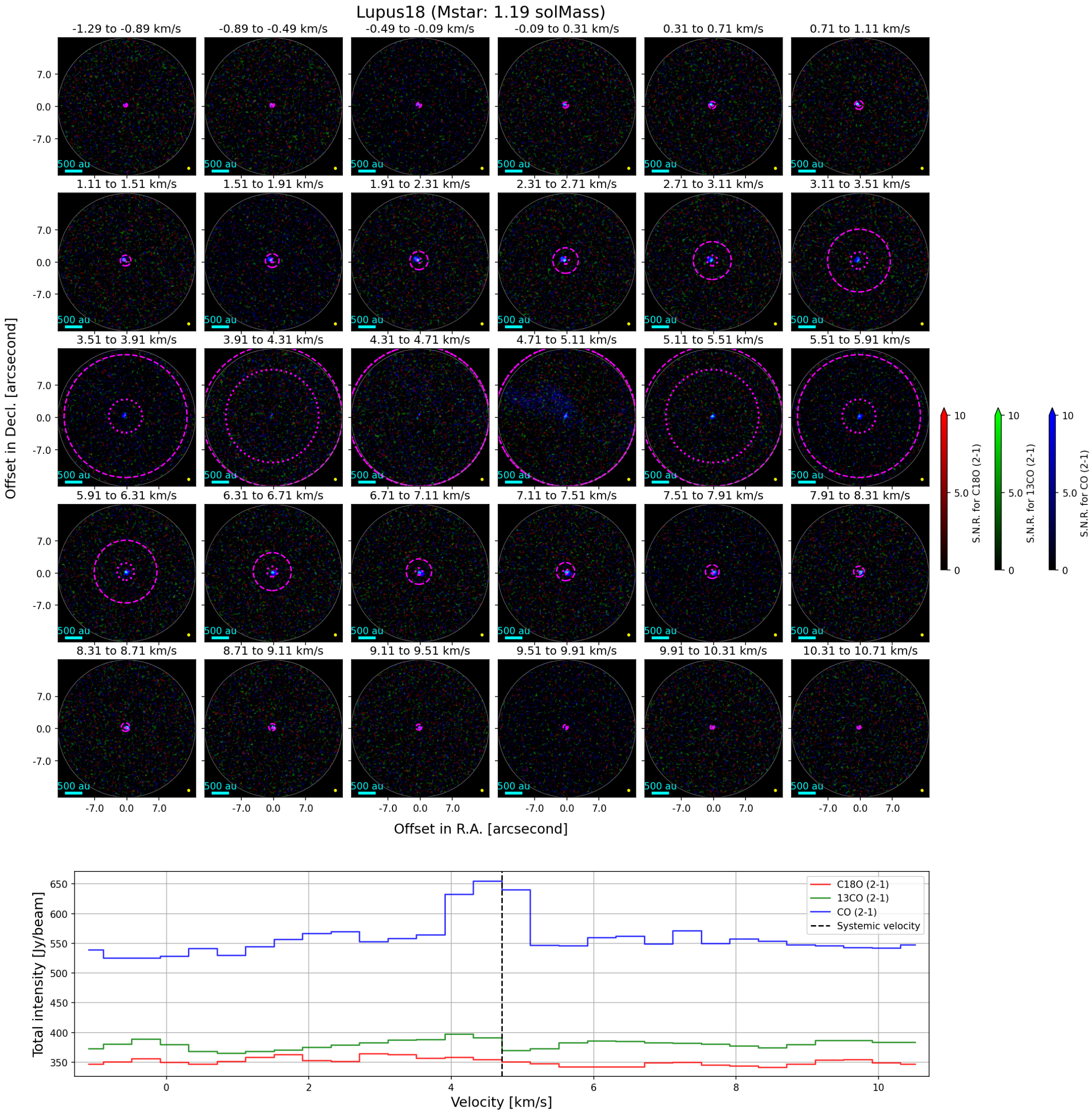

Figure C.36: CO (2–1), ^{13}CO (2–1), and C^{18}O (2–1) channel maps (top panel) and integrated spectra (bottom panel) for Lupus18. See Figure C.1 for more details.

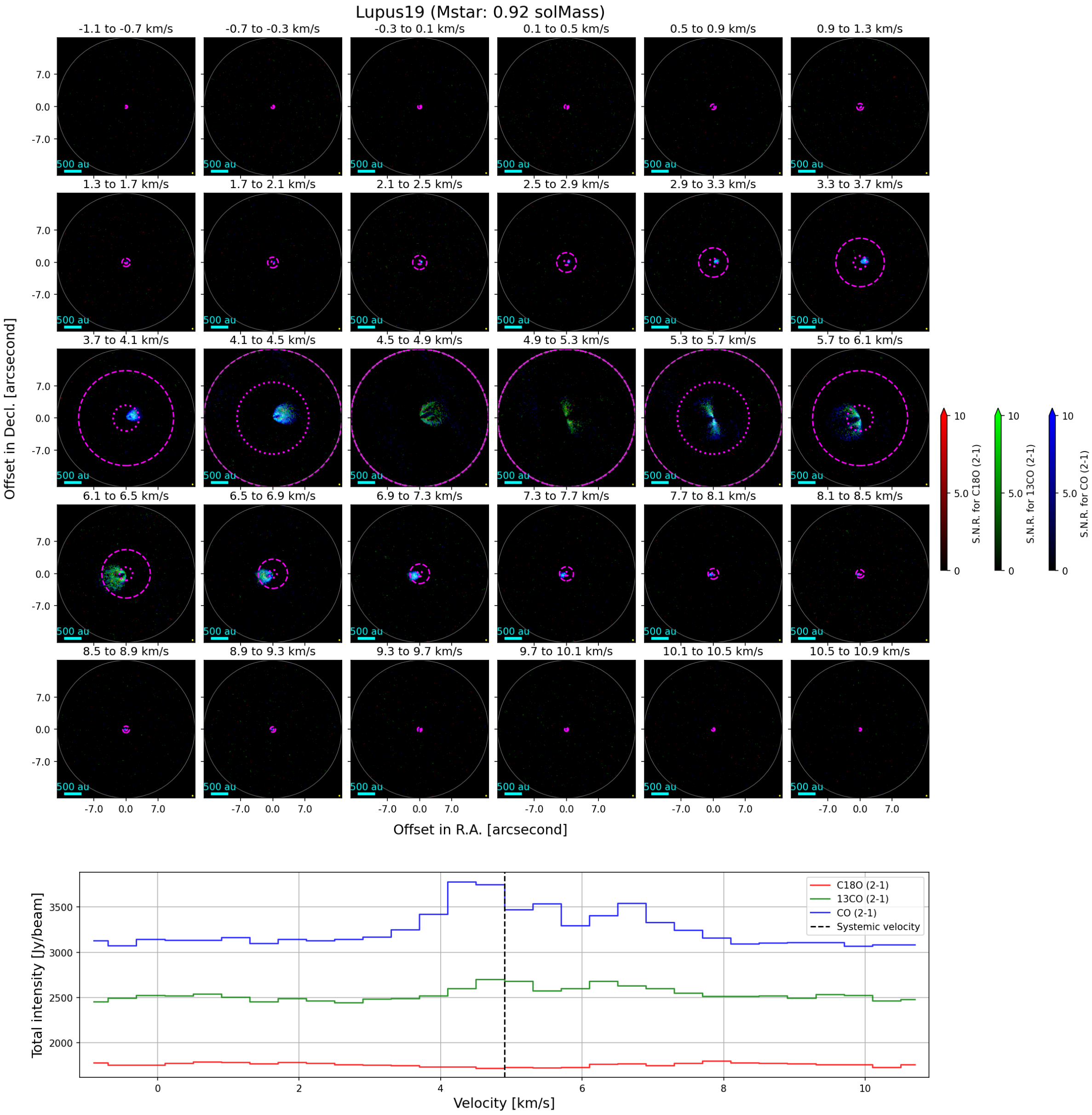

Figure C.37: CO (2–1), ^{13}CO (2–1), and C^{18}O (2–1) channel maps (top panel) and integrated spectra (bottom panel) for Lupus19. See Figure C.1 for more details.

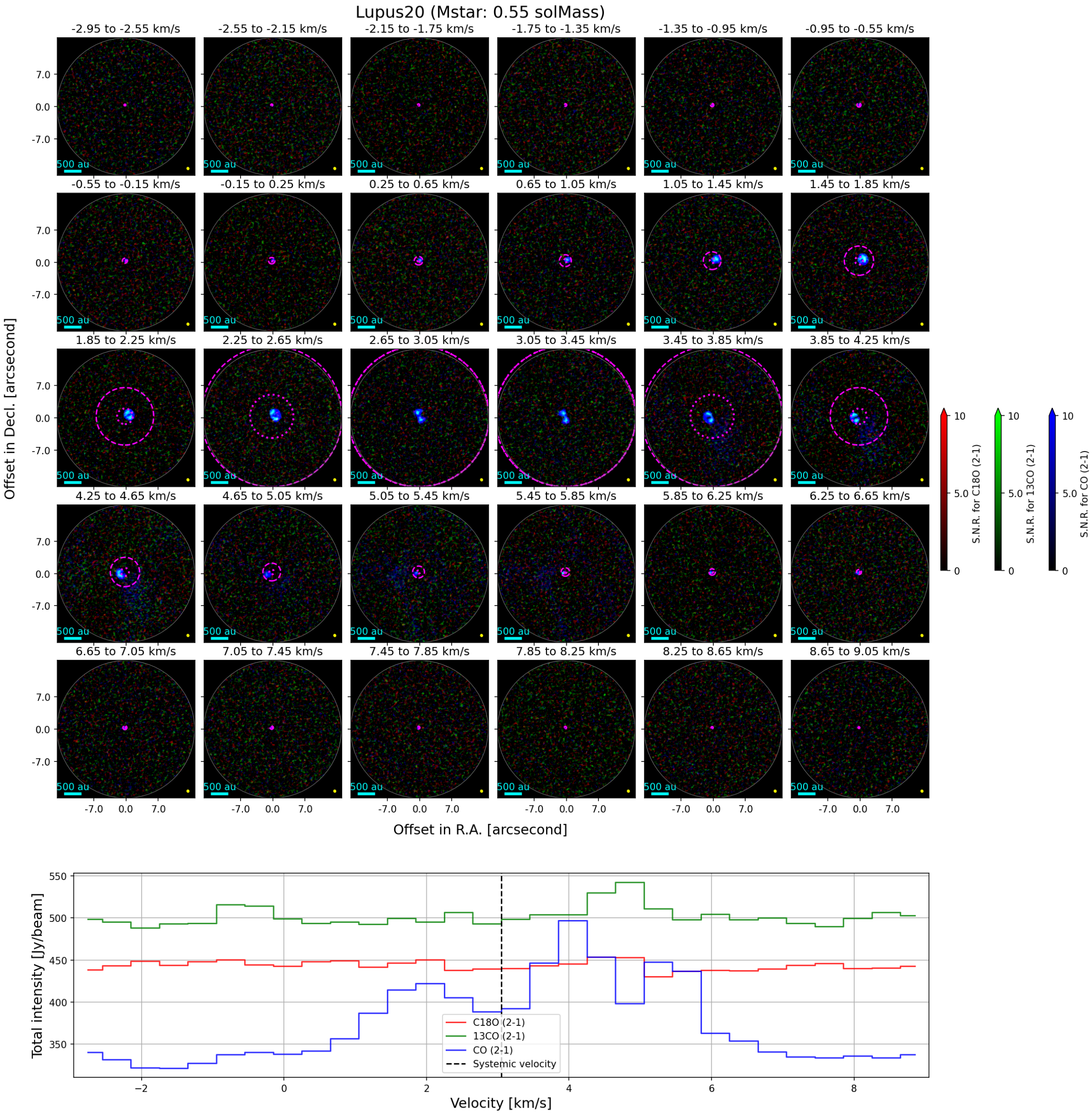

Figure C.38: CO (2–1), ^{13}CO (2–1), and C^{18}O (2–1) channel maps (top panel) and integrated spectra (bottom panel) for Lupus20. See Figure C.1 for more details.

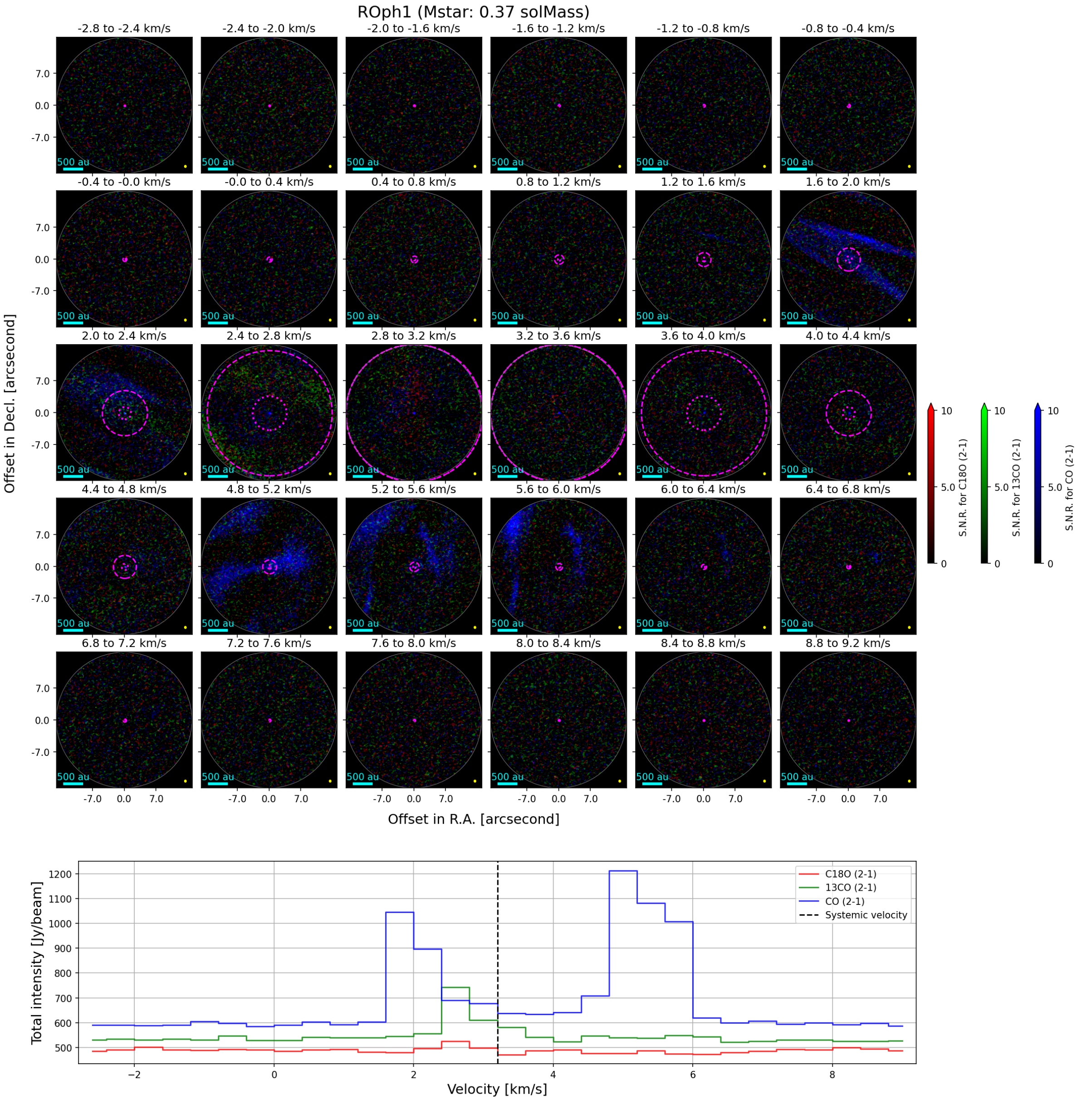

Figure C.39: CO (2–1), ^{13}CO (2–1), and C^{18}O (2–1) channel maps (top panel) and integrated spectra (bottom panel) for ROph1. See Figure C.1 for more details.

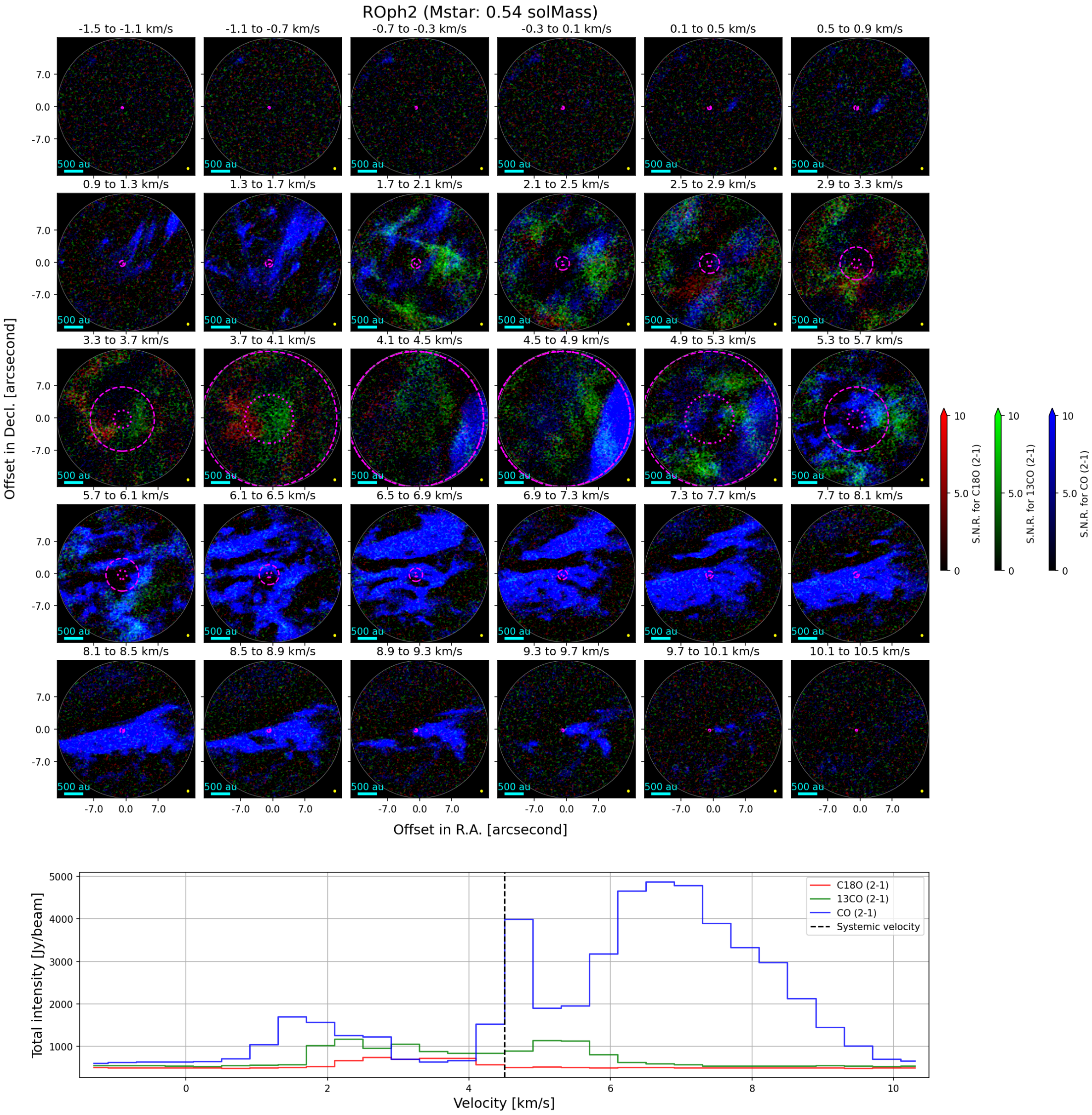

Figure C.40: CO (2–1), ^{13}CO (2–1), and C^{18}O (2–1) channel maps (top panel) and integrated spectra (bottom panel) for ROph2. See Figure C.1 for more details.

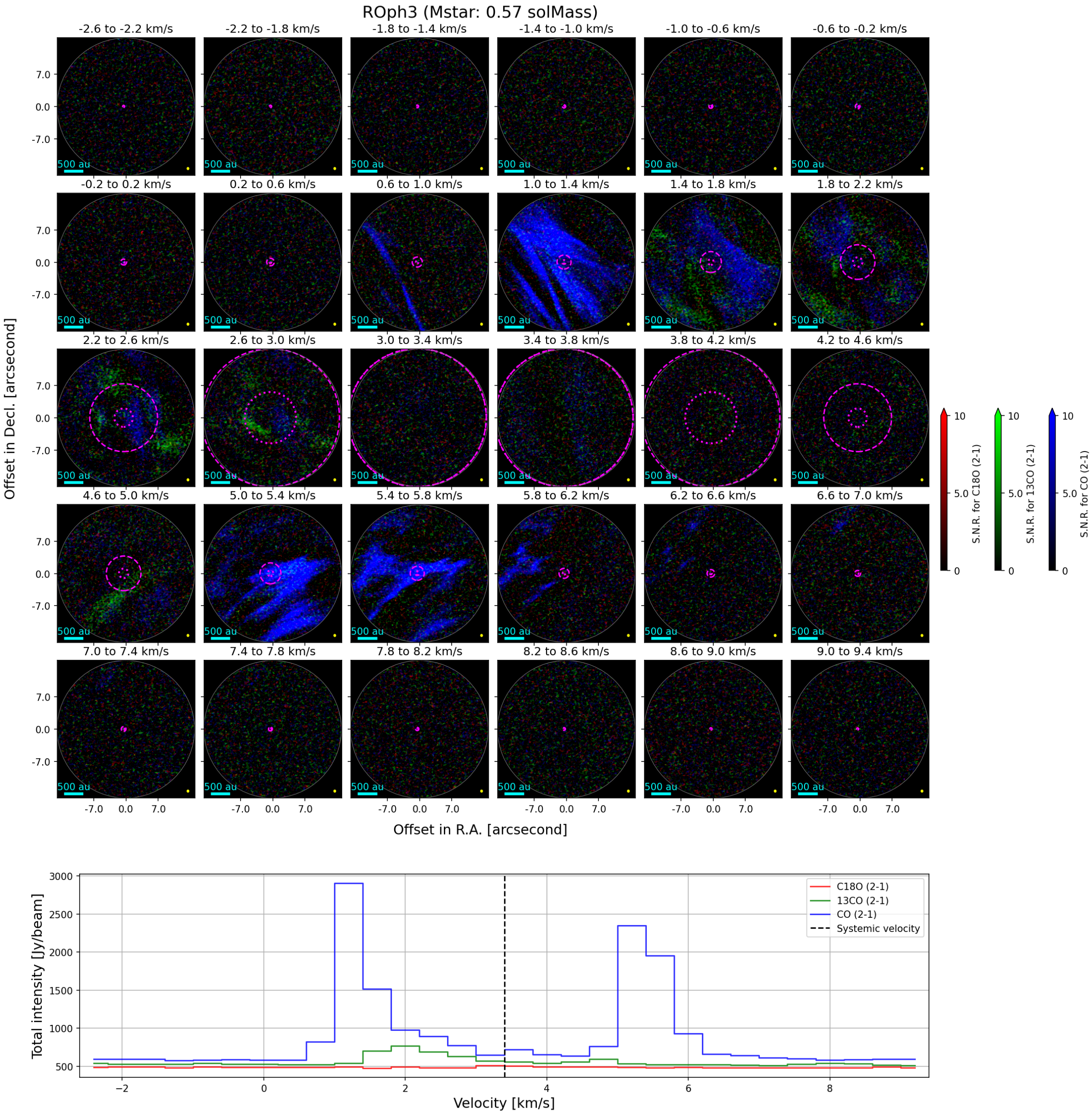

Figure C.41: CO (2–1), ^{13}CO (2–1), and C^{18}O (2–1) channel maps (top panel) and integrated spectra (bottom panel) for ROph3. See Figure C.1 for more details.

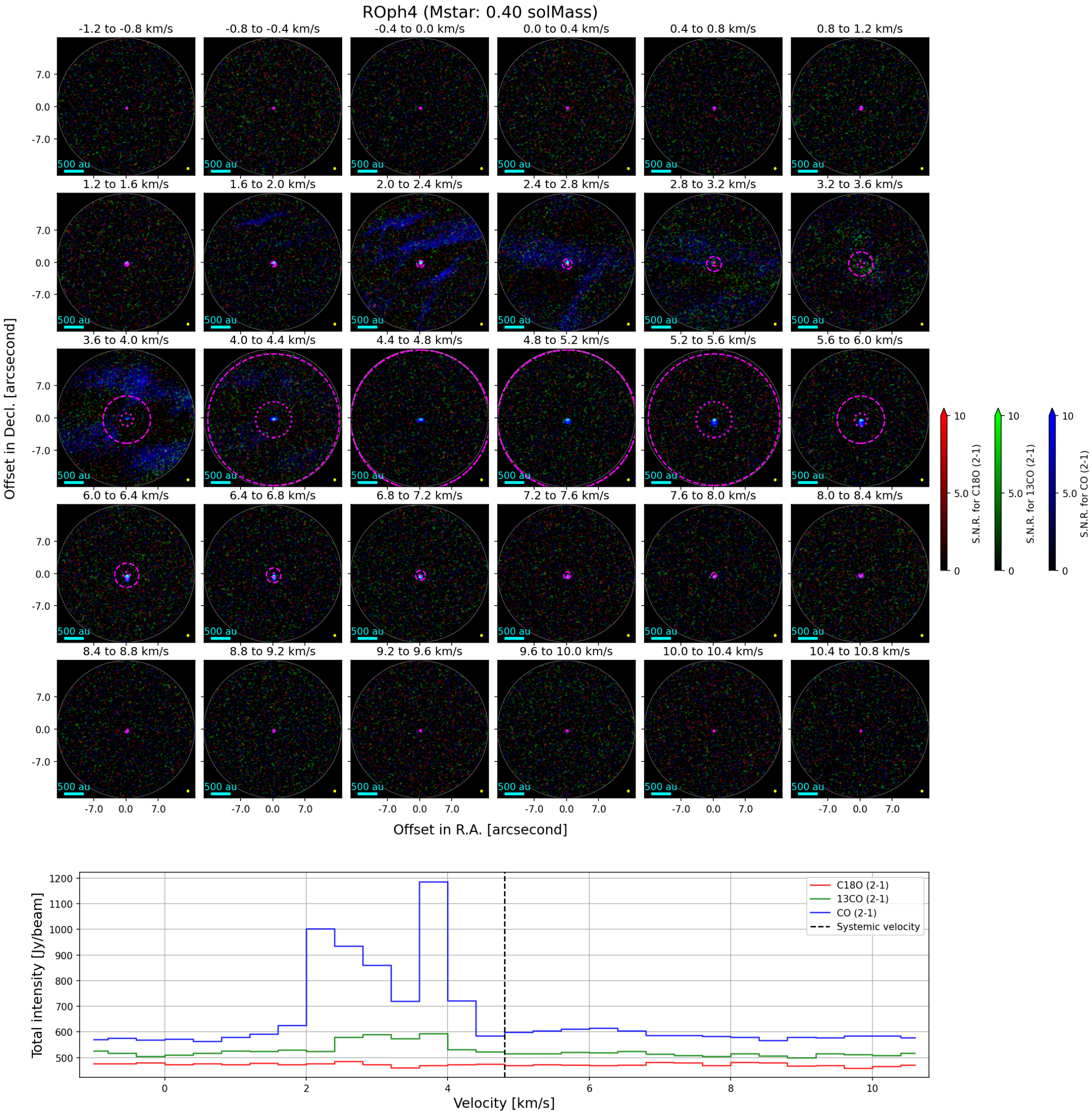

Figure C.42: CO (2–1), ^{13}CO (2–1), and C^{18}O (2–1) channel maps (top panel) and integrated spectra (bottom panel) for ROph4. See Figure C.1 for more details.

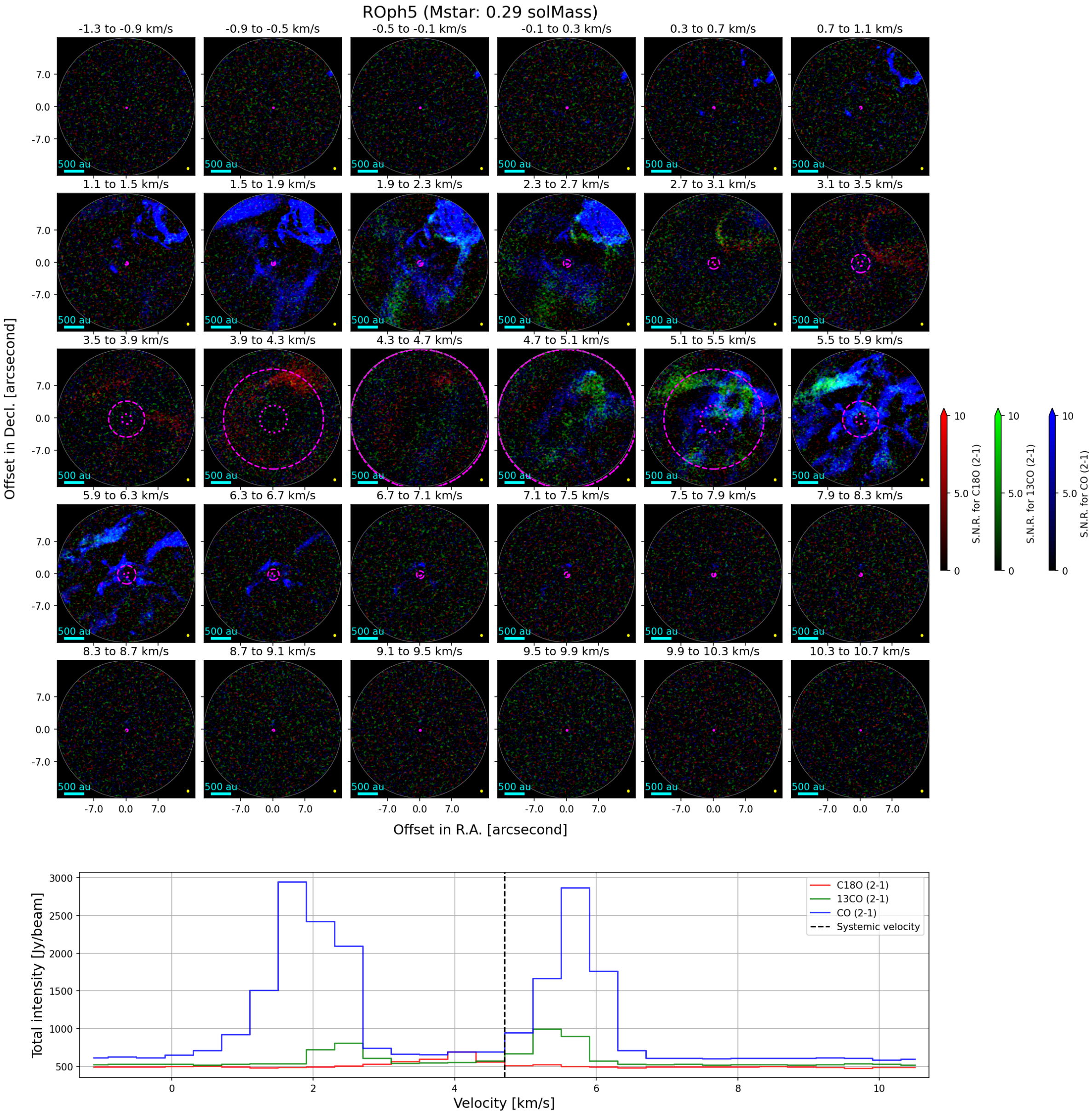

Figure C.43: CO (2–1), ^{13}CO (2–1), and C^{18}O (2–1) channel maps (top panel) and integrated spectra (bottom panel) for ROph5. See Figure C.1 for more details.

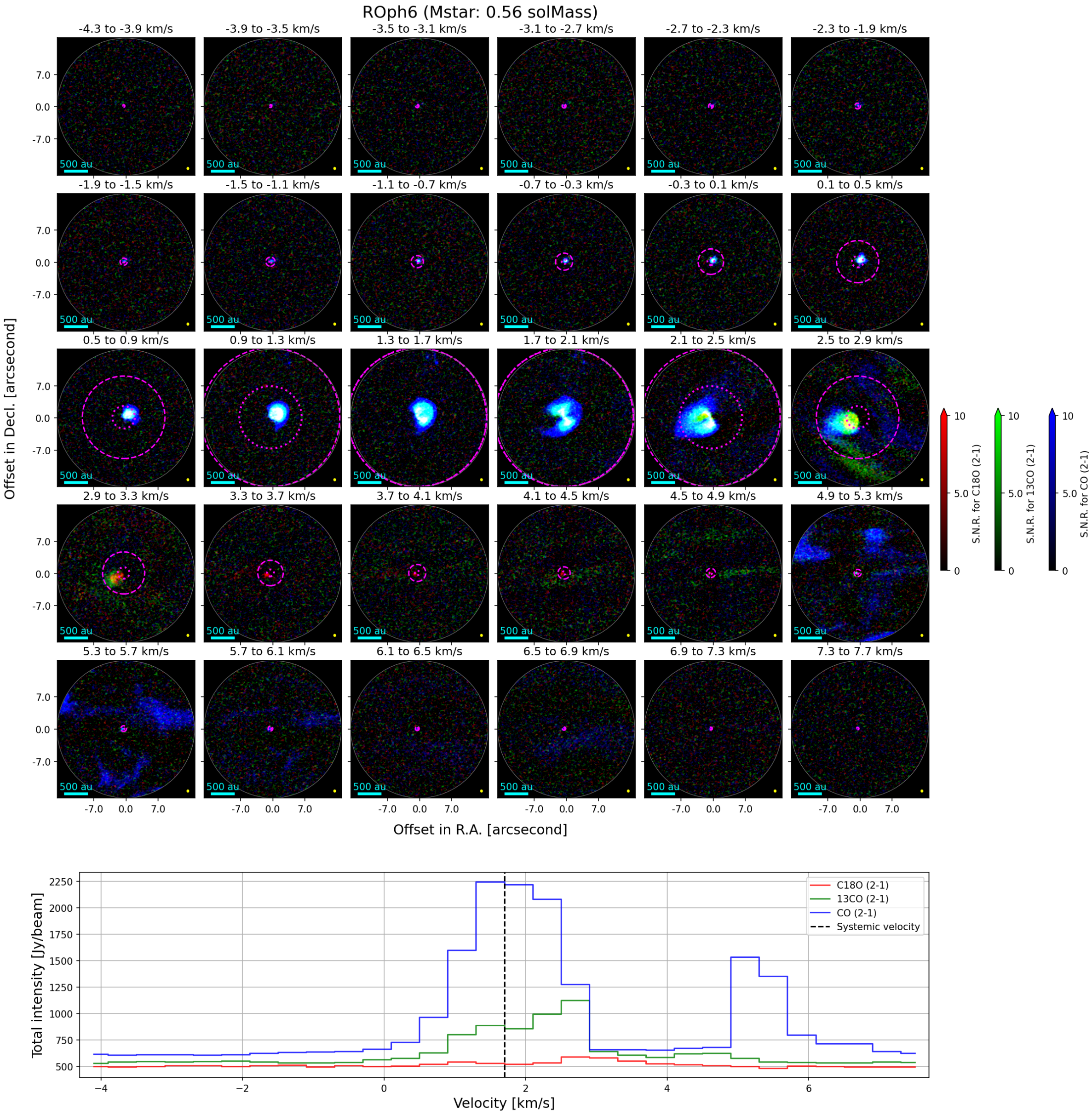

Figure C.44: CO (2–1), ^{13}CO (2–1), and C^{18}O (2–1) channel maps (top panel) and integrated spectra (bottom panel) for ROph6. See Figure C.1 for more details.

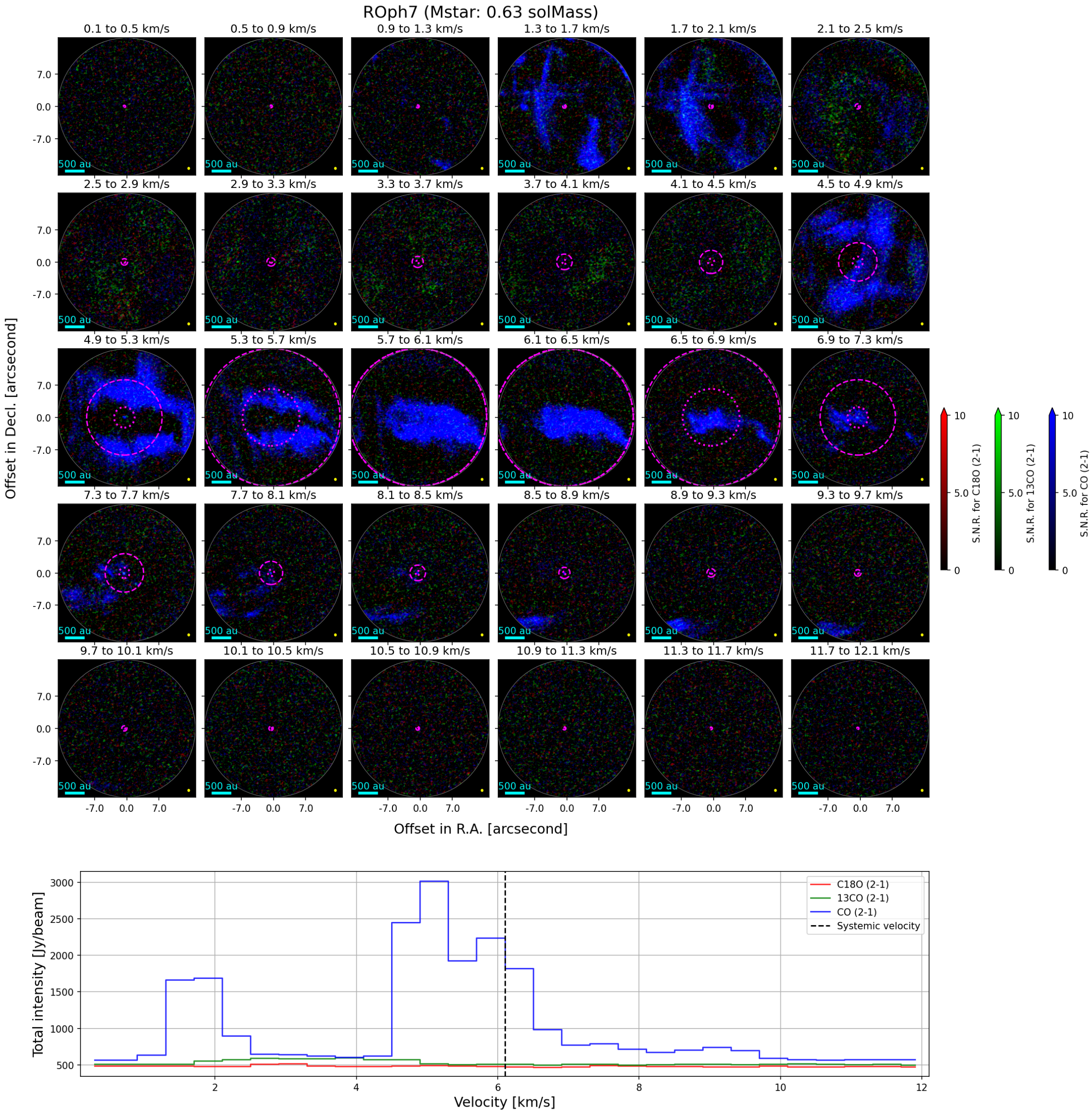

Figure C.45: CO (2–1), ^{13}CO (2–1), and C^{18}O (2–1) channel maps (top panel) and integrated spectra (bottom panel) for ROph7. See Figure C.1 for more details.

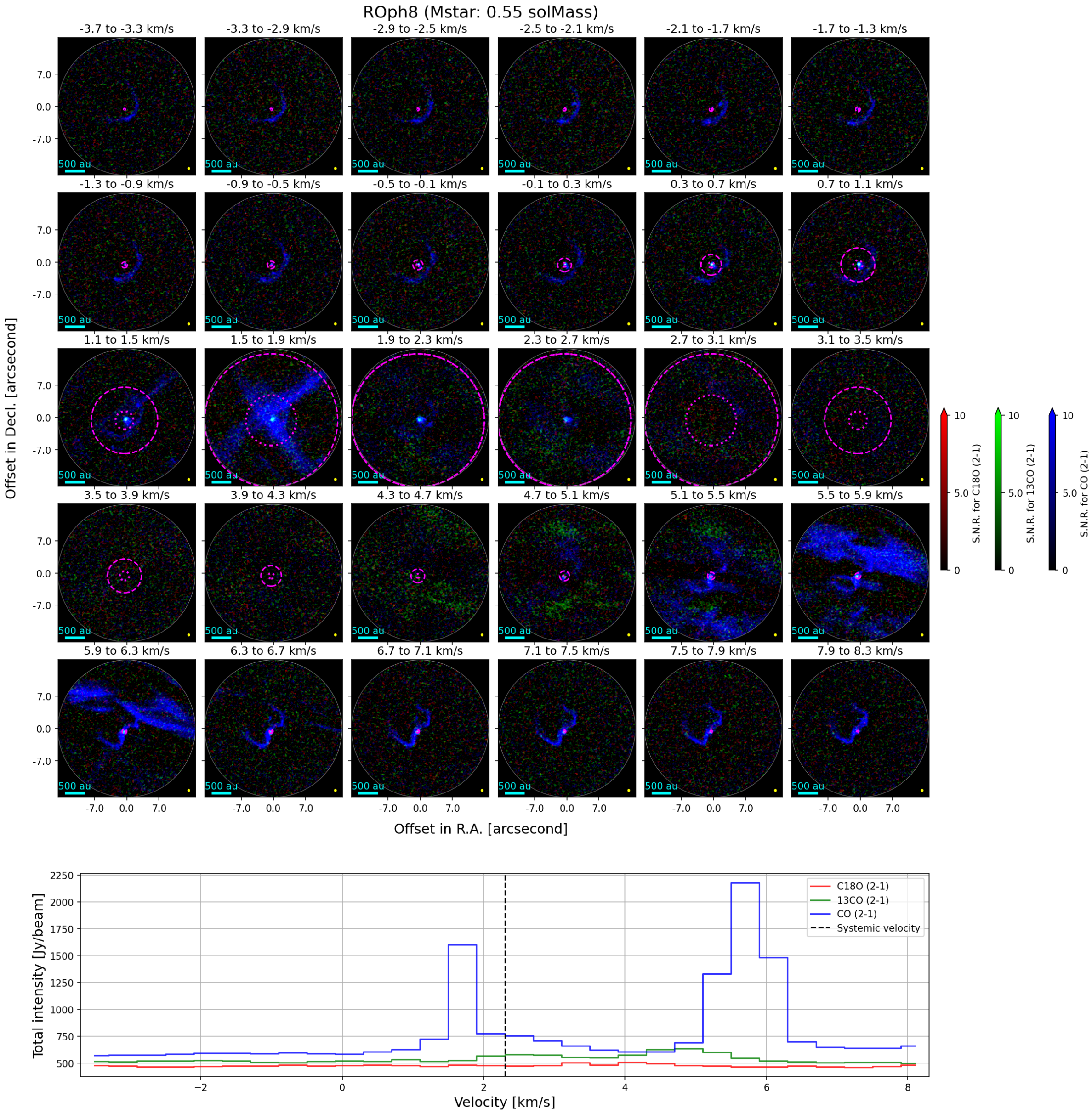

Figure C.46: CO (2–1), ^{13}CO (2–1), and C^{18}O (2–1) channel maps (top panel) and integrated spectra (bottom panel) for ROph8. See Figure C.1 for more details.

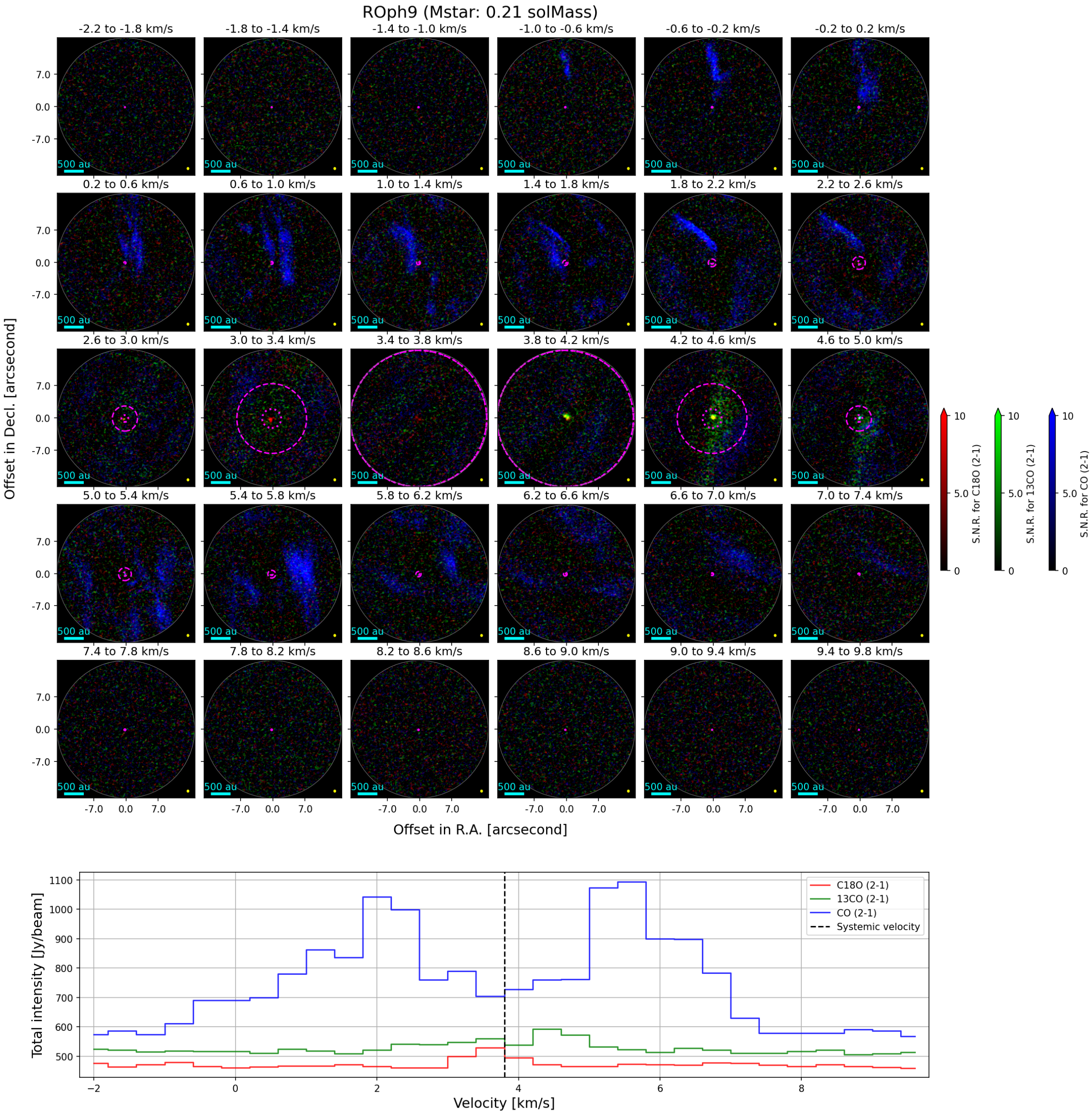

Figure C.47: CO (2–1), ^{13}CO (2–1), and C^{18}O (2–1) channel maps (top panel) and integrated spectra (bottom panel) for ROph9. See Figure C.1 for more details.

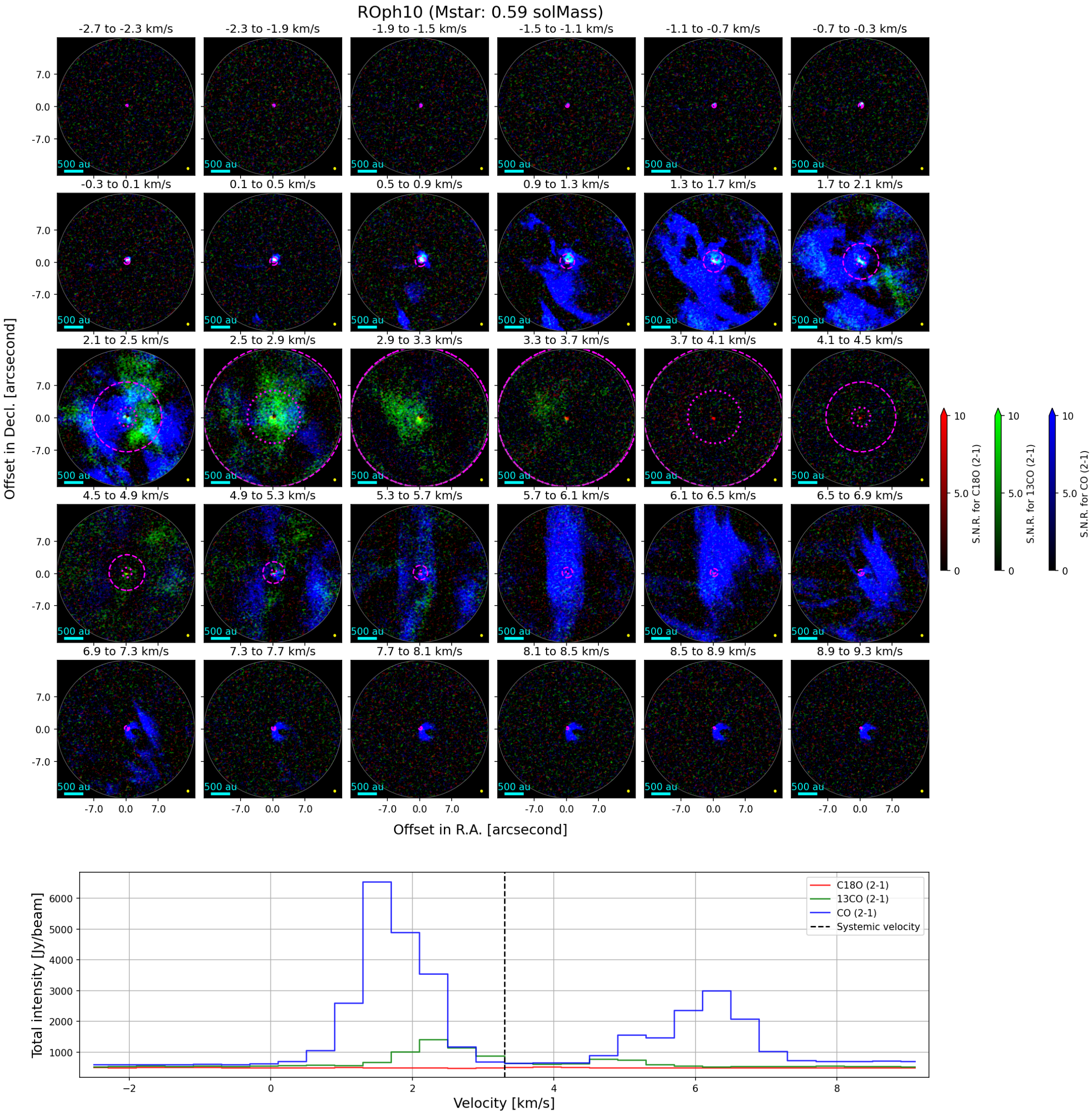

Figure C.48: CO (2–1), ^{13}CO (2–1), and C^{18}O (2–1) channel maps (top panel) and integrated spectra (bottom panel) for ROph10. See Figure C.1 for more details.

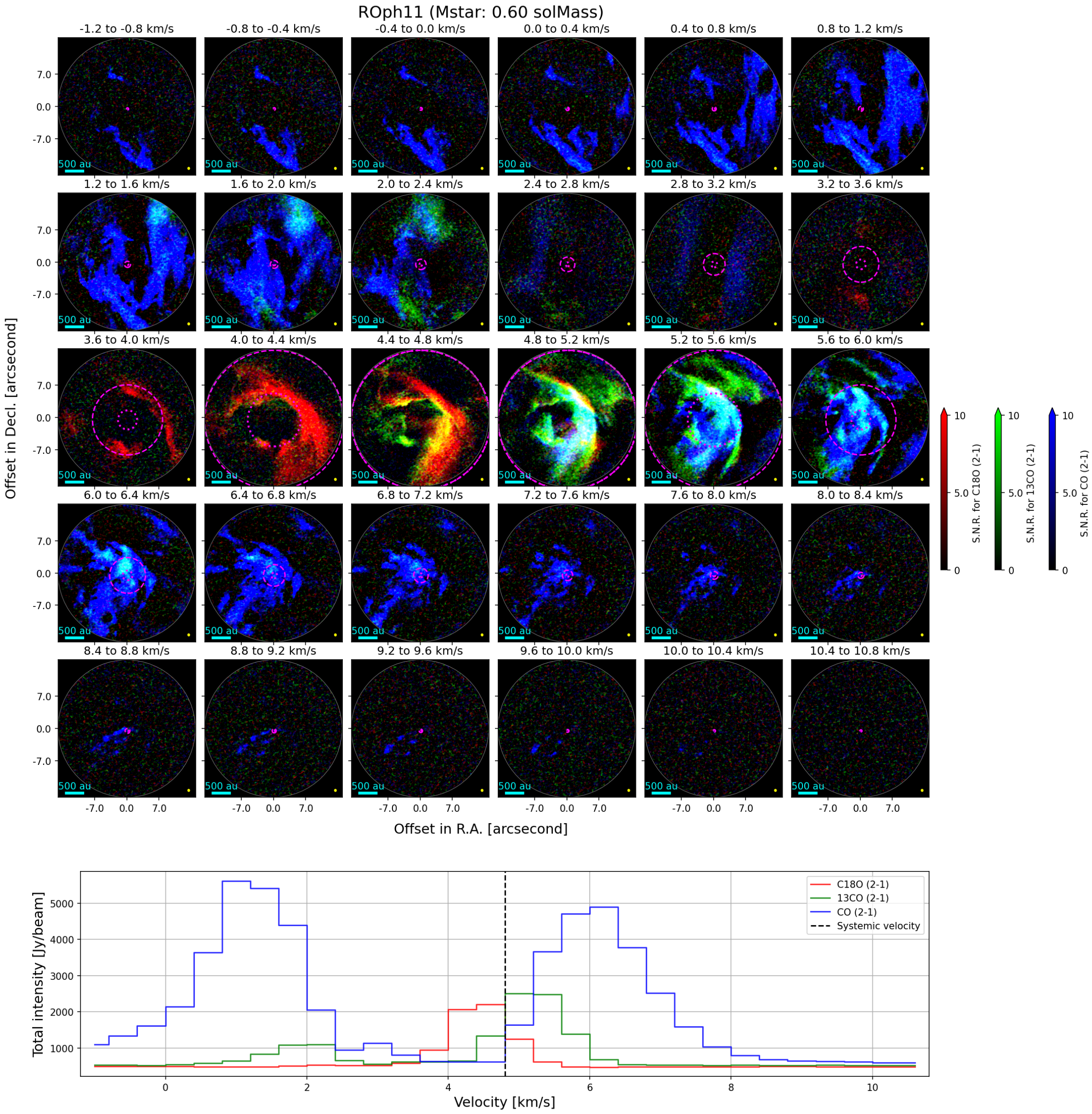

Figure C.49: CO (2–1), ^{13}CO (2–1), and C^{18}O (2–1) channel maps (top panel) and integrated spectra (bottom panel) for ROph11. See Figure C.1 for more details.

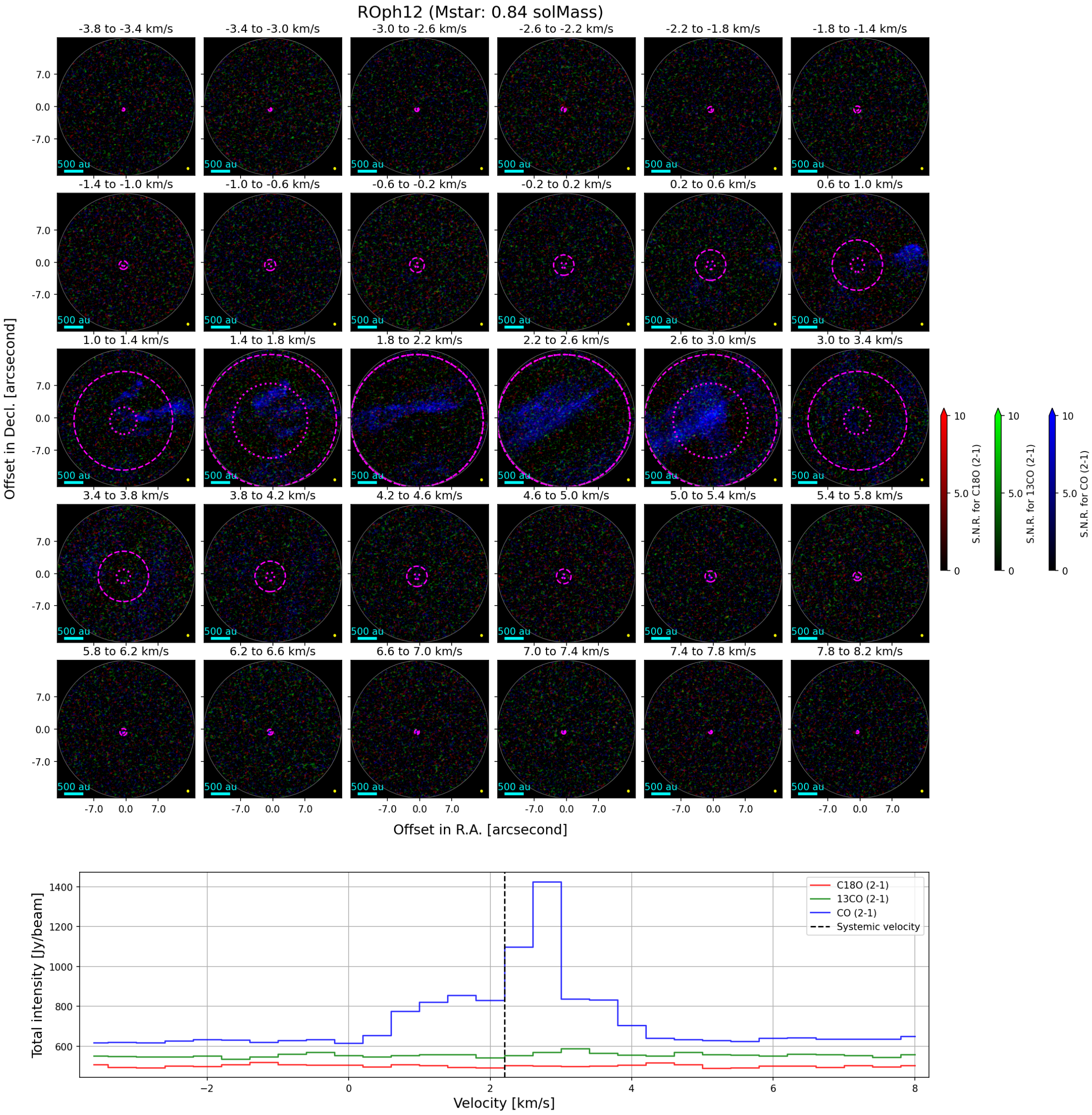

Figure C.50: CO (2–1), ^{13}CO (2–1), and C^{18}O (2–1) channel maps (top panel) and integrated spectra (bottom panel) for ROph12. See Figure C.1 for more details.

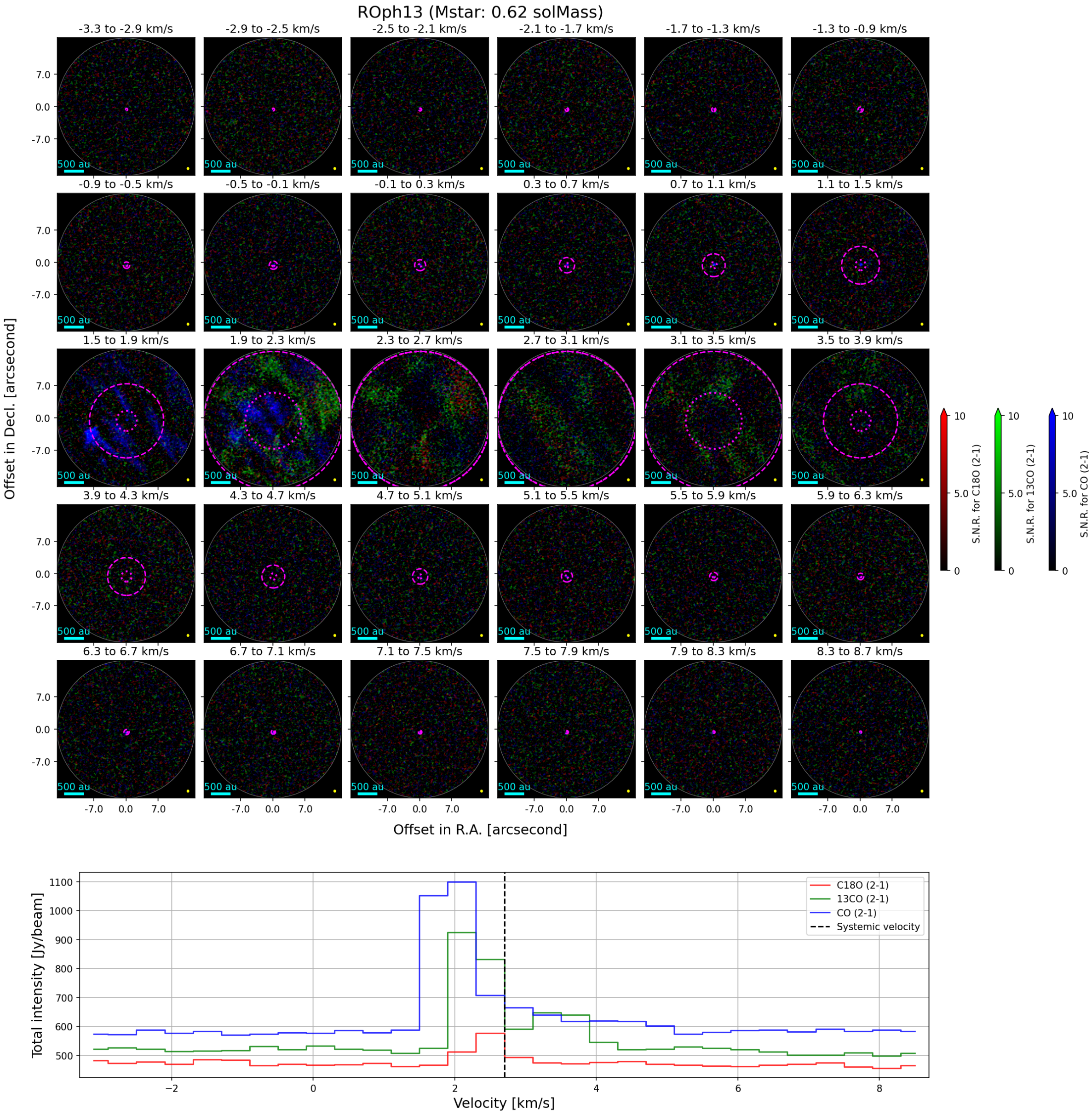

Figure C.51: CO (2–1), ^{13}CO (2–1), and C^{18}O (2–1) channel maps (top panel) and integrated spectra (bottom panel) for ROph13. See Figure C.1 for more details.

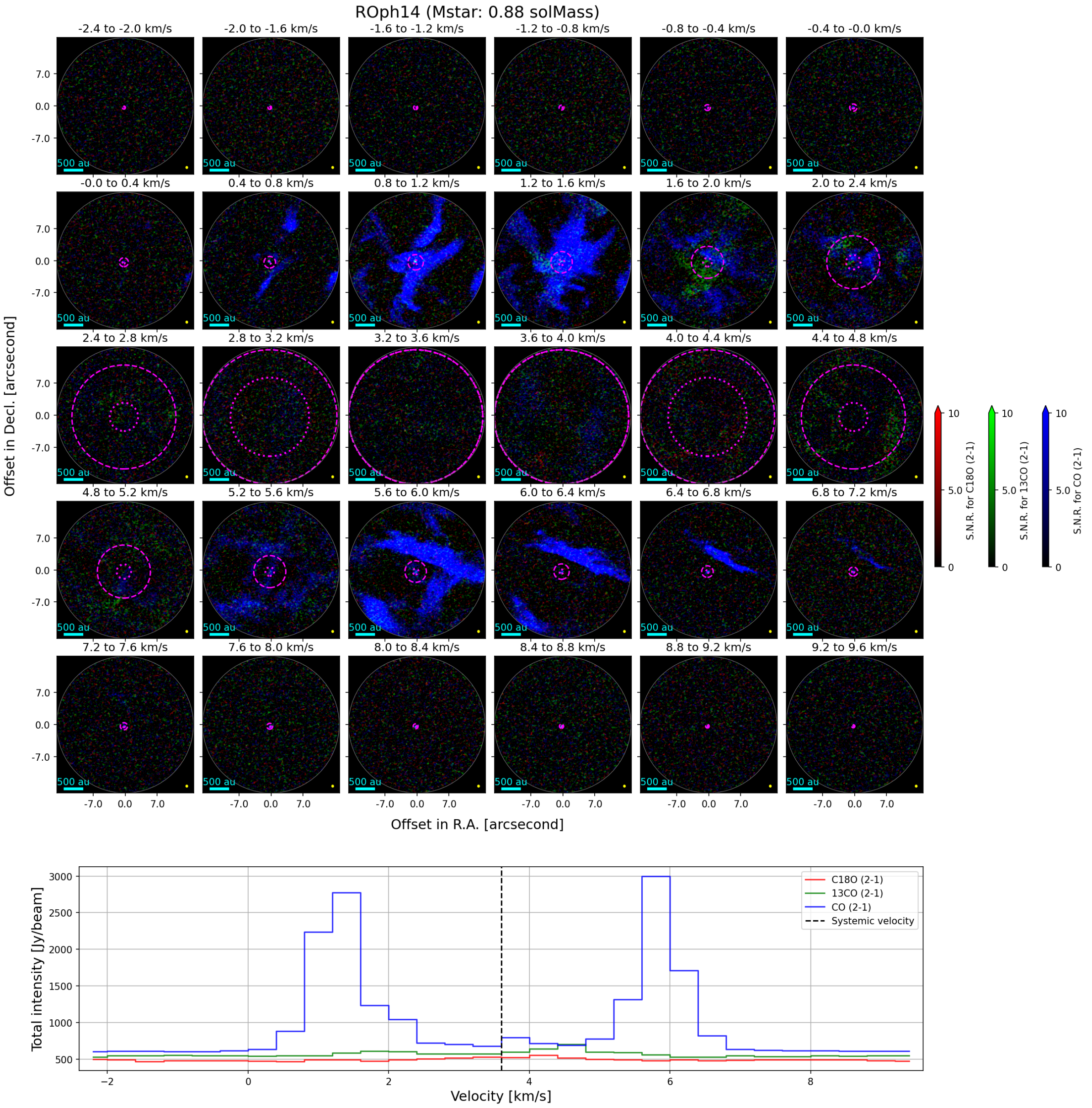

Figure C.52: CO (2–1), ^{13}CO (2–1), and C^{18}O (2–1) channel maps (top panel) and integrated spectra (bottom panel) for ROph14. See Figure C.1 for more details.

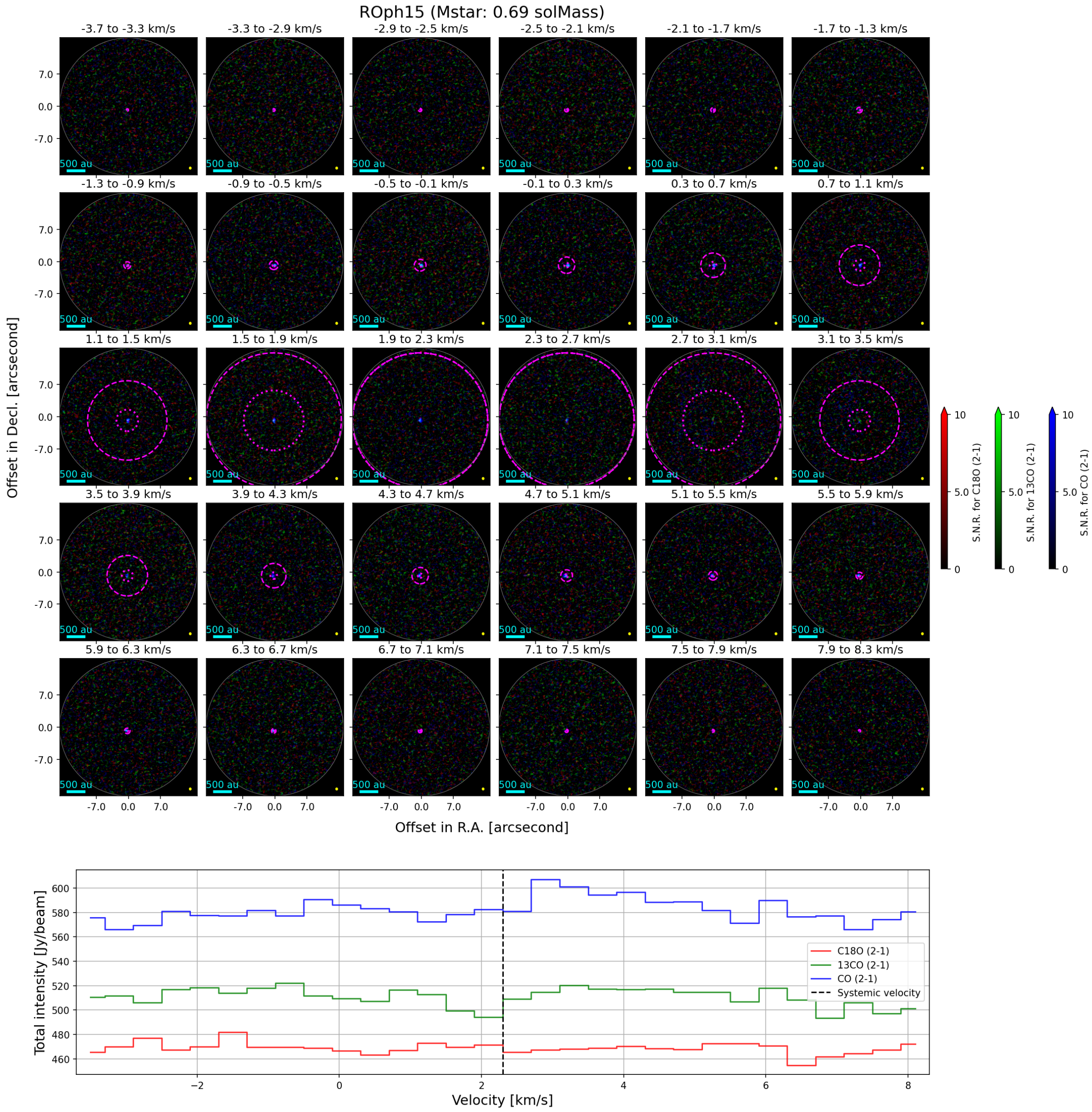

Figure C.53: CO (2–1), ^{13}CO (2–1), and C^{18}O (2–1) channel maps (top panel) and integrated spectra (bottom panel) for ROph15. See Figure C.1 for more details.

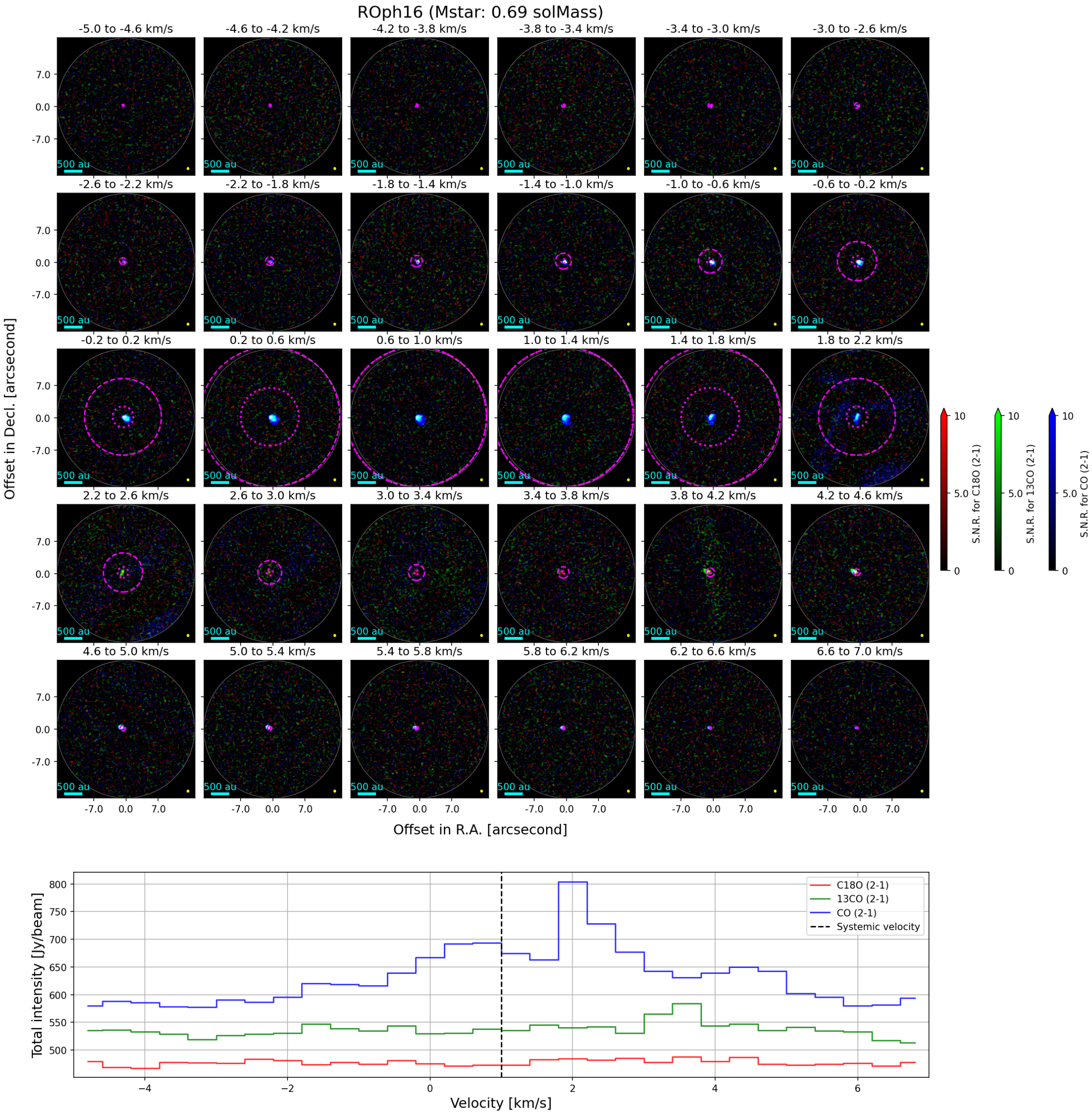

Figure C.54: CO (2–1), ^{13}CO (2–1), and C^{18}O (2–1) channel maps (top panel) and integrated spectra (bottom panel) for ROph16. See Figure C.1 for more details.

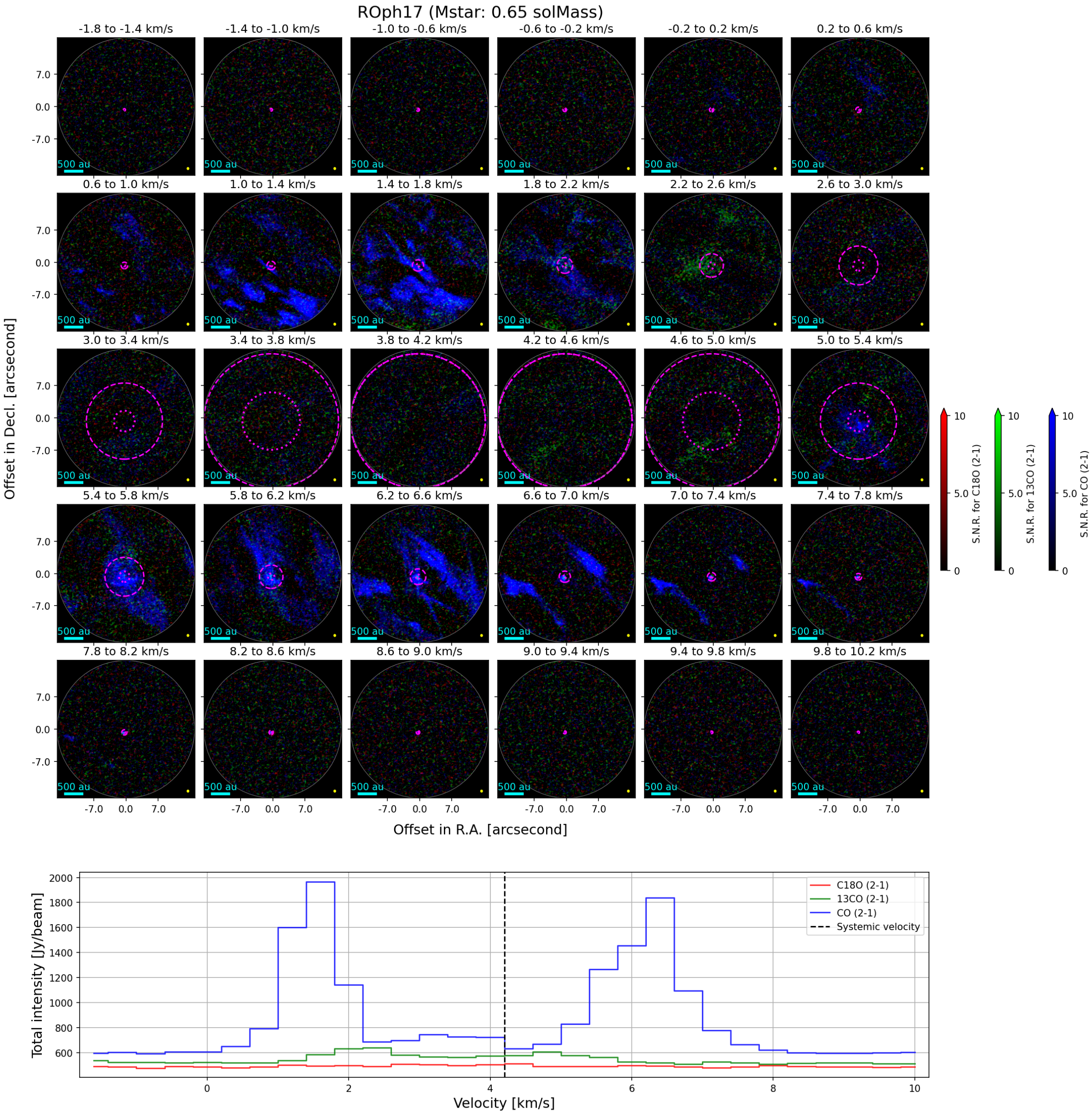

Figure C.55: CO (2–1), ^{13}CO (2–1), and C^{18}O (2–1) channel maps (top panel) and integrated spectra (bottom panel) for ROph17. See Figure C.1 for more details.

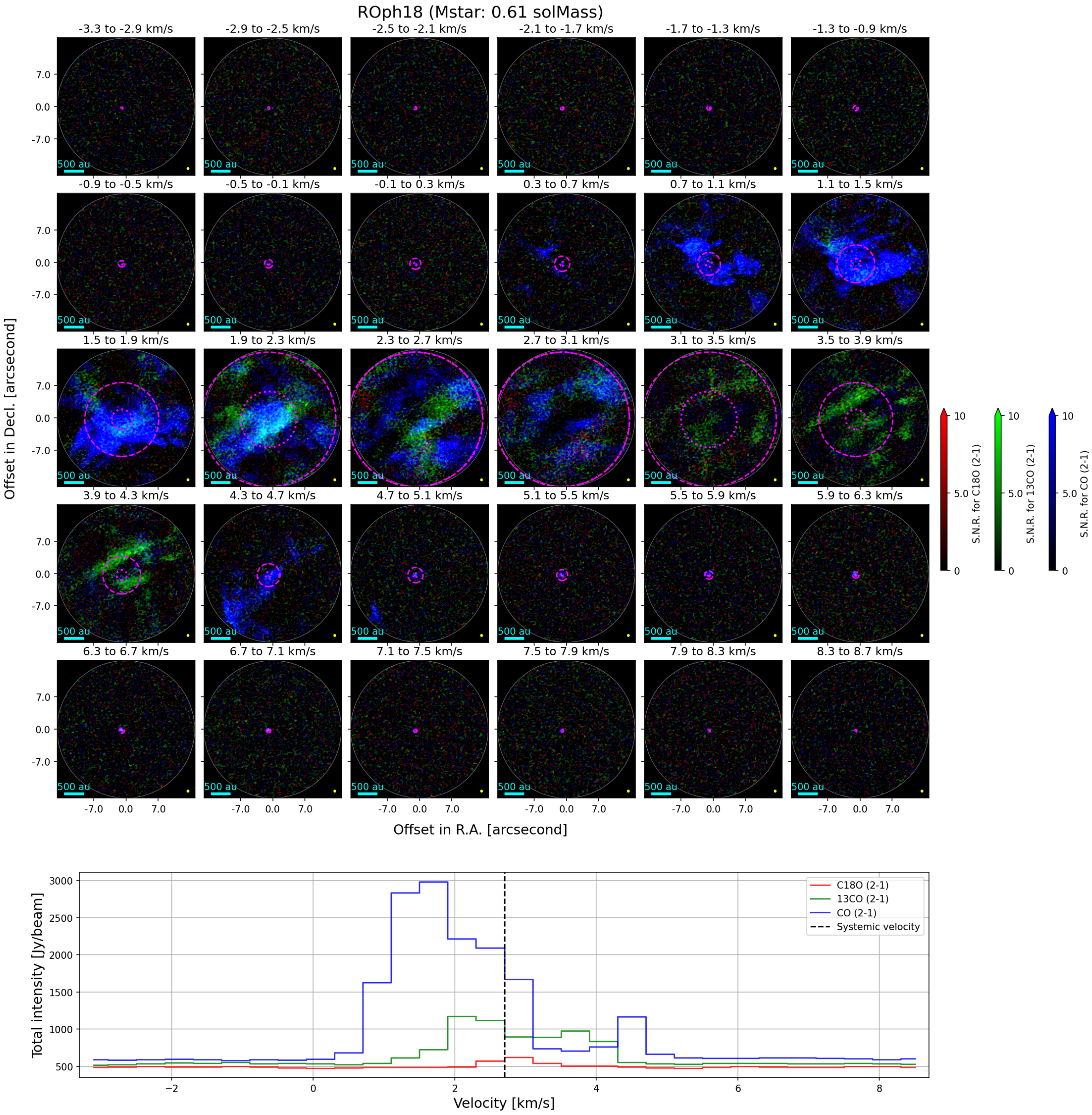

Figure C.56: CO (2–1), ^{13}CO (2–1), and C^{18}O (2–1) channel maps (top panel) and integrated spectra (bottom panel) for ROph18. See Figure C.1 for more details.

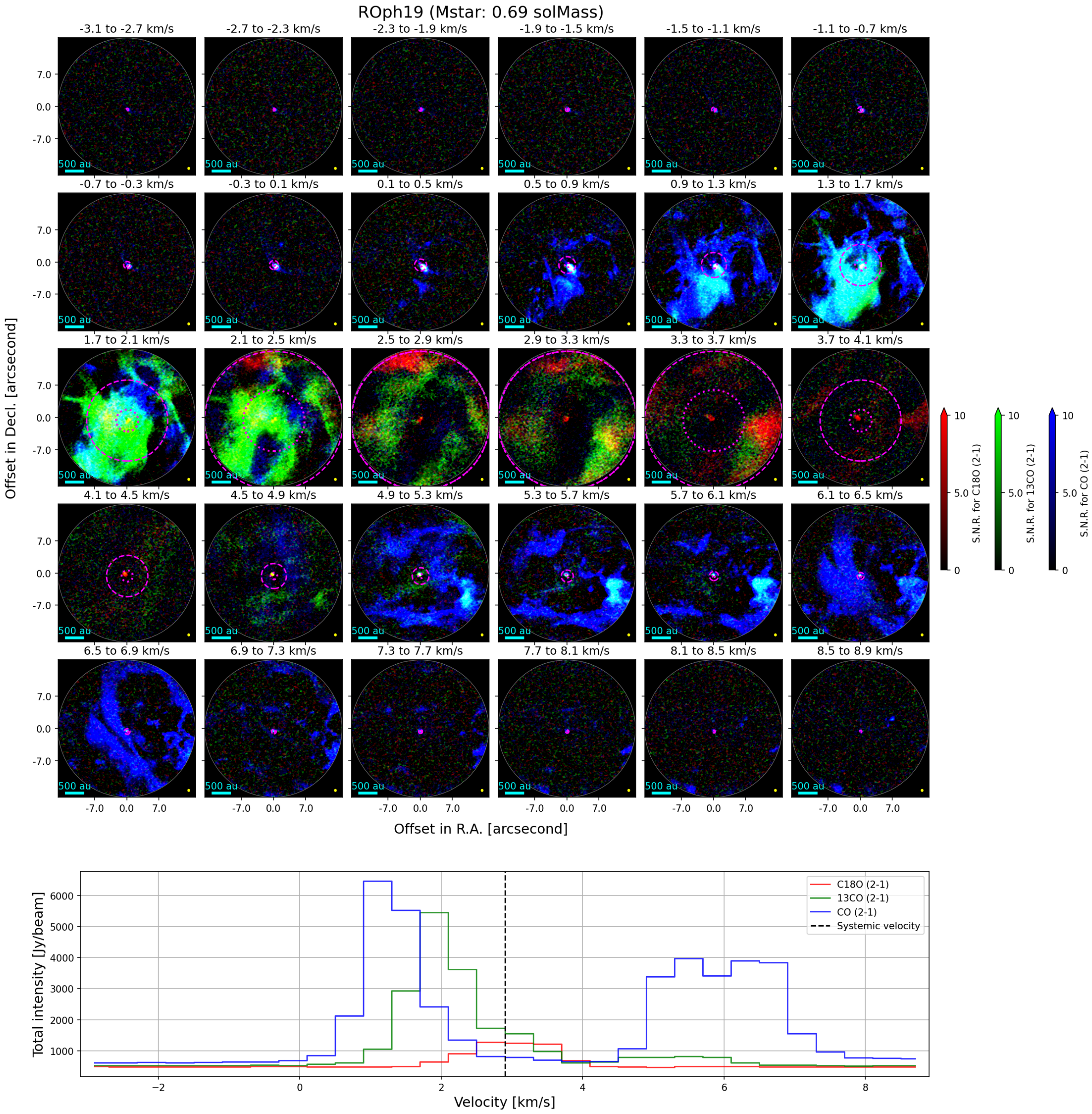

Figure C.57: CO (2–1), ^{13}CO (2–1), and C^{18}O (2–1) channel maps (top panel) and integrated spectra (bottom panel) for ROph19. See Figure C.1 for more details.

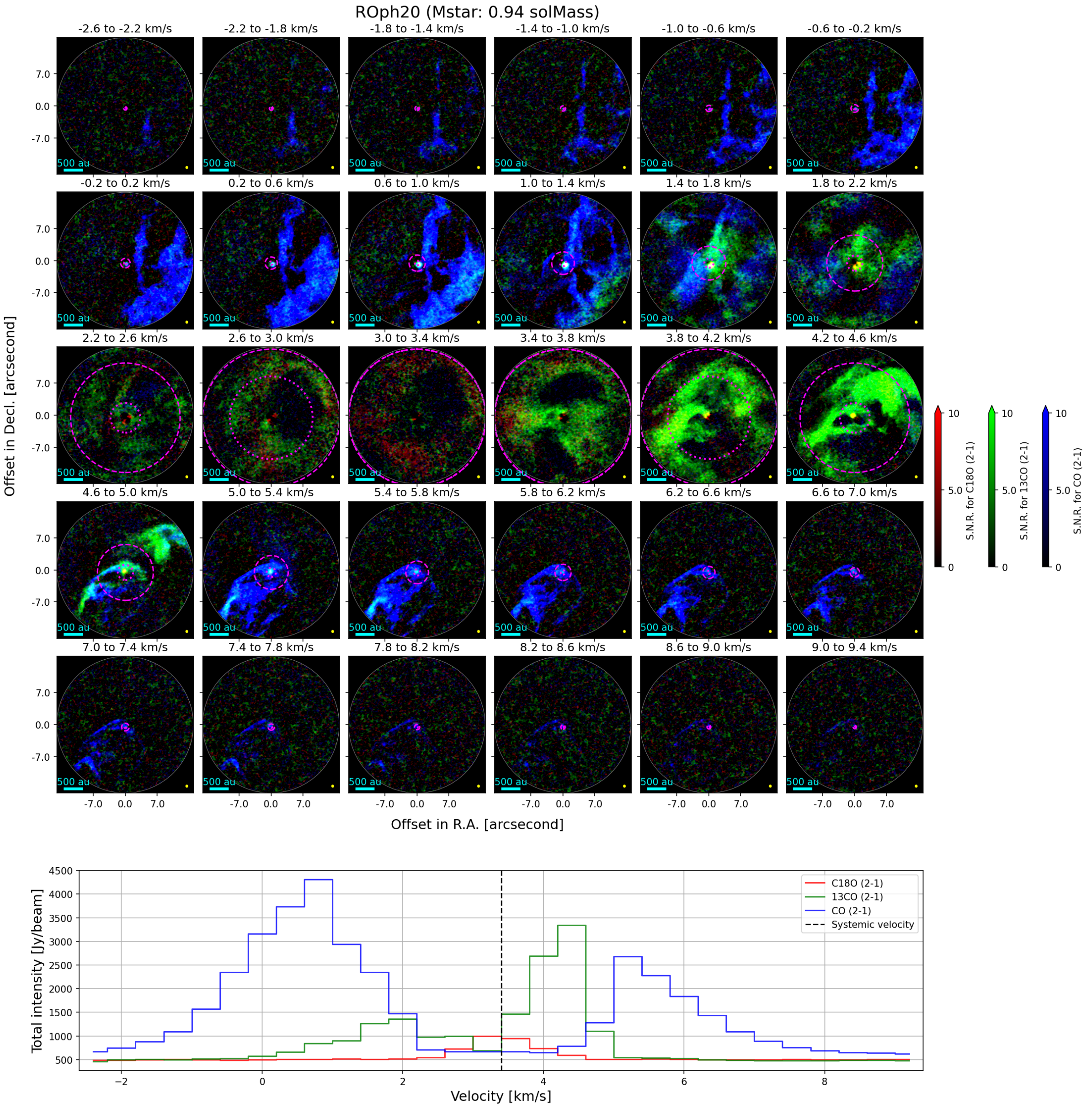

Figure C.58: CO (2–1), ^{13}CO (2–1), and C^{18}O (2–1) channel maps (top panel) and integrated spectra (bottom panel) for ROph20. See Figure C.1 for more details.

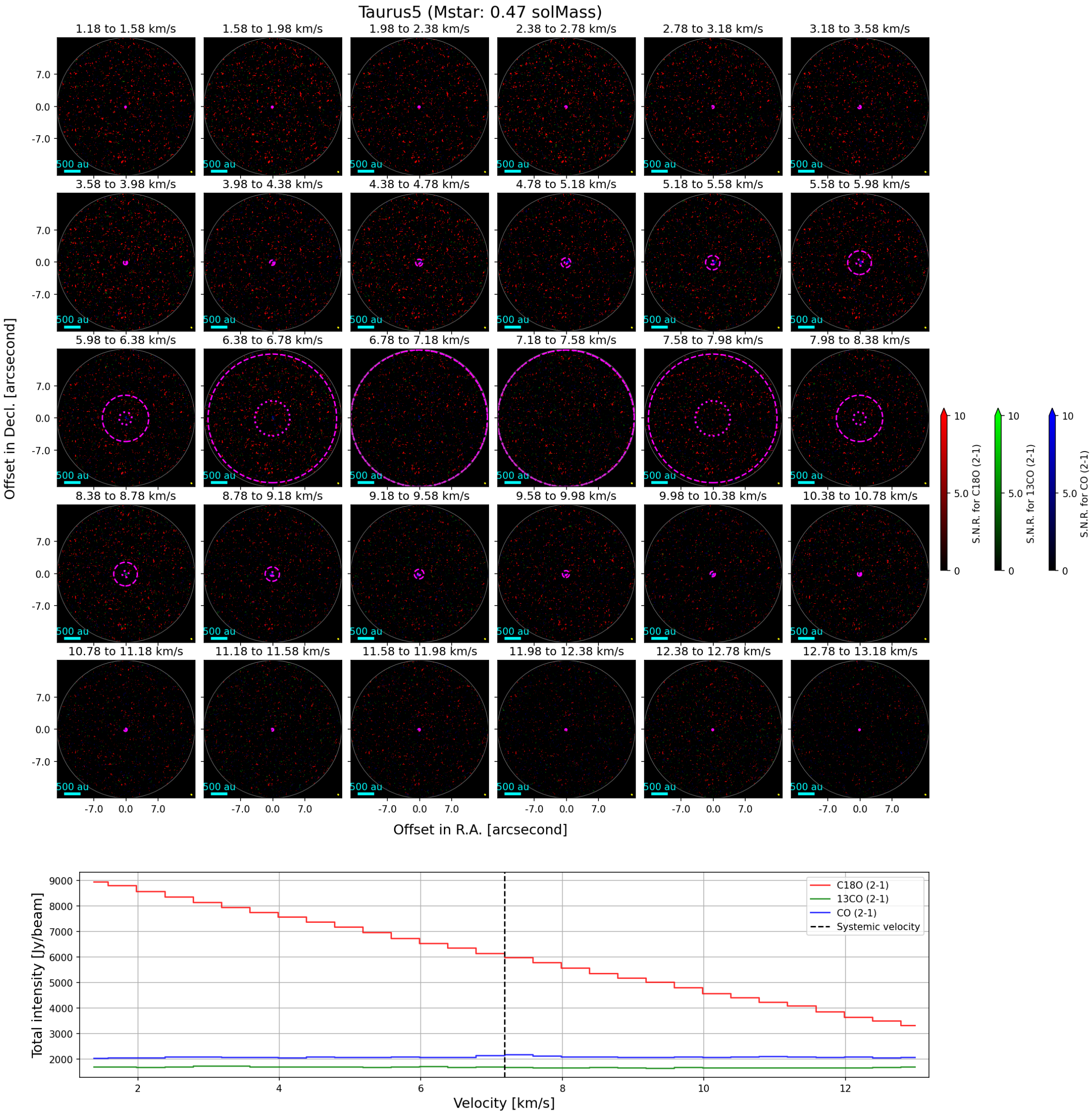

Figure C.59: CO (2–1), ^{13}CO (2–1), and C^{18}O (2–1) channel maps (top panel) and integrated spectra (bottom panel) for Taurus5. See Figure C.1 for more details.

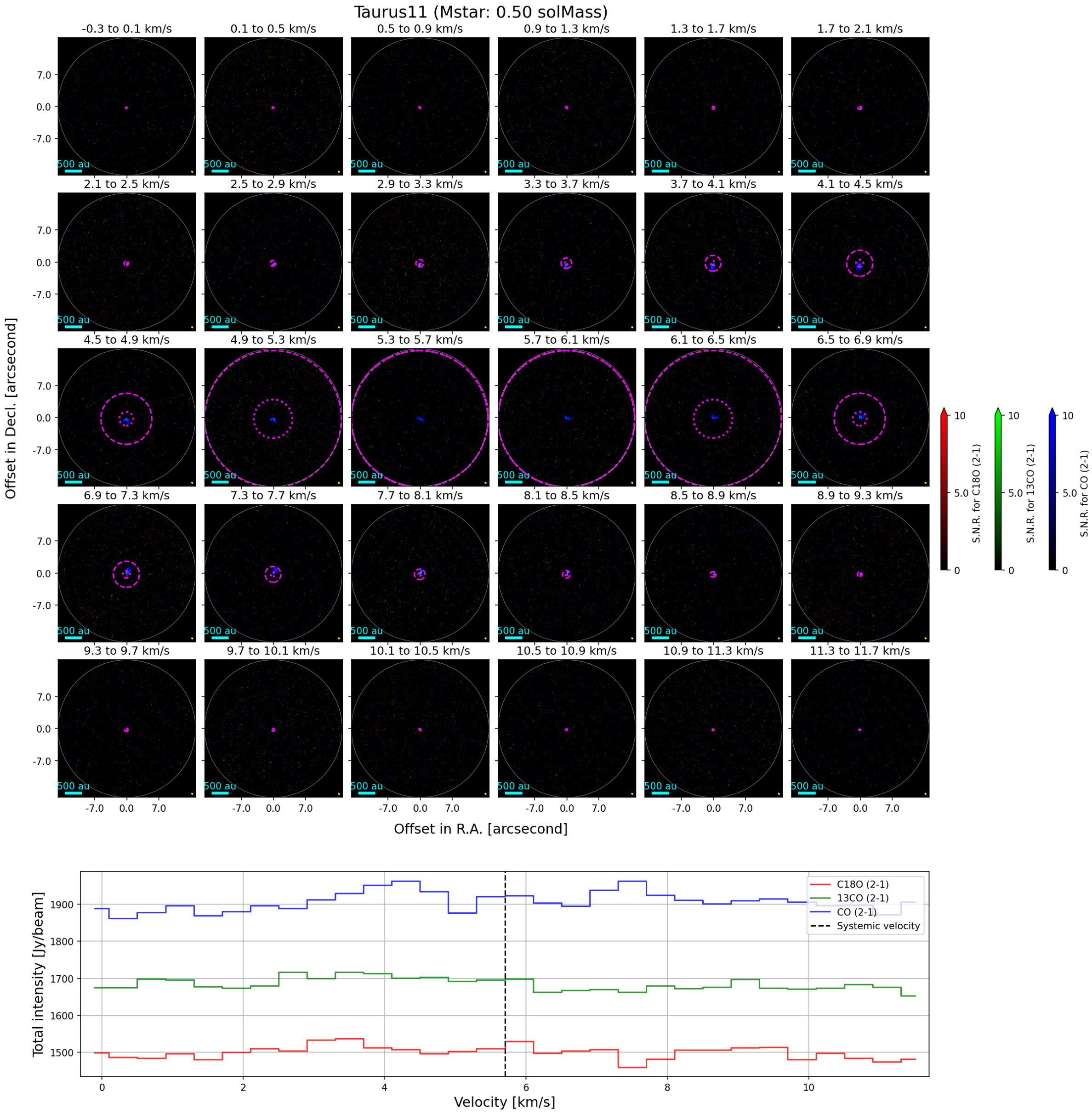

Figure C.60: CO (2–1), ^{13}CO (2–1), and C^{18}O (2–1) channel maps (top panel) and integrated spectra (bottom panel) for Taurus11. See Figure C.1 for more details.

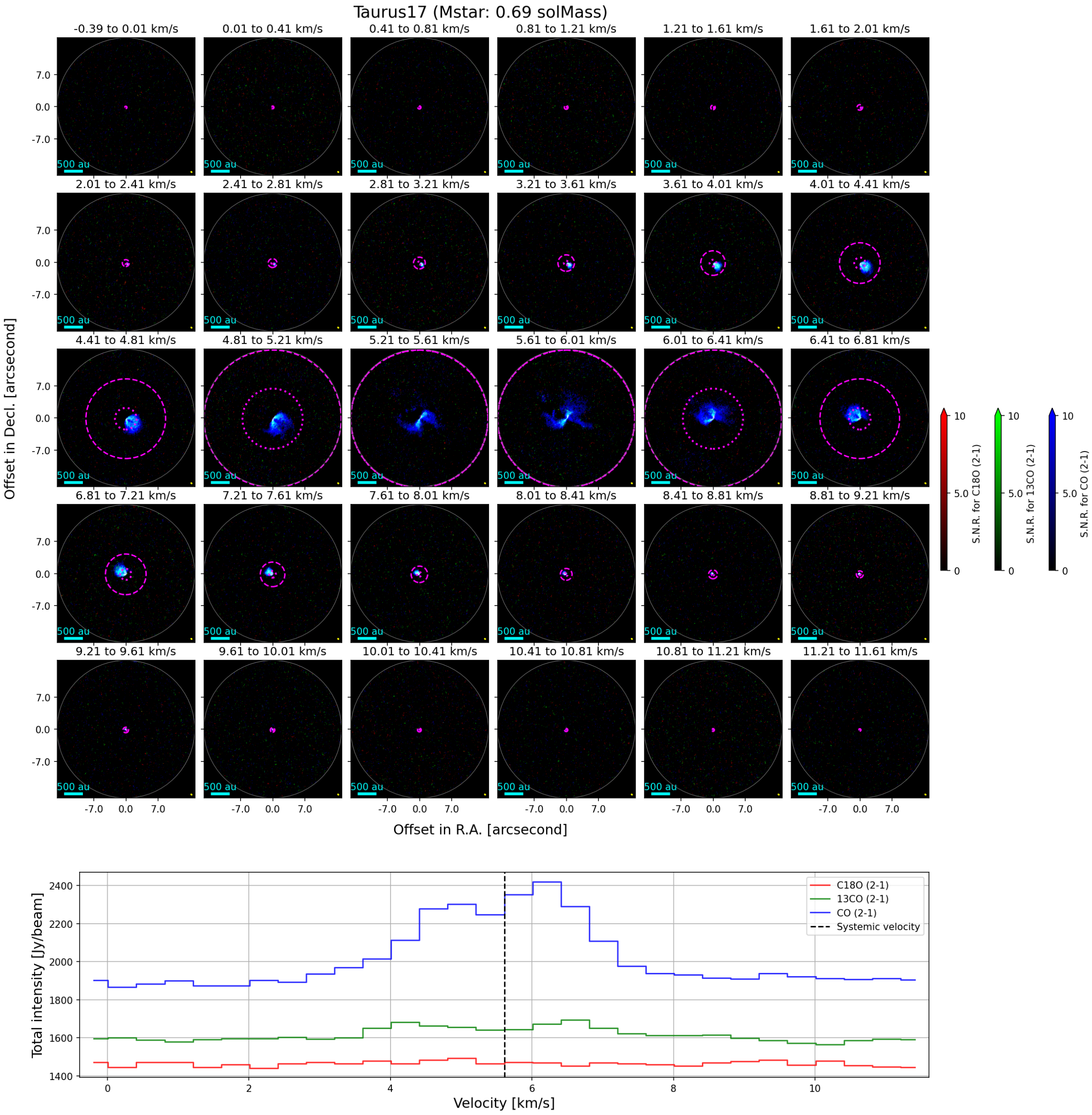

Figure C.61: CO (2–1), ^{13}CO (2–1), and C^{18}O (2–1) channel maps (top panel) and integrated spectra (bottom panel) for Taurus17. See Figure C.1 for more details.

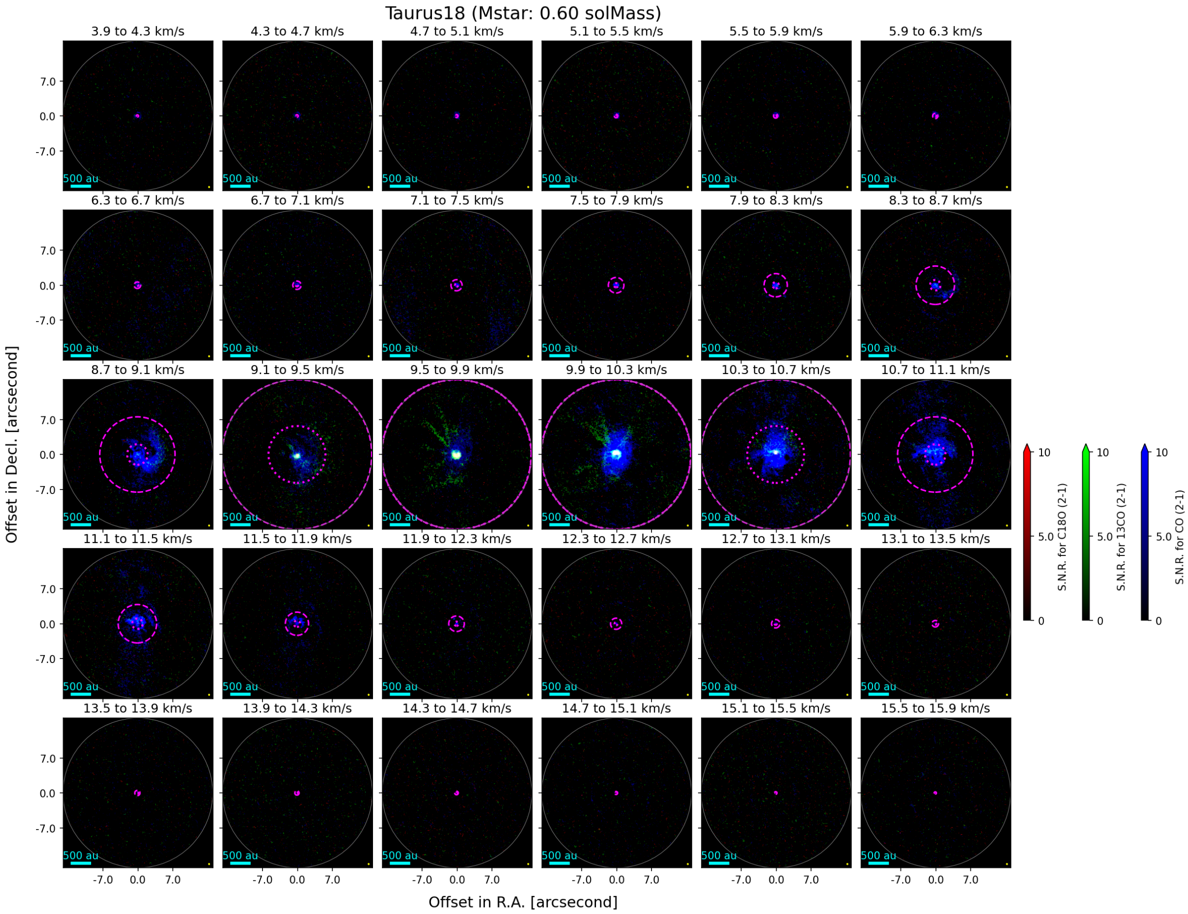

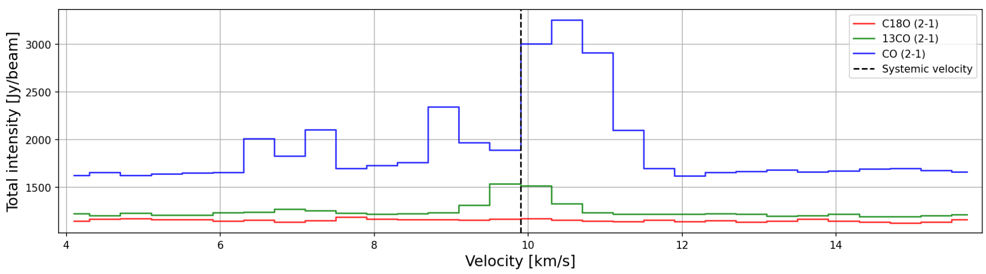

Figure C.62: CO (2–1), ^{13}CO (2–1), and C^{18}O (2–1) channel maps (top panel) and integrated spectra (bottom panel) for Taurus18. See Figure C.1 for more details.

Bibliography

ALMA Partnership et al., 2015, ApJ, 808, L3

Akeson R. L., Jensen E. L. N., Carpenter J., Ricci L., Laos S., Nogueira N. F., Suen-Lewis E. M., 2019, ApJ, 872, 158

Akiyama E., Vorobyov E. I., Liu H. B., Dong R., de Leon J., Liu S.-Y., Tamura M., 2019, AJ, 157, 165

Albrecht S. H., Dawson R. I., Winn J. N., 2022, PASP, 134, 082001

Alves F. O., Cleeves L. I., Girart J. M., Zhu Z., Franco G. A. P., Zurlo A., Caselli P., 2020, ApJ, 904, L6

Andrews S. M., et al., 2018, ApJ, 869, L41

Ankerst M., Breunig M. M., Kriegel H.-P., Sander J., 1999, SIGMOD Rec., 28, 49–60

Ansdell M., et al., 2016, ApJ, 828, 46

Ansdell M., Williams J. P., Manara C. F., Miotello A., Facchini S., van der Marel N., Testi L., van Dishoeck E. F., 2017, AJ, 153, 240

Ardila D. R., Golimowski D. A., Krist J. E., Clampin M., Ford H. C., Illingworth G. D., 2007, ApJ, 665, 512

Bae J., Hartmann L., Zhu Z., 2015, ApJ, 805, 15

Bae J., Isella A., Zhu Z., Martin R., Okuzumi S., Suriano S., 2023, in Inutsuka S., Aikawa Y., Muto T., Tomida K., Tamura M., eds, Astronomical Society of the Pacific Conference Series Vol. 534, Protostars and Planets VII. p. 423 (arXiv:2210.13314), doi:10.48550/arXiv.2210.13314

Balbus S. A., Hawley J. F., 1991, ApJ, 376, 214

Baraffe I., Vorobyov E., Chabrier G., 2012, ApJ, 756, 118

Barenfeld S. A., Carpenter J. M., Ricci L., Isella A., 2016, ApJ, 827, 142

Bate M. R., 2018, MNRAS, 475, 5618

Benisty M., et al., 2023, in Inutsuka S., Aikawa Y., Muto T., Tomida K., Tamura M., eds, Astronomical Society of the Pacific Conference Series Vol. 534, Protostars and Planets VII. p. 605 (arXiv:2203.09991), doi:10.48550/arXiv.2203.09991

Bergin E. A., et al., 2013, Nature, 493, 644

Bohn A. J., et al., 2022, A&A, 658, A183

Bondi H., 1952, MNRAS, 112, 195

Bondi H., Hoyle F., 1944, MNRAS, 104, 273

CASA Team et al., 2022, PASP, 134, 114501

Cacciapuoti L., et al., 2023, arXiv e-prints, p. arXiv:2311.13723

Casassus S., Perez M. S., Jordán A., Ménard F., Cuadra J., Schreiber M. R., Hales A. S., Ercolano B., 2012, ApJ, 754, L31

Cassen P., Moosman A., 1981, Icarus, 48, 353

Cazzoletti P., et al., 2019, A&A, 626, A11

Chevalier R. A., 1983, ApJ, 268, 753

Christiaens V., Casassus S., Perez S., van der Plas G., Ménard F., 2014, ApJ, 785, L12

Cohen M., 1980, AJ, 85, 29

Connelley M. S., Reipurth B., Tokunaga A. T., 2007, AJ, 133, 1528

Cuello N., et al., 2019, MNRAS, 483, 4114

Cuello N., Ménard F., Price D. J., 2023, European Physical Journal Plus, 138, 11

Dong R., Hall C., Rice K., Chiang E., 2015, ApJ, 812, L32

Dong R., et al., 2022, Nature Astronomy, 6, 331

Dullemond C. P., Küffmeier M., Goicovic F., Fukagawa M., Oehl V., Kramer M., 2019, A&A, 628, A20

Dunham M. M., Vorobyov E. I., 2012, ApJ, 747, 52

Dunham M. M., et al., 2014, in Beuther H., Klessen R. S., Dullemond C. P., Henning T., eds, Protostars and Planets VI. pp 195–218 (arXiv:1401.1809), doi:10.2458/azu_uapress_9780816531240-ch009

Dunham M. M., et al., 2015, ApJS, 220, 11

Endres C. P., Schlemmer S., Schilke P., Stutzki J., Müller H. S. P., 2016, Journal of Molecular Spectroscopy, 327, 95

Enoch M. L., Evans Neal J. I., Sargent A. I., Glenn J., 2009, ApJ, 692, 973

Gahm G. F., Petrov P. P., Tambovsteva L. V., Grinin V. P., Stempels H. C., Walter F. M., 2018, A&A, 614, A117

Gaia Collaboration et al., 2023, A&A, 674, A1

Galli P. A. B., et al., 2018, ApJ, 859, 33

Garg H., et al., 2021, MNRAS, 504, 782

Garufi A., et al., 2022, A&A, 658, A104

Garufi A., et al., 2024, A&A, 685, A53

Ginski C., et al., 2021, ApJ, 908, L25

Gupta A., Chen W.-P., 2022, AJ, 163, 233

Gupta A., et al., 2023, A&A, 670, L8

Gupta A., Miotello A., Williams J. P., Birnstiel T., Kuffmeier M., Yen H.-W., 2024, A&A, 683, A133

Hacar A., Clark S. E., Heitsch F., Kainulainen J., Panopoulou G. V., Seifried D., Smith R., 2023, in Inutsuka S., Aikawa Y., Muto T., Tomida K., Tamura M., eds, Astronomical Society of the Pacific Conference Series Vol. 534, Protostars and Planets VII. p. 153 (`arXiv:2203.09562`), doi:10.48550/arXiv.2203.09562

Haffert S. Y., Bohn A. J., de Boer J., Snellen I. A. G., Brinchmann J., Girard J. H., Keller C. U., Bacon R., 2019, Nature Astronomy, 3, 749

Hales A. S., et al., 2024, ApJ, 966, 96

Hall C., et al., 2020, ApJ, 904, 148

Harsono D., Alexander R. D., Levin Y., 2011, MNRAS, 413, 423

Haugbølle T., Padoan P., Nordlund Å., 2018, ApJ, 854, 35

Hennebelle P., Lesur G., Fromang S., 2017, A&A, 599, A86

Hsieh T. H., et al., 2023, A&A, 669, A137

Huang J., et al., 2020, ApJ, 898, 140

Huang J., et al., 2021, ApJS, 257, 19

Huang J., et al., 2022, ApJ, 930, 171

Huang J., Bergin E. A., Bae J., Benisty M., Andrews S. M., 2023, ApJ, 943, 107

Hubble E. P., 1922, ApJ, 56, 400

Hunziker S., et al., 2021, A&A, 648, A110

Ilee J. D., Greaves J. S., 2015, in European Physical Journal Web of Conferences. p. 00009, doi:10.1051/epjconf/201510200009

Jensen S. S., Haugbølle T., 2018, MNRAS, 474, 1176

Jørgensen J. K., Hogerheijde M. R., Blake G. A., van Dishoeck E. F., Mundy L. G., Schöier F. L., 2004, A&A, 415, 1021

Jørgensen J. K., Schöier F. L., van Dishoeck E. F., 2005, A&A, 435, 177

Joy A. H., 1945, ApJ, 102, 168

Kenyon S. J., Hartmann L. W., Strom K. M., Strom S. E., 1990, AJ, 99, 869

Kuffmeier M., Haugbølle T., Nordlund Å., 2017, ApJ, 846, 7

Kuffmeier M., Frimann S., Jensen S. S., Haugbølle T., 2018, MNRAS, 475, 2642

Kuffmeier M., Goicovic F. G., Dullemond C. P., 2020, A&A, 633, A3

Kuffmeier M., Dullemond C. P., Reissl S., Goicovic F. G., 2021, A&A, 656, A161

Kuffmeier M., Jensen S. S., Haugbølle T., 2023, European Physical Journal Plus, 138, 272

Kurtovic N. T., et al., 2018, ApJ, 869, L44

Kuznetsova A., Hartmann L., Heitsch F., 2019, ApJ, 876, 33

Kuznetsova A., Hartmann L., Heitsch F., 2020, ApJ, 893, 73

Kuznetsova A., Bae J., Hartmann L., Mac Low M.-M., 2022, ApJ, 928, 92

Larson R. B., 1969, MNRAS, 145, 271

Lebreuilly U., Hennebelle P., Colman T., Commerçon B., Klessen R., Maury A., Molinari S., Testi L., 2021, ApJ, 917, L10

Lee J.-E., et al., 2023, ApJ, 953, 82

Lesur G., 2021, Journal of Plasma Physics, 87, 205870101

Lodato G., Rice W. K. M., 2004, MNRAS, 351, 630

Magakian T. Y., 2003, A&A, 399, 141

Manara C. F., Morbidelli A., Guillot T., 2018, A&A, 618, L3

Manara C. F., Ansdell M., Rosotti G. P., Hughes A. M., Armitage P. J., Lodato G., Williams J. P., 2023, in Inutsuka S., Aikawa Y., Muto T., Tomida K., Tamura M., eds, Astronomical Society of the Pacific Conference Series Vol. 534, Protostars and Planets VII. p. 539 (`arXiv:2203.09930`), doi:10.48550/arXiv.2203.09930

Marean C. W., et al., 2007, Nature, 449, 905

Marton G., Tóth L. V., Paladini R., Kun M., Zahorecz S., McGehee P., Kiss C., 2016, MNRAS, 458, 3479

McKee C. F., Ostriker E. C., 2007, ARA&A, 45, 565

McMullin J. P., Waters B., Schiebel D., Young W., Golap K., 2007, in Shaw R. A., Hill F., Bell D. J., eds, Astronomical Society of the Pacific Conference Series Vol. 376, Astronomical Data Analysis Software and Systems XVI. p. 127

Mena M. T. V., 2024, Asymmetric infall beyond natal cores to protoplanetary disks, `http://nbn-resolving.de/urn:nbn:de:bvb:19-334538`

Mendoza S., Tejeda E., Nagel E., 2009, MNRAS, 393, 579

Mercimek S., et al., 2023, MNRAS, 522, 2384

Miotello A., 2018, PhD thesis, University of Leiden, Netherlands

Miotello A., et al., 2017, A&A, 599, A113

Miotello A., Kamp I., Birnstiel T., Cleeves L. C., Kataoka A., 2023, in Inutsuka S., Aikawa Y., Muto T., Tomida K., Tamura M., eds, Astronomical Society of the Pacific Conference Series Vol. 534, Protostars and Planets VII. p. 501 (`arXiv:2203.09818`), doi:10.48550/arXiv.2203.09818

Morbidelli A., Raymond S. N., 2016, Journal of Geophysical Research (Planets), 121, 1962

Mulders G. D., Pascucci I., Ciesla F. J., Fernandes R. B., 2021, ApJ, 920, 66

Murillo N. M., van Dishoeck E. F., Hacar A., Harsono D., Jørgensen J. K., 2022, A&A, 658, A53

Nanne J. A. M., Nimmo F., Cuzzi J. N., Kleine T., 2019, Earth and Planetary Science Letters, 511, 44

Nelson R. P., Gressel O., Umurhan O. M., 2013, MNRAS, 435, 2610

O'Dell C. R., Wen Z., Hu X., 1993, ApJ, 410, 696

Öberg K. I., et al., 2021, ApJS, 257, 1

Padoan P., Kritsuk A., Norman M. L., Nordlund Å., 2005, ApJ, 622, L61

Padoan P., Haugbølle T., Nordlund Å., 2014, ApJ, 797, 32

Pascucci I., et al., 2016, ApJ, 831, 125

Pedregosa F., et al., 2011, Journal of Machine Learning Research, 12, 2825

Pelkonen V. M., Padoan P., Haugbølle T., Nordlund Å., 2021, MNRAS, 504, 1219

Pfalzner S., Dincer F., 2024, ApJ, 963, 122

Pineda J. E., Segura-Cox D., Caselli P., Cunningham N., Zhao B., Schmiedeke A., Maureira M. J., Neri R., 2020, Nature Astronomy, 4, 1158

Pineda J. E., et al., 2023, in Inutsuka S., Aikawa Y., Muto T., Tomida K., Tamura M., eds, Astronomical Society of the Pacific Conference Series Vol. 534, Protostars and Planets VII. p. 233 (arXiv:2205.03935), doi:10.48550/arXiv.2205.03935

Pinte C., Teague R., Flaherty K., Hall C., Facchini S., Casassus S., 2023, in Inutsuka S., Aikawa Y., Muto T., Tomida K., Tamura M., eds, Astronomical Society of the Pacific Conference Series Vol. 534, Protostars and Planets VII. p. 645 (arXiv:2203.09528), doi:10.48550/arXiv.2203.09528

Rein H., Liu S. F., 2012, A&A, 537, A128

Ribas Á., Bouy H., Merín B., 2015, A&A, 576, A52

Robitaille T. P., Whitney B. A., Indebetouw R., Wood K., Denzmore P., 2006, ApJS, 167, 256

Rodriguez J. E., et al., 2018, ApJ, 859, 150

Rosotti G. P., 2023, New Astron. Rev., 96, 101674

Schneider G., Wood K., Silverstone M. D., Hines D. C., Koerner D. W., Whitney B. A., Bjorkman J. E., Lowrance P. J., 2003, AJ, 125, 1467

Schöier F. L., van der Tak F. F. S., van Dishoeck E. F., Black J. H., 2005, A&A, 432, 369

Scicluna P., Rosotti G., Dale J. E., Testi L., 2014, A&A, 566, L3

Seifried D., Banerjee R., Pudritz R. E., Klessen R. S., 2013, MNRAS, 432, 3320

Shariff K., Gorti U., Melon Fuksman J. D., 2022, MNRAS, 514, 5548

Shu F. H., 1977, ApJ, 214, 488

Somigliana A., Testi L., Rosotti G., Toci C., Lodato G., Tabone B., Manara C. F., Tazzari M., 2023, ApJ, 954, L13

Stolker T., Dominik C., Min M., Garufi A., Mulders G. D., Avenhaus H., 2016, A&A, 596, A70

Tang Y. W., Guilloteau S., Piétu V., Dutrey A., Ohashi N., Ho P. T. P., 2012, A&A, 547, A84

Tanious M., et al., 2024, A&A, 687, A92

Terebey S., Shu F. H., Cassen P., 1984, ApJ, 286, 529

Testi L., et al., 2014, in Beuther H., Klessen R. S., Dullemond C. P., Henning T., eds, Protostars and Planets VI. pp 339–361 (arXiv:1402.1354), doi:10.2458/azu_uapress_9780816531240-ch015

Testi L., et al., 2022, A&A, 663, A98

Thieme T. J., et al., 2022, ApJ, 925, 32

Thies I., Kroupa P., Goodwin S. P., Stamatellos D., Whitworth A. P., 2011, MNRAS, 417, 1817

Throop H. B., Bally J., 2008, AJ, 135, 2380

Tobin J. J., Hartmann L., Bergin E., Chiang H.-F., Looney L. W., Chandler C. J., Maret S., Heitsch F., 2012, ApJ, 748, 16

Tokuda K., et al., 2018, ApJ, 862, 8

Toomre A., 1964, ApJ, 139, 1217

Ulrich R. K., 1976, ApJ, 210, 377

Unno M., Hanawa T., Takasao S., 2022, ApJ, 941, 154

Valdivia-Mena M. T., et al., 2022, A&A, 667, A12

Valdivia-Mena M. T., et al., 2023, A&A, 677, A92

Valdivia-Mena M. T., et al., 2024, A&A, 687, A71

Virtanen P., et al., 2020, Nature Methods, 17, 261

Visser R., van Dishoeck E. F., Doty S. D., Dullemond C. P., 2009, A&A, 495, 881

Vorobyov E. I., Basu S., 2005, ApJ, 633, L137

Vorobyov E. I., Skliarevskii A. M., Elbakyan V. G., Takami M., Liu H. B., Liu S.-Y., Akiyama E., 2020, A&A, 635, A196

Welch W. J., Hartmann L., Helfer T., Briceño C., 2000, ApJ, 540, 362

Wilking B. A., Gagné M., Allen L. E., 2008, in Reipurth B., ed., , Vol. 5, Handbook of Star Forming Regions, Volume II. p. 351, doi:10.48550/arXiv.0811.0005

Williams J. P., Cieza L., Hales A., Ansdell M., Ruiz-Rodriguez D., Casassus S., Perez S., Zurlo A., 2019, ApJ, 875, L9

Wilson T. L., Rood R., 1994, ARA&A, 32, 191

Winter A. J., Clarke C. J., 2023, MNRAS, 521, 1646

Winter A. J., Benisty M., Andrews S. M., 2024, arXiv e-prints, p. arXiv:2405.08451

Yen H.-W., et al., 2014, ApJ, 793, 1

Yen H.-W., et al., 2017, A&A, 608, A134

Yen H.-W., Koch P. M., Manara C. F., Miotello A., Testi L., 2018, A&A, 616, A100

Yen H.-W., Gu P.-G., Hirano N., Koch P. M., Lee C.-F., Liu H. B., Takakuwa S., 2019, ApJ, 880, 69

Zapata L. A., Rodríguez L. F., Fernández-López M., Palau A., Estalella R., Osorio M., Anglada G., Huelamo N., 2020, ApJ, 896, 132

Zhang Y., et al., 2023, A&A, 672, A145

Zucker C., Speagle J. S., Schlafly E. F., Green G. M., Finkbeiner D. P., Goodman A., Alves J., 2020, A&A, 633, A51

van der Tak F. F. S., Black J. H., Schöier F. L., Jansen D. J., van Dishoeck E. F., 2007, A&A, 468, 627

Acknowledgements

I am extremely grateful to the many people who helped and supported me through the three years of my PhD, too many to mention all.

I want to start by thanking my amazing supervisor at ESO, Dr. Anna Miotello. The research presented in this thesis would not have been possible without her guidance and immense efforts. Beyond science, you taught me that good research does not have to come at the cost of work-life balance.

A big thanks to all the students, postdocs, and staff members of the Star and Planet Formation group at ESO for helping me with countless small and big problems. You all inspire me to be a better scientist.

I am extremely grateful to the ESO community for providing a wonderful environment that fostered not only my scientific but also personal growth. Special thanks to all the *Lost Souls of ESO* for lightening the stress of a PhD. I am deliberately avoiding taking names because there are too many, and I do not want to miss anyone.

I also want to thank my two great fellow mentors, Dr. Paula Sanchez Saez and Dr. Miguel Vioque, for always being there when I needed their advice.

A very big thanks to Nelma Silva for helping me adjust to ESO life from day one. It is hard to imagine my PhD journey without your help. Also, thank you to Adele Rickerby for carrying the legacy and making the complicated arrangements of my Chilean trip.

Huge thanks to all my wonderful collaborators. Your help was crucial for carrying out this novel research. Thanks to Prof. Til Birnstiel for agreeing to be my LMU supervisor and giving me very useful suggestions on my research. Thanks to Prof. Jonathan Williams for hosting me in beautiful Hawai'i, suggesting a great name for my first PhD paper, and encouraging me to develop TIPSY. Thanks to Dr. Michael Küffmeier for our many discussions about late-stage infall, which helped me better understand the importance of my work. Thanks to the DECO collaboration for all the tremendous amount of work they have done so far, without which my third chapter would not have been possible.

I am also very grateful to Akash Gupta, Durganshu Mishra, and all the other friends I had in Munich. You made it so much easier to adjust to life in this different continent. A big shoutout to all my friends elsewhere for adding fun to my life.

Finally, I want to thank my family for their constant support in this crazy endeavor of mine.